UNIVERSITY OF CALIFORNIA SAN DIEGO

Designs of Surface Acoustic Waves for Micro/Nano-scale Particles/Fluid Manipulation

A dissertation submitted in partial satisfaction of the
requirements for the degree
Doctor of Philosophy

in

Engineering Sciences (Mechanical Engineering)

by

Naiqing Zhang

Committee in charge:

Professor James Friend, Chair
Professor Prabhakar Bandaru
Professor Shengqiang Cai
Professor Hemal Patel
Professor Oscar Vazquez-Mena

2021

The dissertation of Naiqing Zhang is approved, and it is acceptable in quality and form for publication on microfilm and electronically.

University of California San Diego

2021

DEDICATION

To my fiancée, with all your love and support.

EPIGRAPH

Knowing yourself is the beginning of all wisdom.

—Aristotle

TABLE OF CONTENTS

LIST OF FIGURES

LIST OF TABLES

ACKNOWLEDGEMENTS

First and foremost, I would like to thank my supervisor, Professor James Friend. He is always positive and encouraging me to think, ask, speak out, and perform my own ideas on the research projects. His kind discussions, sharp ideas, and reasonable suggestions kept me on the right track of research in engineering science throughout the entire five years. The way he thinks about problems and how he handles them has deeply affected me and will be with me in the future. More importantly, his kindness to people, enthusiastic lifestyle, and passion for science will be exemplary throughout my future life and career. I hope he would be always happy and healthy, besides his remarkable success and contribution in research work.

I would like to thank my dissertation committees, Professor Hemal Patel and Professor Prabhakar Bandaru for guiding my experiments and offering opportunities to collaborate with their students. I would like to appreciate my dissertation committees, Professor Shengqiang Cai and Professor Oscar Vazquez-Mena for their insightful comments and constructive suggestions which gains my research experience and improve this dissertation. I would like to thank Professor Ofer Manor in Israel for guiding my experimental and especially theoretical analysis in acoustic streaming. His profound knowledge largely helped the projects in my dissertation. I would like to thank Professor Vish Krishnan for helping me accelerate the projects and try to translate them into practical markets.

I would like to thank all the colleagues and collaborators I met and worked with in the past five years. I would like to thank all my labmates in MADLAB, Dr. Jeremy Orosco, Dr. Amihai Horesh, Dr. Cécile Floer, Dr. Gopesh Tilvawala, Dr. An Huang, Dr. Jiaying Wang, Jiyang Mei, Shuai Zhang, William Connacher, Aditya Vasan, Edward Aminov, Antoine Pallois, Wen Yue for their selfless guidance, effective discussions, and helpful insights in the research path. You all create a lovely, warm-hearted, and humorous lab that I could stay and forget about time and tiredness. I would like to thank all other collaborators, Dr. Juan P. Zuniga-Hertz, Dr. Elizabeth Yan Zhang, Yun Zhou, Mckenzie J. Fannon, and Peter Weigel for helping me on the research

projects.

I would like to thank all my friends I met in San Diego for helping my accommodation to this new city and bringing so much happy time and memories within these five years. I will miss those sports, games, restaurants, and chats with you guys.

Finally, I would like to acknowledge the support and love from my family. I would like to thank my parents for absolute support to what I would like to do. They both kept learning and trying to do all the best in their life, which also drives me to keep moving forward. I would like to thank my fiancée, Mengbi Yao, for her love, accompany, and support as always in these five years. Daily chats and encouragement mean a lot to me, especially in these COVID-19 days. It would eventually be the end of the long distancing and time jet-lag from USA to China. The completion of my dissertation will not be possible without her support all the time.

Chapter 1, in part, is a reprint of the materials as it appears in Lab on a Chip, 2021. William Connacher, Naiqing Zhang, An Huang, Jiyang Mei, Shuai Zhang, Tilvawala Gopesh, and James Friend. ”Micro/Nano Acoustofluidics: Materials, Phenomena, Design, Devices, and Applications” Lab on a Chip 18.14 (2018): 1952-1996. The dissertation author was the secondary investigator and author of this paper.

Chapter 2, in full, has been submitted for publication of the material as it may appear in the Journal of the Acoustical Society of America, Special Issue on the Theory and Applications of Acoustofluidics, 2021. Arik Singh, Naiqing Zhang, and James Friend. “An Investigation of Maximum Particle Velocity as a Universal Invariant — Defined by a Statistical Measure of Failure or Plastic Energy Loss for Acoustofluidic Applications”, Journal of the Acoustical Society of America, Special Issue on the Theory and Applications of Acoustofluidics, 2021. The dissertation author was the secondary investigator and author of this paper.

Chapter 3, in full, is a reprint of the materials as it appears in IEEE Transactions on Ultrasonics, Ferroelectrics, and Frequency Control, 2020. Naiqing Zhang, Jiyang Mei, Tilvawala Gopesh, and James Friend.“Optimized, Omnidirectional Surface Acoustic Wave Source: 152

Degree Y-rotated Cut of Lithium Niobate for Acoustofluidics", IEEE Transactions on Ultrasonics, Ferroelectrics, and Frequency Control, 67.10 (2020): 2176-2186. The dissertation author was the primary investigator and author of this paper.

Chapter 4, in full, is a reprint of the materials as it appears in Lab on a Chip, 2021. Naiqing Zhang, Juan P. Zuniga-Hertz, Elizabeth Yan Zhang, Tilvawala Gopesh, Mckenzie J. Fannon, Jiaying Wang, Yue Wen, Hemal H. Patel, and James Friend. "Microliter Ultrafast Centrifuge Platform for Size-based Particle and Cell Separation and Extraction using Novel Omnidirectional Spiral Surface Acoustic Waves", Lab on a Chip, 21.5 (2021): 904-915. The dissertation author was the primary investigator and author of this paper.

Chapter 5, in full, is a reprint of the materials as it appears in Micromachines, 2020. Naiqing Zhang, Yue Wen, and James Friend. "MHz-order Surface Acoustic Wave Thruster for Underwater Silent Propulsion", Micromachines, 11.4 (2020): 419. The dissertation author was the primary investigator and author of this paper.

Chapter 6, in full, is a reprint of the materials as it appears in Journal of visualized experiments: JoVE, 2020. Naiqing Zhang and James Friend. "Fabrication of Nanoheight Channels Incorporating Surface Acoustic Wave Actuation via Lithium Niobate for Acoustic Nanofluidics", Journal of Visualized Experiments: JoVE 156 (2020). The dissertation author was the primary investigator and author of this paper.

Chapter 7, in full, is a reprint of the materials as it appears in Physical Review Letters, 2021. Naiqing Zhang, Amihai Horesh, Ofer Manor, and James Friend. "Powerful Acousto-Geometric Streaming from Dynamic Geometric Nonlinearity", Physical Review Letters, 2021. The dissertation author was the primary investigator and author of this paper.

Chapter 8, in full, is a reprint of the materials as it appears in Advanced Science, 2021. Naiqing Zhang, Amihai Horesh, and James Friend. "Manipulation and mixing of 200 femtoliter droplets in nanofluidic channels using MHz-order surface acoustic waves", Advanced Science, 2021. The dissertation author was the primary investigator and author of this paper.

Chapter 9, in full, has been submitted for publication of the material as it may appear in the Journal of Micromechanics and Microengineering, Special Issue on Micro-Acoustics and Acoustofluidics, 2021. Naiqing Zhang, Amihai Horesh, Cécile Floer, and James Friend. "Unapodization: A method to produce laterally uniform surface acoustic waves for acoustofluidics", Journal of Micromechanics and Microengineering, Special Issue on Micro-Acoustics and Acoustofluidics, 2021. The dissertation author was the primary investigator and author of this paper.

VITA

2016	B. S. in Mechanics and Engineering Science, Peking University, China
2018	M. S. in Engineering Sciences (Mechanical Engineering), University of California San Diego, USA.
2021	Ph. D. in Engineering Sciences (Mechanical Engineering), University of California San Diego, USA.

PUBLICATIONS

Naiqing Zhang, Amihai Horesh, Ofer Manor, and James Friend. "Powerful Acousto-Geometric Streaming from Dynamic Geometric Nonlinearity", *Physical Review Letters*, Accepted, 2021.

Naiqing Zhang, Amihai Horesh, and James Friend."Manipulation and mixing of 200 femtoliter droplets in nanofluidic channels using MHz-order surface acoustic waves", *Advanced Science*, Accepted, 2021.

Naiqing Zhang, Juan P. Zuniga-Hertz, Elizabeth Yan Zhang, Tilvawala Gopesh, Mckenzie J. Fannon, Jiaying Wang, Yue Wen, Hemal H. Patel, and James Friend. "Microliter Ultrafast Centrifuge Platform for Size-based Particle and Cell Separation and Extraction using Novel Omnidirectional Spiral Surface Acoustic Waves", *Lab on a Chip*, 21.5 (2021): 904-915.

Naiqing Zhang, Jiyang Mei, Tilvawala Gopesh, and James Friend. "Optimized, Omnidirectional Surface Acoustic Wave Source: 152 Degree Y-rotated Cut of Lithium Niobate for Acoustofluidics", *IEEE Transactions on Ultrasonics, Ferroelectrics, and Frequency Control*, 67.10 (2020): 2176-2186.

Naiqing Zhang, Yue Wen, and James Friend. "MHz-order Surface Acoustic Wave Thruster for Underwater Silent Propulsion", *Micromachines*, 11.4 (2020): 419.

Naiqing Zhang, and James Friend. "Fabrication of Nanoheight Channels Incorporating Surface Acoustic Wave Actuation via Lithium Niobate for Acoustic Nanofluidics", *Journal of visualized experiments: JoVE*, 156 (2020).

Jiyang Mei, **Naiqing Zhang**, and James Friend. "Fabrication of Surface Acoustic Wave Devices on Lithium Niobate", *Journal of visualized experiments: JoVE*, 160 (2020).

William Connacher, **Naiqing Zhang**, An Huang, Jiyang Mei, Shuai Zhang, Tilvawala Gopesh, and James Friend. "Micro/Nano Acoustofluidics: Materials, Phenomena, Design, Devices, and Applications", *Lab on a Chip*, 18.14 (2018): 1952-1996.

An Huang, William Connacher, Mark Stambaugh, **Naiqing Zhang**, Shuai Zhang, Jiyang Mei, Aditi Jain, Sravya Alluri, Vincent Leung, Anushi E Rajapaksa, and James Friend. "Practical Microcircuits for Handheld Acoustofluidics", *Lab on a Chip*, (2021).

Gopakumar Kamalakshakurup, Mohammad Aghaamoo, Marzieh Ataei, **Naiqing Zhang**, and Abraham P. Lee. "Shear Dependent Micro-vortices in Liquid-Liquid Flow Focusing Geometry: A Theoretical, Numerical, And Experimental Study", *Physics of Fluids*, 33.3 (2021): 032016.

Zitian Chen, Yusi Fu, Fangli Zhang, Lu Liu, **Naiqing Zhang**, Dong Zhou, Junrui Yang, Yuhong Pang, and Yanyi Huang. "Spinning Micropipette Liquid Emulsion Generator for Single Cell Whole Genome Amplification", *Lab on a Chip*, 16.23 (2016): 4512-4516.

Arik Singh, **Naiqing Zhang**, and James Friend. "An Investigation of Maximum Particle Velocity as a Universal Invariant — Defined by a Statistical Measure of Failure or Plastic Energy Loss for Acoustofluidic Applications", *The Journal of the Acoustical Society of America, Special Issue on the Theory and Applications of Acoustofluidics* (Submitted).

Yun Zhou, **Naiqing Zhang**, Prabhakar Bandaru, and James Friend. "MHz-order Surface Acoustic Waveguide on Lithium Niobate via Microscale Valley-Hall Topological Insulators" (In prepare).

Naiqing Zhang, Amihai Horesh, Cecile Floer, and James Friend. "Unapodization: A method to produce laterally uniform surface acoustic waves for acoustofluidics", *Journal of Micromechanics and Microengineering, Special Issue: Micro-Acoustics and Acoustofluidics* (Submitted).

ABSTRACT OF THE DISSERTATION

Designs of Surface Acoustic Waves for Micro/Nano-scale Particles/Fluid Manipulation

by

Naiqing Zhang

Doctor of Philosophy in Engineering Sciences (Mechanical Engineering)

University of California San Diego, 2021

Professor James Friend, Chair

Surface acoustic wave (SAW) devices have become popular as a practical and effective tool for fluid manipulation, particle/cell sorting and separation in various acoustofluidics and biomedical applications. In this dissertation, we study basic concepts, materials, and designs of SAW for micro/nano-scale particles/fluid manipulation. We propose an optimized Y-rotated cut of lithium niobate for multi-directional SAW propagation, simultaneously minimizing the anisotropic effects while maximizing electromechanical properties.

In microscale acoustofluidics, first, we present a novel omnidirectional spiral SAW design to rapidly rotate a microliter sessile drop to $\sim 10g$, producing efficient multi-size particle separation. We further extract the separated particles for the first time, demonstrating the ability to

target specific particles. Red blood cells and platelets within mouse blood are further demonstrated to be separated with a purity of 93% and 84%, respectively. Second, we describe a new method to measure the opposing force upon the object producing the acoustic radiation. Our example employs a 40 MHz SAW device as a pendulum bob while immersed in a fluid, measuring a 1.5 mN propulsion force from an input power of 5 W power to the SAW device.

In nanoscale acoustofluidics, first, in nanochannels of a height commensurate with the viscous penetration depth of the fluid, we find nonlinear interactions between the surrounding channel deformation and the leading order acoustic pressure field, generating flow pressures three orders of magnitude greater than any known acoustically-mediated mechanism. It enables the propulsion of fluids against significant Laplace pressure, sufficient to produce 6 mm/s flow in a 130–150 nm tall nanoslit. We find quantitative agreement between theory and experiment across a variety of fluids and conditions. Second, we present new regimes of acoustic wave interaction with 200 fL droplets of deionized water. By forming traps as locally widened regions along a fully transparent, high-aspect ratio, 130 nm tall, 20–130 micron wide, 5 mm long nanoslit channel, individual fluid droplets may be propelled from one trap to the next, split between them, mixed, and merged via 40 MHz-order SAW. A simple theory is provided to describe the mechanisms of droplet transport and splitting.

Chapter 1

Introduction

1.1 Background

The problems and promise of microfluidics have served to motivate researchers for over twenty-five years. Small volumes, fast processing, dynamic control, low costs, and hand-held devices compete with numerous difficulties in actuation, manipulation, and eventual integration into practical devices.[433] The goal is to replace each step in a macro-scale process with a micro-scale counterpart and then to seamlessly integrate these parts without compromising the advantages, all embodied by integrated devices that can be used by non-experts. In 2014, Sackmann et al.[328] raised the question: *Why hasn't microfluidics seen widespread adoption?* Becker[19] noted five years prior to that, in 2009, that the success of any new discipline hinges upon a "killer application", and that microfluidics still lacked one. In the eight years since, much has been accomplished in the discipline, with Becker and Gärtner[20] and others finally expressing a cautiously optimistic outlook.

However, an answer overlooked by many researchers is that much of the benefit of microfluidics is lost when actuation still must rely on an external bench-top pneumatic pump connected by a tangle of tubes—for example, the first figure in Whitesides' review. Such a system

is difficult to operate by an expert in a laboratory, let alone a non-expert with a hand-held version. Biological assays represent one of the most important applications for lab-on-a-chip devices, yet requires mixing—difficult via traditional microfluidics where laminar flow is difficult to overcome and diffusion is glacially slow. Passive mixers[205] offer solutions in some cases, but require complex architectures. A good argument was put forth by Collins *et al.*:[57] relying on spatially and temporally distant means of pressure reduces the dynamic control one has over microfluidic processes. Finally, Sackmann et al.[328] point out that macro-scale technologies have likewise been advancing and, in order to compete, microfluidics must do better than simply matching the performance of larger technology for the same tasks, a sort of *red queen*[416] evolutionary problem in developing and applying microfluidics technology. In this review, we will show that the actuation of fluids and particles via acoustic waves can overcome these hurdles and help fulfill the promise of microfluidics.

Vibration as a means to manipulate particles within fluids (and gases) has interested the scientific community since the work of Chladni*et al.*[51], Faraday *et al.*[103], and Kundt *et al.*[190]. Fluid actuation by acoustic waves is complex in analysis but simple in practice, with little hardware required to operate, and offers large actuation forces and force gradients. The seeds of acoustofluidics date from two centuries ago, and acoustics was considered a classic discipline as early as the 1960's. Few new areas of research had developed in acoustics until a recent and dramatic resurgence as a result of interesting results at small scales (*see* reviews on microscale acoustofluidics from Friend *et al.*[109], Ding *et al.*[89], Yeo *et al.*[457], and more recently Destgeer *et al.*[80]).

While some of the effects discussed in this review were known by Chladni, Faraday, Kundt, and their contemporaries, the acoustic devices available to them and fellow researchers until the 1960's were inadequate for small-scale applications. They were either underpowered, providing little more than laboratory curiosities like "quartz wind",[97] or generated ultrasound with wavelengths at centimeter to meter length scales from relatively large, inefficient, and strongly

heating transducers. These devices brought with them a collection of side effects from cavitation to weak acceleration unfortunately incompatible with micro/nano-scale fluidics.

Notably, the phenomenon of surface acoustic wave (SAW) propagation on a substrate was first reported by Lord Rayleigh in 1885,[304] but these were only properly produced with the maturation of microfabrication to form interdigital transducers (IDTs), thin finger-like electrodes formed upon a piezoelectric substrate as described by White and Voltmer in 1965.[432] Many of the most recent reports in micro/nano acoustofluidics have relied on SAW generation at tens to hundreds of MHz, which was not possible prior to IDTs and reduces the acoustic wavelength to a scale compatible with microfluidics. There is an ancillary effect that is arguably far more significant. Because the particle velocity in typical acoustic devices is limited to around 1 m/s regardless of size or frequency due to the limitations in material integrity, selecting higher operating frequencies allows a concurrent increase in particle acceleration, to as much as 10^8 m/s^2. It is this very large acceleration that is responsible for many of the observed effects in acoustofluidics.

1.2 Piezoelectric Materials and Electro-acoustic Waves

Microscale acoustofluidic actuation relies on the generation of acoustic waves in piezoelectric materials. The well-known *direct piezoelectric effect* generates electric charge upon the application of mechanical stress in certain materials; the generation of mechanical strain from the application of an electric field is the *inverse piezoelectric effect*.[168] Atoms or molecules present in the solid lattice structure of the material are either ions in the typical case[23,189] or have strong polarization—a separation of dissimilar charges, forming an electric dipole—in the case of some piezoelectric polymers such as poly-vinylidene fluoride (PVDF).[220,263] In single crystal piezoelectric media formed from ions, the ions exhibit miniscule, thermodynamically favorable misalignment that forms dipoles over each unit cell of the crystal material. This misalignment tends to be identically oriented throughout the crystal, and so its effect accumulates for each

repeated unit in the crystal as *polarization*, growing to become physically significant and present in a natural state as *remanent polarization*.[71] Polycrystalline piezoelectric material exhibits similar behavior, though the orientation of the "misalignment" is unique to the *domains*, one or more of which are present in each crystal grain that forms the material.[95] An extremely large voltage is applied to polycrystalline piezoelectric material in the desired polarization direction for a few minutes to several hours while immersed in an inert fluid[160,285] in order to reorient the polarization of each of these domains to generally lie along a particular direction. This step is necessary to form a useful piezoelectric coupling effect in any such media that lacks remnant polarization.

Piezoelectric materials have long been used to generate and detect acoustic waves. Rochelle salt and quartz were employed in the first large-scale application of piezoelectrics to acoustically detect submarines during World War I.[242] The earliest medical applications were for ultrasonic imaging of tissues in medicine.[93,232] High-power ultrasound has been applied in industrial mixing and cleaning, applications familiar to most researchers.[321,325] Other common uses include non-contact sensors and range-finders;[73,453] more recently, local harvesting of energy from motion to eliminate or reduce the need for batteries have driven innovative use of piezoelectric materials.[326] The simplest of all these piezoelectric ultrasonic devices tend to be driven at resonance via planar electrodes on both faces of a flat and thin piezoelectric element, itself polarized from one to the other planar electrode. These may be sandwiched into a rod to form a Langevin transducer,[195] and rarely other modes of vibration are used, usually to generate more complex motion necessary for actuators or motors.[110,426] Regardless of the application, the waves generated by piezoelectric media was generally limited to bulk acoustic waves (BAW) until the advent and broad acceptance of IDTs,[432] which enabled high frequency SAW. The demonstration by White and Voltmer of spatially periodic thin-film metal electrodes on a piezoelectric quartz bar to produce a traveling SAW was broadly taken up by the electronics industry for use in signal processing at frequencies ranging from 10 MHz to 1 GHz. "True" SAW or Rayleigh waves are

confined within three to four wavelengths of the surface of the material. Leaky SAW (LSAW),[401] Love waves,[130] Bleustein-Gulyaev waves,[130] surface skimming bulk waves (SSBW),[238] and surface transverse waves (STW)[374] are generally categorized as pseudo-SAW (PSAW), may have some limited applications in acoustofluidics, but mainly lie outside the scope of this review.

In order to generate high frequency acoustic waves, a panoply of piezoelectric materials have been used over the last 50 years. Polycrystalline piezoelectrics can be fabricated in more and simpler ways and have greater electromechanical coupling coefficients than single crystalline piezoelectrics, implying a greater ability to transform energy from one form to the other. However, single crystal materials have higher quality factors, and lower damping than polycrystalline materials, and so the choice of material in a given application is not straightforward.[56] Single-crystal piezoelectric media are however generally compatible with microfabrication facilities whereas, for example, lead zirconate titanate (PZT),[169] the most common polycrystalline ceramic piezoelectric material, is not. Furthermore, PZT is toxic, with significant excess lead oxide present along the grain boundaries,[30] and facing regulations that aim to eliminate it from use.[1] There have been some successes in eliminating lead while retaining good performance from polycrystalline ceramics, most notably those derived from potassium sodium niobate (KNN).[330] The granular nature of polycrystalline piezoelectrics limits their use to relatively low frequencies (O(1 kHz–1 MHz)) due to the finite size of the grains and domains within the material that strongly interact with the generation and propagation of acoustic waves at greater frequencies to generate heat.[411] Though some researchers over the years have synthesized polycrystalline ceramic piezoelectric materials with submicron grain size in an aim to increase the useful frequency range to 100 MHz or more,[177] these materials have not been widely employed. The likely reason is the existence of single crystal materials that operate at high frequencies (O(1 MHz–1 GHz)) with superior characteristics.

The materials most popularly used to make SAW devices include quartz, lithium tantalate (LT, $LiTaO_3$) and lithium niobate (LN, $LiNbO_3$). Others include gallium arsenide (GaAs),

cadmium sulfide (CdS), zinc oxide (ZnO), lithium tetraborate ($Li_2B_4O_7$), and langasite ($La_3Ga_5SiO_{12}$).[396] All piezoelectric materials are anisotropic, and because these choices are especially so, the type of wave generated from them is strongly dependent on the material orientation. White and Voltmer[432] used a Y-cut, Z-propagating quartz plate. Shortly after, in the late 1960's Bell Laboratories were credited for the development of lithium tantalate (LT) and lithium niobate (LN) which exhibit significantly stronger electromechanical coupling coefficients than quartz.[140,435] Due to its exceptionally high coupling coefficient relative to other single crystalline materials for SAW, LN has become ubiquitous for this application. Typically, wafers are obtained by growing a boule (*see* Fig. 1.1) of LN from a seed crystal with the desired orientation, which is cut into wafers of the required thickness.

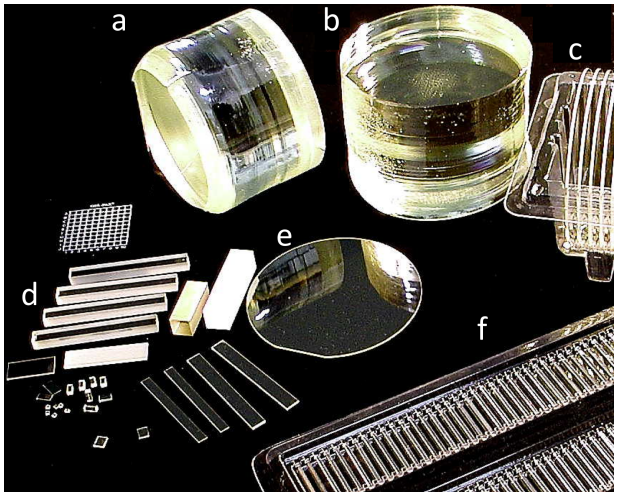

Figure 1.1: (a, b) A boule of LN, (c,e) with wafers and (d,f) other shapes cut for typical applications. *Image provided by Precision Micro-Optics, MA, USA.*

Initially, SAW devices were designed so that waves propagated along the symmetric crystal axes. Later on, as enhanced properties along different rotated cuts were discovered, these cuts gained popularity in various applications. In particular, the *Y*-cut, *Z*-propagating orientation of LN (YZ LN) was extensively used for SAW filters requiring Rayleigh waves. Due to the dependence of wave velocity on the propagation direction in an anisotropic material like LN, waves in rotated cuts propagating in a direction not aligned with a principal axis in the material

translate laterally in a phenomena known as *beam steering*.[241] With further studies, particularly the works of Takayanagi *et al.*[380] and Slobodnik *et al.*,[364] the 131° Y-rotated cut of LN was found to have exceptional electromechanical coupling and low beam steering and became widely used. However, this cut exhibited spurious parasitic waves, and in 1976, Shibayama et al.[351] determined that the 127.86° Y-rotated cut reduced the generation of these parasitic waves and consequently had the highest electromechanical coupling coefficient and lowest insertion loss. The 127.86° Y-rotated X-propagating cut of LN (128° YX LN) became the most popular and widely accepted orientation for applications requiring Rayleigh waves. Other cuts of LN have even higher electromechanical coupling coefficients, but these produce spurious modes and beam steering that preclude them from applications requiring "true" SAW. Among the other cuts, the 36°, 41°, and 64° Y-rotated cuts are the most popular. Table 1.1 lists some of the best-known cuts of LN and their electromechanical coupling constants, where $K^2 = 2\Delta v/v = 2\left(v_f - v_m\right)/v_f$. Here, v_f is the wave velocity in the free substrate and v_m is the wave velocity measured along a short-circuited plane.

Table 1.1: Commonly used cuts of LN and their corresponding electromechanical coupling coefficients and velocities. Reproduced with permission from Shibayama *et al.*,[351] Campbell,[36] Ciplys *et al.*,[53] Soluch *et al.*[369] and Hickernell *et al.*[148]

Cut	$2\Delta v/v$ (%)	Velocity (m/s)
YZ[53]	4.82	3488
ZX[53]	0.53	3798
ZY[53]	2.25	3903
XY[53]	3.58	3748
20° XY[369]	1.6	3727
120° XY[369]	4.1	3403
XZ[53]	5	3483
YX[53]	1.54	3769
36°[36] YX	16.7	4802
41° YX[148]	17.2	4752
64° YX[148]	10.8	4692
128° YX[351]	5.3	3992

Evidently, the 41° and 64° YX cuts of LN have higher electromechanical coupling coefficients than the 128° YX, however, these generate PSAW and not "true" SAW/Rayleigh waves. Cuts that produce non-Rayleigh SAW have been used to make SAW resonator filters[37] (64° YX) and delay lines for liquid sensors[145] (41° YX) among other applications.

The majority of research conducted with SAW for microfluidics has utilized 128° YX LN. Recently, there have been some studies which demonstrate the use of *X*-cut LN.[313] Materials most commonly used in acoustofluidics are anisotropic in nature due to their crystal structure. The 128° YX and *X*-cut LN, for example, can generate SAW of the same frequency and amplitude only in one direction. Any veering from the primary propagation direction is affected by beam steering and changes in frequency and electromechanical coupling coefficients. Kurosawa et al.[194] demonstrated this for a two-axis motor made using the 128° YX LN wafer, showing that the vibration displacement and velocity were 200% higher in the *X*-axis propagation direction compared to the *Y*-axis propagation direction. In order to overcome the anisotropic nature of the substrate, Guo *et al.*[131] and Devendran *et al.*[85] demonstrated perpendicular IDT pairs at 45° to the *X*-axis to create an orthogonal standing wave of the same frequency. However, the issue of *beam steering* remains. The superior electromechanical coupling present along the X axis and the unmatched wave velocities along the X and Y axes contribute to wave propagation with a lateral component. As a result, high frequency SAW devices made using LN substrates are limited to a single direction for acoustic wave propagation if optimal performance is desired.

1.2.1 Acoustic Wave Measurement

A laser Doppler vibrometer (LDV) is an interferometer that uses the Doppler effect to measure vibrations. When light encounters a moving surface, the reflected light incurs a frequency shift depending on the velocity of the surface and the wavelength of the light. In an LDV, the laser is split into a reference beam, directed straight to the photodetector; and a measurement beam, which reflects off the vibrating surface before being combined with the reference beam at

the photodetector. This superposition creates a modulated signal, thus revealing the Doppler shift in frequency (*see* Fig.1.2. Signal processing and analysis provide the vibrational velocity and displacement of a point on the surface in the direction normal to the surface. The in-plane motion can be measured using a different configuration where two measurement beams impinge on a spot with an angle between them, thus yielding interference fringes, though other methods exist[119]. As well, the LDV can be operated in scanning mode so that sequential measurement at many points reveals the vibrational motion of a portion of the surface with desired resolution. These and other advances are covered by Castellini et al.[41] and a more recent review was published by Rothberg et al.[324].

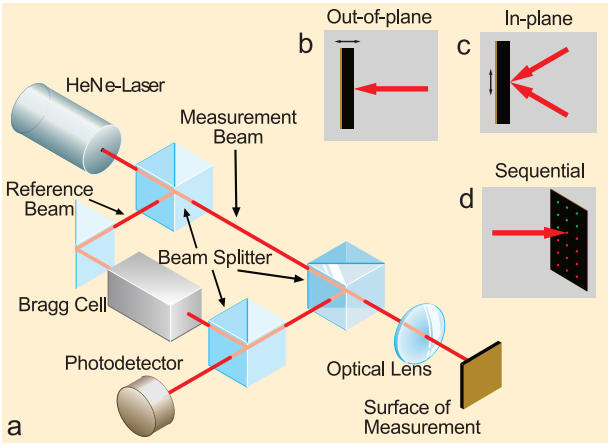

Figure 1.2: a) The interaction of the reference and measurement beams to produce a Doppler shift at the photodetector in this configuration of a Polytec laser Doppler vibrometer. b) Out-of-plane vibration measured by a single beam normal to the surface. c) In-plane vibration measured by two beams aimed at the same point with an angle between them. d) Sequential measurement, which is used to obtain the vibration of the surface in phase.

The LDV has been extensively used in aerospace,[40] automotive,[15] and hard disk drive[471] industries, and for land-mine detection.[327] The technology has also been broadly accepted for use in microelectromechanical systems (MEMS) applications.[431] In the context of acoustofluidics, the LDV is well-suited to measure and characterize vibrational motion in the solid surfaces of devices. While the primary aim is usually the determination of the resonance frequencies and mode shapes of the devices (*see* Fig.1.3, the LDV can also be used to identify the type of waveform obtained:

Lamb, SAW, BAW, Love, etc. The piezoelectric coefficients (as discussed in Section 1.2) of materials used in acoustofluidics can also be measured with remarkable accuracy.[146] Due to the high frequencies and small amplitudes involved (especially in SAW), measurement of the vibration driven velocity has been vital for analytical validation which would otherwise be impossible at the micro/nano scale. This capability has been particularly useful for characterization of nanofluidic devices[247] and cantilevers for atomic-force microscopy (AFM).[329] The technology can also be applied to identify vibrations on fluid surfaces[108] and even in air flow.[417] This capability has been helpful in studying fluid atomization and particularly in confirming the absence of the well-known Faraday wave response at half the excitation frequency.[24]

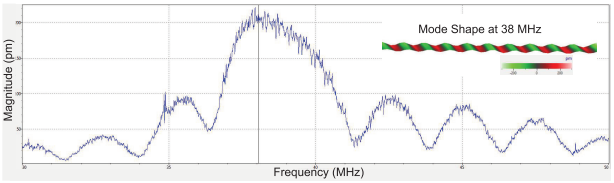

Figure 1.3: The resonance mode of a SAW device is revealed by this graph of amplitude vs frequency at a single point over an averaging period while the device is driven with a multi-frequency signal. Once this resonance is known, a sequential measurement over a region of the surface while the device is driven a the resonance frequency reveals the vibration mode, SAW in this case.

The technology has some limitations and prevailing issues. The choice of interferometer design has important implications for the sensitivity and measurement range of the LDV, especially in scanning mode. For example, the Sagnac design is inherently more mechanically stable than others due its lack of moving parts (more detail on this topic was provided by Tachizaki[378]). Non-ideal behavior of the interferometer has been known to lead to significant error when measuring small displacements. This and other sources of error, particularly alignment-based error, are covered by Siegmund.[362] Unwanted light waves can interfere with the desired interaction between the reference and measurement beams—known as three-wave interference—but the artifacts of this can be predicted.[456] The vibration of rotating objects and the in-plane motion can likewise be measured, but the setup is relatively complex.[136]

Digital holographic (DH) microscopy has been investigated as an alternative to LDV. Data from a high density of points can be obtained simultaneously using DH but, so far it lacks the ability to provide continuous (non-stroboscopic) measurements at frequencies greater than 1 MHz. Poittevin et al.[292] provide a good introduction to the interested reader. He highlight two new papers in this area as indications of what may follow in the future.[203] demonstrate the ability to measure three dimensions of displacement in acoustic waves traveling in a solid simultaneously using three-color DH. Typically, particle tracking is accomplished by optical videography and particle image velocimetry (PIV), but[34] have applied DH to track particles in 3D that are moving under acoustophoresis. In the future, digital holography may enable new insights into previously well studied acoustofluidic phenomena.

1.2.2 Electronic Communication

The first widespread use of SAW was in wireless communication, playing a critical role in that industry to this day.[221] As filters and duplexers, they provide precise and sharp signal filtering and multiplexing[35,222]. These aspects are relevant to the lab-on-a-chip community for two reasons. First, they demonstrate applications where, like lab-on-a-chip devices, space is at a premium in handheld devices. Second, they indicate potential future routes of research in acoustofluidics lab-on-a-chip applications in analogy to the development of the technology for communications.

The working principle of SAW filters for communication[261] is illustrated in Fig. 1.4. An IDT (receiver) transfers the incoming electrical signal into SAW by the inverse piezoelectric effect,[255] where approximately 90% of the energy is transmitted in mechanical form and the remainder is transmitted in electrical form to the output transducer (transmitter), where the SAW is converted back to an electrical signal via the direct piezoelectric effect. The IDT design determines the characteristics of the SAW receiver-transmitter combination: a *filter*. The same basic principle has been used for SAW based biosensors, to be discussed in Section **??**. The

typical frequency response of a SAW filter is shown in Fig. 1.4(b). The desired signal shows least attenuated while the rest of the signals are strongly attenuated. This sharp filtering and high selectivity is what makes SAW filters popular in the wireless communication industry.[35,255] Fig. 1.4 shows the typical frequency response of a SAW duplexer, essentially a combination of two or more SAW filters[271] that provide one-way paths from the transmitter to the antenna to the receiver. The effort made in this discipline solved telecommunications problems at remarkably high frequencies, 1–100 GHz, and laid the groundwork for micro/nano acoustofluidics devices appearing today.

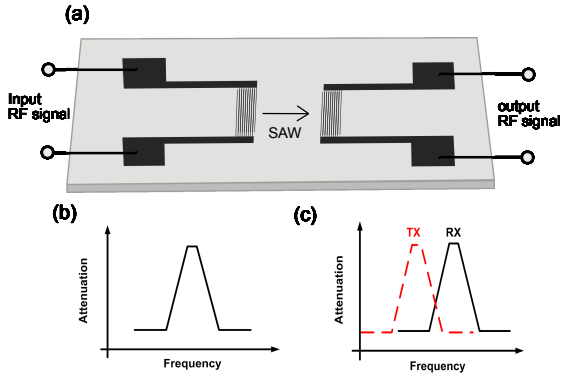

Figure 1.4: (a) The working principle of SAW devices in communication. A pair of IDTs are usually included, functioning as an input source (receiver, Rx) and output source (transmitter, Tx), respectively. Typical frequency characteristics of (b) Typical characteristics response of a SAW filters, and (c) SAW duplexers with similar characteristics as SAW filters shown to pass the signals at two different frequencies for cellular applications.

1.3 Electrode Design

Most acoustofluidic devices use either very simple thickness mode transducers are photolithographically patterned IDTs, which sometimes require complex micro-fabrication. Below we highlight two notable exceptions. Rezk *et al.* proposed a low cost alternative to photolithographic IDT fabrication. Aluminum foil electrodes were simply cut with scissors and clamped in place on a LN substrate to produce a Lamb wave device capable of producing flow in a channel,

mixing in a drop, and atomization from a drop.[309] It is likely that this type of electrode will significantly reduce performance due to poor electrical and mechanical contact, but may still be useful for some applications where cost and complexity are extremely limiting. Another alternative to expensive microfabrication was demonstrated by Nam and Lim[264] in the form of patterned conductive liquid, but this method was able to produce IDTs for SAW rather than Lamb waves. Nam fabricated channels in PDMS taking the negative shape of the intended IDT design and these were then filled with eutectic gallium indium. Azimuthal flow was achieved at 162 mW and colored dye could be mixed with a viscous, 25% glycerin solution within 1 second using 578 mW of power.

The substrate thickness is an important factor in IDT design, as it determines the minimum frequency of the SAW. Most suppliers provide 500 μm thick wafers, and the Rayleigh SAW is known to extend 4–5 λ into the substrate. This places a lower limit on the frequency suitable to form true Rayleigh SAW of about 40 MHz. Using frequencies below this value cause the acoustic wave to penetrate all the way through the substrate to the other side forming, alongside Rayleigh SAW, spurious Lamb waves that can shed energy through the back side of the substrate into its mounting and affecting the wave propagation and device performance. This is not merely a theoretical problem, as we have seen (in unpublished work) strong fluid transport in 20 MHz shear-horizontal SAW (SH-SAW) devices that should show no fluid transport at all. The 36° Y-rotated, X-propagating lithium tantalate cut used in this case also generated Lamb waves that appeared to be responsible for the confusing observations.

More importantly, much of the literature reports the generation of SAW at frequencies well below 40 MHz without noting or apparently being aware that this problem could arise. In our case, we were forced to use 20–30 MHz SAW for many years due to limitations of our laser Doppler metrology equipment, and fortunately this problem no longer exists.

In order to realize full miniaturization and widespread adoption, SAW microfluidics will require high power efficiency. Winkler *et al.* laid out the most important efficiency drains in these

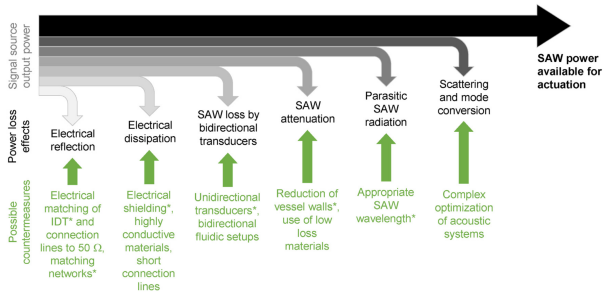

Figure 1.5: Power drains in typical SAW microfluidic devices along with proposed engineering solutions. Reprinted from Winkler et al. [437]

devices and proposed engineering solutions[437] (*see* Fig. 1.5). They covered optimal electrical impedance through IDT design, use of unidirectional IDTs, passive matching circuits, passivation and electrical shielding for submerged devices, and choice of wavelength based on geometry. Many of these solutions were utilized in a recent paper[438] demonstrating an atomization specific device, which will be discussed in section **??**.

Heating occurs in acoustofluidics since energy must inherently be dissipated on chip in order to produce fluid and particle motion and resistive heating can be minimized or controlled but never eliminated. This is sometimes considered an issue (e.g. evaporation in digital microfluidics), but can be controlled to support additional functionallity. Shilton *et al.* described the progress made in studying and using acoustofluidic heating, for example in PCR, in their paper on controlling and optimizing this phenomena.[358] Drops could be reliably heated to a stable temperature up to 12 degrees above room temperature within 3 seconds. The temperature increase was precisely controlled by the frequency and power. This heating was decoupled from the spurious resistive heating due to the IDT.

1.3.1 Straight IDTs

SAW are typically generated by applying an oscillating electrical signal matching the resonant frequency of the IDT. This signal translates into an acoustic wave via the inverse piezoelectric effect as described earlier. In the literature, frequencies in the range 1 MHz–1 GHz

have been used in the study of acoustofluidics, which correspond to wavelengths between 200 and 4 μm for the case of 128 $^\circ$ YX LN, implying a range of feature sizes of 50 to 1 μm. These feature sizes are typically microfabricated by photolithography and lift-off.[230]

The first and simplest IDTs[432] consisted of straight rectangular metal bars—referred to as fingers—deposited onto the surface of a piezoelectric substrate and alternately connected on either end to contact pads or "bus bars" as pictured in Fig. 1.6. This structure creates an array of electric fields of alternating direction between the transducer finger pairs that in turn create, via the inverse piezoelectric effect, alternating regions of compressive and tensile strain in the substrate. Each finger pair thus produces displacement in the substrate that oscillates with the electric field and radiates a SAW.[432] The periodicity of the finger pairs defines the wavelength of the resulting SAW (λ_{SAW}) such that the distance from one finger to the next is $\lambda_{\mathrm{SAW}}/4$. The surface wave velocity (v_R) depends on the material properties of the substrate, the propagation direction, and the thickness of the IDT. Consequently, the center frequency ($f_r = \omega/2\pi = v_R/\lambda_{\mathrm{SAW}}$) of a given device is determined by the choice of substrate, propagation direction, and IDT design.[79,432]

The thickness of the metal film that comprises the IDT, h, is typically chosen so that the film thickness ratio $h/\lambda_{\mathrm{SAW}} \approx 1\%$ so as to strike a balance between the efficient transmission of electric current in thicker films and the lower mass present upon the substrate for thinner films. Excessively thin films can cause premature finger failure and localized heating from ohmic losses,[289] while excessively thick or heavy films can reduce the resonance frequency of SAW in the IDT region compared to the surrounding region that have no fingers, unintentionally producing an acoustic cavity. Slightly thicker films, $h/\lambda_{\mathrm{SAW}} \approx 1\%$, are optimal in most cases for reflectors, structures that appear similar to IDTs but act to reflect the SAW on the piezoelectric surface to form an acoustic cavity or improve the device's efficiency. The details of IDT finger design, and the closely related details of SAW reflector design, are provided in substantial detail in Morgan *et al.*[255] and references therein.

As the SAW propagates through subsequent finger pairs, the wave is diffracted, creating a

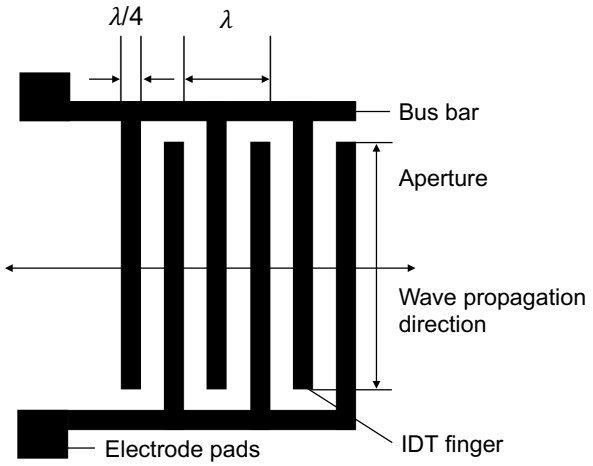

Figure 1.6: A SAW device consisting of comb-like interdigital transducers (IDT fingers), bus bars, and electrode pads on a piezoelectric substrate (e.g. 128–YX LN). The resulting traveling wave propagates as shown (perpendicular to the fingers), which can be observed using a laser Doppler vibrometer (LDV). The periodicity of the finger pairs defines the wavelength of the resulting SAW, λ_{SAW}.

near-field region of largely parallel wavefronts known as the Fresnel region. The far-field region, where the SAW is broadly diffracted along major and minor lobes, is known as the Fraunhofer region. To minimize diffraction losses, the aperture of the IDT must be contained within the Fresnel region. For design purposes, a Fresnel parameter (F) is defined as $F = 4\lambda_{\mathrm{SAW}} D_F / a^2$ where a is the aperture width (shown in Fig. 1.6) and D_F is the distance from the IDT edge. To remain within the Fresnel region, the aperture should be selected such that $F < 1$.

The efficiency of a SAW device is commonly linked to its quality factor,[442] $Q = f_r / \triangle f$, where $\triangle f$ is the width of the resonant peak in frequency space measured at one-half the peak's highest amplitude. The quality factor is influenced by dielectric losses of the piezoelectric materials, loading effects, ohmic losses, and acoustic leakage to the substrate. The number of finger pairs (N_p) of a SAW IDT is an important parameter partially due to its effect on the quality factor.[255] The other aspect that drives the choice of the number of finger pairs in a SAW IDT is the effective piezoelectric coupling coefficient of the substrate, which can be defined in terms of the change of SAW velocity from an open-circuit configuration to a short-circuit configuration,

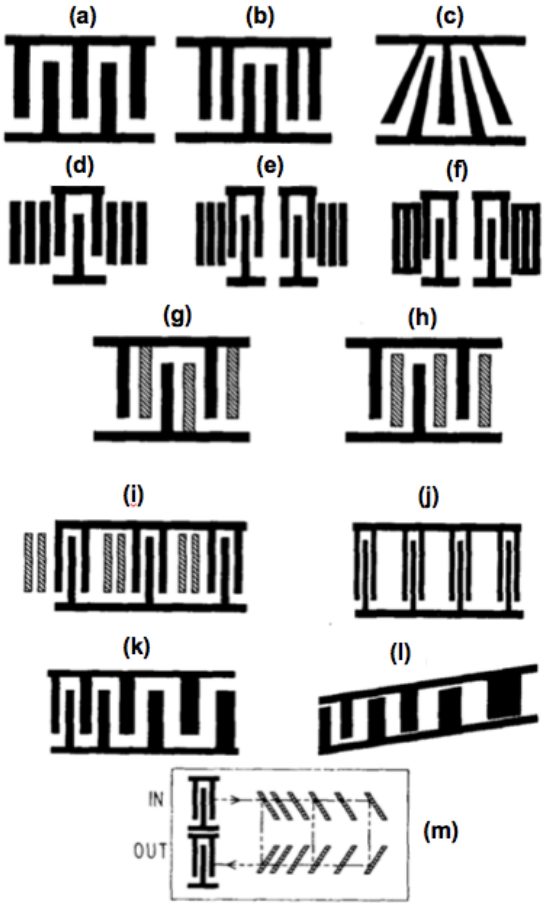

Figure 1.7: Common IDT designs for SAW devices: (a) single electrode IDT, (b) double electrode IDT, (c) slanted-finger IDT (SFIT) on collimating substrate shown with exaggerated tilt, (d) one-port resonator, (e) two-port resonator with open-circuited reflection-grating elements, (f) two-port resonator with short-circuited reflection-grating elements, (g) double-metalization single- phase unidirectional transducer (SPUDT), (h) floating-electrode SPUDT,(i) Lewis-type SPUDT,(j) "conventional" comb-filter, (k) chirped IDT, (i) chirped IDT for slanted-array compressor (SAC), and (m) geometry of a reflective array compressor using etched-groove reflectors. Reprint permis. Campbell (1989).[35]

divided by one-half of the average of that velocity, $2\Delta v/v$. The greater the coupling, the greater the amount of energy that can be transduced in the IDT to mechanical output as a SAW. The amplitude of the SAW increases with N_p up to a material dependent limit, but the bandwidth is likewise reduced. In signal processing applications, optimizing N_p is a complex procedure.[255] However, when the primary concern is transduction power alone, typical in acoustofluidics, the

constraints are simpler. For example, the bandwidth must only be sufficent to allow the device to be driven by signal generation and frequency response analysis equipment.

Optimization begins by defining the electrical admittance ($Y_t(\omega)$) of the IDT, which is dominated by capacitance (C_t), conductance ($G_a(\omega)$), and susceptance ($B(\omega)$), as in $Y_t(\omega) = G_a(\omega) + j(\omega)B(\omega) + j(\omega)C_t$. The equivalent circuit therefore consists of three components in parallel. When a voltage (V) is applied to the transducer, the power that is absorbed and produced are respectively defined as

$$P_a = \frac{1}{2} G_a V^2 \tag{1.1}$$

and

$$P_s = \frac{1}{4} \omega \varepsilon_\infty a N_p^2 \left(\frac{\triangle v}{v} \right) \left(\frac{\sin(x)}{x} \right)^2, \tag{1.2}$$

where ε_∞ is the capacitance per period of a unit-aperture, single electrode transducer, which depends on the substrate. At a certain frequency, the susceptance becomes negative and begins to counteract the capacitive term. When these terms cancel out, the admittance becomes real and directly corresponds to a resistive load, and also corresponds to the most efficient operation of the IDT. This occurs when the following equations are satisfied: $N_p = v\pi Q_t / 2\triangle v$ and $\triangle f / f_r = 1/N_p$. Therefore, N_p=21 for a single electrode IDT, as in Fig. 1.7(a), with a bandwidth of 0.05, while N_p = 26 for the double electrode IDT with a bandwidth of 0.038 on 128° YX LN (*see* Fig. 1.7 (b)).

Figure 1.7 depicts other commonly used IDT designs to fit different design requirements. The double electrode IDT (*see* Fig. 1.7(b)) eliminates the in-phase reflections produced by standard, single electrode IDTs by producing 180° phase shifted reflections that cancel out. The electrode sampling frequency changes from $2f_r$ to $4f_r$. Ma *et al.*[228] presented a self-aligned method to fabricate double electrode IDTs. The slanted-finger IDT (SFIT) (*see* Fig. 1.7(c)) is used to generate a wide-band response filter. The maximum angle that can be achieved depends on the coupling coefficient of the substrate. For example, the limit for a YZ LN substrate is 7° due to beam steering losses. The chirped IDT (*see* Fig. 1.7(k)) has a linear gradient in finger

spacing that allows it to resonate at a wide range of frequencies, allowing the excitation of SAW at different wavelengths by tuning the input signal. Another common method of reducing SAW efficiency loss due to in-phase reflection is by adding reflectors, as shown in Fig. 1.7 (d), (e), and (f). The reflectors are typically the same size as the fingers and are offset by one wavelength from the fingers. Finally, to decrease the reflection loss from a source or finite impedance, a single-phase unidirectional transducer (SPUDT) design is used to cancel out those reflections (Fig. 1.7(g)-(i)).[36,254] Normally waves radiate in both directions from an IDT, but SPUDTs radiate in only one desired direction, towards the right in Fig. 1.7.

1.3.2 Focused IDTs

Compared to the designs described in Fig. 1.7, focused IDTs (FIDTs) can generate SAW with higher intensity by laterally focusing the SAW energy towards the main axis of the IDT, producing what is called a higher beamwidth compression ratio, $\eta_c = W_b/w$, where W_b is the -3 dB transverse bandwidth and w is the equivalent aperture of the FIDT. They have been utilized in many applications, such as signal processing convolvers,[126,239,260] storage correlators,[127] and time-Fourier transformers.[434] High intensity acoustic fields can also be generated, and thus enhance the acoustic-electric effect in order to manipulate electron-hole pairs in GaAs quantum wells.[76] Later in this review we will see examples of their use in acoustofluidic devices.

The FIDTs were first introduced by Kharusi *et al.* in 1972.[181] They proposed a structure that consisted of a series of identical curved fingers, so-called conventional circular-arc-shaped FIDTs (*see* Fig. 1.8(a)), which focus the waves into a narrow rectangular region along the X propagation axis. They discovered that the degree to which the waves were focused and the focal length depended on the anisotropy of the substrate. Their results matched Cohen *et al.*'s finding[55] that the focal length is given by $R_f/(1-2b)$, where R_f is the finger curvature and b represents the anisotropy of the substrate material ($b = 0$ for an isotropic substrate). In addition, they emphasized that the focusing properties of conventional circular-arc-shaped FIDTs do not

improve as N_p is increased. Therefore, this type of FIDT was suggested to not be used on a highly anisotropic material, such as LN. In the 1980s, Fang et al.[101] calculated the amplitude field of circular-arc-shaped FIDTs on YZ LN and confirmed that the acoustic energy could be focused into a long, narrow region about the propagation axis on a substrate with high anisotropy (*see* Fang et al.[101], Fig. 3). Their results showed the beam compression ratio to be about 3% at a distance farther than R_f, which coincided with their experimental data. An important discovery in their work was that the actual focal point for SAW generated from a given set of fingers in the FIDT did not correspond with the geometric focal point. The anisotropy of the substrate typically causes the actual focal point for the SAW to lie up to two times farther away from the IDT than the geometric focal point.

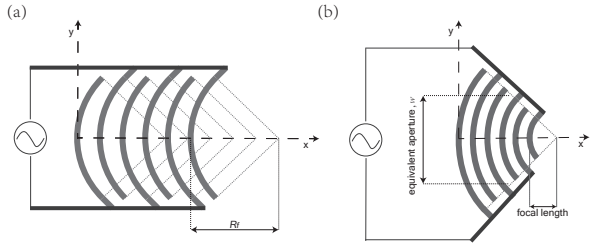

Figure 1.8: Commonly used FIDTs designs: (a) conventional circular-arc structure (characterized by R_f as curvature of transducer finger) and (b) concentric circular-arc structure (characterized by w as equivalent aperture). It shows clearly that the concentric design focuses to a point instead of a narrow region, resulting in better focusing property.

More recently, an alternative FIDT design was investigated by Wu et al.[448],[449] consisting of a series of concentric fingers (*see* Fig. 1.8(b)) that focus the waves to a single spot. These concentric-arc-shaped FIDTs produce higher SAW intensity and beamwidth compression ratios than the conventional circular-arc-shaped FIDTs. The intensity of the SAW is proportional to N_p^2—much stronger than the N_p dependence of a straight IDT with an equivalent aperture. So as N_p increases, concentric-arc FIDTs display a stable amplitude field and better focusing characteristics while the conventional circular-arc FIDTs become unsteady. Moreover, increasing the curvature of the arc does not increase the amplitude, but it does increase the compression

ratio, according to Wu *et al.*'s data.

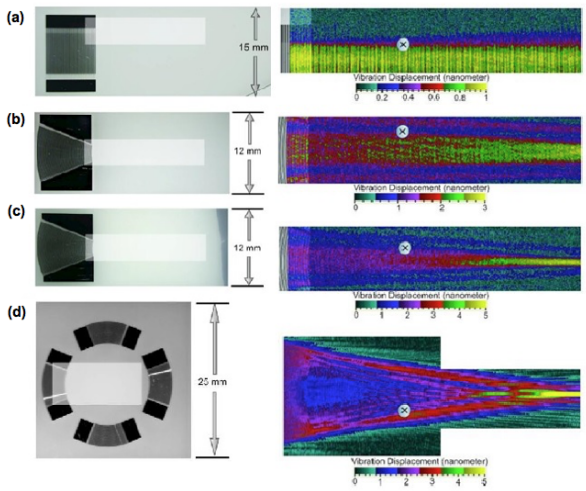

Figure 1.9: The distribution of SAW displacement on a LN substrate of different IDT designs at a center frequency of 30 MHz: (a) straight SPUDT, (b)&(c) focusing elliptical SPUDTs with approximate eccentricities of 0.616 & 0.831 respectively, and a (d) focusing circular SPUDT. It shows that the displacement of the SAW produced by straight SPUDT is uniform on the substrate, a line parallel to the propagation direction for the elliptical SPUDTs, and a single point with a circular SPUDT. Reprint permis. Shilton (2008).[354]

Like the traditional FIDT design, modified circular-arc FIDTs exhibit an actual focal point farther away than the geometric focal point due to the anisotropy of the material, as was discussed earlier in the section. Positive values of b in $R_f/(1-2b)$ tend to defocus the transducer, while negative values of b bring the focal plane closer toward the transducer. Shilton et al.[354] experimentally showed that a concentric-circular FIDT focused to a point $\sim$1.7 times farther than the geometric center (*see* Fig. 1.9 (d)). This agreed with earlier work in which Wu et al.[449] measured the amplitude vs propagation distance of various configurations of concentric FIDTs and concluded that the actual focal length was $\sim$1.5–1.8 times greater than the geometric focal length. Work done earlier by Kharusi *et al.*[181] recognized this phenomena and suggested another type of FIDT design, the group-velocity surface shape. This type of shape, as its name indicates, consists of points tracked by the end of the energy velocity vector and ensures that waves are focused to a single point despite the dependence of wave velocity on propagation direction

in an anisotropic material. The group-velocity surface pattern would become identical to the circular-arc pattern in the case of an isotropic surface. Further investigation by Wu *et al.*[448,449] revealed that this shape is indeed a superior focusing structure, producing a higher intensity and beam compression ratio than the concentric circular-arc shape. An efficient application of this group velocity design was reported by Laude *et al.*[202], as they constructed the IDTs in an fully annular shape following the wave surfaces for *Y* cut and *Z* cut LN. The generated SAWs were experimentally proven to greatly overcome the anisotropy of the piezoelectric substrates and converge to an intense spot at the center.

Besides curved and annular shape of FIDTs, there are more advanced designs worth mentioning. Riaud *et al.*[314] proposed an IDTs array (IDTA), which consisted of 32 unidirectional slightly curved IDTs placed along the wave surface of the substrate to compensate for beam steering. By tuning the input signal of each IDT using the inverse filter method Tanter et al.[390], the IDTA was reported to be able to not only focus the waves at an arbitrary position, but also generate swirling SAWs, with an even higher intensity at the center. Later on, an alternative design, called the single spiraling IDTs, was introduced by the same group[316], *see* Fig. 1.10, which encoded the SAWs like a hologram and induced acoustical vortices when there was fluid on the surface. Applications of these SAW devices will be further discussed in subsection 1.4.2.

Efforts have been made to visualize the amplitude field generated by FIDTs. Tan et al.[386] were able to directly visualize SAW using smoke particles with a mean diameter of 250 nm. The large transverse surface accelerations generated by SAW carry these particles aloft to relatively low vibration regions (*see* Fig. 1.11). Furthermore, Shilton et al.[354] showed SAW propagation patterns generated on a 128° YX LN surface for a straight SPUDT, concentric-elliptic SPUDTs with various eccentricities, and a concentric circular SPUDT by scanning the surface with an LDV (*see* section 1.2.1. Their results (*see* Fig. 1.9) offer clear visual evidence that curved IDT fingers focus SAW while straight SPUDTs do not. However, the smoke particle method allows measurement in larger frequency and amplitude ranges and does so in a shorter time compared to

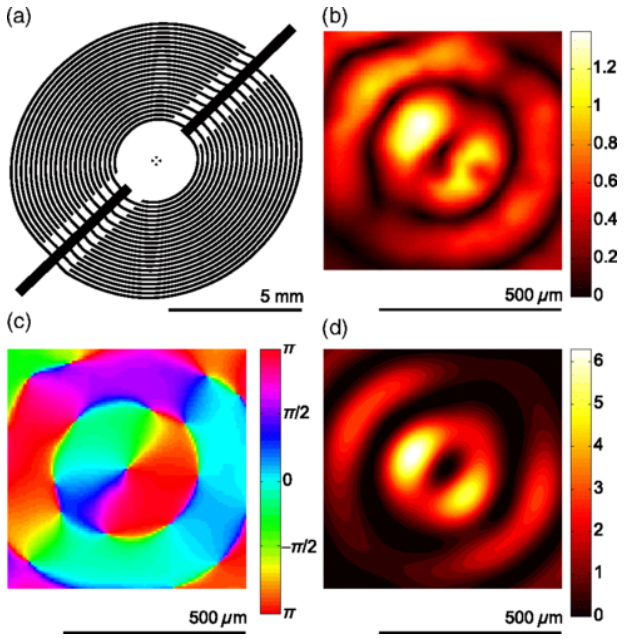

Figure 1.10: (a) Single spiraling IDTs design. (b) Experimental substrate vertical vibration amplitude (max amplitude 1.4 nm_{pp} at 7 V_{rms}). (c) Experimental substrate vertical vibration phase. (d) Calculated potential well from experimental data (max height 6.3 fJ). Figures are reprinted with permission from Riaud (2017).[316] Copyright (2017) American Physics Society.

LDV visualization. Rambach et al.[301] recently introduced another rapid and simple method of visualization using a wetting fluid film on the piezoelectric substrate, where film deformation was induced by acoustic radiation pressure causing a visible contrast between excited and non-excited areas. This method not only makes visualization of the sound path possible, but also possibly exposes the crystal anisotropy and SAW velocity.

The above contributions have allowed FIDTs to be widely employed in acoustofluidic applications where their high intensity and greater bandwidth compression ratio can be utilized. Sessile drop translation and merging, particle concentration and mixing, and cell sorting have all benefited from the use of FIDTs due to their ability to maximize the proportion of acoustic energy that results in efficient acoustic force gradients and acoustic streaming. These advances will be covered in Sections 1.4.2, 1.4.3, and 1.4.4.

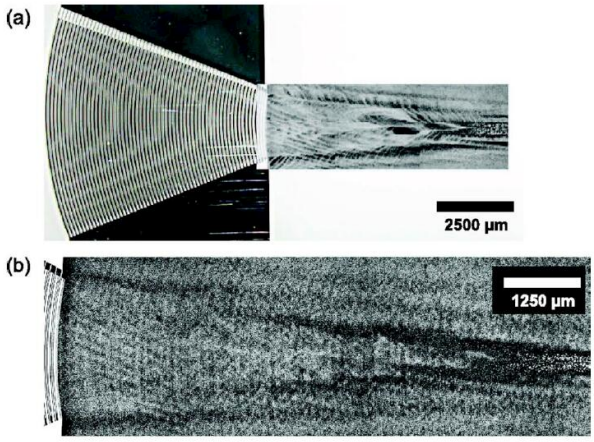

Figure 1.11: Visualization of SAW generated by FIDT with 250 nm sized smoke particles placed on the substrate after (a) 15 s exposure, and (b) after 30 s exposure. The distribution of pattern is achieved by the large transverse surface acceleration that carries the particles aloft to relatively quiescent regions nearby via acoustic streaming. Figures are reprinted with permission from Tan (2007).[385]

1.4 Microscale Acoustofluidics

1.4.1 Principles of Operation

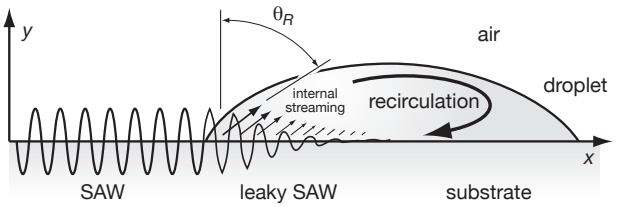

Figure 1.12: Sketch of a SAW acting on a small sessile drop. The acoustic energy is diffracted into the fluid at the Rayleigh angle, θ_R, leading to internal streaming in the small fluid volume, which drives recirculation. Adapted from Li et al.[207]

Surface acoustic waves propagate upon single crystal piezoelectric substrates with weak attenuation. Upon encountering a fluid on the surface (*see* Fig. 1.12), SAW "leaks" into the fluid, forming sound that propagates in the fluid and acting to quickly attenuate the SAW in the substrate. The mechanism of the acoustic energy attenuation is balanced by viscous attenuation and dialative dissipation. This can be described as: $\frac{\partial W}{\partial t} + \nabla \cdot J = \rho_0 v_o [b u_0 \cdot \nabla u_0 - u_0 \cdot \nabla \times \nabla \times u_0]$,

where W is the acoustic energy density, J is the energy flow, $\nabla \times \nabla \times u_0$ describe the viscous attenuation, and $u_0 \cdot \nabla u_0$ describe the dialative dissipation. The sound, a progressive longitudinal acoustic wave, travels through the liquid at a Rayleigh angle $\theta_R = sin^{-1}(v_l/v_R)$ [10], where v_l and v_R represent the speed of sound in the liquid and the speed of the Rayleigh SAW upon the solid substrate, respectively. For example, for the case of SAW traveling from 128° YX LN into water, v_l =1485 m/s and v_R = 3965 m/s, results in $\theta_R = 22°$.

Generally, the acoustic wave will turn into the media with a slower acoustic velocity, analogous to Snell's law. It is important to remember, however, that modal conversion can occur, allowing acoustic waves to travel across interfaces even when the Snell's law prediction suggests total internal reflection would occur, as explained in Hodgson et al. [150] where modal conversion from longitudinal acoustic waves (sound) in a fluid to Lamb waves in a superstrate are found. Furthermore, SAW likewise will leak into viscoelastic solids, particularly those typically used in microfluidics like polydimethylsiloxane (PDMS). While SAW devices can be used in enclosed microfluidics devices that employ PDMS, it is best to minimize the area of PDMS bonding to the piezoelectric substrate over the region carrying the SAW. Inexpensive alternatives to PDMS are possible to mitigate this problem, especially via the use of ultraviolet-sensitive, low-viscosity epoxies for layer bonding. [200]

The length along the surface of the piezoelectric substrate over which a Rayleigh wave decays by a factor of e due to the leakage of SAW into the fluid to transmit sound is the attenuation length $\alpha^{-1} \propto 1/f$: [10]

$$\alpha^{-1} = \frac{\rho_s v_R \lambda_{\mathrm{SAW}}}{\rho_f v_l}, \tag{1.3}$$

where ρ_f and ρ_s are the densities of the fluid and the solid respectively, v_l is the speed of sound in the fluid media and $v_R = f\lambda_{\mathrm{SAW}}$ is the Rayleigh wave phase velocity. The sound wave in the fluid, on the other hand, propagates uniaxially at the Rayleigh angle [209] and has a distinctly different

attenuation length, $\beta^{-1} \propto 1/f^2$:

$$\beta^{-1} = \frac{\rho_0 {v_l}^3}{4\pi^2 f_{\mathrm{SAW}}^2 \left(\frac{4}{3}\mu + \mu'\right)}, \tag{1.4}$$

where f_{SAW} is the SAW frequency and μ and μ' are the shear and bulk viscosities of the fluid, respectively. Values of the solid and fluid attenuation lengths in the LN-water system were measured by Dentry et al.[79] and are listed in Table 1.2.

Table 1.2: Attenuation length of the SAW surface displacement at the LN and water interface, expressed as α^{-1} (*see* Eqn. 1.3) and attenuation length of the sound in water, expressed as β^{-1} (*see* Eqn. 1.4). Reproduced with permission from Dentry (2014).[79]

f_{SAW}(MHz)	α^{-1}(mm)	β^{-1} (mm)
19.7	2.4	120
54.2	0.87	16
122	0.39	3.1
240	0.19	0.80
490	0.097	0.19
936	0.046	0.052

Attenuation of the sound in the fluid induces a momentum flux responsible for the formation of steady state fluid flow: acoustic streaming.[209,359] Acoustic streaming can be crudely classified depending on the acoustic path length permitted in the fluid and the location of viscous attenuation. Schlichting streaming is the result of viscous shear attenuation near the solid-fluid boundary[331] and Eckart streaming is the result of sound attenuation in the bulk of the fluid.[97] Rayleigh streaming arises from Schlichting streaming.[304] Further details on the types of streaming, their respective characteristics, and previous studies are summarized in Table 1 of the review by Friend and Yeo[109]. In cases where a free fluid surface is present, the nature of streaming and how it causes fluid transport is slightly more complex.[310] In later sections, we will explore how streaming produces fluid and particle motion.

Particle behavior in acoustofluidic systems is typically controlled by the following forces: direct and indirect (Bjerknes) acoustic radiation forces, viscous Stokes drag, van der Waals forces,

and electrostatics and electrodynamics. The latter two, van der Waals and electrically-driven forces, tend to be negligible in acoustofluidics, though there have been reports of combining these phenomena to achieve results not possible with acoustics alone. The direct SAW radiation force under a traveling wave was derived by King[186] and is expressed as:

$$F_{rt} = 2\pi\rho_0 A^2 \left(\frac{kr}{2}\right)^6 \left[\frac{1+\frac{2}{9}\left(1-\left(\frac{\rho_0}{\rho_p}\right)^2\right)}{2+\left(\frac{\rho_0}{\rho_p}\right)^2}\right] \tag{1.5}$$

where r is the particle radius, $k = \omega/v_R$ is the wavenumber of SAW, A is the amplitude of the incident wave, ρ_0 is the liquid density, and ρ_p is the particle density. On the other hand, the radiation force under a standing wave is expressed as:[458]

$$F_{rs} = \left(\frac{\pi p_0^2 r^3 \beta_w}{2\lambda_{\mathrm{SAW}}}\right)\left(\frac{5\rho_p - 2\rho_0}{2\rho_p + \rho_0} - \frac{\beta_c}{\beta_w}\right)(\sin(2kx)) \tag{1.6}$$

where p_0 is the acoustic pressure, x is the position of the particle, λ_{SAW} is the wavelength of SAW, and β_c and β_w are the compressibility of the particle and the surrounding fluid, respectively. Notice that the radiation force is proportional to r^6 for a traveling wave, but only proportional to r^3 for a standing wave. However, the reader should consult more recent literature by Bruus,[31] Lauga,[259] and Marston[237] to properly take into account fluid and particle compressibility and other important effects. We finally note that acoustic radiation interacts with surfaces in a more complicated way, demanding care in its treatment.[52]

The stream-wise drag experienced by a particle of radius r can be approximated by the Stokes drag equation, $F_D = 6\pi\mu r v_D$, where v_D is the velocity difference between the surrounding fluid and the particle. Finally, the Bjerknes force, an interparticle force arising from the scattering of the incident acoustic wave can be used to describe the interparticle interactions between

bubbles[69] or compressible particles[138,156,322,429]. The Bjerknes force is defined as:

$$F_B = 4\pi r^6 \left[\frac{(\rho_p - \rho_0)^2 \left(3\cos^2\theta - 1\right)}{6\rho_0 r^4} U^2 - \frac{\omega^2 \rho_0 (\beta_c - \beta_w)^2}{9L^2} {p_0}^2 \right] \tag{1.7}$$

where U is the particle velocity amplitude, L is the distance between two particles, θ is the contact angle between the fluid and particle, and p_0 is the acoustic pressure amplitude.

1.4.2 Fluid Manipulation in Sessile Drops

Sessile drops rest on top of a surface and have been successfully actuated by electrowetting, SAW, and even light using special photoresponsive surfaces,[196] forming virtual walls using optical illumination of photoelectric layers.[161,213] The dominant application of these technologies is in biological assays. The reader is referred to the review by Haeberle *et al.* for a comparison of these and other methods for microfluidic lab-on-a-chip platforms.[134] However, none of the other methods are capable of all the types of actuation described in this section.

Both acoustic streaming within the drop and acoustic radiation force on the free surface of the drop can be induced using SAW. Traveling SAW (TSAW) and standing SAW (SSAW) dominate the literature, but other acoustic modes are also useful in select situations. However, we note that acoustic waves in solids are not easily isolated so that unintended modes are often present. These waves, whether SAW or not, deliver sound into a sessile drop at the Rayleigh angle as described in Section 1.4.1, as long as the wave propagates from a region without the fluid to a region where the fluid is present. In general, the effect of the acoustic wave in the drop depends on the properties of the original wave in the substrate, the properties of the fluid, and the geometry of the drop. We break down manipulation into four regimes: mixing, translation, jetting, and atomization. For each regime, we highlight recent work regarding the basic understanding of the phenomena as well as recent advances in the associated applications. After mixing we pause to consider particles in sessile drops.

Mixing

Acoustic streaming at the Rayleigh angle produces recirculation in a stationary sessile drop (*see* Fig. 1.12). Almost fifteen years ago, Wixforth et al.[441] described the idea of an acoustically-actuated, miniaturized digital droplet lab on a chip, including sessile drop transport and internal mixing with recirculation. The primary internal flow promotes mixing in the drop, but is not generally helpful for other applications such as particle concentration as will be explained in Section 1.4.2. Li et al.[207] demonstrated that an azimuthal flow with a vertical component can be induced in a sessile drop from asymmetric SAW exposure on a LN substrate, driving vortical flow about a tilted axis.[298] Li et al.[207] provided several designs for generating asymmetric SAW as illustrated in Fig. 1.13.

Improvements have been made in producing internal flow in drops by exploring other types of acoustic waves. Shilton *et al.*[354] explored circular and elliptical FIDTs in a similar asymmetric exposure arrangement. Elliptically focused SAW produced more intense streaming and thus stronger primary internal flow while circularly focused SAW produced stronger azimuthal flow, concentrating the SAW power to a single small region of size comparable to the SAW wavelength, accentuating the effects of the asymmetric droplet placement.

Theoretical work on acoustic streaming, which induces mixing in sessile drops, was undertaken by Nyborg in the 1960s who suggested that the nonlinear hydrodynamic term due to the Navier-Stokes momentum equation could be neglected[275]. He argued that streaming and the resulting fluid velocity were both second order phenomena and thus the above term was fourth order and negligible. In the 1970s, Lighthill argued that the nonlinear term was only negligible for slow streaming[209]. Shiokawa followed Nyborg's use of an effective body force for calculating streaming velocity in the theory following his experimental work on manipulation of sessile drops using acoustic streaming[360]. Both authors neglect viscosity and argue that the attenuation, which is fundamental to streaming, comes mostly from refraction of the wave at the solid/fluid interface rather than from viscous attenuation.

Most modern numerical work on streaming has closely followed Shiokawa's procedure including a 3D simulation of low power mixing performed in 2010 by Alghane et al.[5]. They include the nonlinear hydrodynamic term, but continue to neglect viscosity. They experimentally measured the SAW amplitude as a function of input power and separately measured the streaming velocity as a function of input power. Then, in their numerical calculation, they determined streaming velocity in three spatial dimensions as a function of SAW amplitude and correlated these results to their experiments using a fitting relationship between the two measured quantities. The numerical and experimental results illustrate some simple flows in relatively large drops (30 uL) under relatively low power (up to 0.025 W).

In contrast, Vanneste and Bühler[418] contributed a numerical formulation of acoustic streaming that incorporates viscous attenuation. They derive three contributions to the resulting mean flow: internal Eulerian, boundary Eulerian, and Stokes drift. They point out that without viscous dissipation (as formulated above) Reynolds stress and the pressure gradient are balanced and there can be no mean flow generated in the interior. Instead of using the effective body force in the averaged momentum equation, they use an averaged vorticity equation due to Eckart[97]. The authors are able to apply their results to a variety of geometries, but their solutions are only in two dimensions. Importantly, neither of these two numerical simulations accounts for acoustic radiation force and the reflections that result from a finite boundary.

In 2014, Rezk et al.[311] were able to produce *poloidal* flow using a simplified transducer, a pair of L-shaped electrodes that generate Lamb waves. Poloidal flow only occurred above a critical frequency that was found to be dependent on the diameter of the drop. Lamb waves occur in the bulk of the substrate so their attenuation is different from that of SAW, but the concept is the same. The acoustic streaming-driven primary internal flow from the Lamb wave becomes poloidal flow only when both the acoustic energy impinges radially from all sides and the attenuation length of the Lamb wave in the substrate is less than the radius of the drop as in Fig. 1.14. Since the attenuation length is dependent on frequency, the existence of a critical frequency is due to the

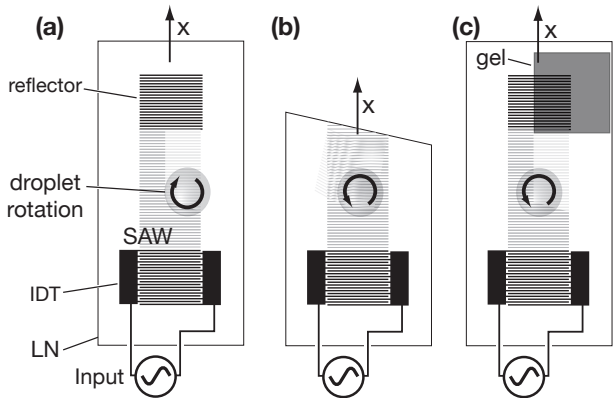

Figure 1.13: Three methods used to produce azimuthal flow via asymmetric SAW actuation. (a) Symmetry is broken offsetting the drop from the center line, (b) Asymmetry is generated from the angled edge of the LN substrate, and (c) Asymmetry is generated by absorbing SAW in one region, while reflecting them in another.

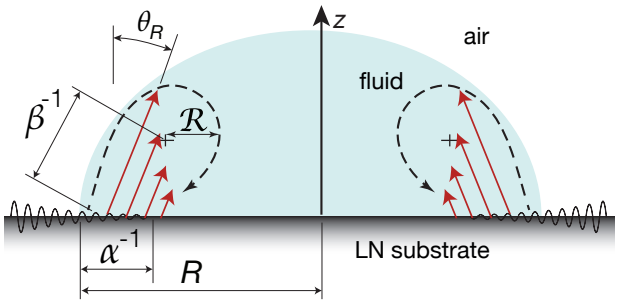

Figure 1.14: Poloidal flow is set up in a sessile drop due to the chosen ratio of drop radius, R, to recirculation length, $\mathcal{R}$, which depends on β, α, and θ_R. Corrected and adapted with permission from[309] Copyright (2014) American Chemical Society.

necessity of this attenuation length being less than the drop radius for the poloidal flow to exist.

At the same time, Riaud et al.[312] described a more complicated acoustic wave that they claim allows greater control over the internal flow. They suggested the use of helical waves (Bessel beams) to generate cyclone-like flow with both poloidal and toroidal streamlines. Theoretically, the shape of vortices in the fluid can be controlled by the boundary conditions of the fluid and the properties of the helical acoustic waves. Specifically, the axial vorticity is controlled by the acoustic field while the azimuthal vorticity is controlled by the boundary conditions. This result is analogous to the conclusions drawn above regarding internal flow produced by asymmetry and different wave-forms.[353] Riaud *et al.* argue mathematically that these effects are decoupled. This

implies that the variables can be independently chosen to produce desired internal flows. They also observed a curious phenomena: fluid flowed *away* from the acoustic energy source when the acoustic beam-width was small compared with the width of the fluid boundary, but flowed *toward* the source when the beam was confined. The authors call these repeller and attractor vortices respectively. The helical acoustic waves used to produce these flow effects can be generated using inverse filtering techniques. In fact, in another paper Riaud et al.[313] demonstrate the production of "swirling SAW" by an array of IDTs; in a more recent paper, Riaud et al.[316] also use these waves for particle manipulation.

Riaud et al.[315] also investigated the effects of viscosity on acoustic streaming flow, showing that it strongly affects the Eckart streaming in the bulk of the sessile drop and therefore should be considered even though it is absent from the velocity expression obtained by a balance of acoustic attenuation and fluid shear. This is an important improvement upon the traditional perspective perhaps best espoused by Lighthill *et al.*[209]: viscosity is crucial to acoustic streaming, yet its specific value is said to not affect the streaming characteristics. This work expands on the simulations by Vanneste *et al.* described earlier. They reproduced experimentally observed flow patterns in sessile drops actuated by SAW with hydrodynamic simulation and were able to show how this relates to the acoustic field. They found that the acoustic field that drives streaming is dominated by a small number of caustics despite the presence of a chaotic field (this chaotic field was quantified earlier by Shilton in the context of flow in microfluidic wells[355]). In the case of a sessile drop on LN they use scaling to reduce the problem to dimensionless numbers for surface attenuation and bulk attenuation that may be used to predict flow patterns in new situations.

One of the major advantages of sessile drop microfluidics is the extremely small sample volumes that are possible. Recently, Shilton et al.[357] were able to shrink the size of sessile drops while maintaining control of the flow for mixing, and Miansari *et al.*[247] were able to crudely manipulate 10 fℓ droplets in a nanoslit using SAW.

Generally, these devices are operated below a critical input power necessary to translate

the sessile drop across the substrate. This critical power depends on the contact line pinning of the drop, in turn dependent upon the wetting properties of the fluid/surface combination; for example, Shilton et al.[353] report the critical power for their arrangement to be 700 mW. Once identified for a given system, this critical power level represents the upper practical limit for inducing mixing, flow, or internal manipulation within the droplet.

Particle, Colloidal, and Cell Manipulation in Sessile Drops

The manipulation of micro-scale objects in fluid by SAW relies on both the acoustic streaming-induced flow described in the previous section and the acoustic radiation force and other forces introduced in section 1.4.1. Acoustic streaming depends upon the properties of the acoustic wave generated by the source and by the geometry and fluid properties of the drop. The size, density relative to the fluid, and compressibility of the particles determine the effectiveness of acoustic radiation forces upon them.

Concentration, separation, or isolation of target particles are typical needs in biochemical analysis. For dilute samples, an effective collection procedure for the targeted particles can significantly reduce the amount of fluid handling.[149] Particle concentration helps to minimize measurement noise and improve detection sensitivity. Acoustic forces can be used to non-invasively position, concentrate, or fractionate particles. In something of a scientific curiosity, standing waves were first identified by the concentration of suspended particles at acoustic pressure nodal or antinodal planes in a fluid by Kundt and Lehmann in 1874.[191] However, the process was slow, with concentration requiring at least several minutes. Recently, researchers have used SAW devices to accelerate and otherwise improve concentration, separation, and centrifugation.

The position of the particles in sessile drops vary with the drag force and acoustic radiation force applied to the particles. Destgeer *et al.* investigated four regimes of particle position[83]. A droplet with $R > \alpha^{-1}$ has reduced potential for symmetrical vortices. Droplet size and SAW

attenuation length also determine whether the acoustic radiation field produces standing waves or traveling waves in the case of counter-propagating IDTs. If $R > \alpha^{-1}$, then TSAW is generated from each side of the drop. If $R < \alpha^{-1}$, then standing waves are set up in the portion of the drop where overlap occurs.

As described in Section 1.4.2, Li produced azimuthal flow in a sessile drop. This type of flow allows particles to be rapidly concentrated at the center of the drop due to shear-induced migration. It is important to note that concentration was only observed in a range of applied power between 150–450 mW while dispersion was observed on either side of this range. This intermediate range of SAW power represents a Goldylocks state below which streaming does not overwhelm particle concentration and above which the particles are transported.[207] Li showed that bio-particles remained viable and were concentrated to within 10% of the drops volume under asymmetric SAW actuation. These results show promise for use in conjunction with the bio-sensors in order to reduce the sensitivity requirements among other applications.

Wilson *et al.* introduced a method using phononic superstrates to achieve programmable complex fluid manipulation on-chip.[436] The phononic structures can produce filter and waveguide effects by scattering and reflecting the SAW without fabricating multiple IDTs on the substrate. They chose a square array of circular holes made in a silicon wafer via dry-etch photolithography and demonstrated centrifugation of 10 μm polystyrene beads and blood cells in a droplet using either a filter-based design or a waveguide-based design. This technique may be useful in certain specialized applications where a single SAW device could be used for multiple types of manipulation depending on the superstrate, which could be switched out as desired. Later on, Riaud et al.[314] claimed an improved result from a set of 32 IDTs patterned in a circle and driven by a programmable circuit in order to effectively drive planar waves. They demonstrated droplet division, merging, and atomization with the platform. Moreover, they later demonstrated particle manipulation and positioning through careful control of the signals input into the IDTs.[316]

As mentioned earlier FIDTs can improve fluid actuation in SAW devices. Shilton found

that a concentric circular-arc SPUDT was capable of concentrating particles in microliter drops in under 1 second, which is an order of magnitude faster than the straight SPUDT.[354]

Destgeer et al.[84] have claimed that the conclusions made by Rezk *et al.* about their poloidal flow, Lamb wave device are incorrectly based entirely on acoustic streaming flow without due consideration of the acoustic radiation force. The experiments by Rezk included only one droplet size (1.5 mm) and single particle size (5 μm), whereas those by Destgeer included a range of particle sizes and droplet volumes, while both researchers varied frequency. Rezk claimed that shear-induced migration caused concentration within the poloidal vortex (*see* Fig. 1.16). Destgeer found that particles were only concentrated when a parameter representing the balance of radiation force to drag force, $\kappa = \pi d_p f_{LW}/c_f$, was greater than unity (*see* Fig. 1.15(a)). Here d_p is the particle diameter, f_{LW} is the frequency of the Lamb waves, and c_f is the speed of sound in the fluid. They were able to accurately predict which combinations of particle size and frequency would result in concentrated rings (*see* Fig. 1.15(b)). However, Destgeer et al.[84] failed to take shear migration into account, important in forming such a ring. It may be that poloidal flow is a necessary, but not sufficient condition for concentration in a ring shape, which requires radiation force. The studies agreed that increasing the frequency, and thus reducing the attenuation length in the substrate, moved the concentrated ring towards the perimeter of the drop. Regardless of the precise mechanism, these studies show that particles can be reliably concentrated to a narrow ring at a tunable radius in a sessile drop without the need for microfabricated IDTs.

Other researchers have also played with this balance between flow forces induced by streaming and direct radiation force in order to separate particles. Wood et al.[443] were able to efficiently separate and align different sized particles within a drop using SSAW. They fabricated two opposing IDTs with different resonance frequencies on a 128° YX LN substrate in order to set up a periodic distribution of pressure nodes. Rogers et al.[323] demonstrated using a 20 MHz device that relatively small particles (2 μm) for which drag force dominates were concentrated in the bulk of the drop, while large particles (30 μm) for which radiation force dominates were

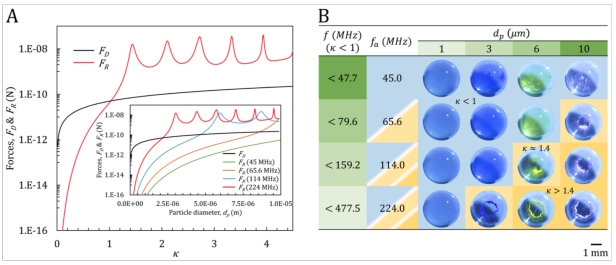

Figure 1.15: A) Force vs κ, where F_D is the drag force and F_R is the radiation force. Notice that F_R overtakes F_D at $\kappa = 1$. The inset shows the similar Force vs drop size relationship for various frequencies. B) Each image corresponds to a frequency, drop size pair and the values of κ for each pair are indicated to show that ring formation occurs for $\kappa > 1$, where radiation force dominates drag. Reprinted (adapted) with permission from G. Destgeer, B. Ha, J. Park and H. J. Sung, *Analytical Chemistry*, 2016, **88**, 3976–3981. Copyright 2016 American Chemical Society.

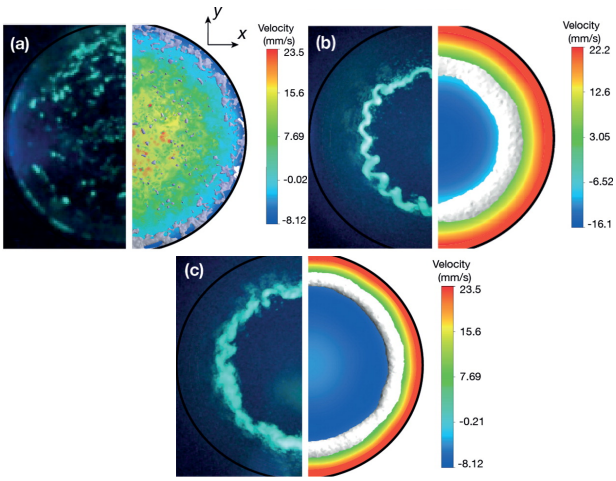

Figure 1.16: Experimental images (left) compared to finite element analysis predictions of fluid velocity (right) for a sessile drop actuated by Lamb waves. a) At 25 MHz no vortex is formed. b) At 157 MHz a clear vortex is formed and the particles collect at the lowest shear area. c) At 225 MHz the vortex and particle ring shift towards the perimeter due to a shortened attenuation length. Adapted with permission from A. R. Rezk, L. Y. Yeo and J. R. Friend, *Langmuir*, 2014, **30**, 11243–11247. Copyright 2014 American Chemical Society.

driven to the periphery. In their experiments, the large particles were concentrated to the free surface of the droplet within 3 seconds under 400 mW of power (*see* Fig. 1.17). Bourquin et al.[27] used slanted IDTs to generate SAW at multiple frequencies from a single device, which allowed them to separate particles according to their size due to the dependence of radiation force on both frequency and particle size. Bourquin et al.[28] later demonstrated particle separation by density using TSAW to generate acoustic streaming inside a droplet. Drag, buoyancy, and gravity forces effect particles to varying degrees based on their density relative to the carrier fluid. As a consequence, when the density of the fluid was between that of the two particles, the high density particles (red beads) were accumulated in the center of the droplet while the low density particles (green beads) were enriched at the periphery. The separation shown was achieved in 3 seconds using 200 mW of power.

The coffee-ring effect is used extensively in stationary sessile drop platforms.[118] Mampallil et al.[231] combined this technique with low frequency SSAW to control evaporative self-assembly of particles from a drop placed on a variety of superstrates. Under uncontrolled circumstances, particles in evaporating drops are pulled towards the contact line by convection. They showed that SAW actuation could trap particles within capillary wave nodal circles and/or SSAW nodal lines and thus prevent this so called "coffee-ring effect." This technique does not require modification of the fluid, particles, or surface involved (unlike other methods). However, in light of the above paragraph on Destgeer's work, it must be noted that their technique does require compatibility between frequency and drop size in order to set-up standing wave nodes. Fig. 1.18 shows how particles were uniformly deposited in a disc rather than concentrated in a ring near the contact line when SAW were used.

Many other biological assay processes can be enhanced by the use of SAW. Cellular spheroids are useful in diagnostics and drug testing since they resemble the structure and functional performance of in vivo tissue.[211] A SAW-driven centrifugation approach was reported to enhance the assembly of cellular spheroids in a micro well plate by Alhasan et al.[6]. Acoustic

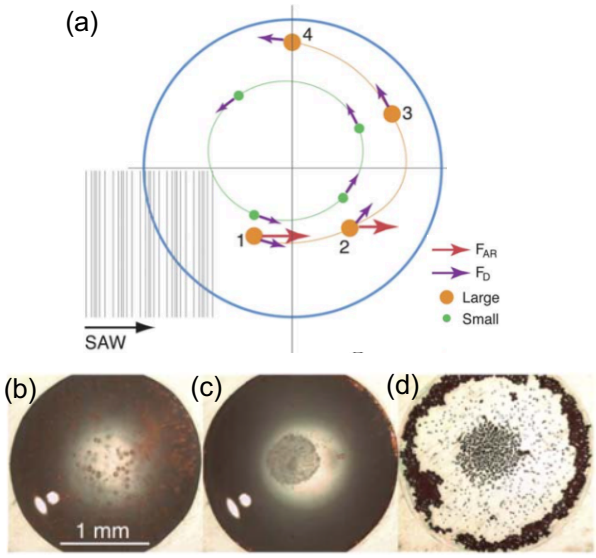

Figure 1.17: (a) Larger particles (the size of which are frequency dependent) are dominated by radiation force with the drag force playing a smaller role on the overall particle trajectory. The larger particles in position 1 are driven toward the free surface of the droplet. The effect of acoustic streaming at positions 1-4, however, causes the particles to circulate within a portion of the droplet before they reach the periphery near position 4. The smaller particles recirculate within the droplet until they concentrate in the center under the influence of drag. From experiment: (b) Initially the pollen and synthetic particles were suspended homogeneously throughout the entire droplet. (c) After 3 s, the pollen particles concentrated in the center of the droplet, and are hence separated from the synthetic particles, which concentrated along the periphery of the droplet. (d) The two species remain separated even after the droplet is fully evaporated after 1 min. Printed with permission[323] from The Royal Society of Chemistry.

radiation was coupled through a fluid on a LN substrate into the micro well plate placed on top of the SAW device. Centrifugation was driven via acoustic streaming generated by SAW. In this technique microcentrifugal flow in the micro wells—a result of geometric asymmetry—aggregates the cells as a precursor to spheroid formation. Kurashina also used ultrasound-generated vortices in well plates to agglomerate cells and reported that spheroids formed by ultrasound were fifteen times larger than without the ultrasound in low cell binding plates.[192]

The influence of flow on particle uptake rates of cells has been studied using SAW-generated acoustic streaming.[376] Acoustic streaming was used to mimic blood flow conditions for cell culturing and the results show that in relatively high shear conditions, particle uptake rates of cells are much lower.

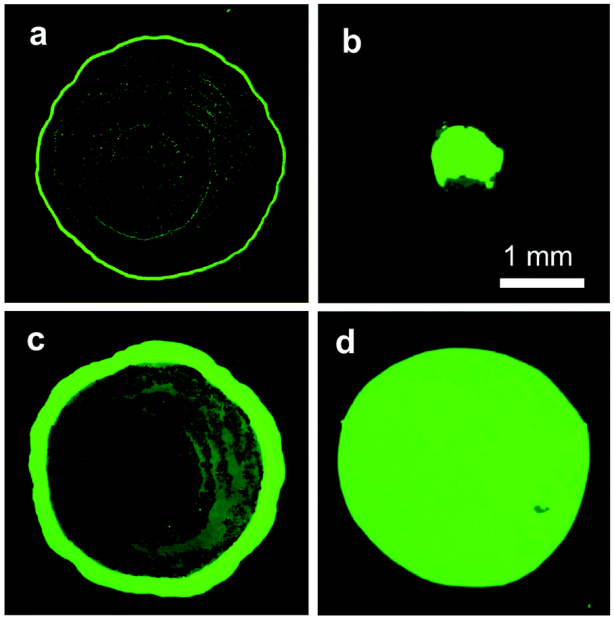

Figure 1.18: The coffee-ring effect is suppressed in a sessile drop containing 2 μm particles when actuated with SSAW. a) An undisturbed drop with 0.1% volume fraction of particles. b) A similar drop actuated by 9.7 MHz SSAW. c) An undisturbed drop with 2.5% volume fraction. d) A similar drop actuated by 20 MHz SSAW. All images are post-evaporation. Printed with permission[231] from The Royal Society of Chemistry.

Sivanantha et al.[363] studied the influence of 132 MHz focused SAW on the adhesive properties of red blood cells that had been affected by malaria and treated with glutaraldehyde (a common disinfectant used in hospitals) but were nonetheless healthy. The detachment behavior of cells initially adhered to the piezoelectric substrate were observed during exposure to acoustic streaming at various values of input power. The results show that healthy red blood cell membranes translate across the substrate before detachment. Rolling and flipping behaviors are observed for treated and malaria-infected cells. Malaria-infected cells also strongly reattached to the surface in the process. Detachment rates for healthy red blood cells were larger than the modified cells. Adhesive properties of cells have also been utilized to sort cells (HEK293 and A7r5 for example) using acoustic streaming flow.[33]

In addition to cell manipulation, SAW has been used to manipulate smaller bio-particles. Taller et al.[381] reported a method to sense micro-RNA, which have potential applications in the

early detection of cancer, with greatly reduced sample volumes by lysing exosomes with SAW. Exosomes are much smaller than most cells and the acoustic radiation force and electric field produced by SAW is uniquely suited to their lysis.

1.4.3 Fluid Manipulation in Closed Channels

We have discussed fluid manipulation in sessile drops, but, at the time of this writing, microfluidic processes necessary for lab-on-chip applications are more commonly accomplished in channels. This is likely due to the relative ease of fabrication of microfluidic chips based on channels and the lack of evaporation. Continuous flow in a microchannel can provide rapid and high-throughput flow manipulation and analysis of a variety of samples. Closed channels also reduce contamination from the surrounding environment during the analysis.

PDMS is widely used to form microfluidic channels. However, there are two major, well-known issues with this material in the context of acoustic waves: heating[133] and attenuation,[173] though each can be controlled and mitigated. In what follows, some researchers choose to accept these drawbacks due to the ease of fabrication, but alternatives like glass or milling directly into LN are available.

Fluid mixing

Mixing is essential for chemical reactions and the promise of miniaturized bio-chemical processes requires chemical reactions. However, at the scales of channel based microfluidics and nanofluidics, extremely low Reynolds numbers make the flow laminar and difficult to effectively mix. In the absence of turbulence, diffusion-based mixing cannot meet the requirements for most chemical mixing in microfluidic applications. In acoustofluidic systems, the nonlinear average effects of acoustics such as acoustic streaming are able to create a net streaming flow in the fluid, and thus will cause rapid and effective mixing. In light of this advantage, applications of rapid and active mixing have recently been developed and demonstrated in acoustofluidic research.

Following the progress made by the rest of the Wixforth group in drop translation, Sritharan et al.[372] also demonstrated SAW-induced mixing in a simple Y-shaped microfluidic chip with two inlets for dissimilar fluids, which were mixed in the third channel. An acoustic wave generated by a SAW device was coupled through the bottom of the chip and was diffracted based on the chip material (silicon, glass, polymer, etc). This is a prime example of an extra capability provided by acoustofluidics beyond those available to conventional microfluidics, powered by external pumps. In very similar devices, Tseng *et al.*[406] compared the mixing efficiency between channels oriented parallel to wave propagation (parallel-type) and those oriented perpendicular to wave propagation (transverse-type). They showed that the parallel-type mixer was more effective and that higher voltages were associated with better mixing. Jo and Guldiken[172] showed that, in the specific case of transverse-type micro-mixers, SSAW was more efficient for mixing than TSAW. Furthermore, Luong et al.[223] reported that, as in sessile drop translation and particle concentration, FIDTs offered greater efficiency than straight IDTs.

The effect of the channel geometry on acoustic mixing has also been investigated. In parallel-type microchannel mixers, Tan et al.[383] noted that a uniform channel flow became a mixing flow when the channel width was larger than the wavelength of the sound in the fluid. This finding suggests the possibility of dynamically choosing between flow and mixing in a single device by controlling the input frequency of the SAW device. Conversely, Miansari and Friend[247] presented active mixing via SAW in nanoslits (nanoscale channel height but width $> 100\ \mu$m). Mixing tended to occur with vortices aligned in the plane of the transducer rather than the typical vortices perpendicular to this plane. The authors suggest that sound waves cannot travel in the fluid due to it's nanoscale height and thus the typical acoustic streaming that causes mixing does not occur. More work is needed to understand nanoscale confinement in the context of fluid/acoustic wave interaction. We will present other aspects of this paper and others dealing with nanofluidics later in this review.

Acoustic mixing not only occurs in channels and sessile drops, but Rezk *et al.*[308] also

presented a uniform mixing method in a simple paper-based microfluidic device using SAW, offering a low-cost and disposable alternative to microchannel mixing. This technique could be especially relevant to diagnostics and other biological testing.

Other modes of acoustic vibration besides SAW have been used for mixing. Piezoelectric elements can produce a large variety of fluid motions in channels and chambers because they can be driven in several different vibrational modes. Among them, the thickness-mode is widely used for active mixing due to large amplitude substrate displacements in this mode. Thickness-mode devices have been used at a range of frequencies in the literature. Rife *et al.* presented mixing in an isolated PMMA chamber (a thin square box) via 50 MHz actuation of two $BaTiO_3$ transducers, but suggested improvements in mixing through larger frequencies and more or larger transducers.[318] Yang *et al.* investigated a very similar glass mixing chamber, but included inlet and outlet ports and chose PZT transducers.[454] Their device proved the concept, but was slow (2 seconds to reach stable mixing), high power (operated at 50-90V), and unsuitable for many applications due to the use of PZT (driving frequencies of 15-100kHz caused fluid heating and cavitation, which are each harmful to many bio-medically relevant fluids). Yaralioglu *et al.* applied a similar idea to perpendicular mixing in a PDMS microchannel using zinc oxide transducers at 450 MHz[455] (*see* Fig. 1.19). They were able to produce turbulent flow across a 300 μm channel at up to 60 μL/min and while using a much lower voltage than Yang, 1.2 V (30mW of power). They experienced minimal heating partly due to low power actuation and partly due to the continuous flow carrying away heat. Up to this point the location of the mixing was determined by the transducers, but Oberti et al.[276] used a large transducer at a much lower frequency (100 Hz) to vibrate the entire device while selecting the location of mixing via a T-junction. The authors did a careful and detailed analysis and determined that the sharp edges of the T-junction caused vortices in the flow that lead to mixing. Phan *et al.* also utilized geometric features in a channel to change the boundary conditions of the flow in order to produce turbulent flow.[415] They fabricated a microscale silicon nitride membrane with a hole etched through it,

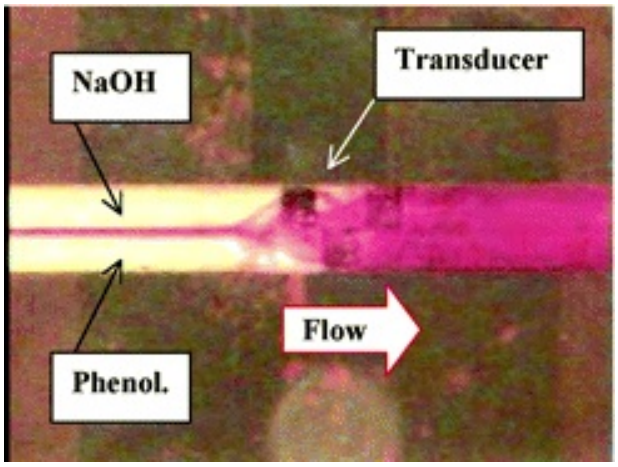

Figure 1.19: Laminar flow before the transducer (left side) and mixing flow after the transducer (right side) with an embedded piezoelectric transducer. A strong acoustic streaming effect is produced for more active and rapid mixing. Reprinted with permission from Yaralioglu et al.[455]. Copyright (2004) American Chemical Society.

which was bonded to the bottom of a Y-channel, that generated strong streaming vortices for fast and homogeneous mixing. At the opposite end of the frequency spectrum, 1.54 GHz was utilized by Cui et al.[70] to achieve rapid (within 1 ms) and homogeneous mixing in a y-channel without geometric features (*see* Fig. 1.20).

Catarino *et al.* compared experimental mixing performance in a T-junction microchannel during flow with numerical analysis on an equivalent system.[42] The distance long the channel required to achieve mixing was measured for pure diffusion and then with acoustic assistance under various flow rates. Their results revealed a moderate reduction in this distance with acoustic assistance from a β-poly(vinylidene fluoride) transducer operated at 40 MHz and 24 V. Their numerical results mirrored the moderate improvement seen in experiment though the absolute value of the mixing distance was only within an order of magnitude. Similar simulations could be used to gauge the impact of adding acoustofluidic mixers to other microfluidic systems (the authors emphasized diagnostic applications).

The mixing performance of acoustic-based micromixers has been further improved via acoustically driven bubbles. The vibration of a bubble membrane induced by acoustic waves can

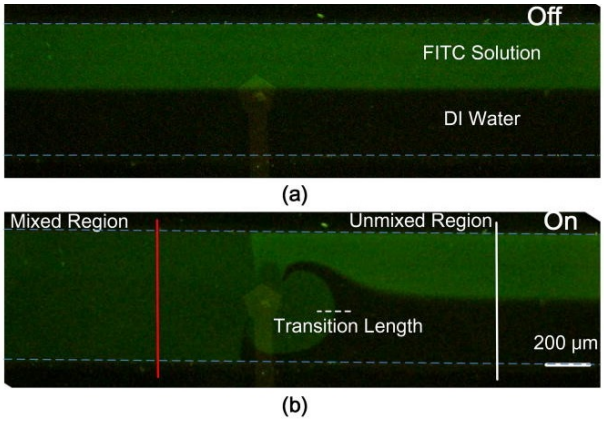

Figure 1.20: (a) Laminar flow and no mixing effect in the absence of acoustic waves. (b) Fast and uniform mixing of water and fluorescent dye in the presence of high frequency SAW within 1 ms. Reprint permis. Cui (2016).[70]

cause acoustic streaming[236,299] and results in a more prominent perturbation of the surrounding fluids than streaming from direct interaction with the substrate. This method can perform effective and rapid mixing at relatively low frequencies, which greatly alleviates the temperature rise in the system during acoustic-based mixing. We will not cover acoustic cavitation in microchannels as this topic has been systematically reviewed by Ohl.[278]

Liu *et al.*[215,216] used a piezoelectric PZT disk to excite air bubbles trapped in the top layer of a chamber. This resulted in complete mixing within 6 seconds using a 40 V_{pp} (peak-to-peak voltage) excitation. Tovar *et al.*[403] and Ahmed *et al.*[3] both designed lateral cavity acoustic transducers (LCATs), microchannels with perpendicular cavities patterned along two sides of the channels (*see* Fig. 1.21 for Tovar's design). Air bubbles are trapped automatically in the cavities when liquid flows through the channel. As a result, these devices are capable of mixing fluids by induced vibration of the fluid/air interface. Wang *et al.*,[423] Ahmed *et al.*,[4] Ozcelik *et al.*,[283] and Bertin *et al.*[21] each trapped air bubbles in a microchannel either by designing the channel geometry or by adding structures in the channel to perform oscillating bubble-induced mixing. The work by Ahmed *et al.* appears in Fig. 1.22. In order to reduce the common problem of bubble leakage, which results in shrinking and poor vibration efficiency, Orbay et al.[279] continuously pumped nitrogen into a microchannel thereby refilling or replacing leaky bubbles.

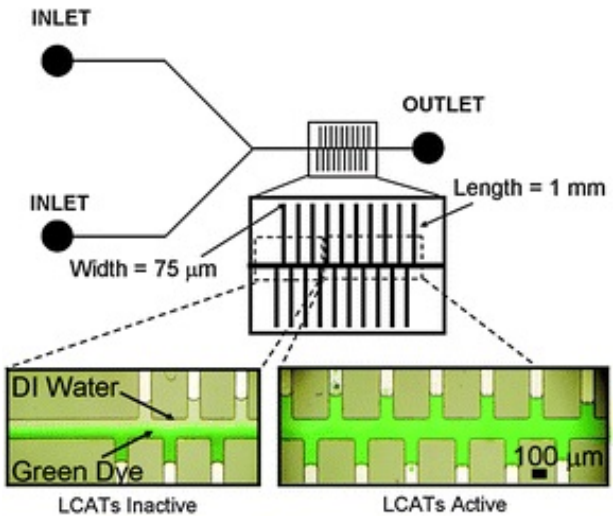

Figure 1.21: Lateral cavity acoustic transducer (LCATs) induced fluid mixing in a channel. The vibration of air-liquid interface caused acoustic streaming in the channel and performed uniform and rapid mixing. Reproduced[403] with permission from The Royal Society of Chemistry.

Combriat *et al.*[64] investigated the flow generated from the pulsating bubbles submitted to an external flow in microfluidic channel. Bubbles with radii between 20 and 50 μm are generated and squeezed in the observation channel (2 mm wide, 25 μm high) and micropits are designed on the upper wall of the channel to trap the bubbles. High speed camera is used to record the flows that are visualized by tracer particles to perform quantitative studies. Closed recirculation zones that isolate a part of the flow around bubbles are observed in the experiments. These zones can be used to enhance mixing in the fluid. Position and size of these zones can be changed to manipulate mixing condition. It if found that closed recirculation zones are upstream when external flow is applied along bubble pair direction and locate downstream when bubbles are perpendicular to external flow. The size of closed recirculation zones can be changed by adjusting external flow rate.

Although bubble-based micromixers are capable of rapid and homogeneous mixing, their disadvantages include bubble instability[4,157] and inconvenient bubble-trapping processes. As an alternative, Huang et al.[158] designed sidewall microstructures known as *sharp edges*. The oscillation of these sharp edges induced by PZT transducers causes acoustic streaming, facilitating

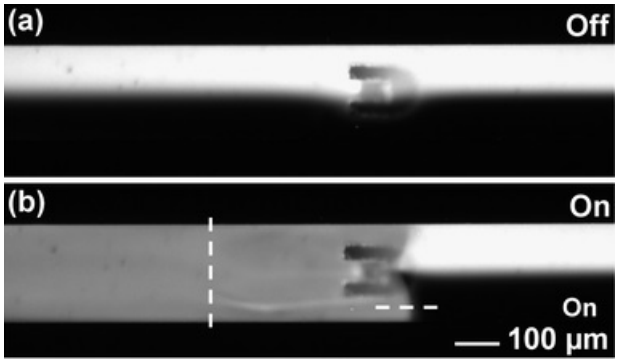

Figure 1.22: (a) No mixing effect in absence of acoustic waves. (b) uniform mixing of water and fluorescent dye in presence of acoustic waves. Reproduced[4] with permission from The Royal Society of Chemistry.

rapid and homogeneous micromixing (*see* Fig. 1.23). Numerical studies of the acoustic streaming that occurs near these sharp edges have been presented by Ovchinnikov et al.[282] and Nama et al.[269]

Fluid pumping

One of the key problems in lab-on-a-chip devices is the ability to provide effective fluid flow against a resistance in a chip-sized device. We now examine several approaches to this problem using acoustic waves.

Acoustic counterflow occurs when fluid in a channel is drawn opposite the direction of SAW propagation due to atomization at the fluid/air interface and coalescence upstream[44] (*see* Fig. 1.24). Masini *et al.* showed that fluid can be turned at right angles and split at an intersection in a 2D array of PDMS channels by this method.[240] Recently Shilton *et al.* performed mechanistic investigations of this technique.[356] The authors showed that the input power required for atomization in a channel did not increase over the frequency range 50–750 MHz. They also observed optimal SAW transmission through the channel when its width, W, was greater than $10\lambda_{SAW}$. This allowed them to produce optimal counter-flow in very small channels by increasing the SAW excitation frequency. They found that flow vortices in the channel scaled with the

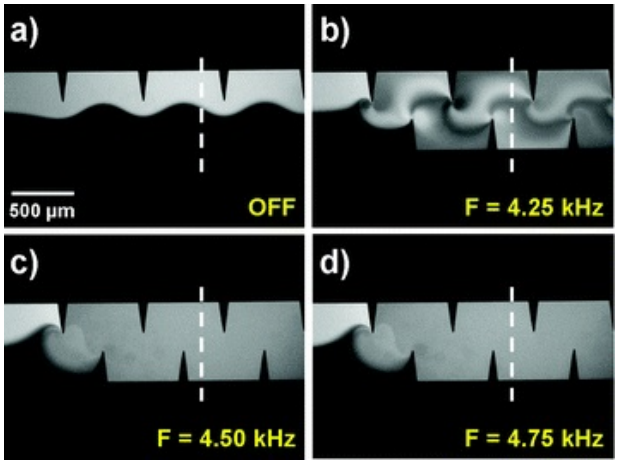

Figure 1.23: Sharp-edge oscillation induced by PZT transducer produced acoustic streaming and performed mixing in the microchannel. With different applied frequencies, the mixing performance differs, as shown in (b), (c), and (d). Reproduced[158] with permission from The Royal Society of Chemistry.

size of the channel if the frequency was adjusted to match $W = 10\lambda_{SAW}$ (unsurprising since β^{-1} decreases with increasing f). Similar to Shilton's work on sessile drops in 2014, these findings could allow further miniaturization of SAW microfluidic devices. As an interesting side note: we have seen that viscosity also plays a role in acoustic attenuation (the cause of streaming vortices) and an earlier studyIto et al.[165] showed that channel vortices were reduced in length with increasing viscosity, which again demonstrates the similar effects of viscosity and acoustic actuation frequency.

Acoustic counter flow cannot be used for closed channel systems where no free air/liquid interface exists. However, conventional pumping (rather than counter-flow) is difficult using SAW since the maximum amplitude of a travelling SAW on a LN substrate is $\sim$10 nm, which produces negligible peristaltic effect in a microscale channel. Instead fluid flow is due to acoustic streaming that tends to promote vortices, which in turn lead to circulation rather than unidirectional flow across the channels entire cross section. A possible solution to this problem was presented by Tan, *et al.*[383,389] They changed the width of the channel relative to the wavelength of sound in the fluid and observed uniform pumping of fluid flow when $W < \lambda_f$. This first demonstration

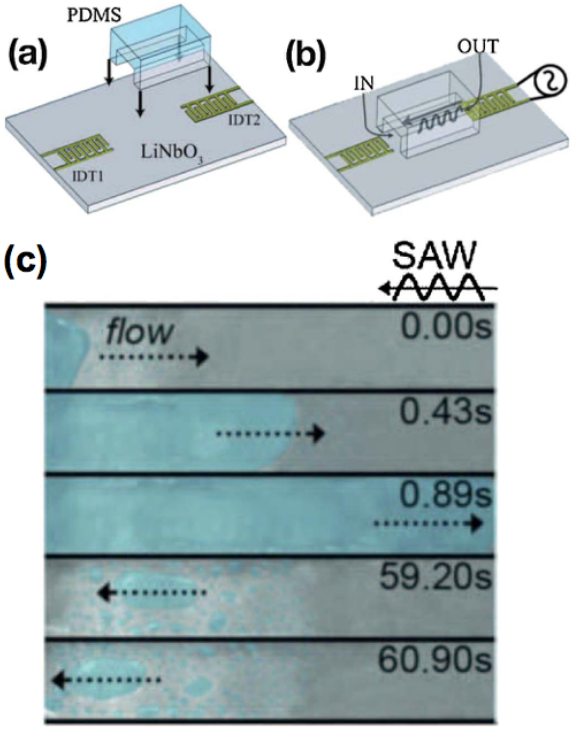

Figure 1.24: A PDMS channel was bonded onto a LN substrate with two straight IDTs at two ends of the channel, as shown in (a), (b). The liquid performed counterflow relative to SAW propagation due to atomization at liquid-air interface and coalescence upstream, as shown in (c).

of SAW-based uniform pumping was accomplished in a short, isolated channel segment with no inlet or outlet. Subsequently,[333] demonstrated a continuous, closed-loop SAW-driven PDMS microchannel pump. Lossy interaction between SAW and PDMS was avoided by elevating the PDMS on water and glass coupling layers. They used a high frequency device (142 MHz) and a wide channel (1 by 0.75 mm) so that λ_f was much greater than W, which would seem to contradict Tan's conclusions. This inconsistency has not been explained and further work is required. A different type of SAW-driven pump device using an open-circuit channel constructed from glass (bonded directly to LN) was presented around the same time by Langelier *et al.*[200] ($W > \lambda_f$ again in this device). The elimination of extra coupling layers from the system greatly increased the pumping efficiency due to increased SAW transmission. It remains unclear how acoustic streaming creates unidirectional flow overall in these channels despite the presence of

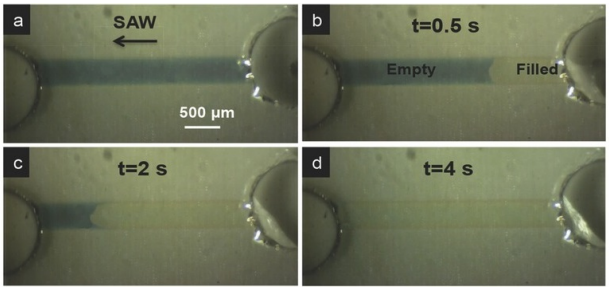

Figure 1.25: LN nanoslit filling with water induced by SAW propagation from the right end of the nanoslit. The capillary filling rate of the hydrophilic LN nanoslit can be increased by 2–5 times when SAW is applied in the same direction. The magnitude of SAW is in the same order as the channel height so that it has a unique pumping mechanism different from SAW-induced pumping in microchannel, which needs to be further investigated. Reprint permis. Miansari (2016).[247]

vortices in the path of the SAW.

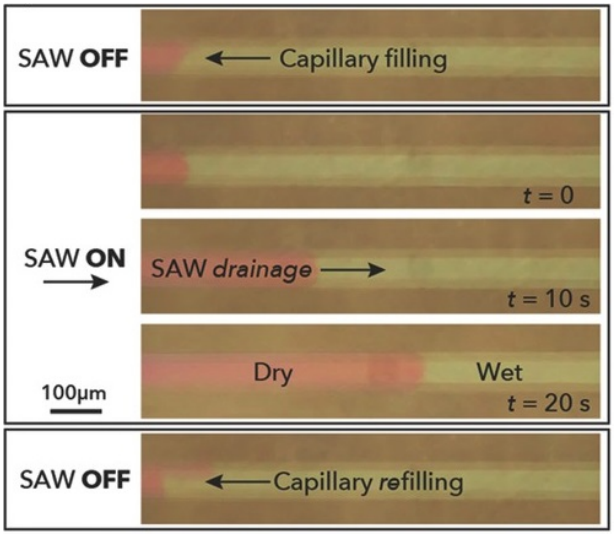

Figure 1.26: Water drainage in LN nanoslit induced by SAW. SAW drained the nanoslit against 1 MPa capillary pressure when SAW was applied in the opposite direction of capillary filling. It showed powerful SAW-induced pumping effect in a nanoscale channel. Reprint permis. Miansari (2016).Miansari and Friend[247]

In addition to mixing, the nanoslit demonstrated by Miansari and Friend[247] was shown to perform SAW-driven pumping at a remarkably large 1 MPa of pressure. The capillary filling rate of the hydrophilic LN nanoslit was increased by 2–5 times when SAW radiation was applied in the same direction as capillary filling, while the nanoslit could be drained against 1 MPa capillary

pressure when SAW radiation was applied in the opposite direction (*see* Figures 1.25 & 1.26). Miansari was also able to pump an isolated droplet back and forth within the nanoslit using the same mechanisms. The reduction of channel dimensions to the nanoscale may remove previously unknown limitations of microchannel pumping.

Closed channel fluid pumping can also be accomplished via induced bubble oscillation[141,199,224] or via air/liquid interface vibration in LCATs.[288,402,404] The pumping mechanism is acoustic streaming in each case. Fang and Lee[102] demonstrated the potential consistency and stability of membrane-induced microchannel pumps by creating an LCAT-based oil/water droplet generator (*see* Fig. 1.27). In addition, Huang et al.[159] presented a programmable acoustofluidic pump based on the acoustic streaming effects due to the oscillation of tilted PDMS sharp-edge structures activated by a piezoelectric transducer. A stable and reliable pumping effect with 8 $\mu\ell$ min^{-1} pumping rate has been achieved.

1.4.4 Particle Manipulation in Closed Channels

SAW-based particle, droplet, and cell manipulation has been a popular topic of investigation in recent years, prompting several reviews on the subject.[14,80,89,120,424] Here, we will review the latest SAW-based manipulation results in four main areas: concentration and focusing, separation and sorting, patterning and manipulation, and droplet production and splitting. We will then cover the use of glass capillary tubes as an alternative to other ways of forming channels.

Concentration and Focusing

Particles and cells that have been focused within a flow cross section can then be easily detected by various methods. This process, cytometry, is a major capability required in biological assays and future lab-on-a-chip devices. Many focusing techniques have been investigated, including hydrodynamic, electrokinetic, and dielectrophoresis (DEP) methods. However, the SAW method is simple, highly efficient, contact-free, and can be applied to focus a wide variety

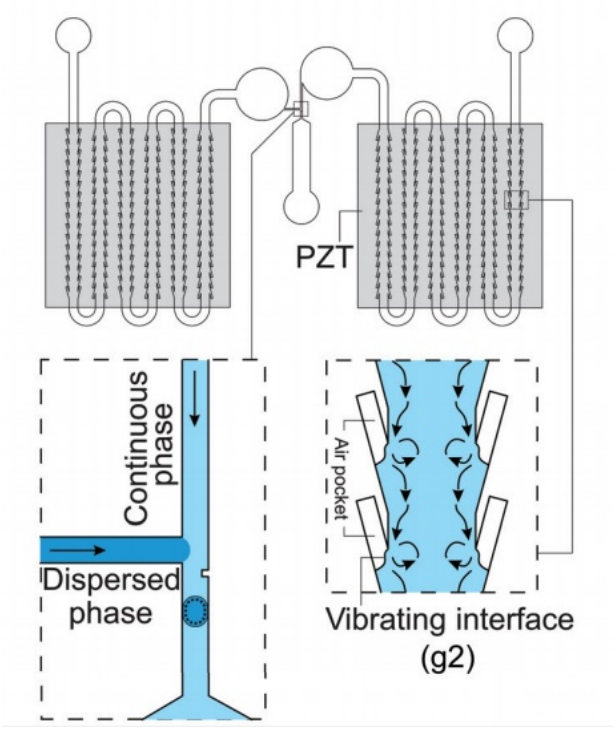

Figure 1.27: Air cavities were trapped when the fluid was pumped into the channel. The vibration of air-liquid membrane produced the acoustic streaming and caused the pumping mechanism in the closed channel. Membrane-induced acoustic streaming instead of SAW-induced acoustic streaming showed better uniformity and effectivity for closed channel pumping in microscale. Droplet generation based on pumping in oil and water phases were demonstrated.

of microparticles. Furthermore, the transparency of LN makes it feasible to integrate with most optical techniques.

Shi et al.[347] demonstrated particle focusing in a microchannel by depositing two IDTs on each side of the channel. The channel width and the wavelength of SAW were specified so that a SSAW formed across the channel width with a single pressure node located at the channel center, collecting particles at this node (*see* Fig. 1.28). Zeng et al.[461] then integrated Bragg reflectors (BR) with the focusing device to enhance SSAW formation. Air cavities were also introduced on both sides of the microchannel and SSAW propagation area in order to reduce absorption by the PDMS walls. Jo and Guldiken[171] utilized these focusing capabilities to perform density-based particle separation.

To perform SSAW-based on-chip flow cytometry, 3D focusing capabilities are desired

in order to maintain constant focal depth during cell detection. Shi et al.[350] discovered that the acoustic radiation force in the z-direction (perpendicular to the device plane) is also non-uniform. Through theoretical and numerical calculations, they showed that this non-uniformity could be used to force particles toward the plane of maximum acoustic kinetic energy which had a constant height with respect to the substrate. Experimental results agreed with these calculations and they were able to perform SSAW-based 3D continuous particle focusing in a microchannel.

TSAW can also be used for particle focusing, as demonstrated by Tan et al.[389]. A single IDT generates a SAW that is subsequently reflected from the opposite channel wall that generates a standing acoustic node within the channel if conditions are engineered correctly. Relatively weak SAW were used in Tan's work to focus particles in an initially homogeneous suspension into equally spaced nodal lines parallel to the channel with a separation of one-half the wavelength

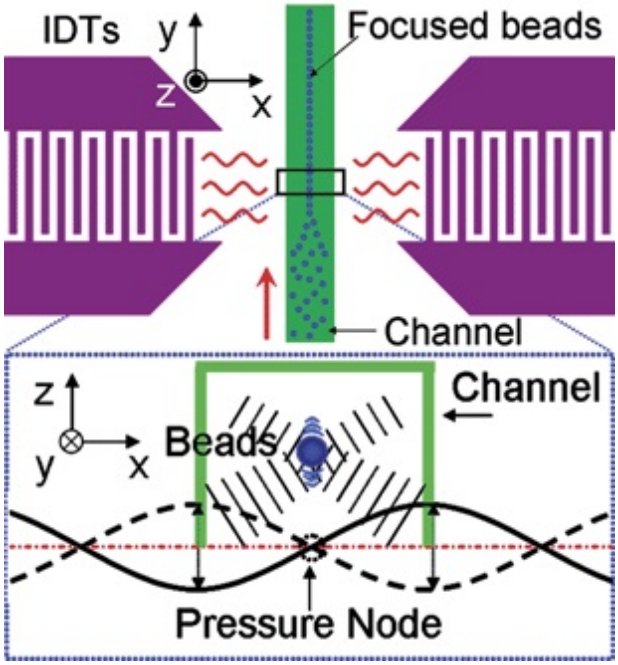

Figure 1.28: Schematic and working mechanism of the SSAW-based focusing device. The IDTs were on the opposite side of the channel. The width of the channel was matched with the wavelength of SAW to generate single pressure node at the center of the channel. The acoustic radiation force led beads into pressure nodes to perform particles focusing. Reproduced[347] with permission from The Royal Society of Chemistry.

(*see* Fig. 1.29). The dependence on wavelength allowed particles to be focused to different locations based on the applied frequency (using a slanted IDT). Witte *et al.* produced a similar device, but added a glass superstrate.[440] A slanted IDT allowed for small differences between superstrates to be compensated for by tuning the resonant frequency. This kind of technique will allow cytometry within disposable inserts, which could allow for quick, clean processing of many samples in sequence on a single device.

Tan *et al.* presented a unique way of performing cytometric functions using TSAW streaming and non-nodal radiation.[388] A double-aperture FIDT enabled asymmetric actuation so that particles could be directed to the left or right as they are propelled along the channel. They also milled the channel cross section into a trapezoidal shape that greatly reduced the formation of standing waves (similar to the effect of an anechoic chamber) so that particles would not be trapped along nodal lines.

Separation and Sorting

The goal of particle separation and sorting is to lead specific particles from their original streamlines to targeted streamlines which finally flow into a sorted outlet. Related SAW techniques can be divided into two general categories: TSAW-based and SSAW-based. Franke et al.[107] first presented continuous droplet sorting in a PDMS microchannel using TSAW. Droplets flowed passively into one channel, but were pushed into the path of a second channel by acoustic streaming when actuated. However, this technique cannot inherently differentiate between particles and thus can only temporally sort. Destgeer et al.[81] were able to continuously isolate particles of a single size from an assortment of particles by utilizing the acoustic radiation force of TSAW. As mentioned earlier, detachable superstrates are potentially useful for applications where biological samples are processed. Ma et al.[226] developed a device similar to Destgeer *et al.*, but with a PDMS superstrate that contained the microfluidic channels. They also developed a platform for separating particles of similar sizes but with different densities using TSAW of

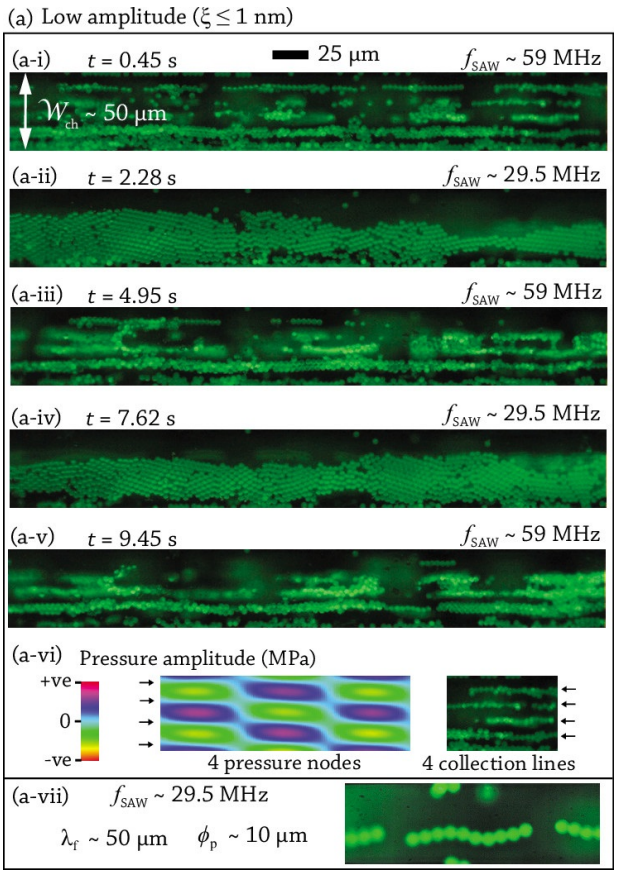

Figure 1.29: Time lapse images of TSAW focusing in a microchannel at amplitudes below 1 nm. Specific lines of focus could be selected by applied frequency and were quickly and easily switched, in this case between 29.5 MHz and 59 MHz. Reprint permis. Tan (2010).[389]

carefully selected frequency.[227]

TSAW methods displace particles from their original laminar flow path, but SSAW methods sort particles into one or more nodal paths regardless of their original path. Also, recall that the acoustic radiation forces due to TSAW and SSAW differ strongly in their dependence on particle size (*see* Eqns. 1.6 and 1.5). Size-based[82,179,265,349] and density-based[171] particle separation have been demonstrated. Numerical studies on SSAW in microchannels has further explained the mechanism of particle separation. A 2D model helped reveal the effect of boundary vibrations and channel properties on particle aggregation near PDMS channel walls.[234]

Wu et al.[446] further scaled down the particle separation technique to submicron scale. Tilted-angle SSAW was utilized to separate 500 nm and 110 nm particles, showing a finer

resolution for particle separation than the standard SSAW configuration. Next, Kishor et al.[187] demonstrated integration of tilted-angle SSAW with a photoacoustic detection technique into an integrated microfluidic platform capable of size-based separation, concentration, and quantitative detection of microparticles. Such integrated platforms show promise for future lab-on-a-chip systems that utilize the functionality described in this review.

The ability to separate microscale particles has also been shown using SFITs. Destgeer et al.[81] was able to separate particles into three size groups by placing SFITs with two distinct frequency ranges on either side of a microchannel. Thus, TSAW could be generated at desired frequencies and locations. Recently, Park et al.[286] demonstrated bidirectional, multichannel droplet sorting using SFITs. They also added a new functionality: dynamic formation of temperature gradients in the channel.

In a more biologically relevant proof of concept, Nam et al.[266] demonstrated a device to separate blood cells from platelets using SSAW. Pressure nodes were set up near the two side walls and blood cells experienced larger acoustic radiation forces, since they are larger than platelets, and moved to the sides of the channel while platelets remained at the center. The authors reported platelet purity up to 98% using this method. They were also able to separate beads of polymer encapsulated cells based on their density.

Using focused SAW of higher frequency (up to 636 MHz), Collins and Ma[59,62] recently demonstrated size-selective particle concentration—as small as 300 nm—via acoustic streaming. In one arrangement, streaming and radiation concentrate particles to one edge of a flow (*see* Fig. 1.30). Note that size selective concentration in sessile drops has been demonstrated down to 200 nm.[84] Concentration generally refers to separating many particles at once into two or more groups, while sorting considers one particle at a time.

Depending on the position and design of the acoustic source, both SSAW[87,347] and TSAW[334] devices can be used for cell sorting, as the acoustic actuation area in the fluid can be well controlled. A high-throughput acoustic cell sorter using focused SAW was introduced by Ren

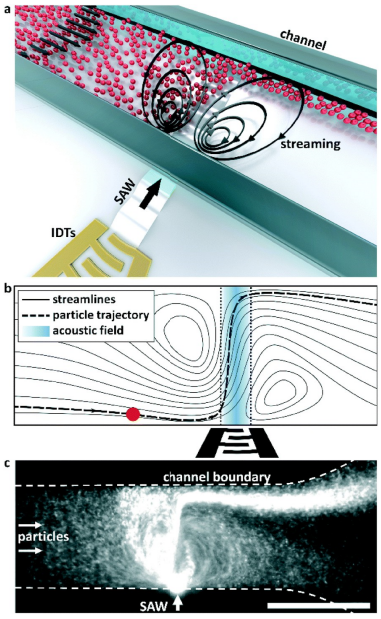

Figure 1.30: Principle of SAW based nanoparticle focusing of using SAW. (a) A conceptual diagram: the combined streaming field and acoustic radiation forces resulting from the coupling of substrate vibrations produced by an IDT on a piezoelectric substrate results in focused particle displacements. (b) A particle (red) is displaced relative to the fluid streamlines by the acoustic radiation force as it passes through a focused SAW beam. The streaming serves to direct the particle laterally to the acoustic beam and maximize its exposure to the acoustic gradients in its periphery. (c) A continuous influx of 300 nm particles is focused in a low velocity flow. Adapted[62] with permission from The Royal Society of Chemistry.

et al.[306] An FIDT allowed them to generate SSAW with higher energy intensity and a narrower beam width resulting in a larger actuation force and a higher sorting resolution (*see* Fig. 1.31). According to their data, the FIDT exerted 4–9 times larger acoustic radiation force than did the straight IDT, indicating that to attain the same sorting effect an FIDT would require only 10–20% of the input power of a straight IDT. Collins et al.[60] demonstrated a very similar system only they used TSAW rather than SSAW and used a higher frequency, 386 MHz, to achieved even finer resolution particle sorting (similar to Fig. 1.31), but with only one FIDT). They shrunk the actuation area to a few tens of micrometers with highly focused SAW that produced large acoustic gradients. With pulse durations of $\sim$100 μs, they were able to nudge particles as small as 2 μm from their path without altering the path of the next particle in sequence.

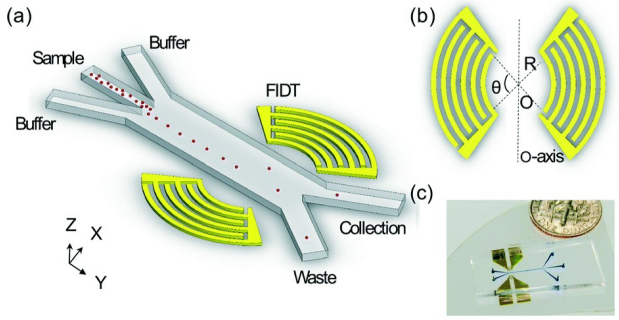

Figure 1.31: (a) Schematic of the SSAW-based sorter excited by FIDT. (b) The concentric geometry of the FIDTs. O is the focal point and the two sets of FIDTs is O-axis symmetric. (c) An optical image of the high-throughput SSAW sorter. Adapted[306] with permission from The Royal Society of Chemistry.

Patterning and Manipulation

The ability to arrange cells and microparticles into desired patterns is important for many biological applications, for example in tissue engineering.[201] Patterning of particles in one and two dimensions using SAW has been recently demonstrated. Wood et al.[443] first performed 1D patterning (also known as alignment) of particles using SSAW in microfluidic systems. As a next step, they performed 2D patterning using two pairs of counter propagating IDTs in orthogonal directions.[444] They used a liquid coupling film similar to that used by Schmid,[334] which cannot support continuous operation due to a lack of inlet and outlet ports. Shi et al.[348] enabled continuous 1D and 2D patterning by bonding PDMS directly to the substrate to form a closed channel. Building on this concept, O'Rorke et al.[281] achieved translation of a patterned array of particles by modulating the frequency of the SAW. The pattern could be translated laterally by up to one wavelength ($\sim$118 μm in this case—a standard, straight $\sim$30 MHz device) by changing the frequency in small increments across the bandwidth of the IDT.

In the last five years, other forms of patterning using SAW have been presented. Ding et al.[88] performed tunable 1D and 2D patterning of microparticles using slanted-finger IDTs

(SFITs), which offer a much larger resonant frequency bandwidth than the standard IDTs used for translation. They showed that, by tuning the frequency applied to the SFITs, they could vary the line spacing of a 2D pattern, for example, from 141 μm to 250 μm. Another novel patterning capability was added by Collins et al.[58] who produced patterning in only a desired section rather than over the entire area between two transducers. They engineered nanosecond pulse signals whose duration was less than the time-of-flight between transducers so that standing waves were only set up in a central region of tunable width. Yet another degree of freedom was demonstrated by Tian et al.[397] who could control both the spatial patterning and the shape of microdroplets themselves, which compose the pattern.

Particle patterning into defined nodal positions is useful, but in addition, some applications require the movement of particles to arbitrary locations. This has been accomplished with a technique known as acoustic tweezers, an old concept[154,155] receiving renewed interest. Compared to optical tweezers, acoustic tweezers require lower power density, are bio-compatible, and are amenable to miniaturization. Nodal position can be tuned by either phase shift[280] or frequency modulation[86,405] (*see* Fig. 1.32). More recently, Devendran *et al.*[85] used an acoustic field combining both traveling and standing wave components along with a swept excitation frequency to collect and isolate particles of different sizes in a static fluid volume. The varied tools created through more and more complex acoustic field control are bound to be useful in other fields where small particles need to be manipulated. One such example is the work by Chen et al.[48] who used acoustic tweezers to trap cells in a micro-channel for cell enrichment. The cells accumulated at SSAW nodes as more and more fluid was passed through the channel. They reported an increase in concentration of originally dilute red blood cell samples (10^5, 10^4 and 10^3 cells per mL) by a factor of 100–1000.

We point the interested reader to a more detailed review of dynamic ultrasonic field control presented by Drinkwater.[94] It includes in-plane manipulators, beam manipulators, and planar array manipulators used for transportation and rotation of individual particles as well as

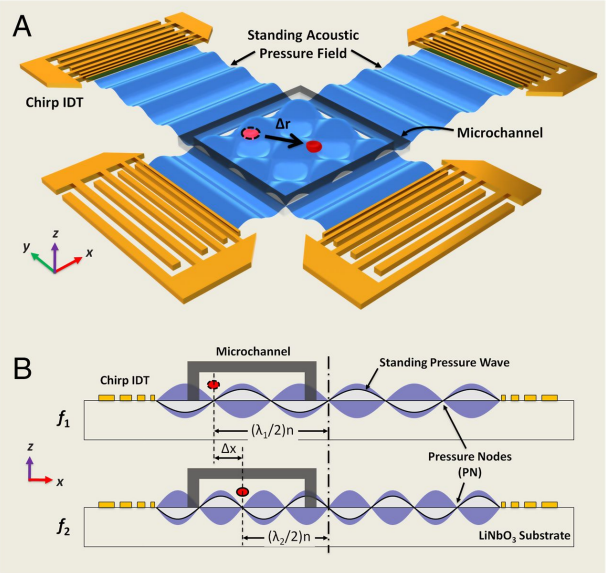

Figure 1.32: Two-dimensional particle manipulation with frequency-control using chirped IDTs. A microchannel was bonded near one side of chirped IDTs. Particles in the pressure nodes were forced to move by changing the location of pressure nodes, which were dependent on the frequencies of SAW [86].

biosensing and microscale assembly in channel-less microfluidic devices.

Droplet Production and Splitting

SAW actuation has become a promising tool for droplet generation, droplet splitting, and droplet manipulation because it is inherently robust and contamination-free. The general idea is to apply acoustic streaming or acoustic radiation force induced by SAW near a fluid-fluid interface in order to produce drops of a dispersed phase within a continuous phase (*see* for example the bottom left of Fig. 1.27).

Schmid and Franke [332] integrated an IDT at the junction of flow-focusing channels as seen in Fig. 1.33. The magnitude of SAW power—rather than channel geometry or flow speed—was used to regulate droplet size. This method relies on increased pressure at the lower inlet due to acoustic streaming. Collins et al. [57] used an FIDT to demonstrate droplet generation from a T-junction in order to encapsulate concentrated particle suspensions. A low-power SAW was

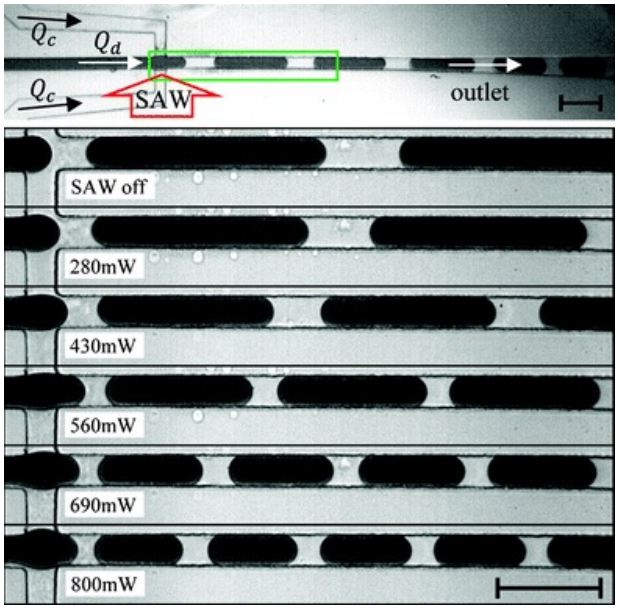

Figure 1.33: SAW was applied at the flow-focusing droplet/plug generation region and regulated the plug size by different SAW power. Stronger SAW power reduced pinch off time due to increased interface pressure, which in turn reduced the size of plugs. Reproduced[332] with permission from The Royal Society of Chemistry.

activated to move and concentrate particles at the interface, then a high-power pulse was used to deform the interface and generate a water-in-oil droplet with encapsulated particles. Based on a similar device configuration, Brenker et al.[29] experimentally and numerically explored the working mechanism of the FIDT-induced T-junction droplet generator. They identified three distinct droplet production regimes depending on the relative speeds of the continuous and dispersed fluid flows.

SAW-induced drop splitting in microchannels has also been demonstrated recently. Sesen et al.[342] performed water-in-oil plug steering and real-time on-demand plug splitting using an FIDT-integrated Y-junction microfluidic device. Two FIDTs (one on each side) were pointed directly at the junction from the direction perpendicular to the inlet channel. Precise acoustic radiation pressure on the oil/water interface allowed the plug to be steered entirely into one outlet or the other or to be split into desired proportions (without actuation the plug would naturally split in half). Jung et al.[175] used SFITs instead of FIDTs to direct acoustic radiation pressure to a

specific region for droplet splitting based on the input frequency. Sesen et al.[343] applied pulsed acoustic streaming in a branched channel to suck a portion of fluid into it thus splitting droplets as they passed (*see* Fig. 1.34).

Sesen et al.[341] also reported on-demand droplet merging using focused SAW. Acoustic radiation forces generated from an FIDT were used to stop the progress of a selected droplet such that successive droplets merged until a certain volume was reached (*see* Fig. 1.35).

Jung et al.[176] demonstrated on-demand droplet capture and release at specific microwells using SFITs. At different frequencies, different parts of the SFITs resonated corresponding to the designed wavelength at that location. Thus the location of a particular microwell could be selected and droplets could be pushed into or out of it as desired.

Particle Manipulation in Capillary Tubes

We have already covered the phenomena where by nodes and anti-nodes form in acoustic resonant cavities which we have called channels. Capillary tubes can also be used as resonant

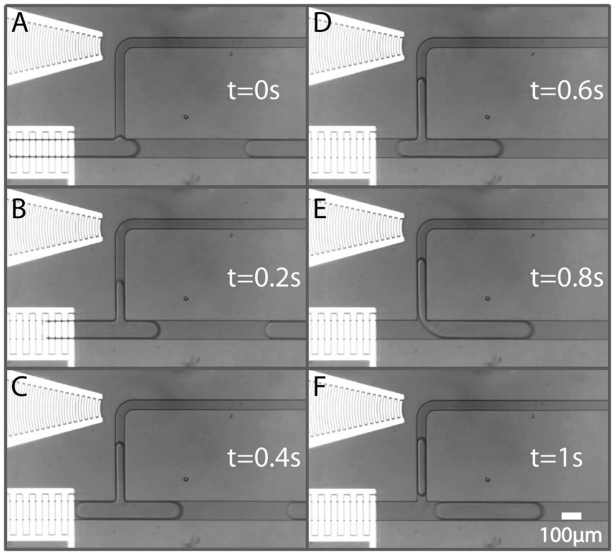

Figure 1.34: Droplet splitting in closed branched microchannel induced by SAW. FIDT-induced acoustic streaming produced a pressure offset between the main channel and the branched channel, and performed as a micropipette in the closed channel. Reproduced[343] with permission from The Royal Society of Chemistry.

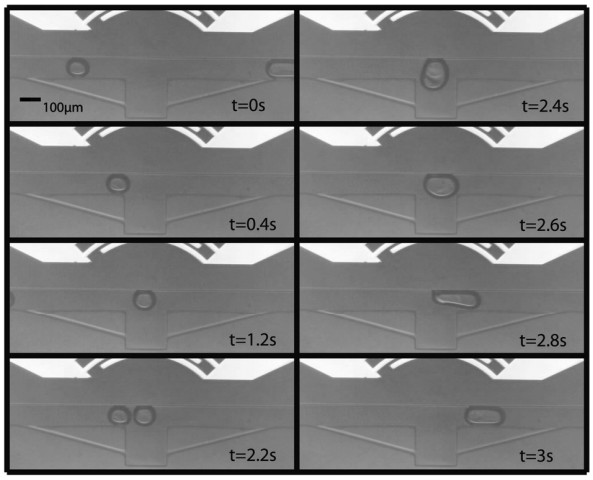

Figure 1.35: Time lapse images of the droplet merging experiment. The first droplet is immobilized across the FIDTs while the next droplet comes and merges with the stationary one. The merged droplet travels downstream because the acoustic energy in the system is not enough to hold a bigger volume droplet. The FIDTs is placed at the right-side while the oil flow is from left to right. Reproduced[341] with permission from The Royal Society of Chemistry.

cavities. They can be bonded to a piezoelectric substrate often more easily than a channel can be fabricated in the substrate or in some superstrate. Being widely used in other industries capillary tubes are easily obtained in many sizes and shapes as ready to use parts that both have well known properties and are disposable.

A review by Lenshof etal. presents a good summary of the work done in this area in the section called ”Capillaries”[206]. They cover the focusing and trapping of particles and the use of these techniques in bio-chemical assays. Another good example, not found in the above review, is the work of Grundy et al.[128]. They applied this technology to rapid diagnostics and were able to reduce, for example, the agglutination time of bacteria from 4 hours to 5 minutes by encapsulating samples within droplets within a capillary tube. Work by Araz et al.[9] is also valuable due to the simplicity of the design in which particles are separated based on size and/or density along the length of the capillary due to bending modes produce by actuation of a C-shaped PZT plate.

We also wish to highlight two works that have been published since the review by Lenshof. Gralinski et al.[124] have performed numerical simulations of particle trapping in capillaries with circular cross sections. They vary several design parameters and discuss the advantages of a

design containing 4 PZT transducers for particle focusing in the center. A follow up paper[125] presents experimental results and also includes patterning along the length of the capillary tube. Recently, Mao et al.[235] published work on coupling SAW into a capillary tube bonded to a LN substrate. They showed that in this case not only are nodes established due to acoustic radiation, but also acoustic streaming establishes a single vortex which allowed them to focus particles in the nanometer size range. We cover this work further in the following section.

1.4.5 Reorientation of Nanoscale Objects

Acoustic waves are widely used for in-situ manipulation of nano-objects because they are simple to produce, highly bio-compatible, contact-free, and capable of rapid actuation. Carbon nanotubes (CNTs) have aroused the interest of researchers in recent decades due to their mechanical strength and electrical conductivity,[367,395] but they also show promise in nanoscale fluid transport.[243,272,430] However, in order to be utilized in these applications, CNTs must be properly oriented. For example, CNTs can be used to reinforce polymer composites, that perform better when the nanotubes are aligned using acoustofluidics.[143]

Strobl et al.[375] utilized SAW to align multi-walled carbon nanotubes (MWNTs) with an angle of 25°–45° on LN with respect to the wave propagation direction. They explained that the MWNT alignment resulted from the piezoelectric field and SAW propagation, thus the acoustic streaming generated by SAW actually shifted the MWNTs from being directly aligned with the piezoelectric field. Ma et al.[225] further discussed the acoustic radiation effect and the dielectrophoretic effect (due to the piezoelectric field) on the patterning mechanism of CNTs. Numerical simulation and corresponding experiments showed that the dielectrophoretic effect dominates over the acoustic radiation effect when patterning CNTs because of their high conductivity and high aspect ratio. Conversely, the acoustic radiation effect dominates when patterning low aspect ratio and less conductive objects. Besides carbon nanotubes, metallic microtubes[188] and nanowires[47] can also be patterned using SAW while dispersed in a liquid via

the dielectrophoretic effect since they are also highly conductive and have high aspect ratios. Seemann et al.[339] then demonstrated that SWNTs and MWNTs can be deposited and aligned between pre-structured metal contact pads on silicon using SAW. The use of silicon makes this technique more compatible with microelectronics applications.

Recently, Miansari et al.[248] also presented deagglomeration and alignment of MWNT bundles on a dry surface via SAW. The absence of fluid on the surface eliminated the influence of streaming so that acoustic radiation forces could deagglomerate the nanotube bundles. The alignment mechanism relied on van der Waals interactions between the nanotubes and a glass slide, which was placed on top of them to constrain out of plane movement.

In some pioneering work on concentrating nanoparticles, Mao *et al.*[235] demonstrated use of a single vortex generated using SAW for focusing 80-500 nm diameter silica and polystyrene particles. These were used to capture fluorescent biomarkers to enrich the emitted signal. By way of extension, Wu *et al.*[447] separated exosomes from whole blood. This was conducted in two stages, first separating larger blood components before the second stage which targets the exosomes. Both these studies potentially lay the foundation for applications such as health monitoring and medical diagnosis among others that would benefit from nanoparticle separation.

1.5 Nanofluidics

When we zoom into the nanometer scale, several interesting and fundamental physical and chemical phenomena become accessible, including nonlinear electrokinetic flow and ion focusing,[291,460] nanocapillarity,[414] mass transport in nanoscale spaces,[178,338] and electrical double layer (EDL) overlap effects.[182,183,295] DNA stretching,[132] detection of single DNA molecules,[106] water purification,[184] and many other practical applications have been demonstrated using these effects.

Several review papers have been published about nanoscale fluid transport[25,338,370,427]

and flow in CNTs[243,272,430] in the last ten years. Extremely high aspect ratio, nanoscale inner diameter, and molecularly smooth hydrophobic graphitic walls make CNTs an ideal applicable material and platform for investigating nanofluidics. Numerical molecular dynamics simulations of nanopumping through CNTs has been presented by Insepov *et al.*,[163] Longhurst *et al.*,[219] and Rinne *et al.*,[319] showing that the nanopumping phenomena can be driven by temperature, AC electric fields, and the friction between gas particles and nanotube walls induced by SAW.

In addition to CNTs, inorganic nanotubes have been synthesized for use as a novel platform for nanofluidics.[122] Their advantages included a controllable inner diameter from 1 to 100 nm, facile functionalization of the inner and outer surfaces, and tunable compositions and aspect ratio. These features effectively provide the ability to mediate the ionic and electrostatic environment, both spatially and temporally. These forces are dominant at the femtoliter scale, which makes inorganic nanotube synthesis a powerful tool for femtoliter biological and chemical analyses.

Acoustic *nano*fluidics exhibits significant differences from acoustic *micro*fluidics and has not yet been as well developed.[98] However, early results are promising. Insepov et al.[163] used molecular dynamics simulation to predict a new nanopumping effect where SAW at the surface of a CNT cause gas flow within. The SAW-induced peristaltic motion along the CNT surface was predicted to pump the gas at 30 km/s. At these small scales, light can be used to create sound. Lin et al.[210] showed optical generation and spatial manipulation of nanoacoustic waves with nanoscale spot sizes. Pezeril et al.[290] was able to optically generate GHz-frequency shear acoustic waves in liquid glycerol. Van van Capel et al.[413] generalized nonlinear ultrafast acoustics at the nanoscale, reviewing both main properties of nonlinear ultrafast acoustic propagation and recent results. These initial investigations have set the stage for further practical applications.

The fabrication of nanoslits and nanochannels,[427] fluidic devices with nanometer scale in one or two dimensions, respectively, has been demonstrated[249,409,445] and applied to a number of applications such as DNA stretching[132,392,393] and single DNA molecule dynamics,[305,412]

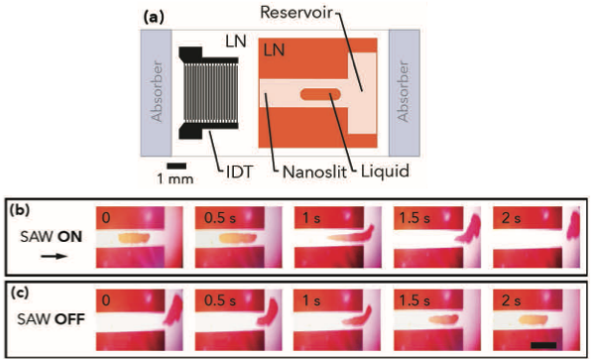

Figure 1.36: Manipulation of a liquid drop within the nanoslit based on SAW-driven acoustic streaming and capillary forces. When SAW was on, the SAW-driven acoustic streaming overcame the capillary force in the T-shape channel and pushed the liquid drop into the reservoir. When SAW was off, the capillary force led the liquid drop into the targeted nanoslit. Reprint permis. Miansari (2016).[247]

due to their flexibility of channel shape and surface properties. More specifically for acoustic nanofluidics, room-temperature bonding of LN to silicon wafers was demonstrated by Takagi *et al.*[379] and has been widely used to achieve enclosed nanochannels for the acoustic propagation of fluid.

Recently, Miansari and Friend[247] developed a novel room temperature LN/LN bonding technique and demonstrated a SAW-induced nanoslit platform for pumping nanoscale flows at up to 1 MPa (*see* Fig. 1.25), manipulating 10 fL drops (*see* Fig. 1.36), and separating nanoscale particles by size. The mechanisms responsible for these results need to be further investigated and explained in the future.

Chapter 2

An Investigation of Maximum Particle Velocity as a Universal Invariant — Defined by a Statistical Measure of Failure or Plastic Energy Loss for Acoustofluidic Applications

2.1 Abstract

Materials under vibration experience internal stress waves that can cause material failure or energy loss due to inelastic vibration. Traditionally, failure is defined in terms of material acceleration, yet this approach has many drawbacks, principally because it is not invariant with respect to scale, type of vibration, nor material choice. Here, the likelihood of failure is instead considered in terms of the maximum vibration or particle velocity for various metals, polymers, and structural materials. The exact relationship between the maximum particle velocity and

the maximum induced stress may be derived, but only if one knows the details of the vibration, material, flaws, and geometry. Statistical results with over thousands of individual trials are presented here to demonstrate a wide variety of vibrations across a sufficient variety of these choices. Failure in this context is defined as either fracture or plastic yield, the latter associated with inelastic deformation and energy loss during vibration. If the maximum permissible cyclical stress in material vibration is known, to at least an order of magnitude, the probability of this type of failure may be computed for a range of vibration velocities in each material. The results support the notion that a maximum particle velocity on the order of 1 m/s is a universal and critical limit that, upon exceeding, causes the probability of failure to become significant regardless of the details of the material, geometry, or vibration. We illustrate this in a specific example relevant to acoustofluidics, a simple surface acoustic wave device. The consequences of particle velocity limit analysis can effectively be used in materials and structural engineering to predict when dynamic material particle velocity can cause inelastic losses or failure via brittle fracture, plastic deformation, or fatigue failure.

2.2 Introduction

In the study of acoustic wave propagation in elastic solids, there is a physical limit to how much materials can vibrate before failing. This phenomenon appears across disciplines, from the study of actuating robotics or microelectromechanical (MEMS) devices[185] to vibration fatigue and crack propagation of complex structures and earthquakes explored by civil engineers and geologists alike[77,250]. If such a physical limit could be found, especially if it were defined in terms of easily measured parameters and the properties of the material being used, the choice of materials and geometry in engineering design could be made simpler. Additionally, finite element modeling of vibrations would be easier, alleviating the need to resort to complex, dynamic stress-strain models to evaluate the risk of failure[135]. In a vast majority of cases, vibration and acoustics

are carried in physical structures with the aim of avoiding inelastic or plastic deformation, fatigue failure, or fracture in these structures. Here, we assume that any of these phenomena represent structural failure.

For years, the acceleration has been used to describe both the potential and severity of failure due to localized peak stress[116]. Termed *shock severity*, it often is presented[273,373] as a number of g's, with $g = 9.81$ m/s^2, representing earth's gravitational acceleration. This concept is applied across many disciplines, from petroleum and geological engineering[469] to planetary dynamics[302] and microdevices[185], and from the formal literature to data sheets for public consumption. A notable example of the latter among many, the 1.8" hard drive used in the last popular portable music player—Apple's classic iPod—is described by Toshiba as being able to tolerate 2000g from a drop and 2g vibration at 15–500 Hz while operating[63]. Gaberson expressed understandable frustration with this use of acceleration to determine the risk of failure, stating "g's as any kind of shock severity is useless, even in the face of 50 years of tradition".

Due to the direct relationship between strain and displacement in a stress wave, maximum displacement has also been occasionally used to determine the likelihood a given material will fail under vibratory conditions[162], though it does not often appear in the published literature outside of earthquake research[67], where even there it is considered to have modest utility[139].

The particle (or vibration) velocity is a potential alternative to these two choices. Remarkably, it may prove to be the most universal quantity in defining the limiting motions of acoustic wave propagation and vibration in materials. Many years ago, Crandall and Hunt separately[68,162] determined that the internal stress and the particle velocity in elastic solids were directly related to each other—to at least an order of magnitude—for a few specific forms of vibration in otherwise flaw-free and continuous structures. Gaberson[116] defined the closely related *pseudovelocity* (V_0) and claimed it to be the most useful quantity to determine the risk of structural damage due to its vibration. The pseudovelocity is defined (using $\triangleq$) as the maximum displacement multiplied by the angular frequency: $V_0 \triangleq \omega \max_{x,t} u(x,t) = 2\pi f U_0$ (please consult the glossary of terms in

Appendix A).

In fact, the particle velocity can serve to define the risk of failure and changes in observed vibration phenomena that otherwise depends upon stress. The basic idea is to define a *maximum particle velocity* to represent the true limit of structural vibration while avoiding failure.

That the particle velocity is not more widely appreciated and utilized does seem to be a consequence of relying on the acceleration in assessing failure risk, as Gaberson describes, probably from the familiarity of using g-loading for predicting static failure. The cleverly presented relationship by Hunt and Crandall[68,162] between stress and particle velocity in unflawed structures appears to be forgotten. At the very least, it appears that this relationship has never been applied to a broader range of materials, other forms of structural vibration, nor structures with flaws or significant damping.

In recent years, disciplines such as *acoustofluidics*[65,109] and *ultrasonic actuation*[426] have arisen that employ much higher frequency acoustic waves to drive observable motion of fluids, cells, particles, motor components, and so on for a variety of purposes. The desire to produce these results from piezoelectric materials operating at resonance to maximize the energy transformed from electrical to kinetic forms results in very large energies concentrated in small volumes, on the order of 0.1 W in a 100 μm box for short periods. In water or most solids one would consider using in these applications, this represents a specific energy of $\sim$100 MW/kg, remarkably exceeding the specific energy of coal, natural gas, and gasoline (termed *higher heating value* in[78]). More energy is trapped in a volume by the mechanical motion induced by high frequency vibration than is released from the same volume by chemical reaction of these common fuels.

It should come as no surprise, then, that failure of these devices is widespread, especially in research and development. The motivation of this work is to identify an overall limit to the vibration as a design tool, using the risk of failure—either inelastic vibration giving rise to significant energy loss or outright failure of the material.

In what follows, we seek to identify a maximum practical particle velocity that fulfills

this criteria. It turns out that the particle velocity does appear to be a useful tool in judging the risk of a broadly defined "failure" from damping, fatigue, fracture, or plastic yielding across a variety of materials and vibration types.

The paper is organized as follows. We first describe the analysis framework used to determine the limiting particle velocity for avoiding probable material failure. This is followed by an update of the classic concept of a material-defined upper limit to vibration amplitude[68,162]. By virtue of the Monte Carlo method, we are able to then introduce extensions to this classic concept, taking in turn the effects upon the maximum particle velocity due to changes in the geometry of the structure, the effects of damping, the presence of cracks in brittle materials or stress concentrations in ductile materials, and the peculiar effects of fatigue. We chain these disparate effects together for a sample run, some of them active, others not, as randomly determined for each run. After tens of thousands of runs, it becomes evident that one can indeed define an overall *maximum particle velocity*, a universal, limiting order-of-magnitude for the particle velocity that, when exceeded, will potentially lead to material failure or inelastically-limited vibration with a probability of 50%. For each effect, randomly chosen parameters are selected over defined, reasonable ranges as necessary to produce a solution. The method is extensible, in that the reader can employ the approach for their situation as required to determine the appropriate maximum particle velocity.

2.3 Analytical and Statistical Analysis of Maximum Particle Velocity Limits

Our goal in this effort is not to exhaust every possible combination of material, vibration, shape, and failure mode. Instead, we consider specific cases that appear to adequately represent the vast range of options. The Monte Carlo method is then employed to choose, at random: a material, the type and presence of a flaw in the material, the details of the vibration, and a

structure carrying the vibration, potentially with geometric constraints. A choice for each of these parameters is made within what we believe to be a reasonable range to define a trial run. This run produces a prediction of the maximum stress present in the structure. This stress may then be compared to the yield stress for the material, corrected to deal with the dynamic nature of the motion and the damping of the material.

The entire aim is to seek a correlation between the order of magnitude of the particle velocity induced in a structure—perhaps with a flaw, significant damping, or constrained geometry—and the overall probability of failure of that material. Using this correlation, we seek to produce an order-of-magnitude estimate for the limiting particle velocity that may exist for a given material, and hopefully for all the materials we have selected for consideration as representatives of most practical engineering materials.

2.3.1 Process of Analysis

It will be later shown in subsection 2.3.2 that an maximum particle velocity $v_{\max}$ may be defined as a material property from the material's yield strength, stiffness, and density. Beyond this value, the material's failure is assured. How the material fails depends on the details.

The strategy is to first select a representative material: diamond, steel, aluminum, copper, polypropylene (PP), polyvinyl chloride (PVC), polymethyl methacrylate (PMMA), glass, concrete, or wood. All materials are presumed to be isotropic for tractability, and in realizing the use of anisotropic or composite media affects the material properties, but does not change them by orders of magnitude. These materials represent, broadly, those used in typical engineering structures that would be subjected to large amplitude vibration.

It is important to note here that mechanical damping is another means to potentially limit the amplitude of vibration or acoustic waves in a structure. Following the classic approach in defining damping, one may define a loss factor for harmonic oscillations, $\eta = D/2\pi W$, where D represents the energy dissipated over each vibration cycle and W represents the combination of

the energy stored and introduced into the system over a given cycle[38]. Unlike the damping ratio, the loss factor, η, remains appropriate here even for strongly nonlinear systems[294].

In many disciplines, however, the quality factor, Q, is a far more familiar and easily determined measure of the damping present in a given vibration that is responsible for energy loss. The greater the Q, the lower the energy lost to damping[38]. The relationship between them is often approximated by $Q \approx 1/\eta$, though the full definition is more complex:

$$\frac{1}{Q} \triangleq \sqrt{1+\eta} - \sqrt{1-\eta}, \tag{2.1}$$

which may be rearranged and expanded to produce an approximate series relation of the loss factor in terms of the quality factor,

$$\eta = \frac{1}{Q} - \frac{1}{8Q^3} - \frac{1}{128Q^5} + O\left[\left(\frac{1}{Q^7}\right)\right], \tag{2.2}$$

where O is the order of the error in the approximation (Bachmann–Landau notation,[12]).

In any case, the ratio of energy lost per cycle, D, to the total energy, W, $D/W \triangleq 2\pi\eta \approx 2\pi/Q$. Notably,

$$\lim_{Q \to 2\pi^+} \frac{D}{W} = 1. \tag{2.3}$$

The key implication of this result is to recognize that, whatever the nature of the vibration induced in a system, if $Q < 10^1$, the limiting particle velocity is not due to material failure. It is instead governed by the energy loss to damping, and acoustic or vibration energy is dissipated too quickly to sustain vibration. Thus, most rubbers and some plastics are unrealistic choices as they will be limited by their acoustic loss during elastic deformation, instead of a failure criteria which might be due to inelastic deformation or fracture.

We then choose the form of acoustic wave propagation, noting that it reduces the particle velocity at which failure is guaranteed from the material-defined value $v_{\max}$ to a limiting particle

velocity, v_{lim}. In other words, for a particular case defined by the type of acoustic wave and the shape of the structure that carries it, v_{lim} defines the threshold between material integrity and failure. By contrast, the intrinsic threshold between material integrity and failure is always defined by v_{max}. Local stress concentrations, fatigue, fracture toughness, and flaws are responsible for the difference.

We represent the reduction from an ideal v_{max} to v_{lim} as a product

$$v_{\text{lim}} \triangleq \prod_{i=1}^{5} \Psi_{ij} v_{\text{max}}, \tag{2.4}$$

for the j^{th} case of N total cases. The type of vibration transmitted through the structure as an acoustic wave—for example, longitudinal or transverse waves—reduces the material's maximum particle velocity by a certain amount, defined by Ψ_{1j}. The frequency of the acoustic wave strongly affects the damping and the effective stiffness of the material, which collectively acts to also reduce the limit particle velocity, represented by Ψ_{2j}. The material may also have a flaw, a hole, crack, or similar penetrating geometry, producing a stress concentration that reduces the limit particle velocity v_{lim} even further—by a factor of Ψ_{3j}. We also consider the possibility of ductile failure (with Ψ_{4j}) or fatigue failure (Ψ_{5j}) in reducing the maximum particle velocity to the limiting particle velocity. The relationship is outlined in Fig. 2.1.

$$\underset{\text{Case limit}}{v_{\text{lim},j}} = \underset{\text{Wave type}}{\Psi_1} \cdot \underset{\text{Frequency}}{\Psi_{2j}} \cdot \underset{\text{Flaw}}{\Psi_{3j}} \cdot \underset{\text{Ductile failure}}{\Psi_{4j}} \cdot \underset{\text{Fatigue failure}}{\Psi_{5j}} \cdot \underset{\text{Material max.}}{v_{\text{max}}}$$

Figure 2.1: From material property-based maximum particle velocity v_{max} to case-specific particle velocity limit v_{lim}, via factors Ψ_{1j} to Ψ_{5j} for the j^{th} run using a selected material. Each factor Ψ_{ij} is briefly defined in the text here and detailed later.

Choosing the material allows us to determine v_{max}. We then define the limit particle velocity as v_{lim} for the j^{th} run such that $j \in \{1,2,\ldots,N\}$, with $N = 10{,}000$ here. We note that $v_{\text{lim},j} \leq v_{\text{max}}$ for all j, and define $v_{\text{lim},j} \triangleq \beta_j v_{\text{max}}$ such that $\beta_j \triangleq \prod_{i=1}^{5} \Psi_{ij}$ and $0 \leq \beta_j \leq 1$ for all

j, as $0 \leq \Psi_{ij} \leq 1$ for all i, j. The probability, $P_{\mathrm{f}}(v)$ that the selected material will fail for a chosen particle velocity, v, is then determined by pairwise comparing this value to each and every $v_{\mathrm{lim},j}$ determined above via the following equation:

$$P_{\mathrm{f}}(v) \triangleq \frac{1}{N} \sum_{j=1}^{N} H\left(v - v_{\mathrm{lim},j}\right), \tag{2.5}$$

where $H(\chi) \triangleq (\chi + |\chi|)/(2\chi)$ except for $H(0) \triangleq 1$, the Heaviside step distribution with a dummy variable χ.

All this analytical machinery states that, upon choosing a particle velocity v, if $v \geq v_{\mathrm{lim},j}$, the probability of failure for the j^{th} run is 1 or 100%. However, the limiting velocity, $v_{\mathrm{lim},j}$, is different for each (j^{th}) case, because the values of Ψ_{ij} will vary from case to case. Thus under some circumstances the failure may not happen, while others will produce failure. The probability $P_{\mathrm{f}}(v)$ takes all N cases into consideration.

We seek to produce a particular order of magnitude estimate for the particle velocity that would lead to a 50% chance of material failure. Given the many possibilities within Ψ_{ij}, this is likely the best we can hope for.

We next consider the basic relationship between failure and the maximum particle velocity in a material before considering the details in computing each Ψ_{ij} term required to find the case-limited particle velocity, v_{lim}.

2.3.2 Material Upper Limit Particle Velocity by Yield Stress in One Dimensional Axial Vibration

We first consider the classic model of one-dimensional planar acoustic waves propagating through a homogeneous media, seeking to set the stage for extensions from this model to produce equally convenient results for other systems.

Internal stress caused by continuous harmonic vibration is a function of material density

and stiffness and is proportional to the maximum particle velocity within the solid. That is, the maximum speed a wave moves inside the material can determine the corresponding maximum stress during one full sinusoidal vibration cycle. As previously stated, cyclical plastic deformation—inelastic deformation—during vibration is undesirable and likely limits the particle velocity as well. Thus, we seek a material-dependent maximum particle velocity limit defined by the material-specific yield stress.

An equation that relates the maximum particle velocity during vibration to the material stress may be derived along the lines of Hunt and Crandall's approach and is expressed using the vibrational Mach number ($M_{\mathrm{v}} = V_0/c$)[68,162], where V_0 and c are the surface particle velocity amplitude and the acoustic wave phase velocity, respectively. Using linear dynamic elasticity for an isotropic, homogeneous media, the following one-dimensional elastic wave equation may be derived:

$$\frac{\partial^2 u}{\partial x^2} = \frac{1}{c_0^2}\frac{\partial^2 u}{\partial t^2}. \tag{2.6}$$

Presuming a harmonic traveling wave of sinusoidal form for displacement $u(x,t)$ produces the solution $u(x,t) = U_0 \sin(\omega t - kx)$ to the wave eqn. (2.6), with the wavenumber $k = 2\pi/\lambda = \omega/c$. Ignoring lateral motion (until later), the strain in a slim rod as this wave propagates along it is $\varepsilon = \partial u/\partial x$ and the particle velocity is $v = \partial u/\partial t$, producing $\varepsilon(x,t) = -v(x,t)/c$. So the maximum strain generated by the passage of the acoustic wave in one dimension is

$$\varepsilon_{\max} = (V_0/c) = M_{\mathrm{v}}. \tag{2.7}$$

The speed of this longitudinal wave is $c = \sqrt{E/\rho}$, where ρ is the material's density and E is its Young's modulus. Thus, the maximum stress is,

$$\sigma_{\max} = E\varepsilon_{\max} = \sqrt{\rho E}V_0. \tag{2.8}$$

We define material failure as equivalent to the condition when the stress at a point in the system exceeds the yield stress limit σ_y where plastic deformation occurs. Though this is not necessarily true failure, in the context of continuous vibration it is not desirable since it produces an irreversible change in the properties of the system.

With this definition in mind, the critical particle velocity associated with the material's failure due to vibration may be defined as

$$v_{\max} \triangleq \frac{\sigma_y}{\sqrt{\rho E}}. \tag{2.9}$$

However, the assumption of a one-dimensional, longitudinally-vibrating, infinite rod is simply unrealistic for most applications, and so the material property-based particle velocity limit in eqn. (2.9) is inadequate. The geometry, flaws, and size of the vibrating specimen may affect the estimate for this limit[68,162]. Damping may limit the maximum possible particle velocity in soft and plastic materials, while imperfections in brittle materials may cause stress concentrations and a higher risk of fracture-driven failure[294]. The particle velocity limit also depends on the lateral dimensions of the structure, sometimes called the "Poisson effect", which can take up elastic energy and effectively act to slow the speed of sound during vibration[13].

2.3.3 Geometric and Acoustic Waveform Effects

In most cases, the vibration under evaluation occurs in complex structures not represented by simple axial wave propagation theory. The complexity of the structure is likely to significantly affect the relationship between particle velocity and material stress. To take this into account, we consider other forms of vibration and use dimensionless parameters Ψ_{ij} to define the maximum particle velocity limits for them.

Other modes of vibration may propagate at speeds of sound different than simple longitudinal waves in thin media. For example, shear waves travel at a slower speed: $c_{\text{shear}} = \sqrt{G/\rho} <$

$\sqrt{E/\rho}$. Torsional waves[214], Rayleigh waves, flexural waves, or Love waves, among others, can also propagate in or upon a material.

This affects the relationship between the limiting material stress and the maximum particle velocity. For example, flexural waves in beams propagate far slower than longitudinal waves, implying the maximum particle velocity is greater for flexural waves. But there is more to consider. In modeling flexural waves in beams, for example, the Timoshenko beam model includes the effects of rotational inertia and lateral shearing ignored in the Euler-Bernoulli beam model, leading to an even slower wave speed in a Timoshenko beam and consequently a greater maximum particle velocity at failure[162]. Changing a model can change the estimate of the maximum particle velocity. The many models devised over the years for beams, membranes, rods, plates, shells, and other structures and the details they demand could easily overwhelm any effort to find a ubiquitous maximum particle velocity, if it exists.

Our approach to this problem is the observation that while these different models are certainly important, they do not affect the relationship between the limiting material stress and the maximum particle velocity beyond about an order of magnitude. Since we *seek to only find the order of magnitude of the maximum particle velocity*, we may choose a representative subset of the models to proceed. While it may be true that including more models of other phenomena would improve our estimate, we contend it is unlikely to significantly change the results. And even then, our aim here is to demonstrate a process for finding the maximum particle velocity across a series of models using a statistical approach, which we believe to be useful for design choices and developing an intuitive feel for what limits the propagation of acoustics and vibrations in materials and structures.

We can furthermore expect that whatever form the vibration might be, in an elastic media the basic relation between the maximum particle velocity and the limiting stress will be analogous to the relation found for longitudinal vibrations, differing only by a constant[162]. Evidence of this is provided in a broader derivation in the Appendix. In lieu of considering every possible form of

vibration, we next consider a pair of simple cases: transverse vibration of a beam and axial wave propagation in a narrow rod.

Transverse vibration of an Euler-Bernoulli beam

To illustrate our point in a concrete manner, we first consider the Euler-Bernoulli beam model for transverse, flexural vibration of a beam, and then return to axial vibration with the Pochhammer-Chree rod model. The Euler-Bernoulli beam equation, for a homogeneous elastic and slender beam, is

$$-EI\frac{\partial^4 w}{\partial x^4} = \rho A\frac{\partial^2 w}{\partial t^2}, \tag{2.10}$$

where I, A, and $w(x,t)$ are the second moment of area of the beam's cross-section, the area of the beam's cross-section, and transverse displacement, respectively, with the displacement dependent upon the axial coordinate x and time t. The corresponding stress is $\sigma(x,y,t) = EI\frac{\partial^2 w}{\partial x^2}$ at any point in the beam. The maximum stress, $\sigma_{\max}$, is located at $y_{\max} = Y$, the maximum distance from the neutral axis along the cross-section of the beam, and is given by

$$\sigma_{\max} = k\sqrt{E\rho}v, \tag{2.11}$$

with $k = \sqrt{EA/I}$ as a factor dependent upon the cross-sectional shape. Since typical beams have a convex cross-sectional shape, this factor, k, is typically greater than one, and may be as small as $k = \sqrt{3}$ for a rectangular cross-section and as large as $k = 2\sqrt{2}$ for a triangular cross-section. We choose to represent k in our modeling as a normally (Gaussian) distributed random value between these two limiting cases. The justification for a normal distribution, instead of, say, a uniform distribution is the observation that these limiting beam shapes are less common than those that produce intermediate values of k. In any case, the net effect upon the results of choosing another distribution for this factor is minor.

The maximum particle velocity limit is *reduced* from the longitudinal wave-based predic-

tion in eqn. (2.9) by a factor of $1/k$. In other words, the limiting particle velocity limit due to the transverse vibration of an Euler-Bernoulli beam is $v_{\text{lim}} = \Psi_{1j} v_{\text{max}}$, where $\Psi_{1j} = 1/k_j$ and k_j is a uniformly random value between $\sqrt{3}$ and $2\sqrt{2}$.

Axial wave propagation in a rod and the Pochhammer-Chree solution

Returning briefly to longitudinal wave vibration, one potential geometric effect that may appear is the lateral confinement and elasticity ignored by the one-dimensional analysis. This is known to introduce an additional degree of freedom to an acoustic wave propagating through the structure. The motion will reduce the speed of sound for the propagation of the wave, leading to a change in the relation between the terms in eqn. (2.7) and consequently eqn. (2.9). We consider a simple elastic, homogeneous, and isotropic round bar with circular cross section as a representative example of this phenomena. As the diameter of the rod, $D \to \infty$, this effect would likewise become negligible, returning us to the original model in subsection 2.3.2. However, for small values of $D < 2\lambda$, the actual speed of sound c_{rod} is reduced as either the Poisson's ratio ν or the diameter-to-wavelength ratio $\Delta = D/\lambda$ is increased[13]. Thus, based on eqn. (2.9), the limiting particle velocity for a longitudinal wave including lateral effects would be $v_{\text{lim},j} = \Psi_{1j} v_{\text{max}}$, where $\Psi_{1j} = c_{\text{rod},j}/c_0$. The index j refers to the j^{th} run using a particular material in the analysis, where $c_{\text{rod},j}/c_0$ is chosen at random with uniform distribution over the range 0.563 to 1 based on physically permissible values of Poisson's ratio, ν, and the diameter-to-wavelength ratio $\Delta = D/\lambda$ according to Bancroft[13].

2.3.4 The Effects of the Frequency of the Acoustic Wave on Damping and Dynamic Material Stiffness

Since the Young's modulus of an isotropic material under vibration actually depends upon the frequency of the vibration[294], significantly stiffening with an increase in the frequency, the

ratio of Young's modulus appropriate for this frequency, the *dynamic* Young's modulus $E(f)$, to its (nearly) static counterpart, E_0, may be approximated from the loss factor,

$$\eta = \frac{\pi}{2} \frac{\log(\frac{E(f)}{E_0})}{\log(\frac{f}{f_0})}, \tag{2.12}$$

where we suppose $f_0 = 1$ Hz, $E_0 \sim E(f_0)$ represents low-frequency vibration[294]. Therefore, we may define the reduction in the limiting particle velocity due to damping and the frequency of the acoustic wave as

$$\Psi_{2j} = \sqrt{\frac{E_0}{E(f_j)}} = \left(10^{-\frac{2\eta}{\pi}}\right) \frac{f_0}{f_j}. \tag{2.13}$$

Later, when we use eqn. (2.13) to statistically determine the limiting particle velocity by producing N total runs for each material, the frequency f_j as a random value between 10^0 Hz and 10^9 Hz on a base-ten logarithmic scale, a typical range for the majority of acoustic phenomena.

2.3.5 Effects of Flaws as Stress Concentrations and Cracks

Flaws in most engineering materials can significantly reduce the failure stress. Depending on the orientation and size of the flaw, a stress concentration may locally form around the flaw and contribute to broader failure of the material. It is overwhelmingly difficult to pursue broad treatment of elastoplastic fracture mechanics applied to the many forms of stress and flaw shapes that may arise in practical situations. Moreover, the micromechanics of failure in flawed media is a complex subject under study for many years[72]. Instead of being drawn into these aspects, instead we once again choose an exemplar to represent an order-of-magnitude estimate of this phenomena: elliptical cracks in a material, uniaxially loaded by stress, σ, as the vibration or acoustic wave propagates through the system, producing a large range of stress concentration factors due to variance in their size and orientation. If the material is also brittle, then the material may separately fail by exceeding its critical fracture toughness.

Ductile failure

Stress concentrations in a ductile material around a flaw may produce plastic yielding that represents failure as an acoustic wave is transmitted through it. For example[8], in an elliptical crack of length $2a$ by $2b$, the stress produced near the crack tip, σ_c, is greater than the uniaxial stress σ_y by a factor ϕ representing the stress concentration. For this crack geometry, $\sigma_c = \phi\sigma_y$, where $\phi = 1 + 2(a/b)$. This implies that once $\sigma_c \to \sigma_f$, the failure stress or $\sigma_c \to \sigma_y$, the yield stress, the result is at least local plastic yielding that would be undesirable in continued vibration. At worst, the material fails. With this potential flaw representing the class of myriad flaws that may be present in ductile materials, the limiting particle velocity will be the maximum particle velocity scaled by the factor $\Psi_{3j}^{-1} \triangleq \phi_j = 1 + 2(a_j/b_j)$. For our statistical analysis, we require the ratio (a_j/b_j) to be randomized between 0.1 to 10 on a base-ten logarithmic scale.

Brittle failure

In a brittle material, the stress in the vicinity of a sharp-tipped crack is generally dependent on the square root of the distance from the crack tip, and it and the growth of the crack to eventual failure both depend upon the *fracture toughness* K_C, a material property. The *stress intensity factor*, K, may be calculated for a given stress and crack size, and here we choose as our exemplar the plane strain mode I fracture toughness, K_{IC}. As a defined property of brittle materials, it may be used to determine the failure stress, $\sigma_f = K_{IC}/\sqrt{a\pi}$, for a crack of length $2a$ centrally located in a thin, semi-infinite plate material. The crack is presumed to be perpendicularly oriented to the direction of the stress.

Failure in flawed material for a given analysis is either due to brittle or ductile failure

The randomly preselected crack size for each run is a_{sj}, randomly defined between 10^{-6} and 1 mm on a base-ten logarithmic scale. Depending on this crack length, some materials may either fail via brittle or ductile failure. To determine which, we determine the critical crack size

for brittle failure,

$$a_{\mathrm{c}} = \frac{1}{\pi}\left(\frac{K}{\sigma_{\mathrm{y}}}\right)^2, \tag{2.14}$$

where σ_{y} is the yield stress. For the j^{th} run, if $a_{sj} > a_{\mathrm{c}}$, the material will fail from the brittle crack, and the limiting particle velocity is further reduced due to this by a factor $\Psi_{4j} = \sqrt{\frac{a_{\mathrm{c}}}{a_{sj}}}$. If, however, $a_{sj} < a_{\mathrm{c}}$, the material will fail by exceeding the ductile yield stress, σ_{y}, before brittle failure becomes a problem, and so $\Psi_{4j} = 1$.

2.3.6 Effects of Endurance and Fatigue

Ductile materials may also fail under cyclical stresses well below the material's yield stress. Cyclical vibrations from acoustic wave transmission and vibration, in particular, may exceed a material's endurance limits due to fatigue that accumulates with time. As with the other effects, the many ways this effect may impact a given material's response to vibration depends upon the characteristics of the material and the vibration, and so we again constrain our analysis into a tractable version by limiting the number of vibration cycles to at most 10^6 and a frequency between 0.1 kHz to 1 MHz on a base-ten logarithmic scale when fatigue is relevant. Fatigue arises in the context of structural vibration and in this context is only relevant over this limited frequency range. The fatigue endurance-limited stress of such a material after 10^6 cycles is written as σ_{E}, and is less than the yield stress σ_{y}. We define in the statistical analysis the effect this would have on the limiting particle velocity as $\Psi_{5j} \triangleq \sigma_{\mathrm{E}}/\sigma_{\mathrm{y}}$.

2.4 Results

The probability of failure of eleven selected materials—diamond, steel, aluminum, copper, polypropylene (PP), polyvinyl chloride (PVC), Polymethyl methacrylate (PMMA), glass, concrete, wood, and lithium niobate—illustrates a consistent trend towards failure at a particle velocity of $v = O[0.1 - 10]$ m/s (Fig. 2.2). The results produced by $N = 10,000$ runs per material is

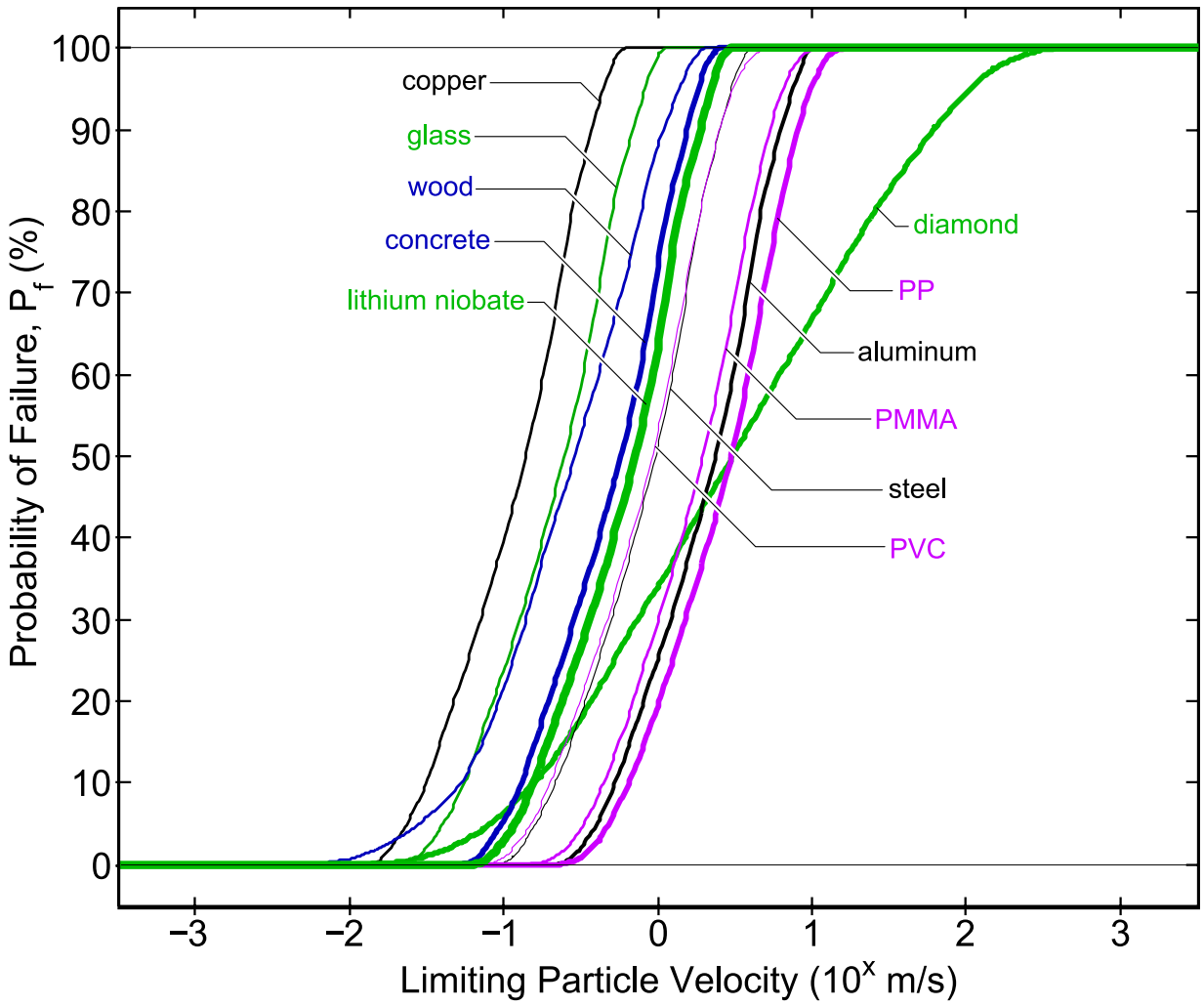

Figure 2.2: The probability of failure P_f versus particle velocity v for eleven selected materials (*see* text). Ten thousand (N) runs for each material choice produces a nearly continuous distribution of failure probability with respect to the particle velocity. The result is nearly sigmoidal, but with small yet important discrepancies between materials and over v. These arise from the effects of the different forms of acoustically-driven failure.

monotonically increasing with respect to the particle velocity in the plot, with the horizontal axis plotted as a base-ten logarithm for clarity. There is no scatter in this data nor error bars to provide as each (j^{th}) result lies at a specific combination of the particle velocity and probability of failure.

We then nondimensionalize the particle velocity as $\hat{v} \triangleq v/v_{\max}$, remembering that $v_{\max}$ is a material property. By further considering the probability of failure based on this dimensionless particle velocity $v/v_{\max}$, the data appears to collapse to produce a similar probability of failure

for a given dimensionless particle velocity $\hat{v}$ regardless of the chosen material in Fig. 2.3, with the notable exceptions of diamond and wood. These two examples indicate the importance of the toughness of flawless diamond, the fragility of diamond with flaws, and the unique failure characteristics of wood. Other single crystal and composite media are likely to exhibit similar results.

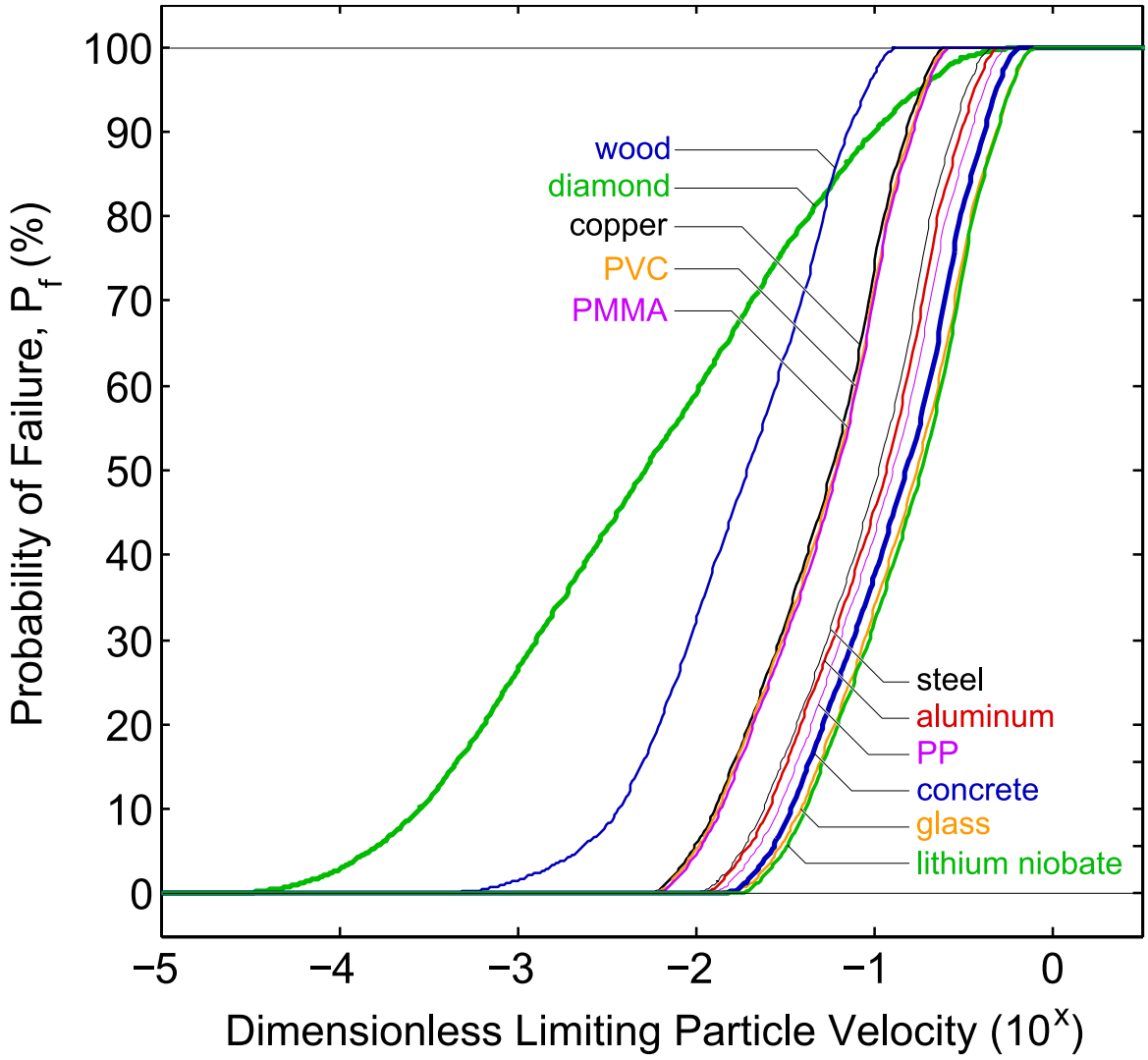

Figure 2.3: Probability of failure P_f versus the dimensionless particle velocity $\hat{v}$ for the eleven selected materials. Diamond exhibits a broader range of particle velocities over which failure may occur because of its unique toughness without flaws and fragility with flaws. Most of the other materials, except for wood, fall into a narrowly defined group.

Referring to the results in Figs. 2.2 and 2.3, the probability of failure at low vibration

velocities with $P_f \approx 0$ until 10^{-2} m/s, where wood, copper, diamond, and glass are first to exhibit nonzero failure probabilities, followed by steel, lithium niobate, aluminum, and the polymers. Diamond produces a different distribution of failure probabilities with respect to particle velocity than the other materials, partially a consequence of its hardness and high yield stress, and partially because it is more fragile than most of the other materials when it has a flaw.

Table 2.1: Particle velocity, dimensional (v) and dimensionless ($\hat{v}$), for each of the selected materials where the probability of failure at $P_f = 50\%$ over all $N = 10000$ cases per material.

Material	v (m/s)	$\hat{v}$ (—)
Copper	0.14	0.06
Glass	0.25	0.18
Wood	0.30	0.02
Concrete	0.58	0.15
Steel	0.96	0.11
Polyvinyl Chloride (PVC)	0.93	0.04
Aluminum	2.40	0.12
Acrylic (PMMA)	2.04	0.05
Diamond	3.09	0.005
Polypropylene (PP)	3.02	0.10
Lithium Niobate (LN)	0.69	0.19
Mean	1.31	0.09
95% Confidence Interval	0.46 – 1.58	0.034 – 0.12

Crucially, consider the distribution of particle velocities at which $P_f = 50\%$ for the chosen materials, as tabulated in Table 2.1. The results indicate that the mean particle velocity at $P_f = 50\%$ is 1.31 m/s for these eleven materials, incorporating various forms of vibration, frequencies, flaws, and fatigue. With the 95% confidence interval from 0.46 to 1.58 m/s ($10^{-0.07\pm0.27}$ m/s) for v_{lim} predicted from logistic regression of all the data for all materials, it appears reasonable to conclude that a limiting particle velocity of $v_{\text{lim}} = O[1 \text{ m/s}]$ exists. Furthermore, by non-dimensionalizing the data, a dimensionless limiting particle velocity also may be predicted to be $\hat{v}_{\text{lim}} = O[0.1]$ with a 95% confidence interval within 0.034 to 0.12 ($10^{-1.19\pm0.28}$) via logistic regression.

2.5 Discussion of These Results in the Context of an Acoustofluidics Example

Surface acoustic waves (SAW) are both classic and modern, with wide use in communications since the classic development of interdigital transducer (IDT) electrodes in 1965[432] and numerous acoustofluidics applications in the past twenty years[65,111]. Only in acoustofluidics has it become necessary to drive the devices near their structural limits, leading to rapid device failure. The maximum particle velocity on the substrate has been empirically shown to be $O[1$ m/s$]$, but there has been no theoretical analysis nor experimental results to show why this actually occurs or might be important. Here, we present the surface particle velocity amplitude on a lithium niobate (LN) substrate due to IDT-generated SAW. The velocity is measured via laser Doppler vibrometer, exhibiting a maximum particle velocity of $O[1$ m/s$]$.

2.5.1 Experimental Setup and Results for Surface Acoustic Wave Particle Velocity Measurement

We designed and fabricated SAW interdigital transducer (IDT) devices on double-side polished 128° Y-rotated cut LN (Precision Micro-Optics Inc., Burlington, MA,USA) for surface acoustic wave generation and propagation. The fabrication and usage details, including images of the devices, are provided in ample detail elsewhere[246]. A wavelength of $\lambda = 100$ μm was selected for an operating frequency of $\sim$40 MHz (from $f = v/\lambda$) to define each IDT, comprised of twenty simple finger pairs with finger and gap widths of $\lambda/4$ and an aperture of 2 mm. For lithium niobate wafers of 500 μm thickness, 40 MHz is approximately the minimum frequency that may be used to generate useful Rayleigh SAW. Lower frequencies typically reported in much of the acoustofluidics literature are actually generating Lamb waves instead[65]. Standard UV photolithography (using AZ 1512 photoresist and AZ 300MIF developer, MicroChem,

Westborough, MA) was used alongside sputter deposition and lift-off processes to fabricate the 10 nm Cr / 1 μm Au IDT upon the 500 μm thick LN substrate[65]. Absorbers (Dragon Skin™, Smooth-On, Inc., Macungie, PA) were used at the center and periphery of the device to prevent edge reflections and spurious bulk waves. Surface acoustic waves were generated by applying a sinusoidal electric field to the IDT at resonance using a signal generator (WF1967 multifunction generator, NF Corporation, Yokohama, Japan) and amplifier (ZHL–1–2W–S+, Mini-Circuits, Brooklyn, NY, USA). The actual voltage, current, and power across the device were measured using an oscilloscope (InfiniVision 2000 X-Series, Keysight Technologies, Santa Rosa, CA). The particle velocity perpendicular to the substrate surface was measured using a laser Doppler vibrometer (LDV, UHF–120SV, Polytec, Waldbronn, Germany).

By increasing the voltage of the signal delivered to the IDTs, the particle velocity of the SAW perpendicular to the substrate surface also increases—to a limit. The particle velocity increases linearly when the voltage is relatively small, up to an apparent limit at about 1.2 to 1.4 m/s; this limit at $O[1]$ m/s appears when the input signal is relatively large, and remains relatively constant until the device fails at around 20 V.

This device is a simple version of the many such devices used for acoustofluidics. The SAW is converted into sound propagating in a fluid in contact with such a substrate. Because this sound is intense and produces compressibility in the fluid, a combination of the density variations and particle velocity—in the presence of viscosity sufficient to cause a phase shift between them—altogether gives rise to acoustic streaming. Acoustic streaming is transmitted most often via the streamwise acceleration or the Reynolds stress, and scales with ρU^2, where ρ and U are the fluid density and amplitude of the LN surface's particle velocity, respectively. Since $U \sim 1$ m/s for the LN substrate at its limit, the steady acoustic pressure is ~ 1 kPa for most fluids. This is a relatively weak pressure limit and is difficult to improve upon, a key reason why acoustic streaming in its traditional form is not very effective in high-pressure applications. However, there are other approaches that may produce useful results[466,467]. The key point is that while

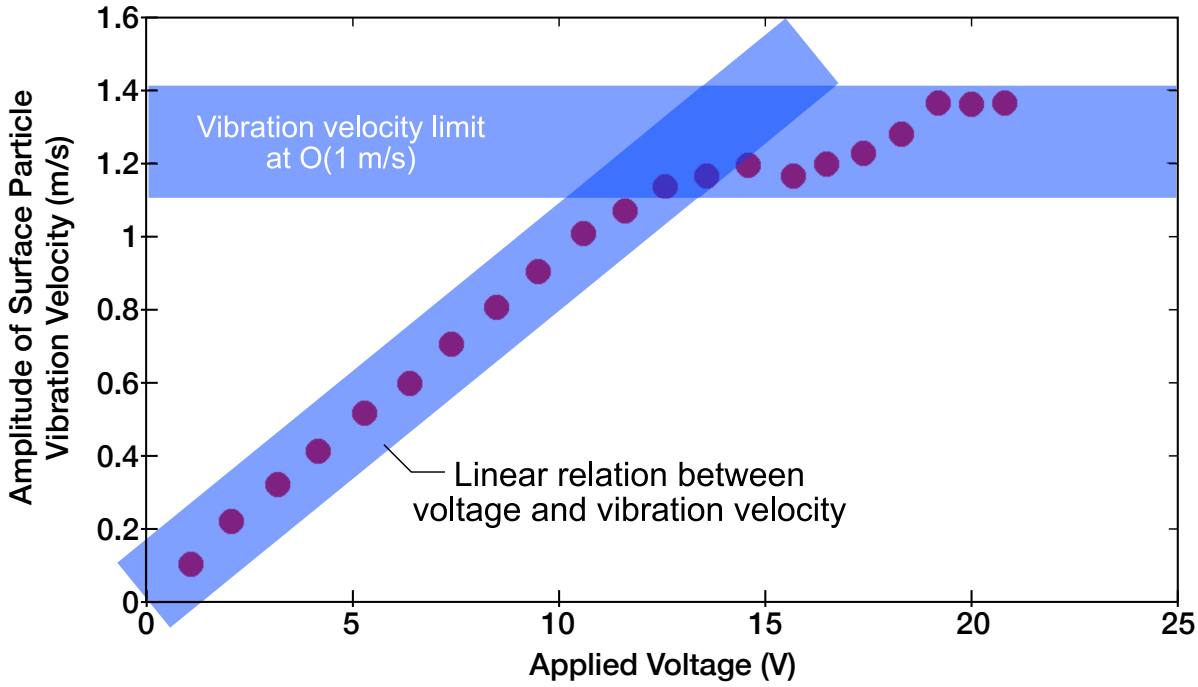

Figure 2.4: Particle velocity of SAW generated and propagating upon a lithium niobate substrate versus the applied voltage on the IDT. There is a linear relation between an increasing applied voltage and the particle velocity, until 15 V, at which point the particle velocity becomes essentially constant between 1.2 and 1.4 m/s, corresponding to the estimated particle velocity limit of $O[1\text{ m/s}]$ from the earlier analysis.

there are many advantages to using acoustic waves in propelling fluids via acoustic streaming, seeking to do so against anything more than a modest pressure head is unlikely to work.

2.6 Conclusions

We have sought to define a limiting particle velocity for acoustic waves and vibrations as defined upon the concept of material failure in a variety of conditions and material choices. The relationship between maximum particle velocity and maximum stress during vibration has been found and used for this purpose. While the limit particle velocity is not merely defined by material failure, it can be treated in this way by noting that the appearance of inelastic material responses—plasticity, significant anelastic damping—may be included as "failure" in the context

of acoustic waves and vibrations because these phenomena will limit the particle velocity all the same.

The particle velocity limits were defined in terms of the maximum particle velocity, a material property. Dimensionless parameters Ψ_{ij} were defined to represent geometric effects and modes of vibration, damping, cracks and imperfections, endurance and fatigue, and the weakening of the material due to cracks in brittle materials. Statistical results were presented using the Monte Carlo method for eleven different materials of $N = 10000$ specimens each, randomizing the geometry, wave modes, and frequency to relate the probability of material failure to the limiting particle velocity. A limiting particle velocity of $v_{\text{lim}} = O[1 \text{ m/s}]$ exists with a 95% confidence interval from 0.46 to 1.58 m/s ($10^{-0.07\pm0.27}$ m/s) predicted from logistic regression of all the data for all materials, types of vibration, and failure modes considered in this study. The nondimensional limit is $\hat{v}_{\text{lim}} = O[0.1]$ with a 95% confidence interval from 0.034 to 0.12.

The concept of the limiting particle velocity as an invariant at $O[1 \text{ m/s}]$ is useful when one recognizes that the classic use of acceleration as a failure criteria does not apply in acoustic devices. Acceleration is not invariant with respect to frequency. Similarly, the displacement amplitude cannot be used because it is likewise dependent upon the frequency. Regardless of the phenomenon and its frequency, one may begin with the assumption that failure of a material may be a risk when $O[1 \text{ m/s}]$. Beyond failure, anelastic response of materials may equally arise at this particle velocity, suggesting it as a practical limit to motion that may be induced in a material without extraordinary effort or damaging the material's integrity. In other words, even if the material does not fail, it may fail to produce larger amplitude responses due to energy losses. This was illustrated via a simple experiment where SAW was generated across the surface of lithium niobate.

The consequences of particle velocity limit analysis can effectively be used in materials and structural engineering to predict when dynamic material vibration velocity can cause failure in various forms (i.e., brittle fracture, repeated plastic deformation, fatigue failure). Furthermore,

this analysis may be useful in predicting the potential amplitude and frequency limits of actuators that rely on resonant or driven vibrations. In the future, material structures evaluated for vibration failure via finite element modeling of complex geometry, damping, and flaws may be simplified. Rather than calculating the likelihood of dynamic failure by localized time-dependent stress-strain relationships, strain energy, expressions, or bespoke failure models, the local nodal velocity could be used as a proxy for predicting failure and the presence of damaging vibrations.

Finally, the implications of $O[1\text{ m/s}]$ as a limiting particle velocity are profound when exploring the highest end of the frequency range $f = 1$ Hz to 1 GHz that we considered. With $v_{\text{lim}} = O[1\text{ m/s}]$, we have a maximum displacement of only $u_{\text{lim}} = (2\pi f)^{-1} v_{\text{lim}} O[0.1\text{ nm}]$ at 1 GHz, yet an acceleration of $\alpha_{\text{lim}} = 2\pi f v_{\text{lim}} O[10^{10}]$ m/s^2. Such large accelerations are responsible for many of the peculiar phenomena observed and reported in acoustofluidics, and will surely be the source of more interesting results to come.

2.7 Appendix

2.7.1 Key Parameters and Notations

Parameter	Notation	SI Units
“Defined as”	$\triangleq$	—
Acceleration	α	m/s
Crack size	a	m
Critical crack size	a_c	m
Cross section area	A	m^2
Sound velocity in solid, longitudinal, one dimensional	c_0	m/s
Sound velocity in solid, longitudinal, circular rod	c_{rod}	m/s
Circular rod diameter	D	m
Young’s modulus	E	Pa
Frequency of vibration	f	Hz
Ductility factor	F_{duct}	m
Shear modulus	G	Pa
Second moment of area	I	m^4
Fracture Toughness	K_{IC}	$Pa\sqrt{m}$
Wavelength in solid	λ	m
Poisson’s ratio	μ	—
Vibrational Mach number	M_v	—
Number of cases per material	N —	
Order of approximation error[12]	O	¡varies¿
Probability of failure	P_f	%
Factor reducing maximum particle velocity to produce limiting particle velocity	Ψ_{ij}	—
Density	ρ	kg/m^3
Stress	σ	Pa
Endurance limit	σ_E	Pa
Brittle fracture failure stress	σ_f	Pa
Yield strength	σ_y	Pa
Time	t	sec
Longitudinal displacement	u(x,t)	m
Vibration velocity	v	m/s
Limiting vibration velocity	v_{lim}	m/s
Maximum vibration velocity	v_{max}	m/s
Circular frequency	ω	rad/s
Transverse displacement	w(x,t)	m
Distance to neutral axis (bending)	y	m

2.7.2 A Derivation of the Relationship Between the Maximum Particle Velocity and the Stress for a Planar Acoustic Wave in an Elastic Medium

Introduction

The purpose of this appendix is to illustrate to readers the general applicability of the concept relating the particle velocity to the strain, and consequently the material properties. We progress through a brief derivation of the governing equations and a simple solution of them for an isotropic material. Solutions for anisotropic materials, coupled media, and finite deformations build upon this basic approach, though often demand computation to produce solutions.

The equation of motion for a solid elastic material

Derivation of Newton's second law for an infinitesimal volume of elastic media[11] produces

$$\nabla \cdot \mathbf{T} + \mathbf{f} = \rho \frac{\partial^2 \mathbf{u}}{\partial t^2}, \tag{2.15}$$

and, in component notation, we are able to write

$$\frac{\partial T_{ik}}{\partial x_k} + f_i = \rho \frac{\partial^2 u_i}{\partial t^2}. \tag{2.16}$$

The equations relate the stress $\mathbf{T}$, body force $\mathbf{f}$, and particle displacement $\mathbf{u}$ in the elastic material. We note in passing the occasional use of the *momentum density* ([M][L]$^{-2}$[T]$^{-1}$) in the literature, defined as $\mathbf{p} = \rho \mathbf{v}$ where $\mathbf{v} = \frac{\partial}{\partial t}\mathbf{u}$, so that

$$\nabla \cdot \mathbf{T} + \mathbf{f} = \frac{\partial \mathbf{p}}{\partial t}. \tag{2.17}$$

From the strain (**S**)-displacement (**u**) relationship, noting $\nabla_s = \left(\nabla + \nabla^T\right)$ is the symmetric gradient operator and $(\cdot)^T$ is the transpose operator,

$$\nabla_s \mathbf{u} = \mathbf{S} \Rightarrow \nabla_s \mathbf{v} = \frac{\partial \mathbf{S}}{\partial t} \tag{2.18}$$

using a time derivative on both sides.

For a standard elastic solid, the strain is the stress multiplied by the compliance or $\mathbf{S} = \mathbf{s} : \mathbf{T}$, with : as the double-dot product, and so

$$\frac{\partial \mathbf{S}}{\partial t} = \mathbf{S} : \frac{\partial \mathbf{T}}{\partial t} \Rightarrow \nabla_s \mathbf{v} = \mathbf{S} : \frac{\partial \mathbf{T}}{\partial t}, \tag{2.19}$$

where $\mathbf{v} = d/dt(\mathbf{u})$ is the particle velocity, producing

$$\mathbf{c} : \nabla_s \mathbf{v} = \frac{\partial \mathbf{T}}{\partial t}. \tag{2.20}$$

Here we also use the definition of the stiffness **c** such that $\mathbf{c} : \mathbf{s} = \delta$, with δ as the identity tensor. If we take $\nabla \cdot \mathbf{T} + \mathbf{f} = \rho \frac{\partial}{\partial t} \mathbf{v}$ and take its derivative with respect to time, t,

$$\begin{aligned} \nabla \cdot \frac{\partial \mathbf{T}}{\partial t} + \frac{\partial \mathbf{f}}{\partial t} = \rho \frac{\partial^2}{\partial t^2} \mathbf{v} \Rightarrow \\ \nabla \cdot (\mathbf{c} : \nabla_s \mathbf{v}) + \frac{\partial \mathbf{f}}{\partial t} = \rho \frac{\partial^2}{\partial t^2} \mathbf{v} \Rightarrow \\ \nabla_{i\alpha} c_{\alpha\beta} \nabla_{\beta j} v_j + \frac{\partial}{\partial t} f_i = \rho \frac{\partial^2}{\partial t^2} v_i, \end{aligned} \tag{2.21}$$

the equation of motion in component form, written in terms of the particle velocity v_i, stiffness $c_{\alpha\beta}$, and the body force f_i. In this form, we have chosen to abbreviate the component notation by taking advantage of the inherent symmetry present in even a very anisotropic material, such that the full fourth-order stiffness tensor c_{ijkl} may be written as $c_{\alpha\beta}$ where $\alpha, \beta \in \{1, 2, \ldots, 6\}$.

Assuming a harmonic propagating wave

Suppose we have a harmonic wave, an acoustic wave propagating along $\mathbf{e}_\eta = a_1\mathbf{e}_1 + a_2\mathbf{e}_2 + a_3\mathbf{e}_3$, and assume the unit vectors $\mathbf{e}_i$ form a right-handed orthogonal coordinate system. Then the terms in eqn. (2.21) will be proportional to $e^{\iota(\omega t - k(\mathbf{e}_\eta \cdot \mathbf{r}))}$.

This lets us greatly simplify the operators $\nabla_{i\alpha}$ and $\nabla_{\beta j}$, replacing them, respectively, with matrices

$$\iota k \begin{bmatrix} a_1 & 0 & 0 & 0 & a_3 & a_2 \\ 0 & a_2 & 0 & a_3 & 0 & a_1 \\ 0 & 0 & a_3 & a_2 & a_1 & 0 \end{bmatrix} \equiv \iota \mathfrak{k}_{i\alpha} k \equiv \iota k_{i\alpha} \tag{2.22}$$

and

$$\iota k \begin{bmatrix} a_1 & 0 & 0 \\ 0 & a_2 & 0 \\ 0 & 0 & a_3 \\ 0 & a_3 & a_2 \\ a_3 & 0 & a_1 \\ a_2 & a_1 & 0 \end{bmatrix} \equiv \iota \mathfrak{k}_{\beta j} k \equiv \iota k_{\beta j}. \tag{2.23}$$

If we set the applied forces, $f_i = 0 \forall i \in \{1,2,3\}$, then $\nabla_{i\alpha} c_{\alpha\beta} \nabla_{\beta j} v_j + \frac{\partial}{\partial t} f_i = \rho \frac{\partial}{\partial t} v_i$ becomes

$$-k^2 \mathfrak{k}_{i\alpha} c_{\alpha\beta} \mathfrak{k}_{\beta j} v_j = -\rho\omega^2 v_i. \tag{2.24}$$

By defining the *Christoffel matrix* $\Gamma_{ij} \equiv \mathfrak{k}_{i\alpha} c_{\alpha\beta} \mathfrak{k}_{\beta j}$,

$$k^2 \Gamma_{ij} v_j = \rho\omega^2 v_i. \tag{2.25}$$

From the *Christoffel equation* (2.25) we may obtain $(k^2\Gamma_{ij} - \delta_{ij}\rho\omega^2)v_j = 0$, the *slowness equation*. Little more can be done to solve this equation without knowing the details of the material's

anisotropy, but let us consider the simplest case here.

In an isotropic medium produces the expected relationship between the particle velocity and the strain

Let us presume the wave is in an isotropic medium, noting that $c_{12} = \frac{1}{2}(c_{11} - c_{44})$ and the substantial symmetry present in the media otherwise, leaving only two independent constants to define it.

The Christoffel matrix becomes

$$[\Gamma_{ij}] = [\mathfrak{k}_{i\alpha}][c_{\alpha\beta}][\mathfrak{k}_{\beta j}] = \begin{bmatrix} c_{11}a_1^2 + c_{44}(1-a_1^2) & (c_{12}+c_{44})a_1a_2 & (c_{12}+c_{44})a_1a_3 \\ (c_{12}+c_{44})a_2a_1 & c_{11}a_1^2 + c_{44}(1-a_2^2) & (c_{12}+c_{44})a_2a_3 \\ (c_{12}+c_{44})a_3a_1 & (c_{12}+c_{44})a_3a_2 & c_{11}a_3^2 + c_{44}(1-a_3^2) \end{bmatrix} \tag{2.26}$$

Suppose we assume that the wave is propagating along $\mathbf{e}_3$. Since the material is isotropic, it does not matter which direction we choose. Then $\mathbf{e}_\eta = 0\mathbf{e}_1 + 0\mathbf{e}_2 + 1\mathbf{e}_3$ and $\mathbf{k} = k\mathbf{e}_\eta = k\mathbf{e}_3$: $k^2\Gamma_{ij}v_j = \rho\omega^2 v_i$ becomes

$$k^2 \begin{bmatrix} c_{44} & 0 & 0 \\ 0 & c_{44} & 0 \\ 0 & 0 & c_{11} \end{bmatrix} \begin{bmatrix} v_1 \\ v_2 \\ v_3 \end{bmatrix} = \rho\omega^2 \begin{bmatrix} v_1 \\ v_2 \\ v_3 \end{bmatrix} \tag{2.27}$$

and so $k^2c_{44}v_1 = \rho\omega^2 v_1$, $k^2c_{44}v_2 = \rho\omega^2 v_2$, and $k^2c_{11}v_3 = \rho\omega^2 v_3$.

A shear wave is propagating along $\mathbf{e}_3$ with $\mathbf{v} = \mathbf{e}_1 v_1 e^{\imath(\omega t - kx_3)}$ where x_i is a coordinate along $\mathbf{e}_i$ that must have $k^2c_{44} = \rho\omega^2$. Likewise, another shear wave exists such that $\mathbf{v}' = \mathbf{e}_2 v_2 e^{\imath(\omega t - kx_3)}$ with $k^2c_{44} = \rho\omega^2$. Finally, $\mathbf{v}$" $= \mathbf{e}_3 v_3 e^{\imath(\omega t - k\chi_3)}$ with $k^2c_{11} = \rho\omega^2$ as the longitudinal wave. These bulk waves have different speeds depending on c_{44} and c_{11}.

Now it is useful to note the particle displacement $\mathbf{u}$ can be found through integration of the particle velocity $\mathbf{v}$,

$$\mathbf{u} = \int \mathbf{v}\, dt = \frac{v}{\imath\omega} e^{\imath(\omega t - k x_3)} \mathbf{e}_3, \tag{2.28}$$

and so the resulting strain along the $\mathbf{e}_3$ direction is

$$S_{33}\mathbf{e}_3 = \frac{\partial \mathbf{u}}{\partial z}\mathbf{e}_3 = -\frac{vk}{\omega} e^{\imath(\omega t - k x_3)} \mathbf{e}_3. \tag{2.29}$$

Since

$$\frac{vk}{\omega} = \frac{2\pi v}{2\pi f \lambda} = \frac{v}{f\lambda} = \frac{v}{c_0} \tag{2.30}$$

where c_0 is the speed of sound, we find that the magnitude of the longitudinal strain is a ratio of the particle velocity to the speed of sound in the media for the longitudinal wave described by $\mathbf{v}''$,

$$|S_{33}| = \frac{vk}{\omega} = \frac{v}{c_0}. \tag{2.31}$$

The shear wave solutions will produce similar results.

2.8 Acknowledgement

We are grateful to the University of California for provision of funds and facilities in support of this work. The work presented here was generously supported by a research grant from the W.M. Keck Foundation to J. Friend. The authors are also grateful for the support of this work by the Office of Naval Research (via grants 12368098 and N00014-20-P-2007), and substantial technical support by Eric Lawrence, Mario Pineda, Michael Frech, and Jochen Schell among Polytec's staff in Irvine, CA and Waldbronn, Germany. Fabrication was performed in part at the San Diego Nanotechnology Infrastructure (SDNI) of UCSD, a member of the National Nanotechnology Coordinated Infrastructure, which is supported by the National Science

Foundation (Grant ECCS–1542148).

Chapter 3

Optimized Y-rotated Cut of Lithium Niobate for Acoustofluidics, Minimizing Anisotropy while Maximizing Electromechanical Coupling to Generate Omnidirectional Surface Acoustic Wave Propagation

3.1 Abstract

Surface acoustic waves (SAW) have long been generated and propagated on 128-degree Y-rotated X-propagating cut lithium niobate (128YX LN) for telecommunications, and more recently for fluid actuation, particle manipulation, and various biological and chemical applications. The 128YX LN cut is known to most effectively generate Rayleigh SAW along the X direction alone.

Any SAW veering from this propagation direction is affected by beam steering and changes in resonance frequency and electromechanical coupling coefficients, consequently limiting the use of LN in various acoustofluidics applications where more diverse configurations would be beneficial. Here we propose an optimized Y-rotated cut of LN for multi-directional surface acoustic wave propagation, simultaneously minimizing the anisotropic effects while maximizing electromechanical properties of LN for acoustofluidics applications. The $\mathcal{L}_2$-norm of these properties was evaluated under rotational transformation to produce a physical model with closed governing equations for surface wave propagation on the surface of a piezoelectric material. This was then utilized to obtain the surface wave velocity and coupling coefficient of the specific Y-cut LN with respect to propagating direction. Next, the averaged coupling coefficients of various Y-cuts of LN in all propagating directions were calculated and integrated to simultaneously minimize anisotropy and maximize the electromechanical properties of the LN substrate. A 152-deg. Y-rotated cut was found to be the optimal choice under these constraints, enabling multi-directional surface acoustic wave propagation with greater coupling and lower variation in wave performance for SAW generated across the surface in any direction. Experimental devices were designed, fabricated, and tested on this specific Y-cut LN and served to verify the supporting analysis and the superior isotropicity of the 152-deg. Y-rotated cut in generating SAW.

3.2 Introduction

Surface acoustic waves are acoustic waves within radio frequency range that offer millions to billions of gravity accelerations suitable for efficient fluid-structural coupling, and consequently have become popular in a variety of micro to nano-scale acoustofluidic devices and applications, such as fluid transportation, droplet jetting, atomization, microcentrifugation, etc.[65,89,109]. Despite existing limitations in generating, controlling, and propagating surface acoustic waves (SAW) within and from lithium niobate (LN) substrates, SAW has consistently demonstrated remarkable

promise in controlling fluid and particle behavior in many lab-on-a-chip applications, such as acoustic nanofluidics and acoustophoresis[212,247]. Lithium niobate is ubiquitous in SAW generation and propagation due to its large coupling coefficient relative to other single crystalline materials for SAW (and other waveforms[56]), absence of hysteresis and heating common in polycrystalline piezoelectric materials[180], and outright convenience in comparison to ZnO, AlN, and other thin-film piezoelectric materials.

In 1976, Shibayama *et al.*[351] found the 127.86° *Y*-rotated cut to be optimal for generating Rayleigh SAW along a single axis, even though the 131° *Y*-rotated cut had previously demonstrated[364] the highest electromechanical coupling coefficient and lowest insertion loss. The 127.86° cut reduced the generation of parasitic bulk waves that rendered the 131° an inferior choice in actual use, and since then the 127.86° *Y*-rotated, *X*-propagating cut of LN (128YX LN) has become the most popular and widely accepted orientation for applications requiring Rayleigh SAW waves. The 128YX cut can efficiently generate SAW only along the *X*-axis direction, a fact irrelevant in telecommunications where this is sufficient, but important in acoustofluidics where the ability to change the wave propagation direction to go around obstacles, deflect into features, and produce two-dimensional acoustic wave structures in a piezoelectric substrate would be beneficial. Any SAW generated at an angle to the *X*-axis propagation direction encounters beam steering and a reduction in electromechanical coupling, an issue known for many years in microrobotic[193] and acoustofluidic applications. Worse, since the SAW propagation velocity changes as well, either the frequency must change to deliver a SAW of the same wavelength or the generating electrodes' dimensions must be carefully tailored to obtain a specific operating frequency. Even in doing so, it has been demonstrated that the vibration displacement and particle velocity is twice as large along the *X*-axis than the *Y*-axis for SAW on 128YX LN[194] with similarly sized electrodes and driving conditions due to the significant difference in electromechanical coupling along these propagation directions.

Certainly, an alternative route would be to employ thin-film, deposited piezoelectric poly-

crystalline ceramic materials such as ZnO or AlN, on a silicon or similar solid substrate[344,451] to offer isotropic in-plane behavior. These thin films offer flexibility in electrode designs, wave generation and propagation, and other features[114] potentially useful in acoustofluidics. For example, isotropic SAW has been generated on ZnO thin films to produce a needle-shape liquid column on a free liquid surface[197,204,459,462]. However, these materials possess low electro-mechanical coupling coefficients in comparison to LN, and are unable to generate large power transmission from electrical to mechanical domains commensurate with typical acoustofluidics applications due to their clamped, thin-film configuration, and require additional steps in ultraviolet lithography. Therefore, a cut of a single crystal bulk material that has minimal in-plane anisotropy and a large electromechanical coupling coefficient would still be superior in seeking more efficient and effective piezoelectric materials for liquid actuation and acoustofluidics applications.

Here, we propose an optimized Y-rotated cut of LN for multi-directional SAW propagation minimizing anisotropy and maximizing electromechanical properties for acoustofluidic applications. Rotational transformation of the material properties of LN is shown with an $\mathcal{L}_2$-norm-based comparison to isotropic material properties to find the LN cut with the least anisotropic in-plane properties, that is, the closest to isotropic properties possible along the surface plane of the substrate. A physical model with closed governing equations for surface wave propagation on the LN is then used to determine the open and short-circuit surface wave velocity and, consequently, the electromechanical coupling coefficient along any direction on the substrate. The coupling coefficients of a given Y-cut of LN for SAW propagating in all planar directions are then calculated. These results are combined with the results of the in-plane anisotropy analysis to identify an optimized Y-rotated cut of LN. The optimization seeks to provide multi-directional SAW propagation by minimizing planar anisotropy and maximizing planar SAW electromechanical properties, producing as a result the 152° Y-axis rotated cut. To ascertain the result of this analysis, SAW devices were designed, fabricated, and tested on this LN substrate, providing practical results demonstrating both the ability to generate and propagate SAW in directions beyond the

standard X-axis of 128YX LN, and a consistent method for tailoring the selection of the cut to fit desired design goals. It is essential for the development of acoustofluidic devices based on SAWs and would be relevant to improve acoustical tweezers based on IDTs or multi-transducers arrays[86,313,316,405].

3.3 Determination of the "Least" In-Plane Anisotropic Y rotated Cut of LN

Since the stiffness tensor underpins the mechanical elastic properties of a material and determines its wave propagation and generation modes and its electro-mechanical properties, we consider how rotational transformation of the LN stiffness tensor affects its apparent anisotropy in comparison with isotropic materials. For those unaware, isotropic materials are inherently unable to offer piezoelectricity, and our aim here is instead to minimize the anisotropy in the surface plane of the LN upon which the SAW will be generated and propagated. While X-axis or X and Y rotated cuts could be considered in a more general exploration using the methods we propose, obtaining such cuts is a practical problem: LN producers do not offer such flexibility in the material orientation nor are set up to do so for research-relevant quantities of wafers.

3.3.1 Rotational Transformation of the Stiffness Tensor

We consider a variety of Y-rotated LN cuts with a focus on offering the least anisotropic response along the 360° of the plane as opposed to solely the greatest coupling for a particular Rayleigh-SAW propagation direction. The latter has previously been studied and resulted in initially the 131° Y-rotated cut and soon after the 127.86° Y-rotated cut. We also consider the electromechanical coupling, discussed later, but first consider rotational transformation of Y-cut LN, as shown in Fig. 3.1(a). Coordinate $Oxyz$ is the original principal axes of LN; coordinate

$Oxy'z'$ is based on the LN substrate surface plane because of the angled Y-rotated cut. The coordinate $Oxy'z'$ is transformed from the coordinate $Oxyz$ by rotating angle θ along X axis with $\theta + 90^\circ$ Y-rotated cut, explained by the right schematic of Fig. 3.1(a). To begin simply, we note the relationship between original and rotated unit vectors as

$$\begin{pmatrix} \mathbf{e}_1 \\ \mathbf{e}_2 \\ \mathbf{e}_3 \end{pmatrix} = \begin{pmatrix} 1 & 0 & 0 \\ 0 & \cos\theta & -\sin\theta \\ 0 & \sin\theta & \cos\theta \end{pmatrix} \begin{pmatrix} \mathbf{e}'_1 \\ \mathbf{e}'_2 \\ \mathbf{e}'_3 \end{pmatrix} = [A] \begin{pmatrix} \mathbf{e}'_1 \\ \mathbf{e}'_2 \\ \mathbf{e}'_3 \end{pmatrix} \tag{3.1}$$

with the Euler transformation matrix $[A]$ defined as shown. In index notation, the equation can be written as

$$\mathbf{e}_m = A_{mn}\mathbf{e}'_n. \tag{3.2}$$

Expressing the stiffness tensor c^E_{ijkl} in two different coordinate systems by using eqn. (3.2), the component notation ($i, j, k, l \in \{1,2,3\}$), and enforcing the Einsteinian summation convention[399] with superscript E referring to a constant electric field, we have

$$\begin{aligned} c^{E\prime}_{pqrs}\mathbf{e}'_p\mathbf{e}'_q\mathbf{e}'_r\mathbf{e}'_s &= c^E_{ijkl}\mathbf{e}_i\mathbf{e}_j\mathbf{e}_k\mathbf{e}_l \\ &= c^E_{ijkl}A_{ip}A_{jq}A_{kr}A_{ls}\mathbf{e}'_p\mathbf{e}'_q\mathbf{e}'_r\mathbf{e}'_s. \end{aligned} \tag{3.3}$$

Details of the notation are provided for the reader's convenience in the Appendix. The rotational transformation from the original stiffness tensor component can be then found to be

$$c^{E\prime}_{pqrs} = c^E_{ijkl}A_{ip}A_{jq}A_{kr}A_{ls}, \tag{3.4}$$

producing a transformation matrix that depends on θ. The transformed stiffness tensor $c^{E\prime}_{pqrs}$ also depends on θ, the angle about Y of rotation for the cut to be considered. The wafer surface and wave propagation planes are both plane xOy'.

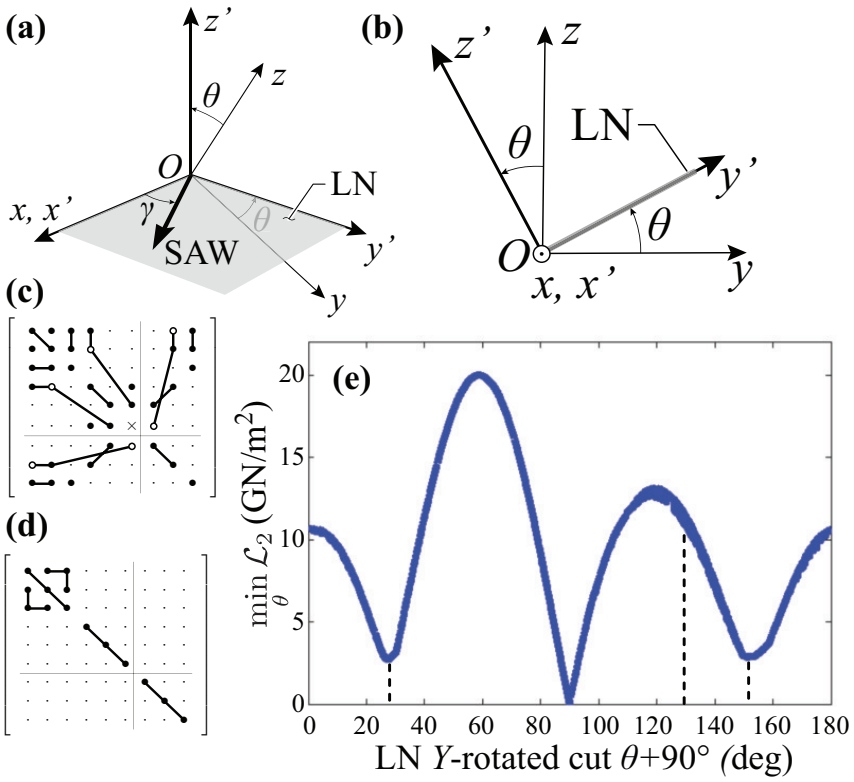

Figure 3.1: (a) A schematic showing the LN substrate plane xOy' and principal axes of LN $Oxyz$. SAW propagation direction γ is the angle of propagating SAW on the surface of LN substrate plane xOy' with respect to positive x direction, as depicted in the schematic. (b) Definition of cut angle $\theta + 90^\circ$. (c) An illustration of the symmetry in a trigonal $3m$ media such as LN, combining the elastic, piezoelectric, and dielectric tensors' matrix representations. (d) The analogous symmetry for isotropic materials indicates the absence of piezoelectricity. Details regarding the meaning of the symbols used in (c,d) these matrices are provided in the Appendix. (e) The minimum $\mathcal{L}_2$-norm plotted with respect to the cut angle $\theta + 90^\circ$ for LN indicates three minima, a purely isotropic response with $\theta = 0^\circ$, the well-known Z-cut, $\theta = 62^\circ$ and $\theta = 118^\circ$, which indicates 152° and 28° Y-rotated cut respectively. The dashed lines indicate 28°, 128°, and 152° Y-rotated cut respectively for better visualizing the improvement of isotropy between the minimum $\mathcal{L}_2$-norm and that at 128° Y-rotated cut.

3.3.2 Identifying the Least Anisotropic In-plane Y-cut of LN by Norm Comparison with Isotropic In-plane Materials

To investigate the extent of *planar* anisotropy in plane xOy' of θ-rotated LN, a double inner product between the unit vector $\mathbf{e}'_3$ normal to the substrate surface and the stiffness tensor in the rotated coordinate system shown in eqn. (3.3) may be taken:

$$\mathbf{e}'_3 \cdot (c^{E\prime}_{pqrs}\mathbf{e}'_p\mathbf{e}'_q\mathbf{e}'_r\mathbf{e}'_s) \cdot \mathbf{e}'_3 = c^{E\prime}_{3qr3}\mathbf{e}'_q\mathbf{e}'_r. \tag{3.5}$$

To determine which orientation of LN produces the most isotropic in-plane properties, we then consider the stiffness tensor for an isotropic material. It is well-known that isotropic materials cannot be piezoelectric as at least asymmetry through a reflection (for example, Hermann-Mauguin group ∞mm) is necessary, but this aspect is treated later via exploration of the electromechanical coupling. Noting the symmetry of the trigonal ($3m$) LN's mechanical, piezoelectric, and electrical intrinsic properties (*see* Appendix A for the definition and representations of the corresponding tensors) in Fig. 3.1(b) versus isotropic media in Fig. 3.1(c), it becomes apparent what quantities that describe the LN's stiffness must be changed to become more isotropic. Subsequently, the same operations were performed on the stiffness tensor for the isotropic material as the trigonal LN. We begin with the double inner product to determine the expression for the stiffness along the plane xOy',

$$\mathbf{e}'_3 \cdot (c^{\text{iso}}_{pqrs}\mathbf{e}'_p\mathbf{e}'_q\mathbf{e}'_r\mathbf{e}'_s) \cdot \mathbf{e}'_3 = c^{\text{iso}}_{3qr3}\mathbf{e}'_q\mathbf{e}'_r, \tag{3.6}$$

where $c^{\text{iso}}_{3qr3} = \begin{pmatrix} x_2 & 0 & 0 \\ 0 & x_2 & 0 \\ 0 & 0 & x_1 \end{pmatrix}$ and x_1 and x_2 are any arbitrary positive real numbers.

As expected, LN does not have a cut with an entirely isotropic plane xOy' after some rotation θ. Instead, the point of this effort is to explore how to *minimize* the anisotropy on xOy'. To this end, we seek the minimum of the Euclidean norm of the difference between

the anisotropic stiffness tensor in the plane and its isotropic counterpart[229,345], written as $\min_\theta \mathcal{L}_2 \equiv ||c^{E\prime}_{3qr3} - c^{\text{iso}}_{3qr3}||_2$ by varying x_1 and x_2 for each specific given angle θ, which describes the specific differences between the in-plane stiffness for $\theta + 90^\circ$ degree Y-cut LN and an analogous isotropic material. In the analysis, the dielectric components are simply assumed to be $\varepsilon_{11} = \varepsilon_{22} = \varepsilon_{33} = 1$ for the isotropic material and are in any case irrelevant to the computations needed in this study. A custom MATLAB (MathWorks, Natick, MA, USA) code was used to calculate and plot the norm $\mathcal{L}_2$ versus $(\theta + 90^\circ)$ as shown in Fig. 3.1(d) with increments in θ of 0.1°. For our calculations, LN is presumed to have the following values for the stiffness: $c^E_{11}, c^E_{12}, c^E_{13}, c^E_{14}, c^E_{33}, c^E_{44}, c^E_{66} = 2.030, 0.53, 0.75, 0.09, 2.45, 0.60, 0.75 \times 10^{11} N/m^2$ [366].

Notably, when $\theta \to 0$ or 180°—known as *Z-cut LN*—a popular view is that $\min_\theta\{\mathcal{L}_2\}$ should go to zero and the cut is "isotropic in the plane" xOy'. This is true for the stiffness tensor, as made clear from Fig. 3.1(d). However, as shown in Fig. 3.5 in Appendix B, Z-cut LN in fact remains anisotropic in the plane. Instead of using the stiffness tensor, the evidence is provided there by computing the norm of the piezoelectric stress tensor $\mathbf{e}$ for LN versus the zero tensor value for an isotropic material, all upon the plane xOy'. If the material were truly isotropic in the plane, this value would also go to zero, because the piezoelectricity would be absent in the plane. While the norm of the piezoelectric stress tensor does not go to zero as $\theta \to 0$ or 180°, it does go to a minimum value. This suggests both the piezoelectric coupling and this particular cut's ability to generate SAW will be poor. In fact, Z-cut LN is known to be poor for surface wave generation and propagation[428]. Despite its in-plane stiffness isotropy, the Z-cut is therefore deemed to be unsuitable for further consideration.

Fig. 3.1(d) indicates two other possibilities for minimization of the anisotropy of LN on the xOy' plane: Y-rotated cut angle $= \theta + 90^\circ = 28^\circ$ and 152°. The 152° cut, in particular, is close to the ubiquitous 128° YX cut[351] used for SAW, and so cuts around 152° may be interesting to further explore from the perspective of electromechanical coupling. The 28° cut as the other minimum would also be an possible alternative for SAW generation and propagation while

minimizing the effect of anisotropy.

3.4 Calculation of Coupling Coefficient for Electromechanical Properties

There is a universal relationship between the coupling coefficient, K^2, and the open and short-circuited SAW velocities v_o and v_m, respectively[35]:

$$K^2 = \frac{2(v_o - v_m)}{v_o} \tag{3.7}$$

One approach to determine the effectiveness of any particular Y-rotated cut defined by θ in comparison to the 128YX cut of LN is to determine the surface wave velocities v_o and v_m and then use eqn. (3.7) to compare the coupling coefficients between $\theta + 90^\circ$ Y-cut LN and 128° Y-cut LN.

3.4.1 Determining the Velocity of Open and Short-circuited SAW

The set of linear equations describing acoustic wave propagation in an arbitrary, anisotropic piezoelectric medium is, in standard component notation, as follows[399]:

$$\begin{aligned}
\frac{\partial T_{ij}}{\partial x_i} &= \rho \frac{\partial^2 u_j}{\partial t^2}, \\
S_{kl} &= \frac{1}{2}\left(\frac{\partial u_k}{\partial x_l} + \frac{\partial u_l}{\partial x_k}\right), \\
\frac{\partial D_i}{\partial x_i} &= 0, \\
E_i &= -\frac{\partial \varphi}{\partial x_i}, \\
T_{ij} &= c'_{ijkl} S_{kl} - e'_{nij} E_n, \\
D_m &= e'_{mkl} S_{kl} + \varepsilon'_{mn} E_n,
\end{aligned} \tag{3.8}$$

where T_{ij} is the stress tensor component, ρ is the mass density, u_j is the mechanical displacement, S_{ij} is the strain tensor component, D_i is the electric displacement, E_i is the electric field, x_i is a spatial coordinate, and φ is the electric potential. The primed quantities refer to a rotated coordinate system in which the stiffness tensor (c'_{ijkl}), the piezoelectric stress tensor (e'_{ijk}), and the permittivity tensor (ε'_{ij}) are given in terms of A_{ij} and the unrotated quantities as follows:

$$\begin{aligned} c'_{ijkl} &= A_{ir}A_{js}A_{kt}A_{ln}c_{rstn}, \\ e'_{ijk} &= A_{ir}A_{js}A_{kt}e_{rst}, \\ \varepsilon'_{ij} &= A_{ir}A_{js}\varepsilon_{rs}. \end{aligned} \tag{3.9}$$

By substituting and simplifying eqns. (3.8), the entire set can be reduced to

$$\begin{aligned} c'_{ijkl}u_{k,li} + e'_{kij}\varphi_{,ki} &= \rho\ddot{u}_j, \\ e'_{ikl}u_{k,li} - \varepsilon'_{ik}\varphi_{,ki} &= 0. \end{aligned} \tag{3.10}$$

The dot notation refers to differentiation with respect to time, while an index preceded by a comma denotes differentiation with respect to a space coordinate. The coordinates are set such that the material surface is plane xOy'. The material is located only along $z' < 0$, and so eqns. (3.8–3.10) are only valid for $z' < 0$. The region $0 \leqslant z' \leqslant h$ is set to be a thin, perfect electric conductor where Laplace's equation describes the electric potential φ,

$$\nabla^2\varphi = 0, \tag{3.11}$$

where $h = 0$ and $h = \infty$ refer to electrically shorted and open surfaces, respectively.

Equations (3.10) and (3.11) together with boundary conditions form a complete set of governing equations for acoustic wave propagation upon or within an arbitrary, anisotropic piezoelectric medium. Taupin *et al.*[391] recently used semi-analytical finite element method

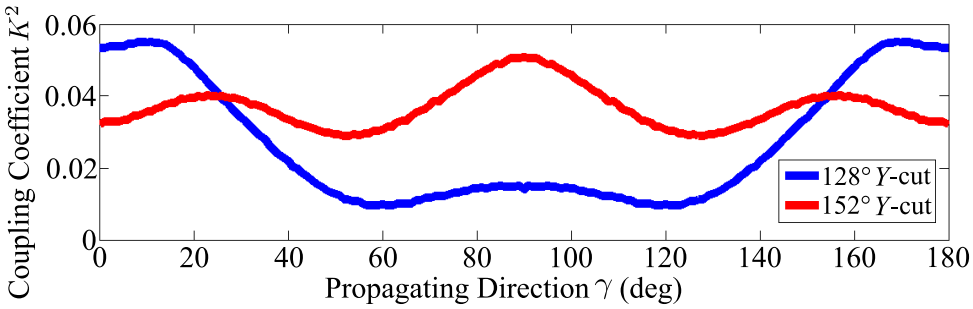

Figure 3.2: The calculated electromechanical coupling coefficient, K^2, of Y-cut LN with respect to the propagation direction of the SAW along the xOy' plane for 152° Y-cut LN in comparison to 128YX LN. The coupling coefficient is superior in 152° Y-cut LN for propagation angles roughly between 30° and 150° and inferior outside this range.

to study guide wave propagation in viscoelastic multilayered anisotropic plates by computing displacement, dispersion, slowness curves, and energy propagation. Although it cannot be used directly to surface wave on a non-viscous piezoelectric material plane in this case from the bulk guided wave in viscous multilayered material, it is still a useful method for wave propagation calculation that would be necessary to mention. Here, we followed a closely related Tiersten method[399] and concept of partial waves by Farnell[104] for free and layered infinite half-space problems to determine the SAW propagation velocities in a given direction along a plane as detailedly presented in the Appendix.

3.4.2 Numerical Calculations and Results of Surface Wave Velocities and Coupling Coefficients

The transcendental equation obtained by setting the determinant of the matrix of coefficients of equations (3.26) equal to zero determines the surface wave velocities. Because the resulting transcendental equation can not be analytically solved, a numerical method is utilized to determine the open and short-circuit SAW velocities as described in detail in the Appendix. Briefly, we first define a particular propagation direction on the LN surface using the angle γ from the material's X axis. Knowing that the SAW velocity, v_S, will be in the range of 3000 m/s

to 5000 m/s[16,113], we then determine $\alpha^{(l)}$ from eqn. (3.22), and obtain the determinant from eqn. (3.26). Since $h = 0$ and $h = \infty$ correspond to a short-circuited and open-circuited surface, respectively, the minimum of the determinant produces SAW velocities for these respective conditions as v_m and v_o along the propagation direction defined by γ upon the plane xOy', the surface of the LN wafer that uses this particular $(\theta + 90^\circ)$-rotated cut. In order to accurately identify this minimum of the determinant, increments of only 1 m/s in the SAW open and short-circuit phase velocities in $\gamma = 1^\circ$ steps were used.

Substituting the calculated velocities v_m and v_o into eqn. (3.7) produces the coupling coefficient K^2 for each value of γ, as shown in Fig. 3.2. The SAW coupling coefficient of 152° Y-rotated cut LN is notably larger than 128° Y-rotated cut LN over a majority of the propagation directions, between a $\gamma \approx 30^\circ$ and $\gamma \approx 150^\circ$. Outside this range and, as expected, near the X-propagating direction ($\gamma = 0^\circ$) the traditional 128YX cut of LN is superior.

The 152° Y-cut LN is quantifiably more isotropic in the xOy' plane. For example, the standard deviation of the electromechanical coupling coefficient, K^2, over the range $\gamma = 0^\circ$ to 180° in 152° Y-cut LN is 66.5% lower than in 128° Y-cut LN, indicating an improved uniformity on electromechanical coupling coefficient of 152° Y-cut LN. Furthermore, and somewhat surprisingly, the average electromechanical coupling coefficient, K^2, over $\gamma = 0^\circ$ to 180° in 152° Y-rotated cut LN is 37.0% greater than 128° Y-cut LN, indicating a greater overall ability to produce SAW. Therefore, for omnidirectional surface wave actuation on LN, a 152° Y-rotated cut LN is significantly both less anisotropic and more electromechanically efficient than the 128° Y-cut, and is superior to other Y-rotated choices. The reader should remember that for *unidirectional* SAW, the 128YX cut remains superior.

3.5 Choosing a Cut via the Ratio of the Electromechanical Coupling Coefficient to the Euclidean Norm

The Euclidean norm has been used on the in-plane portion of the stiffness tensor in a comparison between the anisotropic LN and an arbitrary isotropic material to produce two candidate cuts. These two cuts were shown to offer less anisotropy than the 128YX cut and therefore may prove to be more useful in acoustofluidic applications. The well-known *Z*-cut of LN that has already been excluded is a good example of why the electromechanical coupling coefficient is as important to consider as the anisotropy: the *Z*-cut is ideally isotropic in the plane but offers very weak electromechanical coupling, making it an unsuitable choice. A somewhat tedious computational method has been provided to determine the electromechanical coupling coefficient for SAW propagating in a given direction defined by γ upon the surface of a $(\theta + 90^\circ)$-rotated cut of LN.

A combination of these two aspects are needed to identify a cut of LN that would best serve both purposes—in-plane isotropy and large electromechanical coupling to generate SAW—that are, to some extent, at odds with each other. In what follows, a remarkably simple method is proposed to identify an optimum θ angle of *Y*-rotated cut LN which both minimizes the in-plane anisotropy and maximizes the overall planar electromechanical effect among all propagating directions.

We define $\Phi \equiv K_a^2/\mathcal{L}_2$ as a *figure of merit* and the ratio of the averaged coupling coefficient, K_a^2, to the $\mathcal{L}_2$ norm as a single parameter that includes the effects of both the planar anisotropy and electromechanical coupling. The averaged coupling coefficient is defined as

$$K_a^2 \equiv \sum_{\gamma=0^\circ,1^\circ,\cdots}^{180^\circ} K^2/(\frac{180^\circ}{\Delta\gamma}+1) \tag{3.12}$$

for each specific cut angle, θ, of *Y*-rotated LN, where $\Delta\gamma = 1^\circ$ is the step size and resolution of propagating direction for averaged coupling coefficient calculation. The larger Φ is, either

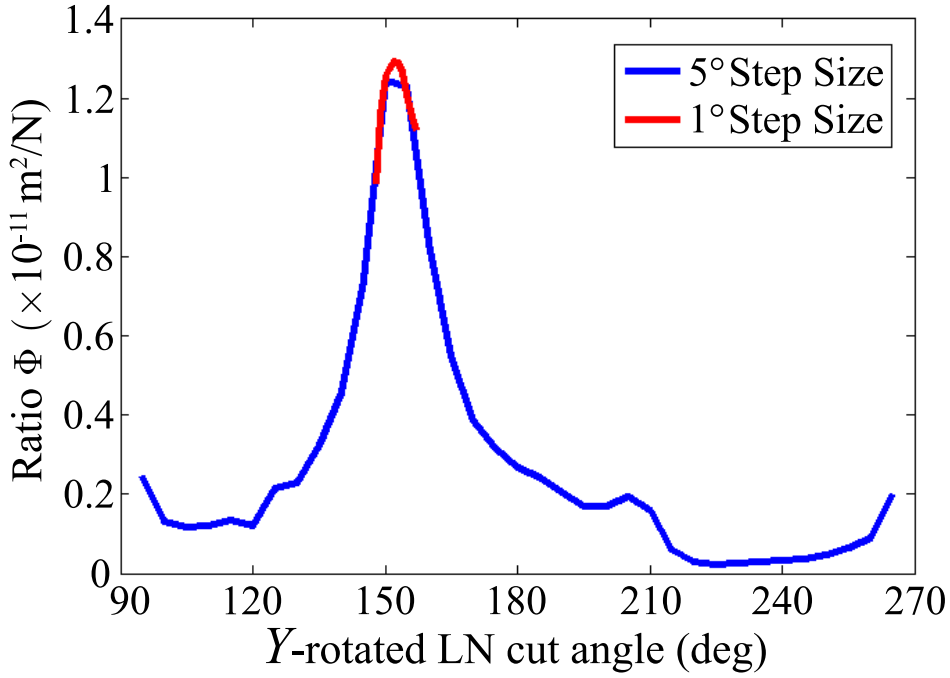

Figure 3.3: The ratio, Φ, of the in-plane averaged coupling coefficient over all possible SAW propagation directions, $\gamma \in \{0^\circ, 180^\circ\}$ to the Euclidean norm of the in-plane stiffness tensor between the Y-cut LN and an isotropic material, given by $\Phi \equiv K_a^2 / \mathcal{L}_2$, is shown with respect to $\theta + 90^\circ$, the Y-rotated cut angle of LN. Larger values of Φ imply improvements in the isotropy or electromechanical coupling. The other candidate cut at $\theta + 90^\circ = 28^\circ + 180^\circ$ that exhibits a local minimum in Fig. 3.1 shows relatively poor electromechanical coupling, and consequently is not worthy of further consideration. Due to the expense of the calculation, the density of values of $(\theta + 90^\circ)$ at which Φ is calculated is increased only around 150° where there is a clearly defined peak. Indeed, the maximum value for Φ is at $\theta + 90^\circ = 152^\circ$.

the overall in-plane electromechanical effect will be greater or the material's anisotropy will be reduced—or both. Maximizing Φ with respect to the Y-rotated cut, $\theta + 90^\circ$, will then correspond to the optimal choice that collectively minimizes anisotropy and maximizes the electromechanical coupling for use in multi-directional SAW propagation.

Considering the computational cost of these calculations and the fact that the relevant material properties are at least smooth to second order (class $\mathcal{C}^2$ as required by eqns. (3.8)), a low-resolution-calculation of the cumulative coupling coefficient for $\theta = 0^\circ$ to 180° in 5° steps and 5 m/s increments in the SAW open and short-circuit phase velocity for calculation of the minimum of the determinant produced from eqn. (3.26) is reasonable. According to Yamanouchi *et al*.[452], the velocity of traveling SAW is slower than leaky SAW on Y-cut LN. Thus, we identified the slower traveling SAW velocity by finding the local minimum of the determinant from eqn. (3.26). Figure 3.3 shows the result, where the highest value of Φ occurs between $\theta + 90^\circ = 145^\circ$ to 155°. To more accurately determine the specific optimum, a higher-resolution calculation of $\Phi = K_a^2/\mathcal{L}_2$ was conducted from $\theta + 90^\circ = 145^\circ$ to 155° in 1° steps and 1 m/s increments in the SAW open and short-circuit phase velocity. As shown in Fig. 3.3, the $\theta + 90^\circ = 152^\circ$ Y-rotated cut produces the maximum $K_a^2/\mathcal{L}_2$ of any value of θ for LN, representing the optimum choice to minimize planar anisotropy and maximize planar electromechanical coupling in multi-directional SAW propagation applications. More accurate calculations to further refine $\theta + 90^\circ$ between 151.5° and 152.5° could be conducted, though most suppliers of LN are unable to economically produce small batches of LN with a custom orientation at an accuracy better than 0.5°.

3.6 Experimental Methods and Results

To compare with our computational results, we designed and fabricated a device on double-side polished 152° Y-rotated cut LN (Jiaozuo Commercial FineWin Co., Ltd, Jiaozuo, Henan, China) for surface acoustic wave generation and propagation.

3.6.1 Device Design and Fabrication

As depicted in Fig. 3.4(a), twenty-four finger pairs were used in each of fifteen interdigital transducers (IDT) arranged in a circular pattern about a central point with 24° of angular separation between them. A wavelength of $\lambda = 100\ \mu$m was selected for an operating frequency of $\sim$40 MHz (from $f = v/\lambda$) to define each IDT, comprised of twenty simple finger pairs with finger and gap widths of $\lambda/4$ and an aperture of 2 mm. Standard UV photolithography (using AZ 1512 photoresist and AZ 300MIF developer, MicroChem, Westborough, MA) was used alongside sputter deposition and lift-off processes to fabricate the 10 nm Cr / 1 μm Al IDT upon the 500 μm thick LN substrate[65]. Absorbers (Dragon Skin™, Smooth-On, Inc., Macungie, PA) were used at the center and periphery of the device to prevent edge reflections and spurious bulk waves. SAW was generated by applying a sinusoidal electric field to the IDT at resonance using a signal generator (WF1967 multifunction generator, NF Corporation, Yokohama, Japan) and amplifier (ZHL–1–2W–S+, Mini-Circuits, Brooklyn, NY, USA). The actual voltage, current, and power across the device were measured using an oscilloscope (InfiniiVision 2000 X-Series, Keysight Technologies, Santa Rosa, CA). The spatiotemporal variations in the wave displacement and velocity amplitude along the underlying substrate were measured using a laser Doppler vibrometer (LDV, UHF–120, Polytec, Waldbronn, Germany).

3.6.2 Experimental Data and Analysis

Instantaneous displacement and phase measurements were made using the LDV along the propagation directions determined by the placement of the IDTs in Fig. 3.4(a). For example, Fig. 3.4(b) illustrates the SAW amplitude and phase propagating along the $\gamma = 108°$ direction, with 807 mW at 33.956 MHz AC input applied on the device, demonstrating the generation of traveling surface acoustic waves. With standing wave ratio (SWR) of 1.47, it indicates a good traveling wave upon the 152° Y-rotated cut LN xOy' surface, where SWR is the ratio

of the maximum and minimum amplitude of the wave, indicating a pure traveling wave when SWR $= 1$ and a pure standing wave when SWR $= \infty$. To compare the experimental results with the computational results, the relative energy $E \propto A^2$ was used and scaled to fit the computational results, correlating the amplitude of SAW on LN surface with the electromechanical coupling energy[351]. The amplitudes, A, in each propagation direction are averaged among the LDV scanning region to obtain more accurate results. As shown in Fig. 3.4(c), the experimental and computational results fit well with a high correlation coefficient of 0.93, verifying the results of the calculations and the underlying method to arrive at a useful cut.

3.7 Conclusions

A technique to optimize the Y-axis rotation angle for a given set of design characteristics has been provided. It has been used to minimize the in-plane anisotropy and maximize the electromechanical coupling to enable multi-directional generation and propagation of SAW upon LN. Producing three candidates—Z-cut, 28° Y-rotated cut, and 152° Y-rotated cut LN—the method ultimately provided sufficient results to select the 152° Y-rotated cut. This cut provides significant improvements of 66.5% in in-plane isotropy and 37.0% in electromechanical coupling over the ubiquitous 128YX LN used in today's acoustofluidic devices.

The technique combines classic analysis approaches with an $\mathcal{L}_2$-norm comparison of the stiffness and piezoelectric stress tensor to an isotropic analogue while varying the Y-rotated cut angle $\theta + 90°$. To determine the effect of these rotations upon the equally important electromechanical coupling of SAW propagating along any direction on the plane of the Y-rotated substrate for each value of θ, a physical model with closed-form governing equations for SAW propagation on the surface of a piezoelectric material was used to obtain open and short-circuit SAW phase velocities. These velocities were then used to compute the averaged coupling coefficient over all possible SAW propagation directions upon the LN substrate, defined by γ with respect to the

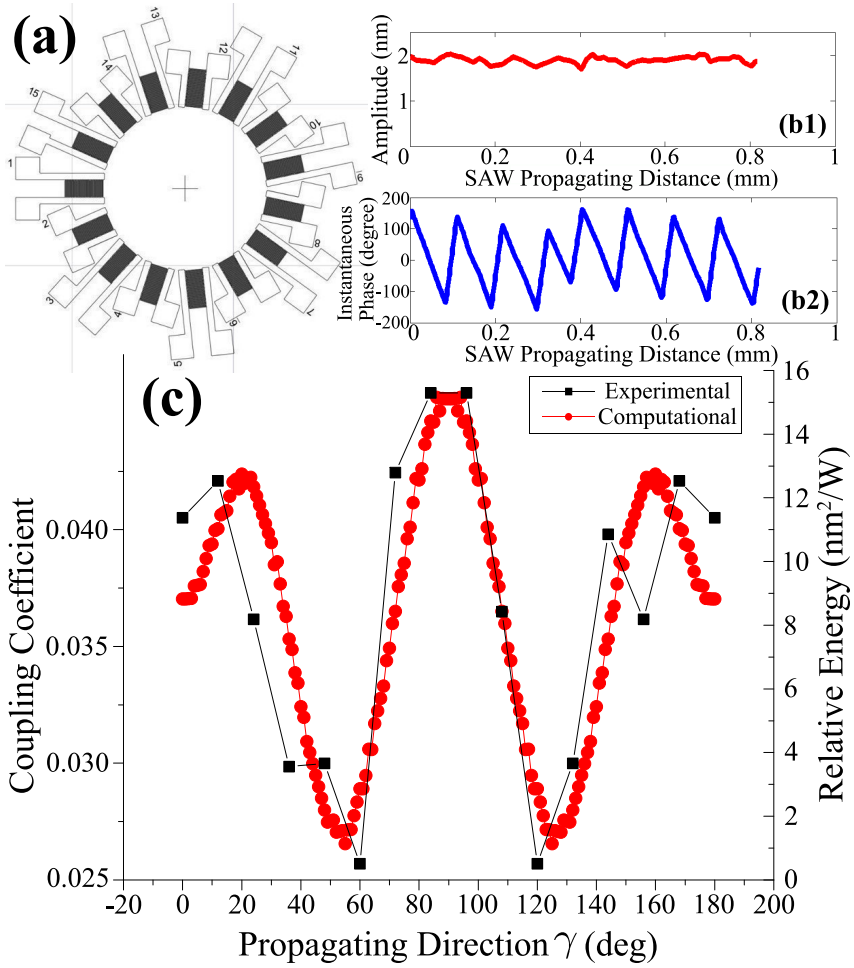

Figure 3.4: Our (a) experimental IDT configuration for testing the ability to generate and propagate SAW across the surface of the rotated LN cut. All fifteen IDTs have an identical design. The ability to generate SAW upon the LN substrate was determined using an LDV along the SAW propagation path, as measured from the exit end of the IDT towards the center of the wafer (the cross shown at the center of the (a) IDT design). For example, the (b) spatial distribution of the instantaneous displacement and phase of the LN substrate transverse to plane xOy' along $\gamma = 108^\circ$ shows a good quality traveling SAW (*see* text for details). A measure of the energy of the SAW with respect to its propagation direction is (c) provided for the fifteen directions defined by the IDTs in our (a) experiment upon 152° Y-rotated cut LN. This closely corresponds to the numerically determined coupling coefficient provided in the same figure, indicating the veracity of the analysis. The lines provided are solely shown as a guide to the eye.

X axis. Next, a figure of merit composed of a ratio of the averaged coupling coefficient to the Euclidean norm of the planar anisotropy was defined and used to determine the value of θ that minimizes the in-plane anisotropy and maximizes the electromechanical coupling. This procedure produced the 152° Y-rotated cut of LN as the clearly optimal choice.

Finally, an experimental device was designed, fabricated, and tested using the 152° Y-cut LN substrate, serving not only to verify the analysis and calculations, but also demonstrating the ability to effectively form SAW in directions other than along the X axis as a practical demonstration of the continued utility of lithium niobate for the demanding requirements of acoustofluidics. This technique can be adapted to serve other materials, other orientations, and other design goals as required, providing a new perspective in materials selection in acoustics and ultrasound as built upon the comprehensive analysis framework provided in the past.

3.8 Appendix

3.8.1 Customary Definition and Representations of the Stiffness, Piezoelectric, and Dielectric Tensors

The stiffness tensor c_{ijkl} is a fourth-order tensor where the number of coefficients is $3^4 = 81$. But due to the symmetry of the tensor, we have $c_{ijkl} = c_{jilk} = c_{ijlk} = c_{jikl}$ and the number of independent coefficients is reduced to 36. It is customary to reduce the fourth-order tensors to a second-order representation $c_{ijkl} = c_{\alpha\beta}$ where $i,j,k,l \in 1,2,3$ and $\alpha,\beta \in 1,2,3,4,5,6$: $(11) \leftrightarrow 1, (22) \leftrightarrow 2, (33) \leftrightarrow 3, (23) = (32) \leftrightarrow 4, (31) = (13) \leftrightarrow 5, (12) = (21) \leftrightarrow 6$. In the same way, the third-order piezoelectric tensor can be represented as a 3×6 matrix. Thus, the stiffness, piezoelectric, and dielectric tensors' matrix representations are combined together into one (*see*

Fig. 3.1(a,b)):

$$\begin{bmatrix} \mathbf{c}^E & \underset{\sim}{\mathbf{e}} \\ \mathbf{e} & \underset{\sim}{\varepsilon}^S \end{bmatrix}. \tag{3.13}$$

where c^E is a reduced 6×6 stiffness matrix; e is reduced 3×6 piezoelectric stress matrix; $\underset{\sim}{e}$ is the transpose of reduced 3×6 piezoelectric stress matrix; $\underset{\sim}{\varepsilon}^S$ is the transpose of the 3×3 dielectric matrix, such that each $\cdot$ represents a zero value, the $\bullet$ and $\circ$ represent non-zero values, the connecting lines between non-zero values indicate equality, and a line connecting a $\bullet$ and $\circ$ indicate these values have opposing signs. The $\times$ symbol represents $(c_{11} - c_{12})/2$. Figure 3.1(a) shows the tensors' matrix representations of the 3m crystal material according to its principal axes' coordinate system.

3.8.2 Analysis of Piezoelectric Stress Tensor of LN to Quantify the In-Plane Isotropy

Similar to the analysis of stiffness tensor in Section II, here we investigate the in-plane anisotropy present in a given cut of LN via the piezoelectric stress tensor. Closely following the method described in Section II, we have

$$e'_{pqr} = e_{ijk} A_{ip} A_{jq} A_{kr}, \tag{3.14}$$

for the piezoelectric stress tensor where

$$[A] = \begin{pmatrix} 1 & 0 & 0 \\ 0 & \cos\theta & -\sin\theta \\ 0 & \sin\theta & \cos\theta \end{pmatrix}.$$

To investigate *planar* anisotropy in plane xOy' of $(\theta + 90^\circ)$-rotated LN, a double inner product between the unit vector $\mathbf{e}'_3$ normal to the substrate surface and the piezoelectric tensor in

the rotated coordinate system shown in eqn. (3.14) may be taken;

$$\mathbf{e}'_3 \cdot (e'_{pqr}\mathbf{e}'_p\mathbf{e}'_q\mathbf{e}'_r) \cdot \mathbf{e}'_3 = e'_{3q3}\mathbf{e}'_q. \tag{3.15}$$

As isotropic materials do not have piezoelectricity, all components of piezoelectric stress tensor for an isotropic material are zero:

$$e^{iso}_{ijk} \equiv 0 \text{ for all } i,j,k \in \{1,2,3\}. \tag{3.16}$$

Taking into account the $3m$ crystal class of LN, the $\mathcal{L}_2$ norm of the in-plane components of the piezoelectric stress tensor of LN in comparison to an isotropic material may be written as

$$e_{norm} = \sqrt{e'^{\,2}_{313} + e'^{\,2}_{323} + e'^{\,2}_{333}} \tag{3.17}$$

e_{norm} represents not only electromechanical coupling of LN, but also the magnitude of the in-plane anisotropy of the piezoelectric stress tensor. This quantity strongly depends upon the LN Y-rotated cut angle $\theta + 90^\circ$.

A custom code for MATLAB (MathWorks, Natick, MA, USA) was used to calculate and plot e_{norm} versus $\theta + 90^\circ$ as shown in Fig. 3.5 with increments in θ of 0.1°. The positive value of e_{norm} indicates its anisotropy in all propagation directions. However. the minimum of e_{norm} turns to be when $\theta + 90^\circ \rightarrow 90^\circ$ or 270°, in other words Z-cut LN, so these selections for $\theta + 90^\circ$ represent the most isotropic of any cut of LN. However, the result also indicates a low coupling coefficient for these values of $\theta + 90^\circ$, and consequently a relatively poor ability to generate SAW.

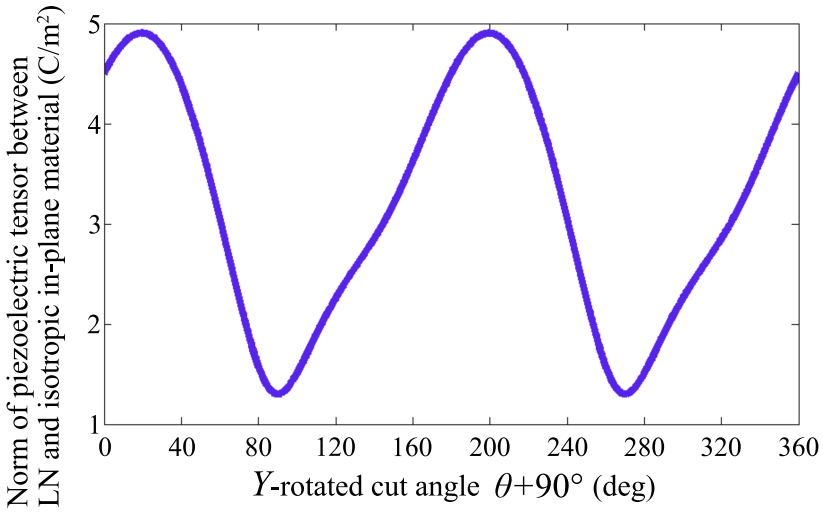

Figure 3.5: Norm of piezoelectric tensor between LN and isotropic in-plane material with respect to LN Y-rotated cut angle $\theta + 90°$. The positive, non-zero value of e_{norm} for all values of $\theta + 90°$ indicates LN always has piezoelectric properties in the plane, and therefore must likewise be always anisotropic in the plane.

3.8.3 Method to Determine the Open and Short-circuit SAW Phase Velocity

To investigate the SAW phase velocity in different propagation direction γ on θ angle of Y-rotated LN, we further apply rotational transformation with respect to γ along z' axis. Specifically, after coordinate rotation along x axis with θ angle, we further rotate the coordinate along z' axis with angle γ to perform the SAW propagation along the rotated main axis. Similar to eqns. (3.9), the stiffness tensor (c''_{wxyz}), the piezoelectric stress tensor (e''_{wxy}), and the permittivity tensor (ε''_{wx}) are the corresponding material properties after rotational transformation with θ angle along x axis and γ angle along z' axis:

$$\begin{aligned} c''_{wxyz} &= B_{wi}B_{xj}B_{yk}B_{zl}c'_{ijkl}, \\ e''_{wxy} &= B_{wi}B_{xj}B_{yk}e'_{ijk}, \\ \varepsilon''_{wx} &= B_{wi}B_{xj}\varepsilon'_{ij}, \end{aligned} \tag{3.18}$$

where rotational transformation matrix

$$B = \begin{pmatrix} \cos\gamma & -\sin\gamma & 0 \\ \sin\gamma & \cos\gamma & 0 \\ 0 & 0 & 1 \end{pmatrix}. \tag{3.19}$$

In this section of Appendix, we denote x as x_1, y' as x_2, and z' as $-x_3$ to perform a general solution in $Ox_1x_2x_3$ coordinate system. We here use $c_{\alpha\beta}$, $e_{w\alpha}$, ε_{wx} instead of c''_{wxyz}, e''_{wxy}, ε''_{wx} to reduce to second-order representation based on symmetry of tensors, where $w,x,y,z \in 1,2,3$ and $\alpha,\beta \in 1,2,3,4,5,6$: $(11) \leftrightarrow 1, (22) \leftrightarrow 2, (33) \leftrightarrow 3, (23) = (32) \leftrightarrow 4, (31) = (13) \leftrightarrow 5, (12) = (21) \leftrightarrow 6$. We would perform a general analysis and solution of open and short-circuit SAW phase velocity along the rotated Ox' axis after rotational transformation of θ angle along x axis and the subsequent γ angle along z' axis for the SAW phase velocity with any particular propagation direction γ on θ angle Y-rotated cut of LN.

Solutions of eqns. (3.10) and (3.11) are assumed to be of the standard, complex traveling-wave form in which v_S is the wave velocity and α describes the exponential decay into the crystal such that

$$\begin{aligned} u_i &= \beta_i e^{-\alpha\omega x_3/v_S} e^{j\omega(t-x_1/v_S)} \\ \varphi &= \beta_4 e^{-\alpha\omega x_3/v_S} e^{j\omega(t-x_1/v_S)} \end{aligned} \qquad i \in \{1,2,3\}. \tag{3.20}$$

As indicated above, the surface waves under consideration are assumed to be travelling in the x_1 direction. The displacements and potentials are considered to be independent of the x_2 coordinate.

Substituting eqns. (3.20) into eqns. (3.10) and (3.11) produces a linear homogeneous system of four equations with four unknowns, β_1, β_2, β_3, and β_4:

$$\begin{pmatrix} c_{55}\alpha^2+2c_{15}j\alpha-c_{11}+\rho v_S^2, & c_{45}\alpha^2+(c_{14}+c_{56})j\alpha-c_{16}, & c_{35}\alpha^2+(c_{13}+c_{55})j\alpha-c_{15}, & e_{35}\alpha^2+(e_{15}+e_{31})j\alpha-e_{11} \\ c_{45}\alpha^2+(c_{14}+c_{56})j\alpha-c_{16}, & c_{44}\alpha^2+2c_{46}j\alpha-c_{66}+\rho v_S^2, & c_{34}\alpha^2+(c_{36}+c_{45})j\alpha-c_{56}, & e_{34}\alpha^2+(e_{14}+e_{36})j\alpha-e_{16} \\ c_{35}\alpha^2+(c_{13}+c_{55})j\alpha-c_{15}, & c_{34}\alpha^2+(c_{36}+c_{45})j\alpha-c_{56}, & c_{33}\alpha^2+2c_{35}j\alpha-c_{55}+\rho v_S^2, & e_{33}\alpha^2+(e_{13}+e_{35})j\alpha-e_{15} \\ e_{35}\alpha^2+(e_{15}+e_{31})j\alpha-e_{11}, & e_{34}\alpha^2+(e_{14}+e_{36})j\alpha-e_{16}, & e_{33}\alpha^2+(e_{13}+e_{35})j\alpha-e_{15}, & -\varepsilon_{33}\alpha^2-2\varepsilon_{13}j\alpha+\varepsilon_{11} \end{pmatrix} \begin{pmatrix} \beta_1 \\ \beta_2 \\ \beta_3 \\ \beta_4 \end{pmatrix} = \begin{pmatrix} 0 \\ 0 \\ 0 \\ 0 \end{pmatrix}. \tag{3.21}$$

The determinant of the 4×4 matrix at left must be zero for a non-trivial solution to exist, producing

$$A_8\alpha^8 + jA_7\alpha^7 + A_6\alpha^6 + jA_5\alpha^5 + A_4\alpha^4 + jA_3\alpha^3 + A_2\alpha^2 + jA_1\alpha + A_0 = 0, \tag{3.22}$$

where the coefficients A_n with $n = 0, 1, ..., 8$ are real and a particular value of v_S has been assumed. Since the electromechanical fields must be bounded, or go to zero as $x_3 \to \infty$, only the roots with non-negative real parts are allowed. If the unknown in eqn. (3.22) is considered to be $j\alpha$ instead of α, then the polynomial in $j\alpha$ has purely real coefficients. Thus, either the roots $j\alpha$ are real or occur in conjugate pairs. Therefore, the roots α are either pure imaginary or occur in pairs with positive and negative real parts. In general, four roots with positive real parts occur for piezoelectric crystals. Upon obtaining the admissable values of α from eqn. (3.22), the corresponding values of β_i can be found for each α from eqn. (3.21).

In addition to the equations for $x_3 > 0$, the differential eqn. (3.11) for $-h \leqslant x_3 \leqslant 0$ must be satisfied together with appropriate boundary conditions at $x_3 = 0$ and $x_3 = -h$. Assuming that the crystal surface is stress free ($T_{3j} = 0$ at $x_3 = 0$), the mechanical boundary conditions at each point of the surface of the crystal are

$$T_{3j}\big|_{x_3=0} = c_{3jkl}u_{k,l} + e_{k3j}\varphi_{,k}\big|_{x_3=0} = 0; \quad j \in \{1,2,3\}. \tag{3.23}$$

The boundary conditions for the electric potential are continuity of φ at $x_3 = 0$ and, without loss of generality, $\varphi(-h) = 0$. Also, the normal component of the electrical displacement must be continuous across the surface of the crystal. The combined electromechanical fields (mechanical displacement and electric potential) may be expressed as a linear combination of the fields associated with the admissible values of α for $x_3 > 0$, following the method shown by

Farnell and other many years ago as the *concept of partial waves*[104,258], that is,

$$\begin{aligned} u_i &= \sum_{l=1}^{4} B^{(l)} \beta_i^{(l)} e^{-\alpha^{(l)} \omega x_3 / v_S} e^{j\omega(t - x_1/v_S)} \\ \varphi &= \sum_{l=1}^{4} B^{(l)} \beta_4^{(l)} e^{-\alpha^{(l)} \omega x_3 / v_S} e^{j\omega(t - x_1/v_S)} \end{aligned} \qquad i \in \{1,2,3\}. \tag{3.24}$$

In the region $-h \leqslant x_3 \leqslant 0$, the potential is a solution of Laplace's eqn. (3.11). A solution satisfying the continuity condition at $x_3 = -h$ is

$$\varphi = \sum_{l=1}^{4} B^{(l)} \beta_4^{(l)} \left(\frac{\omega h}{v_S}\right) \sinh\left(\frac{\omega}{v_S}(x_3 + h)\right) e^{j\omega(t - x_1/v_S)} \tag{3.25}$$

Finally, the component of **D** normal to the surface $x_3 = 0$, D_3, must be continuous across the surface. Inside the crystal the electrical displacement is given by $D_i = e_{ikl} u_{k,l} - \varepsilon_{ik} \varphi_{,k}$, while in the region $-h \leqslant x_3 \leqslant 0$, $\vec{D} = -\varepsilon_0 \nabla \varphi$. Substituting the expressions for the waves in eqns. (3.24) in eqn. (3.23) and expressing the continuity of D_3 at $x_3 = 0$ in terms of eqns. (3.24) produces the following set of homogeneous equations for the so-called *partial field amplitudes* $B^{(l)}$:

$$\begin{aligned} &\sum_{l=1}^{4} (\beta_1^{(l)}(jc_{15} + \alpha^{(l)} c_{55}) + \beta_2^{(l)}(jc_{56} + \alpha^{(l)} c_{45}) + \beta_3^{(l)}(jc_{55} + \alpha^{(l)} c_{35}) + \beta_4^{(l)}(je_{15} + \alpha^{(l)} e_{35})) B^{(l)} = 0 \\ &\sum_{l=1}^{4} (\beta_1^{(l)}(jc_{14} + \alpha^{(l)} c_{45}) + \beta_2^{(l)}(jc_{46} + \alpha^{(l)} c_{44}) + \beta_3^{(l)}(jc_{45} + \alpha^{(l)} c_{34}) + \beta_4^{(l)}(je_{14} + \alpha^{(l)} e_{34})) B^{(l)} = 0 \\ &\sum_{l=1}^{4} (\beta_1^{(l)}(jc_{13} + \alpha^{(l)} c_{35}) + \beta_2^{(l)}(jc_{36} + \alpha^{(l)} c_{34}) + \beta_3^{(l)}(jc_{35} + \alpha^{(l)} c_{33}) + \beta_4^{(l)}(je_{13} + \alpha^{(l)} e_{33})) B^{(l)} = 0 \\ &\sum_{l=1}^{4} (\beta_1^{(l)}(je_{31} + \alpha^{(l)} e_{35}) + \beta_2^{(l)}(je_{36} + \alpha^{(l)} e_{34}) + \beta_3^{(l)}(je_{35} + \alpha^{(l)} e_{33}) \\ &- \beta_4^{(l)}(j\varepsilon_{13} + \alpha^{(l)} \varepsilon_{33} + \varepsilon_0 \coth\left(\frac{\omega h}{v_S}\right))) B^{(l)} = 0. \end{aligned} \tag{3.26}$$

The transcendental equation obtained by setting the determinant of the matrix of coefficients of

this system equal to zero determines the surface wave velocities for a given set of $\alpha^{(l)}$ [16,113]. This set of transcendental equations is known to lack any explicit solutions[2]. Thus we use numerical analysis to identify the open and short-circuit SAW phase velocities $v_o = v_S$ and $v_m = v_S$ when $\omega h = \infty$ and $\omega h = 0$ respectively, as detailed in Section III B.

The open and short-circuit SAW phase velocities v_o and v_m determined from this process for propagation upon the surface of 152° and 128° Y-rotated cut LN are shown in Fig. 3.6(a,b). The phase velocities are plotted with respect to the angle γ between the SAW propagation direction and the X axis, indicating that the differences in surface wave velocities between 152° and 128° Y-rotated cut LN are minor.

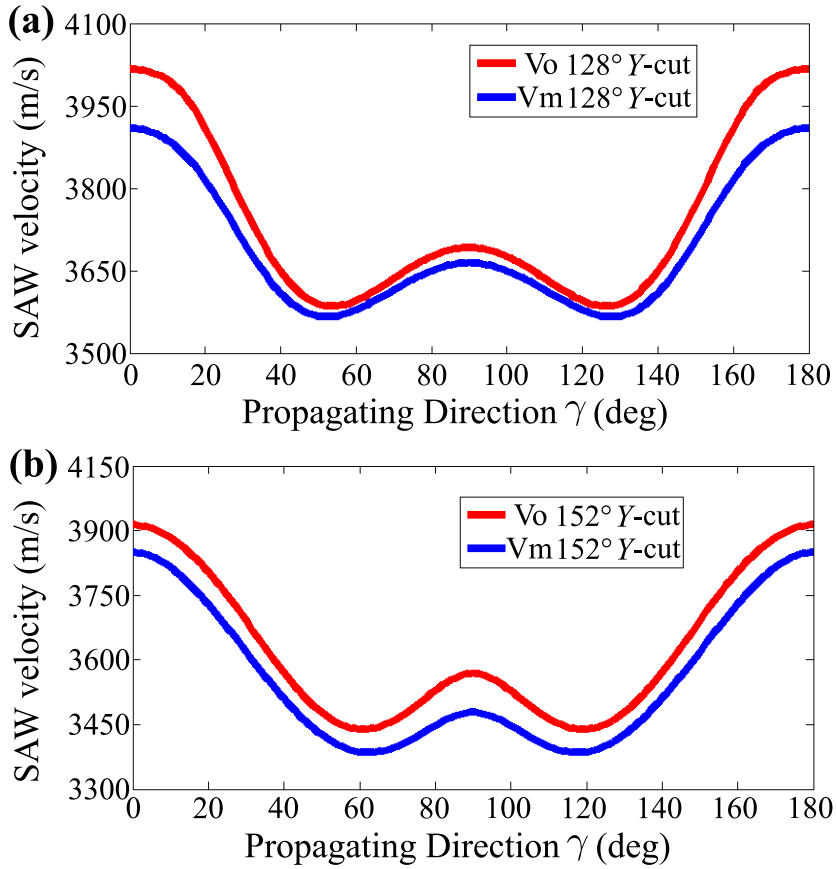

Figure 3.6: The open-circuit and short-circuit SAW phase velocity on the surface of (a) 128° *Y*-cut LN and (b) 152° *Y*-cut LN plotted with respect to the propagation direction defined by the angle γ measured from the *X* axis of the LN substrate.

3.8.4 LDV Scan of Instantaneous Wave Displacement and Phase along a Specific Propagation Direction

3.9 Acknowledgement

We are grateful to the University of California and the NANO3 facility at UC San Diego for provision of funds and facilities in support of this work. This work was performed in part at the San Diego Nanotechnology Infrastructure (SDNI) of UCSD, a member of the

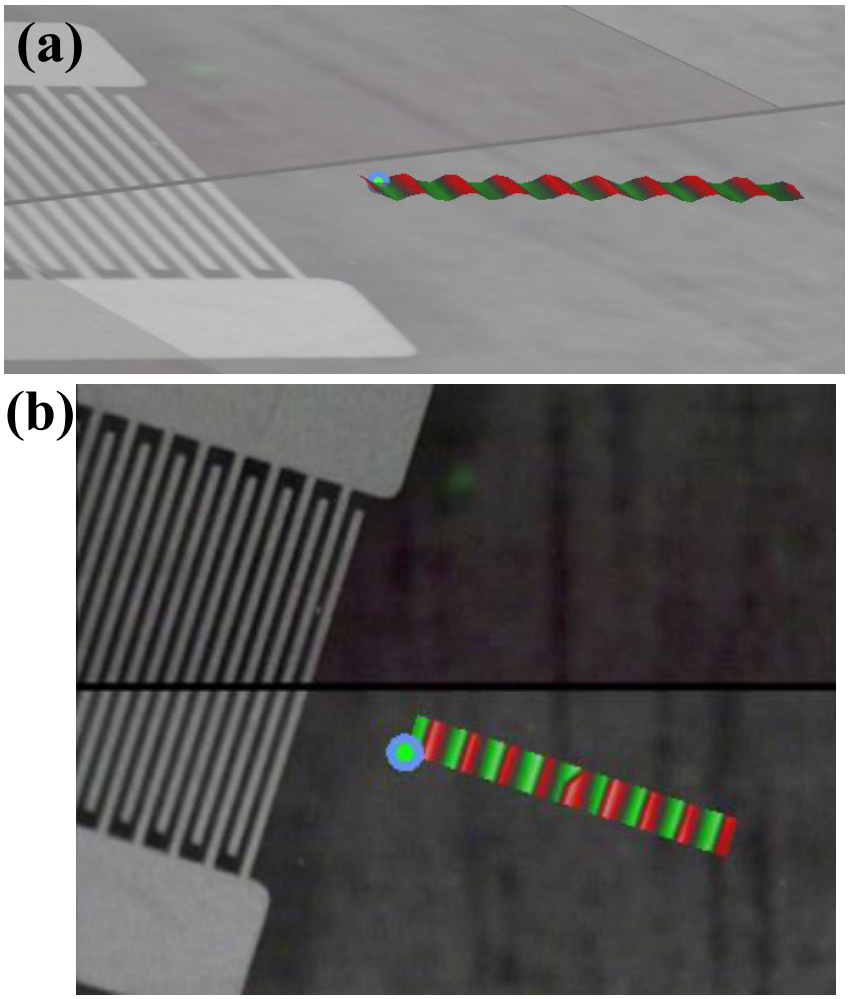

Figure 3.7: Laser Doppler vibrometer scans of (a) instantaneous amplitude and (b) phase of SAW generated by the IDTs along the $\gamma = 108^\circ$ direction; the other IDTs produce similar results. Note the finger width and gap between the fingers is $\lambda/4 = 25\ \mu$m in these plots indicating the scale.

National Nanotechnology Coordinated Infrastructure, which is supported by the National Science Foundation (Grant ECCS–1542148). The work presented here was generously supported by a research grant from the W.M. Keck Foundation. The authors are also grateful for the support of this work by the Office of Naval Research (via Grant 12368098), and substantial technical support by Polytec's staff in Irvine, CA and Waldbronn, Germany.

Chapter 4

Microliter Ultrafast Centrifuge Platform for Size-based Particle and Cell Separation and Extraction using Novel Omnidirectional Spiral Surface Acoustic Waves

4.1 Abstract

Asymmetric surface acoustic waves have been shown useful in separating particles and cells in many microfluidics designs, mostly notably sessile microdroplets. However, no one has successfully extracted target particles or cells for later use from such samples. We present a novel omnidirectional spiral surface acoustic wave (OSSAW) design that exploits a new cut of lithium niobate, 152 Y-rotated, to rapidly rotate a microliter sessile drop to $\sim 10g$, producing efficient multi-size particle separation. We further extract the separated particles for the first time,

demonstrating the ability to target specific particles, for example, platelets from mouse blood for further integrated point-of-care diagnostics. Within $\sim$5 s of surface acoustic wave actuation, particles with diameter of 5 μm and 1 μm can be separated into two portions with a purity of 83% and 97%, respectively. Red blood cells and platelets within mouse blood are further demonstrated to be separated with a purity of 93% and 84%, respectively. These advancements potentially provide an effective platform for whole blood separation and point-of-care diagnostics without need for micro or nanoscale fluidic enclosures.

4.2 Introduction

Surface acoustic wave devices have become popular as a practical and effective tool for fluid manipulation, particle and cell sorting and separation, and fluid jetting and atomization in various acoustofluidics and biomedical applications in recent years[65,89,109,284,398,468]. They offer substantial energy density in 40–100 MHz high-frequency, short-wavelength acoustic waves, providing useful acoustofluidic effects when coupled with liquid[79,209,410]. Due to various acoustic radiation forces exerted on particles and cells of different sizes and properties, rapid separation of particles and cells in liquid media using SAW has been one of the most popular and effective methods in microscale acoustofluidics applications for biomedical diagnostics[212,352]. SAW-based separation in enclosed channels has produced high throughput needed in practical applications[61,206]. Traveling surface acoustic waves (TSAW) and standing acoustic waves (SSAW) have both been used to continuously separate particles and cells based on their size and mechanical properties[81,171,227,266,267,349]. However, the need for a microchannel fabrication process and a syringe pump to complete the separation and provide a method of extraction complicates the system and renders its use in a clinical setting problematic, especially when the cost of single-use sterile microchannels are considered. Another SAW-based separation technique is to place a sessile microliter liquid drop on top of the piezoelectric substrate where SAW is

generated, passing sound into the drop, in turn producing rapid separation of particles and cells within[83,207]. This simple method does not require an external pumping system nor a sophisticated channel fabrication and bonding process. Since only a microliter sample is required—a mere pinprick of blood, for example—the method is potentially quite convenient for clinical use. The potential for sterile sample testing using a superstrate[150] improves the likelihood of eventual clinical use.

Importantly, none of these past approaches have actually *extracted* the separated components from the sessile drop after centrifugation, a key problem in the technique's future use. Bourquin et al.[28] presented enrichment of malaria-infected red blood cells at periphery of the droplet based on density difference using SAW-induced separation in sessile drop, enabling effective detection directly from the droplet, and many of the references in this introduction describe various methods for separating particle and cell components in a sessile drop in a similar way. However, after shutting off the acoustic wave, diffusion slowly recombines the components, destroying the separation.

For most point-of-care diagnostics and biomedical applications, further analysis and integrated tests of separated samples are necessary. There remains a need to centrifuge a sessile drop, separate cell or particle components in that drop based on size, acoustic properties, or both, and enable an efficient *extraction* of target cells or particles from the sessile drop sample. In this paper, a method for centrifugation of a sessile drop and extraction of particles and cells from that drop is described.

It is important to first, however, point out an important part of piezoelectric material choices and electrode design to enable sessile drop centrifugation. In the last decade, straight interdigital transducers (IDTs) with a sessile drop asymmetrically located at the edge of the SAW propagation (aperture) producing spinning of the drop and particle concentration and separation within[207,323]. Different acoustic radiation and centrifugal forces based on particle sizes and mechanical properties have been utilized to perform temporary separation in this arrangement.

Destgeer et al.[83] suggested in a later study that four distinct regimes of particle concentration exist in a sessile drop under asymmetric SAW actuation. Focusing IDTs have been used to locally enhance the SAW intensity to improve sessile drop spinning, with some consideration of the focused shape of the IDT[354]. However, anisotropic substrates, the difficulty in repeatedly and accurately placing sessile drops, and large energy losses because of the offset position reduce the attractiveness of this approach with straight or focusing IDTs.

For a rather different purpose, an annular IDT has been demonstrated to generate focusing SAW from all directions to a single, diffraction-limited spot[202]. The IDT finger shape was designed based on the slowness curve of SAW propagating across anisotropic LN so that the generated surface acoustic waves converge to a small spot at the center of the transducer, limited only by diffraction. However, this IDT design simply focuses energy at one spot, without the necessary asymmetry to generate fluid spinning in the droplet and consequent particle separation. There has, in the past few years, been a flood of interest in locally generated torsional waves in fluids by either an array of radially placed IDTs or weak spiral IDT structures to produce particle entrapment[17]. While all these works are excellent, they do not address the fact that, in the most widely used cut of LN today in acoustofluidics and telecommunications, 127.86 Y-rotated LN, the piezoelectric coupling is an order of magnitude less along the Y axis of the substrate compared to the X axis, producing a far weaker SAW in the Y direction. Other choices are possible, including zinc oxide[147] and aluminum nitride[32], but these thin-film materials are generally limited to 2 μm or less thickness and have relatively poor piezoelectric coupling coefficients, making them poor by comparison to single crystal, bulk LN for high-power applications such as acoustofluidics. Lead zirconate titanate (PZT) is another popular polycrystalline choice, but is not only toxic with elemental lead present in the interstitial grain boundaries that can easily contaminate a fluid sample, it also is lossy and rapidly heats, especially at high frequencies.

Rather than relying on an asymmetric technique, arguably a better approach to spinning a sessile drop would be to have SAW propagate inwards from all directions, tangentially converging

to a circle of defined diameter equal to or smaller than the drop size to produce a net moment about a vertical axis. Using this idea, we conceive an axisymmetric, omnidirectional spiral SAW to induce planar recirculating acoustic streaming in a droplet, causing its rapid rotation. We exploit a recent discovery of a different cut of LN, 152° Y-rotated LN[465] that is able to support SAW in an arbitrary direction with nearly the same piezoelectric coupling and other relevant material properties. Combining the choice of this material and our unusual IDT design produces a result that enables rapid sessile drop rotation sufficient to produce centrifugation superior to past results.

4.3 Concept and Design

A unique spiral IDT design underpins our effort to generate rotational symmetric SAW in a central circular region so that energy can be efficiently transferred into the sessile drop for improved fluid spinning and consequent particle and cell separation. The SAW at any point generated by the spiral IDT is designed to propagate along a constant offset angle relative to its radial direction, α, into the middle circular region. The spiral equation in polar coordinates (r,θ) to produce the spiral IDT of the OSSAW is (see details of the derivation in the Appendix):

$$\theta = \sqrt{\frac{r^2}{R_0^2}-1} - \tan^{-1}\sqrt{\frac{r^2}{R_0^2}-1} - \sqrt{\frac{R_1^2}{R_0^2}-1} + \tan^{-1}\sqrt{\frac{R_1^2}{R_0^2}-1}. \tag{4.1}$$

where R_0, R_1, and R_2 are the radii of circles that define the tangent circle for the inward propagating SAW, the outer edge of the spiral IDT, and the inner edge of the spiral IDT, respectively, as illustrated in Fig. 4.1.

The omnidirectional spiral design is obtained by azimuthally shifting and duplicating a single finger pair to produce the complete set of IDT fingers (*see* Fig. 4.1). The number of duplications required in this simple IDT format is determined by an equality between the finger

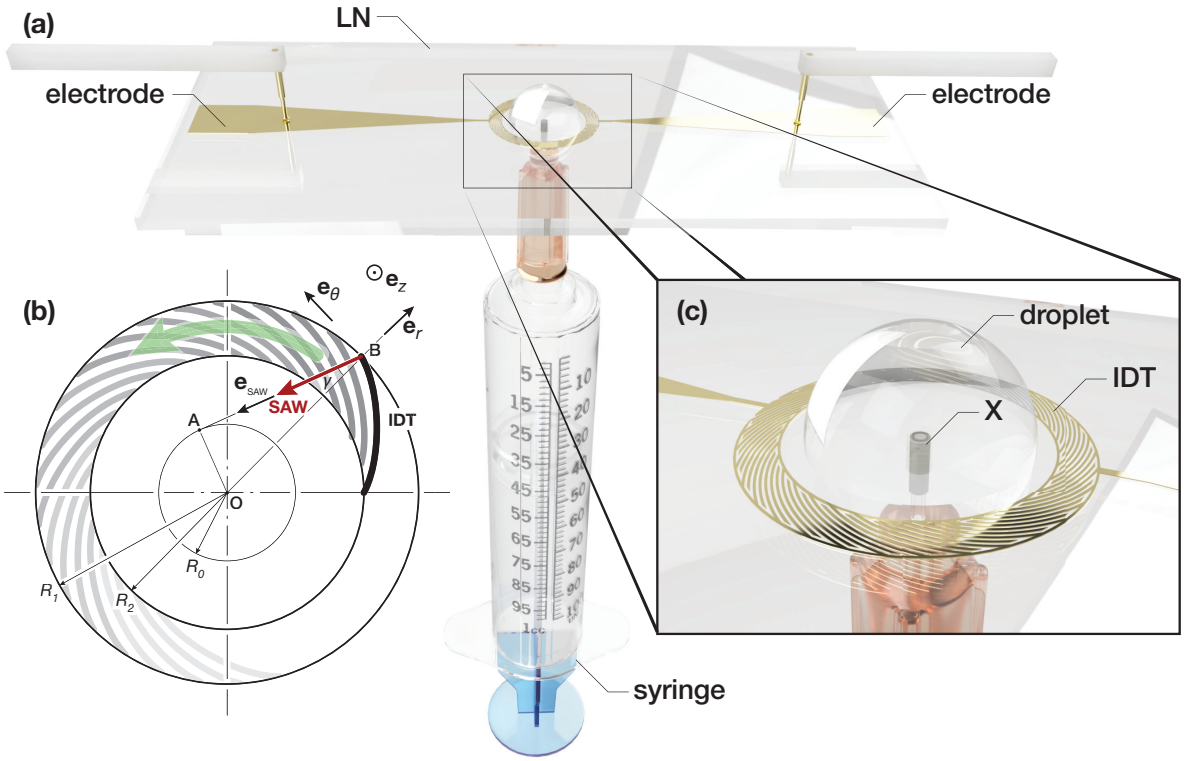

Figure 4.1: The (a) omnidirectional spiral surface acoustic wave (OSSAW) device concept for centrifugation and separation of samples, based on (b) the use of a spiral interdigital electrode structure defined in detail in the Appendix, an extraction syringe, and a 152° Y-rotated cut of lithium niobate to allow SAW to be generated along the substrate surface. The bold spiral line represents the spiral IDT finger; the red arrow represents the SAW it generates from the outer end of the finger, propagating inwards. The outward propagating SAW is absorbed with polymer absorbers (not shown for clarity). The SAW propagating direction is orthogonal to the spiral line and tangent to a defined circle of radius R_0. The IDT fingers are defined between the outer and inner radii R_1 and R_2. A closer view (c) of the OSSAW electrode with a $\mu\ell$-order droplet within shows the spiral IDT, the bus bars that connect, independently, the inner and outer fingers of the IDT, with an independent connection from the outside to the inner bus bar at left in the closeup, and the (X) location of the laser-drilled hole used for extraction after centrifugation.

width, the gap between them, and one quarter of a wavelength. We have

$$R_2 \frac{2\pi}{n} \sin\alpha = \frac{\lambda}{4} = \frac{v}{4f}, \tag{4.2}$$

where R_2 is the inner radius of the spiral IDT; $n/2$ is the number of spiral IDT fingers; α is the offset angle for SAW propagation; λ, f, v are wavelength, frequency, and phase velocity of

surface acoustic wave propagating on LN respectively. This simplifies to

$$n = \frac{8\pi f R_2 \sin\alpha}{v} \tag{4.3}$$

where the number of spiral lines n are dependent on the wave frequency f, radius of inner circle of spiral IDTs R_2, SAW offset angle α, and SAW phase velocity v.

Crucially, in this concept the in-plane anisotropy of the piezoelectric substrate is not considered. We are able to make this remarkable assumption by using a new cut of LN, the 152° Y-rotated (152Y) LN cut, instead of the conventional 128° Y-rotated cut. This new cut has been shown through an exhaustive analysis to be an optimal choice to simultaneously minimize in-plane anisotropy and maximize electromechanical coupling for omnidirectional surface acoustic wave propagation[465]. The combination of this cut with the spiral design facilitates the type of azimuthally distributed SAW important in enhancing the sessile drop rotation through more intense acoustic streaming and acoustic radiation force via coupling from all propagation directions. An alternative approach would be to reshape the spiral electrode pattern in order to match the "slowness curve" and best make use of an existing anisotropic cut of lithium niobate like the 128° Y-rotated cut[202]. However, this does not overcome the poor electromechanical coupling of any acoustic wave away from the X axis in that cut, and indeed in most other cuts of LN.

4.4 Device Fabrication and Functionality

4.4.1 Device Fabrication

Equation (4.1) was discretized into points, equally spaced at 1 μm, along a single spiral line (MATLAB, Mathworks, Natick, MA USA), and formed into a complete array using computer-aided drafting (AutoCAD, Autodesk, San Rafael, CA, USA) according to the number of spiral lines, n in Eqn. (4.3), as defined and fabricated for three different operating frequencies of 40 MHz,

56.5 MHz, and 100 MHz, later shown to be useful for choosing the threshold size for particle separation within the sessile droplet. An operating frequency of 56.5 MHz was chosen to produce a $\sim$5 μm particle/cell separation threshold, taking into account particle compressibility[90,186,259], by designing the spiral IDT electrode to operate with a wavelength of $\lambda \sim 70$ μm (from $f = v/\lambda$). A polymer mask was produced (CAD/Art Services, Inc., Bandon, OR USA) from this result. Standard UV photolithography (using AZ1512 photoresist and AZ300MIF developer, MicroChem, Westborough, MA USA) was used alongside sputter deposition and lift-off processes to fabricate the 5 nm Cr/ 400 nm Au IDT upon a 500 μm-thick, double-polished 152Y LN substrate (Jiaozuo Commercial FineWin Co., Ltd, Jiaozuo, Henan, China)[65,246,463]. The whole wafer was diced into fifteen 26.7 mm $\times$ 12 mm LN chips (Disco Automatic Dicing Saw 3220, Disco Corporation, Tokyo, Japan). Absorbers (DragonSkin, platinum-cure silicone rubber, Smooth-On, Inc., Macungie, PA, USA) were used at the periphery of the device to prevent edge reflections and spurious bulk waves. SAW was generated by applying a sinusoidal electric field to the IDT at resonance using a signal generator (WF1967 multifunction generator, NF Corporation, Yokohama, Japan) and amplifier (ZHL–1–2W–S+, Mini-Circuits, Brooklyn, NY USA). The instantaneous voltage and current were measured and used to compute the true power input on an oscilloscope (InfiniiVision 2000 X-Series, Keysight Technologies, Santa Rosa, CA USA). The spatiotemporal variations of the SAW displacement and velocity amplitude along the underlying substrate were measured using a laser Doppler vibrometer (LDV, UHF–120, Polytec, Waldbronn, Germany).

4.4.2 Wave Morphology

Surface acoustic waves propagating inward from the OSSAW spiral structure may pass through the center and outward to interfere with SAW from the opposite side, unless a fluid droplet is present to "leak" and absorb the acoustic wave in the substrate[311] before this can happen. This is a key design parameter in selecting the frequency of the SAW and the inner diameter of the OSSAW structure, R_2. It also defines the fluid sample size, because the sessile

drop must both fit within the inner diameter of this spiral ring IDT and completely occupy the space to ensure complete absorption of the SAW from the substrate.

In other words, the sample volume defines the appropriate frequency to choose for the SAW device, presuming the contact angle does not change significantly. If another fluid sample volume is desired, the design of the IDT should change to provide a matching frequency so that complete attenuation occurs.

In our case, the attenuation length of the SAW in the substrate underneath a fluid is $\alpha^{-1} = (\rho_s v_R \lambda_{SAW})/(\rho_f c_f) \sim 0.9$ mm, where ρ_s and ρ_f are the density of LN and water, v_R is the velocity of the SAW on the LN substrate, and c_f is the sound velocity in water[79], respectively. Upon positioning a 1.5 $\mu\ell$ drop in the middle of the device with a radius of 1 mm, SAW from the opposite direction is absorbed by the liquid, eliminating possible interference.

To confirm this concept, a diced OSSAW device including a spiral IDT of inner radius $R_2 = 0.5$ mm was scanned via LDV. A small drop of DragonSkin silicone rubber was placed and cured in the middle of the inner region of the device as a direct substitute for a fluid droplet. This absorbs the SAW propagating from the opposite side of the device in a manner similar to a water or other fluid drop, but does not evaporate nor change shape during the scan. The spatial phase distribution is plotted in Fig. 4.2(a) while being driven at 2.6 W and 56.5 MHz. The phase pattern indicates an inward propagating SAW at an oblique angle as desired, though there are discrepancies in the axisymmetry of the wave morphology.

The ability to generate SAW along directions away from the X axis is significantly better in this 152° Y-rotated cut LN than 127.86° Y-rotated LN. Both the speed of sound and the electromechanical coupling, on average, change much less than with the 127.86° Y-rotated cut popular for unidirectional X-axis propagating SAW. It is impossible to completely eliminate in-plane anisotropy without also eliminating the piezoelectric coupling necessary to efficiently generate SAW across the plane of the surface. This is why Z-cut and X-cut LN, both isotropic in the plane of the surface, are poor choices for SAW generation. The details of the analysis

that produces the 152° Y-rotated cut as an optimal choice are provided in the literature[465], as is information on why the anisotropy is necessary.

The rather broad resonance frequency exhibits a peak at 56.5 MHz as shown in the frequency response plot in Fig. 4.2(b).

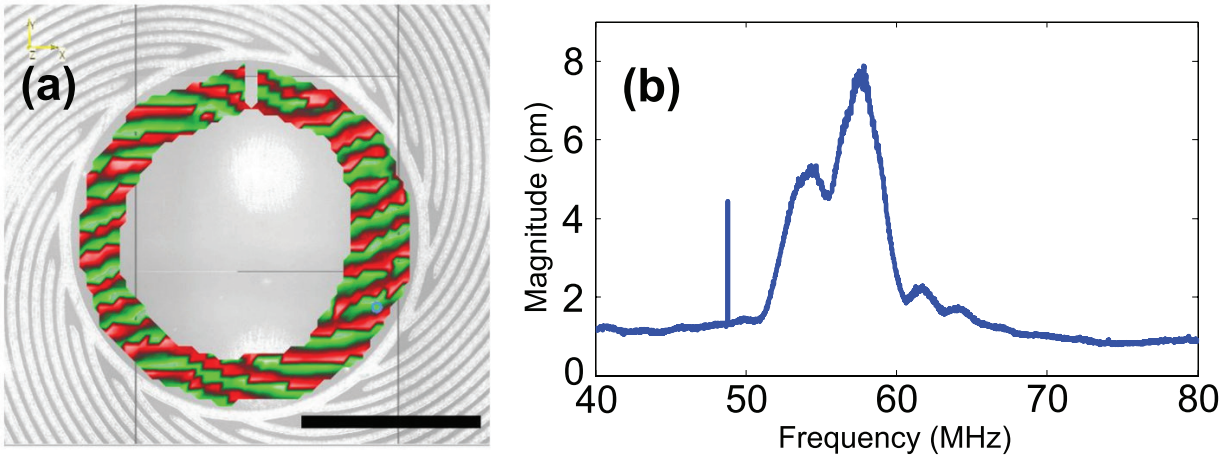

Figure 4.2: (a) An LDV phase scan of the OSSAW inner annular region, showing inward, obliquely propagating waves (scale bar: 0.5 mm). (b) The OSSAW device exhibits a resonance at 56.5 MHz according to the LDV-measured frequency spectrum. Note: the peculiar "notch" at the top of each image is due to a strange limitation in the LDV software: a measurement cannot be made in a complete annular region; it must be broken.

4.4.3 OSSAW Droplet Spinning Functionality

The key purpose of the OSSAW design is to enhance the ability to spin sessile microliter-scale fluid droplets, as investigated here. A method to form an aligned and precisely sized wetting region has been devised for this purpose. It is important to accurately place the droplet at the center of the OSSAW structure with cylindrical symmetry. Doing so without surface modification, whether by hand or machine, is difficult. The entire surface of the OSSAW substrate was coated with a hydrophobic submicron film (Aquapel, Pittsburgh, PA USA). A precise circular region of $R_2 = 0.5$ mm radius was etched by an excimer (exciplex) laser ($\lambda = 189$ nm, firing rate of 40 Hz, power of 0.16 W, and 5 shots, LaserShot, Optec, Frameries Belgium). The weak and

brief laser machining acted to remove this coating from the region, returning it to the naturally hydrophilic state of bare, polished LN without damage. This enables repeatable and precise droplet placement—even by hand with a standard pipette.

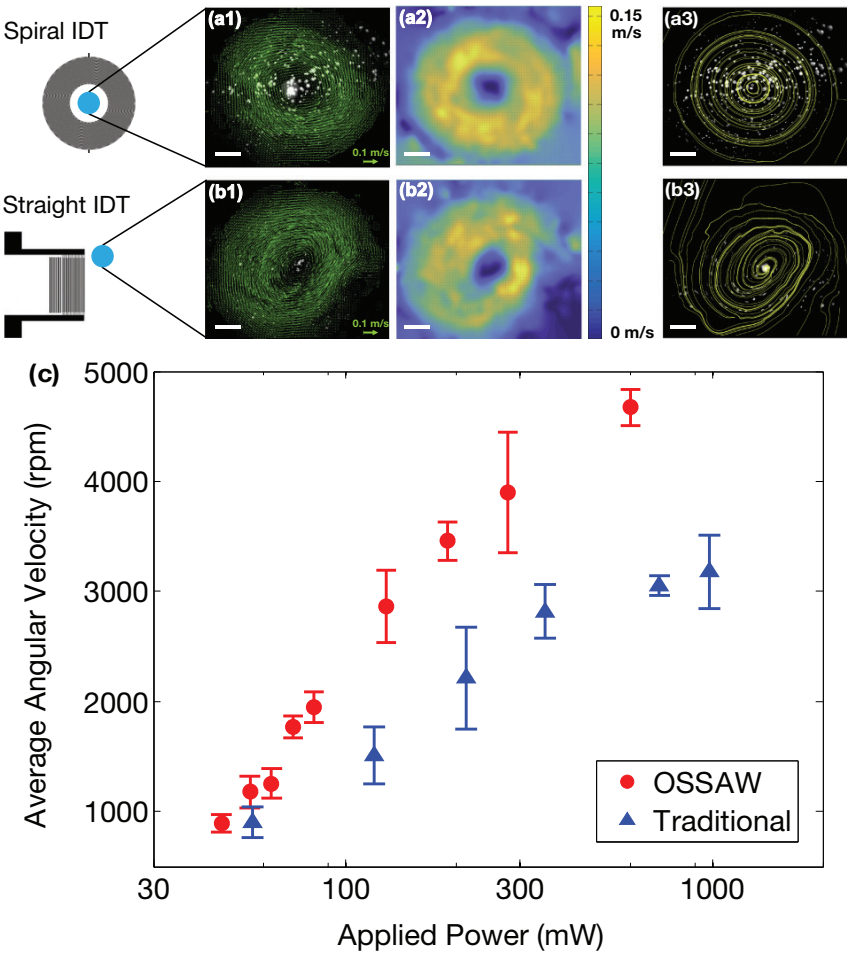

Figure 4.3: A comparison between (a) OSSAW and (b) traditional offset droplet spinning using a straight IDT configuration may be made from (a1,b1) vector velocity, (a2,b2) velocity magnitude, and (a3,b3) particle streamlines for a 1.5 $\mu\ell$ DI water droplet. Average eccentricities of 0.28 and 0.81, respectively, were computed from the streamlines of (a3) the OSSAW and (b3) traditional straight IDT devices. These streamlines were calculated using PIVlab, suggesting an improved axisymmetric droplet spinning via OSSAW. (c) The OSSAW also produces a greater average angular velocity (rpm) for a given applied power. The maximum possible rotation speed from the traditional design at any power is 3180 rpm; the droplet is ejected from the surface at greater input powers. However, with OSSAW, a speed of 4670 rpm may be achieved, at which point atomization begins to appear. The error bars represent the standard deviation ($n = 5$ for each data point).

It is important to examine how the acoustic streaming-driven flow evolves when using the OSSAW device, and a useful comparison is the traditional placement of a fluid drop on a standard SAW IDT aperture's edge as illustrated in Figure 4.3. Fluorescent polystyrene 1 μm particles (PolyBead Microspheres, Polysciences, Inc., Warrington, PA USA), a size less than the transition threshold to be influenced by direct acoustic forces, 5 μm, were mixed into a deionized (DI) water suspension for tracking acoustic streaming immediately prior to placing a 1.5 $\mu\ell$ fluid drop of the suspension onto the OSSAW device (Fig. 4.3a). Due to the hydrophilicity in the central region and the hydrophobicity outside it, the droplet remains in the hydrophilic region, the center of the OSSAW device. A similar approach was used for the traditional SAW droplet concentrator configuration with straight IDTs as a benchmark control (Fig. 4.3b). The concentration of the particles was 4×10^9 particles/mℓ, chosen for ease of visualization and particle tracking. The effect of concentration on the behavior of acoustofluidic concentration and separation is weak and has been explored in past work[65].

Microparticle image velocimetry (μPIV) was performed while viewing the sessile drop from above, using a high-speed camera (at 500 fps, K2 DistaMax lens, Infinity Optical, Centennial, CO USA and Fastcam Mini UX, Photron, San Diego, CA USA). We used an open-access PIV analysis tool (PIVlab)[394]. This tool is able to track visible fluorescence particles and accommodates appearance and disappearance of particles from the view due to the edges, migration from the focal plane and towards or away from the objective lens (i.e., out of focus), or superposition from the camera's perspective. This method of PIV is sometimes called "poor-man's PIV" because it does not require special two-shot rapid laser illumination. Instead, the PIV is computed from individual and equally spaced frames of the video taken at 500 fps.

We set the variable zoom, long working distance microscope lens at 5X magnification to ensure the depth of field is larger than the depth of the droplet and the field of view is larger than the drop size. This prevents particle loss or gain in the video. The radial position and circumferential velocity of all visible particles, well over 1000 per experiment, were determined

by the software after manually identifying the center of rotation and representing the droplet as a circulating vortex. In our experiments, this was consistently at the center of the drop. The radial velocity is computed but not used. Some—fewer than 5% in each run—of the particles are adherent on the substrate or clearly adjacent the substrate, and these are ignored by retaining the velocities of only those particles that exhibit a circumferential velocity greater than 10% of the mean circumferential velocity of all the observed particles. The angular velocity of each of the remaining particles was determined by its circumferential velocity divided by its radial distance from the drop center, and the average angular velocity was then calculated. The error bars represent the standard deviation of all of the points over five distinct runs, each with a fresh droplet run in the system.

From the μPIV velocity and streamline plots in Fig. 4.3a-c, the OSSAW device clearly produces a more axisymmetric streaming pattern in the sessile drop than the traditional offset design. To quantify this for the reader, consider the eccentricity of the streamlines traced out by the particles as the flow rotates in the drop (*see* Fig. 4.3(a3, b3)); an eccentricity of zero is ideal, representing a circular path, while an eccentricity of one is a line. With OSSAW, the average eccentricity of the streamlines is 0.28, substantially more "circular" than an eccentricity of 0.81 from a traditional straight IDT-based design. The distortion in the traditional approach has long been known to lead to instability that limits its maximum rotation speed[354]. The OSSAW provides uniform energy input, reducing interfacial deformation due to asymmetry in the acoustic streaming that can grow to eject the droplet. While other methods have been proposed to spin droplets using straight and curved IDT structures[354], fundamentally those approaches do not offer the symmetry of incident SAW provided by OSSAW.

Further, the OSSAW produces greater rotation speed at the same applied power, and can perform fluid spinning up to about 4600 rpm, representing about $\sim$10 g (98.7 m/s^2) of acceleration (Fig. 4.3(c)). This limit is defined by the appearance of atomization from the drop surface. Nearly uniform throughout, the drop rotation speed is 59% faster on average per unit power for the

OSSAW device versus the traditional approach. It is important to note the presence of an Ekman layer adjacent the substrate of about 50 μm in depth,[192] and in this region the flow is slower, as it is with all acoustofluidic devices.

4.5 Size-based Particle Separation via OSSAW

4.5.1 Separation Mechanism

OSSAW appears to concentrate larger objects at the center of the droplet and smaller objects at the periphery, consistent with other sessile drop rotation devices from the past[83,192,207]. As the dominant force at the length scale of objects greater than a threshold particle size, R_{th}, the acoustic radiation force overwhelms the radial inertia due to centripetal acceleration, often and erroneously referred to as *centrifugal forces*. Taking a balance between the acoustic radiation force and the centripetal acceleration-induced radial force, it becomes possible to determine this threshold particle size. Based on analysis from King[186] and later Doinikov[90] concerning the acoustic radiation pressure on a sphere in a plane progressive wave,

$$F_{AR} = 2\pi\rho_f \frac{(2\pi f)^4}{c_f^6} R^6 \dot{\xi}^2 \frac{1+\frac{2}{9}(1-\frac{\rho_f}{\rho_p})^2}{(2+\frac{\rho_f}{\rho_p})^2} \propto R^6 \tag{4.4}$$

for $fR/c_{SAW} \ll 1$, where ρ_p is the particle density, f is the frequency of the acoustic wave, c_f is the sound velocity in fluid medium, R is the particle radius, and $|\dot{\xi}|$ is the fluid particle velocity. The radial force produced by their inertia in countering the centripetal acceleration that would be required for them to follow the circular path as the drop spins may be depicted as

$$F_c = \omega^2 r(\rho_p - \rho_f)\frac{4}{3}\pi R^3 \propto R^3, \tag{4.5}$$

where ω is the instantaneous angular velocity of the particle and r is the instantaneous radius of the particle trajectory. When the particle's radius R is large relative to the threshold R_{th} defined by the equality of $F_{\text{AR}} = F_c$,

$$R_{\text{th}}^3 = \left(\frac{r\omega^2 c_f^6}{24\pi^4 f^4 \dot{\xi}^2} \right) \frac{(\rho_f - \rho_p)\left(2 + \frac{\rho_f}{\rho_p}\right)^2}{\rho_f \left(1 - \frac{\rho_f}{\rho_p}\right)^2}, \tag{4.6}$$

the acoustic radiation force overwhelms the inertial motion of the particles. Because of the strongly nonlinear sixth-order dependence of F_{AR} upon R in eqn. (4.4), the transition from acoustic radiation force-dominated particle motion to motion governed by the hydrodynamics as the particle size increases is very rapid. Particles smaller than the threshold R_{th} will radially cross streamlines to the periphery of the drop due to their inertia—if the OSSAW is sufficiently powerful to cause the particles' inertia to be significant in comparison to other local effects such as shear migration.

It is perhaps best noted here that the *direction* of the acoustic force is not oriented radially to exactly oppose centripetal acceleration-induced particle motion. In our configuration, it is oriented $\alpha = 22.5^\circ$ from the radial direction, implying the equality between the radial force due to the acoustic wave and the centripetal acceleration is instead $F_{\text{AR}} \cos\alpha = F_c$, and so the particle size threshold would become $R'_{\text{th}} = \sqrt[3]{1/\cos\alpha} R_{\text{th}}$. But notice that $\sqrt[3]{1/\cos\alpha} \approx 1.027$, very nearly one, and so the effect is negligible. If the reader chooses, however, to orient the acoustic wave from the IDT such that α is much larger, this effect may be important to consider.

In principle, it is straightforward to identify the appropriate frequency to set the threshold particle radius R_{th} to produce significant acoustic forces on particles larger than the threshold that are nearly absent on particles smaller than this threshold. But this is true only if the sessile drop rotation velocity, ω is always the same. When switching from water to blood, for example, the viscosity changes as well, and this affects the drop's rotation velocity. One could try to compensate by changing the input power, which changes the droplet rotation speed, ω. However,

this will also change the particle velocity in the fluid $|\dot{\xi}|$. Careful study of eqn. (4.6) shows that $R_{\text{th}}^3 \sim \omega^2/\dot{\xi}^2 \sim P_{\text{in}}/P_{\text{in}} \sim 1$, where P_{in} is the input power, implying that the threshold particle size is not dependent upon the power input. This arises because $\omega^2 \sim P_{\text{in}}$ from Fig. 4.3 (to a coefficient of determination $R^2 \approx 0.9$)—as expected because the square of the streaming velocity scales with the input power—and $\dot{\xi}^2 \sim P_{\text{in}}$ from numerous places in the literature[109].

Consider two cases, the first polystyrene particles in water, and the second murine blood cells in plasma, diluted to 6% hematocrit. These two cases are tested later, but let us consider what would be appropriate here in the context of frequency selection. Suppose we wish to separate 1 μm PS particles in water from larger PS particles. It is possible to spin a 1.5 $\mu\ell$ droplet of water at $\omega = 4000$ rpm using 1 W into the OSSAW device, nearly independent of the frequency choice. At $f = 100$ MHz this would set the threshold particle size at $R_{\text{th}} = 1.23$ μm. Choosing $f = 40$ MHz gives $R_{\text{th}} = 4.17$ μm. Either choice works, but the former likely would produce more selective results.

More importantly, notice the effect of now switching to blood. Even diluted, the viscosity is significantly increased and the rotation velocity of a 1.5 $\mu\ell$ droplet of this fluid is much lower at $\omega = 1800$ rpm with the same input power, $P_{\text{in}} = 1$ W. This causes the threshold particle size to be only $R_{\text{th}} = 0.72$ μm at $f = 100$ MHz, and $R_{\text{th}} = 2.45$ μm at $f = 40$ MHz.

In reality, the desire to perform the separation as quickly as possible, paired with the need to avoid local interparticle effects that manifest over longer periods of time, encourages one to seek the fastest drop rotation speed possible for the fluid under study. While a detailed analysis is possibly instructive, it is easier to simply fabricate and test a number of devices to search for the one arrangement that produces the quickest separation results.

4.5.2 Multi-size Particle Separation

Polystyrene (PS) particles (Polysciences, Inc., Warrington, PA, USA) with diameters of 1, 5, and 43 μm were selected to demonstrate size-selective microscale separation via the OSSAW

device. These particles were mixed into DI water with concentrations, respectively, of 4×10^9, 6.3×10^7, and 1×10^5 particles/mℓ as representative concentrations. As noted earlier, the effect of concentration on the behavior of acoustofluidic concentration and separation is weak and has been explored in past work[65]. A 1.5 $\mu\ell$ droplet of this suspension was immediately transferred by pipette onto the hydrophilic circular region at the center of the OSSAW device (Fig. 4.4a). An operating frequency of 40 MHz was chosen to produce a threshold separation particle size of $R_{\text{th}} = 4.17$ μm for $\omega = 4000$ rpm using 1 W, just slightly smaller than the intermediate PS 5 μm particle size.

After applying $\sim$1 W input power to the OSSAW device, the particles separated and concentrated at different locations in the droplet in $\sim$1 s (Fig. 4.4(b)). The smallest particles (1 μm), relatively unaffected by the ARF, collected at the periphery of the droplet; the intermediate particles (5 μm) collected as an annular ring in the droplet; and the largest particles (43 μm) collected at the center of the droplet. This marks the first time rings of particles have been consistently seen, and may indicate the benefit of using axisymmetric acoustic waves in manipulating the droplet and particles within. It also indicates that there is a possibility of obtaining, reliably, an intermediate result between concentration at the drop's center or edge when the particle size is approximately the same as R_{th}.

4.5.3 Blood Cell Separation

The utility of OSSAW is best examined through a potential application, and blood cell separation was considered a potential clinical use of the technology. Fresh whole blood was extracted from live mice (strain C57BL/6J, Jackson Laboratories, ME USA) and kept in an ethylenediaminetetraacetic acid-coated microtube (EDTA–K3, Becton Dickinson, Franklin Lakes, NJ USA) to prevent clotting prior to use. The blood was diluted with phosphate buffered saline (PBS) to a ratio of 1:5, representing a hematocrit of 6%, with bovine serum albumin (BSA) added (1.6% by weight). Murine red blood cells are biconcave, spherical, and about 4–7 μm in diameter,

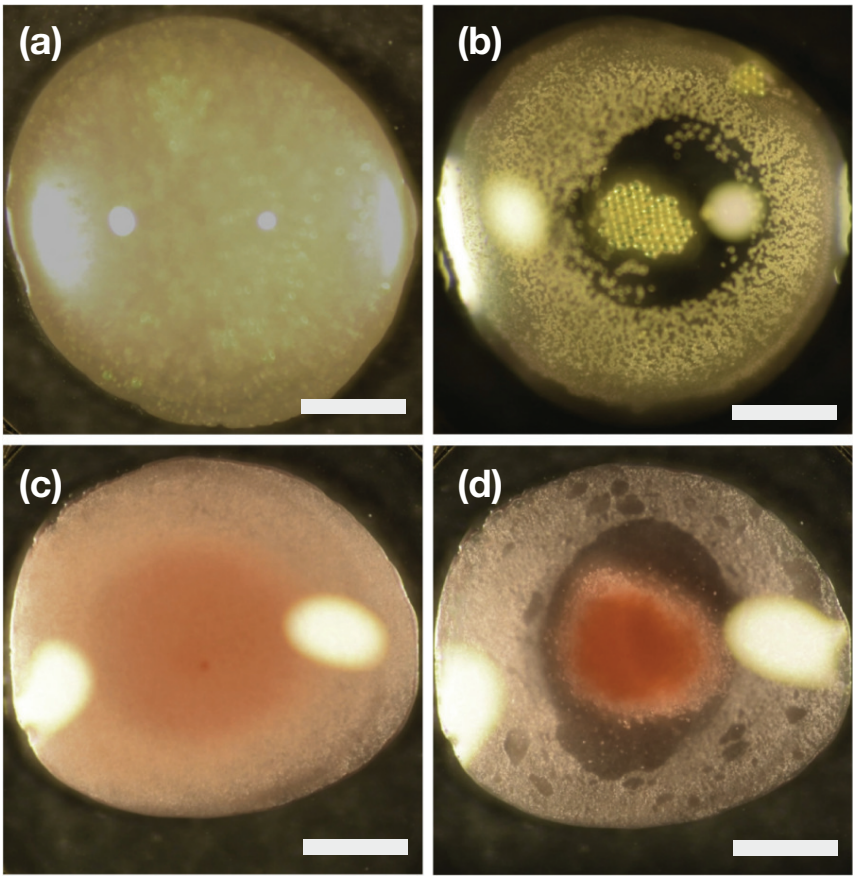

Figure 4.4: A (a) 1.5 $\mu\ell$ drop with 1 μm (red), 5 μm (green), 43 μm (green) polystyrene (PS) particles randomly distributed within. (b) After OSSAW separation, showing 1 μm, 5 μm, 43 μm PS particles separated from periphery to center of the droplet. (c) 1.5 $\mu\ell$ diluted mouse blood before separation. (d) After OSSAW separation, red blood cells and the occasional white blood cell appear at the drop's center, while platelets and smaller components of blood appear at the drop's periphery The bright dots on the droplets are specular reflections of externally placed lights from the droplet surface (scale bar: 0.5 mm).

similar to human blood, and number about 7–13 $\times 10^6$ particles per $\mu\ell$ of whole blood.[277] Murine platelets, however, are smaller at 0.5 μm in diameter and are more numerous (730,000/$\mu\ell$)[420] and heterogeneous than their human counterpart (1-2 μm in diameter)[336]. White blood cells (WBCs) are rare in small blood samples.

Based on the lower drop rotation speed of $\omega = 1800$ rpm at $P_{\text{in}} = 1$ W into the OSSAW device, we selected $f = 40$ MHz to produce a separation threshold of $R_{\text{th}} = 2.45$ μm between the platelet and RBC diameters. After depositing a 1.5 $\mu\ell$-sized droplet onto the OSSAW device and

operating it for 5 s, the larger cells (RBCs and WBCs, latter very rare) were found concentrated in the middle of the drop, while the platelets were found at the periphery (Fig. 4.4(d)).

4.6 Extraction and Isolation Platform

4.6.1 Experimental Setup

An extraction platform was devised to extract separated portions of particles or blood components from the center of the droplet to perform true size-based separation and isolation for further analytical and biological analysis. As shown in Fig. 4.1(a,c), a 100 μm hole was drilled at the center of the OSSAW device from the back side of the LN chip using an excimer (exciplex) laser at a wavelength of 189 nm, a firing rate of 300 Hz, and an instantaneous power of 100 W for each "shot". The hole was drilled using 120 groups of ten repeated shots, refocusing the laser's focal plane into the hole between groups as it progressed by 50 μm increments (LaserShot, Optec Laser Systems, Brussels, Belgium). Glass capillary tubes, 80μm outer diameter (OD) and 50 μm inner diameter (ID), were introduced into the hole for extraction after separation (see Fig. 4.9(a)). A 1 mℓ syringe was attached to the glass capillary tube using hot glue (see Fig. 4.9(b)). The complete extraction platform is provided in Fig. 4.9(c), showing components necessary for system alignment, tube insertion, particle extraction, and tube extraction.

4.6.2 Extraction Results and Separation Performance

The as-separated portion of the blood sample at the droplet's center was extracted from the hole using the glass capillary tube placed into the underside of the OSSAW device (Fig. 4.5). By contrast, the separated portion at the drop periphery was collected using a fine pipette tip from the top of the OSSAW device.

It is possible to extract samples using either method, and depending on the reader's ability

to introduce holes into LN and the desired extraction workflow, one or the other choice may prove more suitable. In the latter case, with extraction from above, it is important to note that leaving the acoustic wave on as supplied from the SAW prevents cell adhesion to the substrate and consequently improves the extraction results. In extracting particles from below, this is less of a problem.

For particle separation, we discarded the 43 μm PS particles and selected only the 1 μm and 5 μm PS particles. The larger 43 μm particles tend to clog the 50 μm extraction capillary tube. The 5 μm and 1 μm PS particles were mixed in equal numbers in the sample (i.e., the quantity ratio was 1:1), with a concentration of 4×10^5 particles/mℓ. Due to this smaller particle pair, we chose the 100 MHz OSSAW to produce $R_{\text{th}} = 1.23$ μm. This frequency is higher than the initial 56.5 MHz OSSAW device in Figs. 4.2 and 4.3 and the 40 MHz used for the PS particle and murine blood separations in Fig. 4.4. Separation was initially performed using the OSSAW at 1 W for 1 s on a 1.5 $\mu\ell$ fluid sample.

As-separated particles were then extracted with fluid from the center and edge, and the two extracted fluid-particle samples were analyzed using flow cytometry (Attune NxT Flow Cytometer, ThermoFisher, Waltham, MA, USA), distinguishing the particle size by forward scatter and side scatter. The numerical purity of 5 μm beads at the drop center was 83%, while the numerical purity of the 1 μm beads at the drop periphery was 97% (see Fig. 4.6(a,b)). Numerical purity in this context is defined by the number of target particles divided by the total number of particles in the extracted sample.

For blood cell separation, the OSSAW was operated at 1 W and a frequency of 40 MHz in order to place the separation size threshold $R_{\text{th}} = 2.45$ μm between the platelet and RBC diameters. Two 0.75 $\mu\ell$ samples were extracted from the periphery and center of a 1.5 $\mu\ell$ diluted (6% hematocrit) and OSSAW-separated mouse blood droplet were transferred into individual wells of a 96-well assay plate (Fisher Scientific, Waltham, MA, USA) with staining buffer (PBS + 1.6% BSA) to assess cell viability, perform antibody staining, and minimize non-specific binding.

Antibodies targeting TER119 (Fluorescein isothiocyanate (FITC)), CD45 (Alexa Fluor 594), and CD41 (Alexa Fluor 700) (all Biolegend, San Diego, CA, USA) were used to stain RBCs, WBCs, and platelets, respectively. Incubation was performed for 30 min at 4°C in the dark after introducing the antibodies. Flow cytometry (ZE5 Cell Analyzer, Bio-Rad, Hercules, CA, USA) was then performed to identify the cell separation performance of OSSAW. As shown in Fig. 4.6(c,d), OSSAW isolates platelets at the drop periphery and RBCs at the drop's center with 83.8% and 92.7% numerical purity, respectively. The plot omits CD45 used to stain WBC, as the number of WBCs in 1 $\mu\ell$ samples—a few per sample—is insufficient to produce statistically valid, quantifiable results via flow cytometry. The few WBCs that do appear in a given sample are consistently extracted with the RBCs.

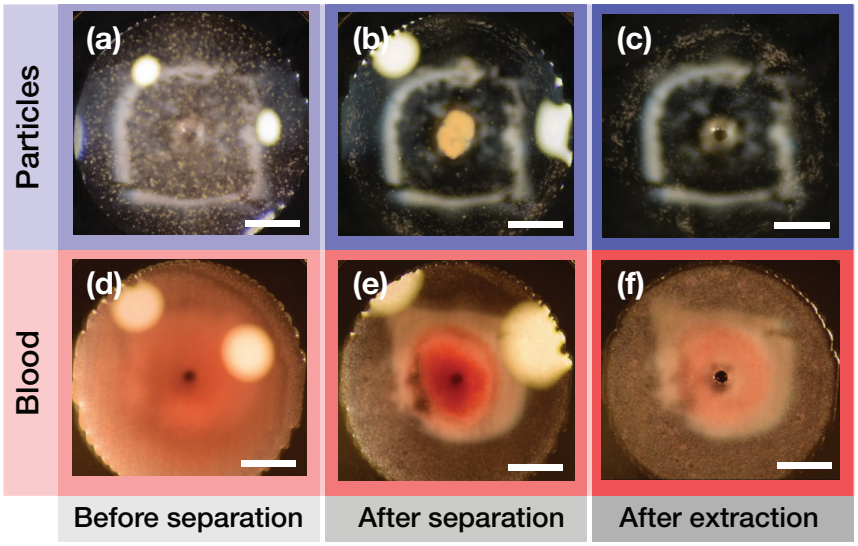

Figure 4.5: (a–c) Separation and extraction of 5 μm (green) polystyrene particles from 1 μm (red) polystyrene particles in a 1.5 $\mu\ell$ DI water droplet (a) Before separation: droplet with 1 μm and 5 μm randomly distributed particles. (b) After separation: 5 μm particles concentrate in the middle of the drop, while 1 μm particles are at the periphery of the drop. (c) After extraction: 5 μm particles are extracted through a glass capillary tube from the middle hole of the device; the 1 μm particles are extracted from a pipette and glass capillary tube introduced at the drop periphery from above (not shown). (d–f) Separation and extraction of red blood cells (RBCs) from mouse blood. (d) Before separation: 1.5 $\mu\ell$ mouse blood on OSSAW device (e) After separation: RBCs concentrate in the middle of the drop, while platelets appear at the periphery. (f) RBCs are extracted via a glass capillary tube from a hole through the middle of the OSSAW device. (Scale bar: 0.5 mm.)

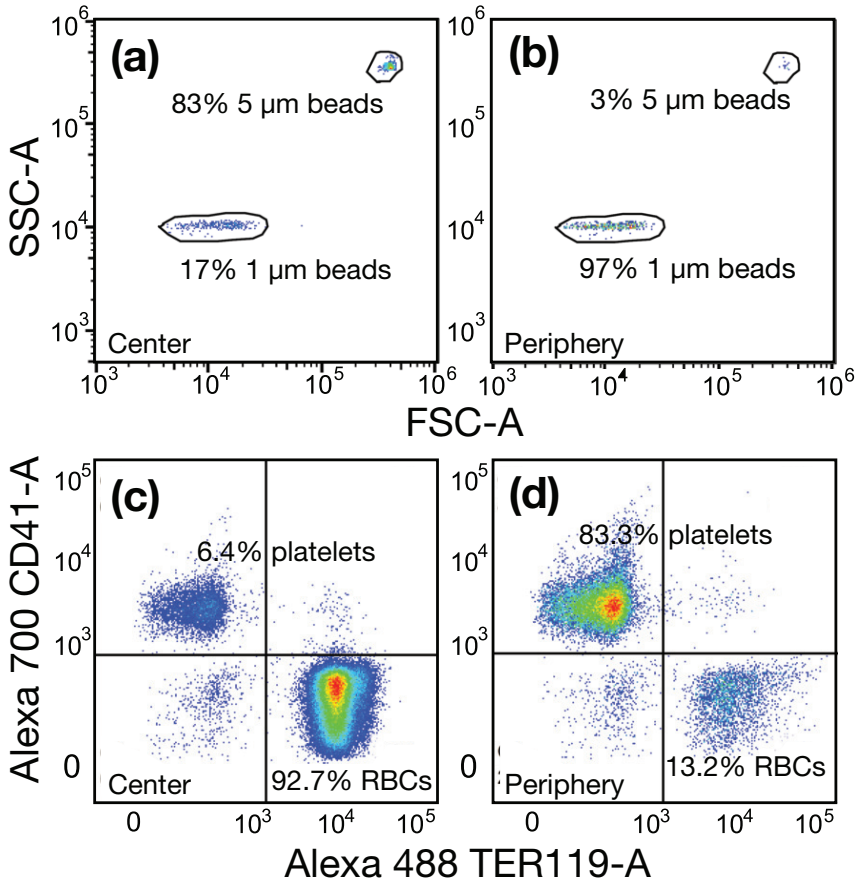

Figure 4.6: Separation performance via OSSAW after separation and extraction by flow cytometry. By providing 100 MHz OSSAW into a microliter scale fluid drop, (a) 5 μm PS particles concentrate at the center, while (b) 1 μm PS particles migrate to the periphery. With diluted murine blood (6% hematocrit), 40 MHz was used instead to separate (c) murine RBCs concentrated at the drop's center, while (d) murine platelets migrated to the periphery.

4.7 Conclusions

In this paper, we demonstrated a novel omnidirectional spiral SAW design—OSSAW—and presented the utility of efficient axisymmetric fluid spinning at up to $\sim 10g$, producing effective separation of particles and cells in a microliter drop. The maximum rotation speed of 4500 rpm is roughly twice the speed of classic configurations like the common offset straight IDTs arrangement, and OSSAW offers this advantage at lower input powers. By using OSSAW, particles of different sizes and mouse blood may each be separated. We also demonstrated the

unique appearance of rings for particles of size similar to the threshold size R_{th}, suggesting a possible means to produce greater discretion in separation of mixed particle samples. The importance of considering the fluid viscosity was illustrated through a comparison of water and blood-based samples, through its effects on the drop rotation speed, not, counterintuitively, due to any changes in the acoustic phenomena.

Table 4.1: A comparison of separation performance using SAW in microfluidics devices from the literature.

Method	Composition	Throughput	Purity	Ref.
SSAW* in channel	Beads with different densities	8-18 $\mu\ell$/min	98%	[14]
SSAW in channel	polystyrene & melamine beads	0.2-2 $\mu\ell$/min	98.8%-89.4%	[15]
SSAW in channel	platelets & RBCs	0.25-5 $\mu\ell$/min	74.1% & 99%	[16]
SSAW in channel	0.87 μm & 4.17 μm PS beads	NA	80%	[17]
TSAW† in channel	3 μm & 10 μm particles	100-300 $\mu\ell$/h	100%	[18]
TSAW in channel	10/15 μm PS & PMMA beads	1-4 $\mu\ell$/min	95%	[19]
TSAW in droplet	1, 3, 6, 20, 45 μm PS particles	5 $\mu\ell$	NA	[20]
TSAW in droplet	1 μm & 10 μm PS particles	5 $\mu\ell$	NA	[21]
FSAW‡ in droplet	6 μm & 31 μm PS particles	1.5-3 $\mu\ell$	NA	[24]
OSSAW in droplet	5 μm & 1 μm PS particles	1.5 $\mu\ell$ drop	83% & 97%	—
OSSAW in droplet	platelets & RBCs	1.5 $\mu\ell$ drop	83% & 93%	—

*SSAW is a standing SAW, †TSAW is a traveling SAW, and ‡FSAW is a focusing SAW.

Furthermore, we devised an extraction platform to withdraw concentrated particle and cell samples composed of either specific particle sizes or mouse blood components after using the OSSAW, for the first time in a sessile-drop based device. The approach provides a separation purity above 80% according to flow cytometry. While these results are comparable to other separation techniques, including past SAW-based methods in Table 4.1, the many advantages of a surface acoustic wave-based approach—biocompatibility, fast fluidic actuation via large forces despite small scale, contact-free manipulation, on-chip integration, and flexibility in design—suggest ample opportunity for improving this approach for applications into the future.

With further work, this simple approach provides yet another acoustofluidic tool to deliver on the promise of true lab-on-a-chip diagnostics.

4.8 Appendix

4.8.1 Derivation of the Equation to Describe the OSSAW IDT Finger Pattern

The derivation of the equation to describe a spiral pattern for the OSSAW's interdigital transducer (IDT) finger electrodes is provided as follows, referring to Fig. 4.1(b). It is important to note here that, to our knowledge, this spiral structure is not represented by a defined spiral from the literature. It is neither an Archimedian spiral of $r = a + b\theta$, Fermat spiral $r = a\sqrt{\theta}$, nor a Doyle spiral $r = \theta + \sqrt{\theta}$.

Using polar coordinates (r, θ) with unit vectors $\mathbf{e}_r$ and $\mathbf{e}_\theta$ in a standard right-handed coordinate system with $\mathbf{e}_z$ pointing towards the reader, we seek to generate SAW from every point on the IDT to propagate into the inner $r \leq R_2$ region such that the SAW is always tangent to a circle of radius R_0. Due to circular symmetry, we restrict our consideration to one spiral finger, and enforce the condition $r(\theta = 0) = R_1$. The position vector for a point, B, somewhere on a finger of the spiral IDT as defined from the center, O, is $\mathbf{r} = r(\theta)\mathbf{e}_r$, with $r(\theta)$ indicating that the radial position r explicitly depends on the azimuthal angle θ. Note that $\mathbf{e}_r$ serves as the unit vector along the coordinate direction θ. Taking a time derivative of this vector produces the "velocity" of the point B,

$$\frac{d\mathbf{r}}{dt} = \dot{r}\,\mathbf{e}_r + r\dot{\theta}\,\mathbf{e}_\theta, \tag{4.7}$$

where the dots over r and θ are shorthand for a time derivative. Of course the point B is not moving, but this helpfully indicates the tangent direction to the IDT finger, $\mathbf{e}_t = \dot{\mathbf{r}}/|\dot{\mathbf{r}}|$. The inward-propagating SAW travels, therefore, from B in a direction perpendicular to $\mathbf{e}_t$, along $\mathbf{e}_{\mathrm{SAW}} = \mathbf{e}_z \times \mathbf{e}_t$. Explicitly writing $\mathbf{e}_{\mathrm{SAW}}$ in terms of the orthogonal unit vectors $\mathbf{e}_r$ and $\mathbf{e}_\theta$, we find

$$\mathbf{e}_{\mathrm{SAW}} = -\cos\gamma\,\mathbf{e}_r + \sin\gamma\,\mathbf{e}_\theta. \tag{4.8}$$

We may also write from eqn. (4.7)

$$\mathbf{e}_{\mathrm{SAW}} = \mathbf{e}_z \times \frac{\dot{\mathbf{r}}}{|\dot{\mathbf{r}}|} = \mathbf{e}_z \times \left(\frac{\dot{r}\mathbf{e}_r}{\sqrt{\dot{r}^2 + r^2\dot{\theta}^2}} + \frac{r\dot{\theta}\mathbf{e}_\theta}{\sqrt{\dot{r}^2 + r^2\dot{\theta}^2}} \right), \tag{4.9}$$

producing

$$\mathbf{e}_{\mathrm{SAW}} = \frac{-r\frac{d\theta}{dt}\mathbf{e}_r + \frac{dr}{d\theta}\frac{d\theta}{dt}\mathbf{e}_\theta}{\sqrt{\left(\frac{dr}{d\theta}\frac{d\theta}{dt}\right)^2 + r^2\left(\frac{d\theta}{dt}\right)^2}} = \frac{-r\mathbf{e}_r + r'\mathbf{e}_\theta}{\sqrt{(r')^2 + r^2}}, \tag{4.10}$$

by eliminating $d\theta/dt$ and defining $r' = dr/d\theta$.

Note that $\sin\gamma = \overline{OA}/\overline{OB} = R_0/r$. Using this and equating like terms from eqns. (4.8) and (4.10) along the $\mathbf{e}_\theta$ direction by using $\mathbf{e}_\theta \cdot \mathbf{e}_{\mathrm{SAW}}$ for both expressions, we find

$$\sin\gamma = \frac{r'}{\sqrt{(r')^2 + r^2}} = \frac{R_0}{r}, \tag{4.11}$$

producing, with a little algebra,

$$d\theta = \sqrt{\frac{1}{R_0^2} - \frac{1}{r^2}}\, dr. \tag{4.12}$$

Equation (4.12) is an ordinary differential equation that relates r and θ. We integrate it from $(r,\theta) = (R_1, 0)$ to (r,θ), producing

$$\begin{aligned} \theta &= \int_{R_1}^{r} \sqrt{\frac{1}{R_0^2} - \xi^{-2}}\, d\xi \\ &= \sqrt{\frac{r^2}{R_0^2} - 1} - \tan^{-1}\sqrt{\frac{r^2}{R_0^2} - 1} - \sqrt{\frac{R_1^2}{R_0^2} - 1} + \tan^{-1}\sqrt{\frac{R_1^2}{R_0^2} - 1}. \end{aligned} \tag{4.13}$$

This expression relating the radial coordinate r to the azimuthal coordinate θ may then be used to produce the spiral IDT of the OSSAW, as explained in the main text.

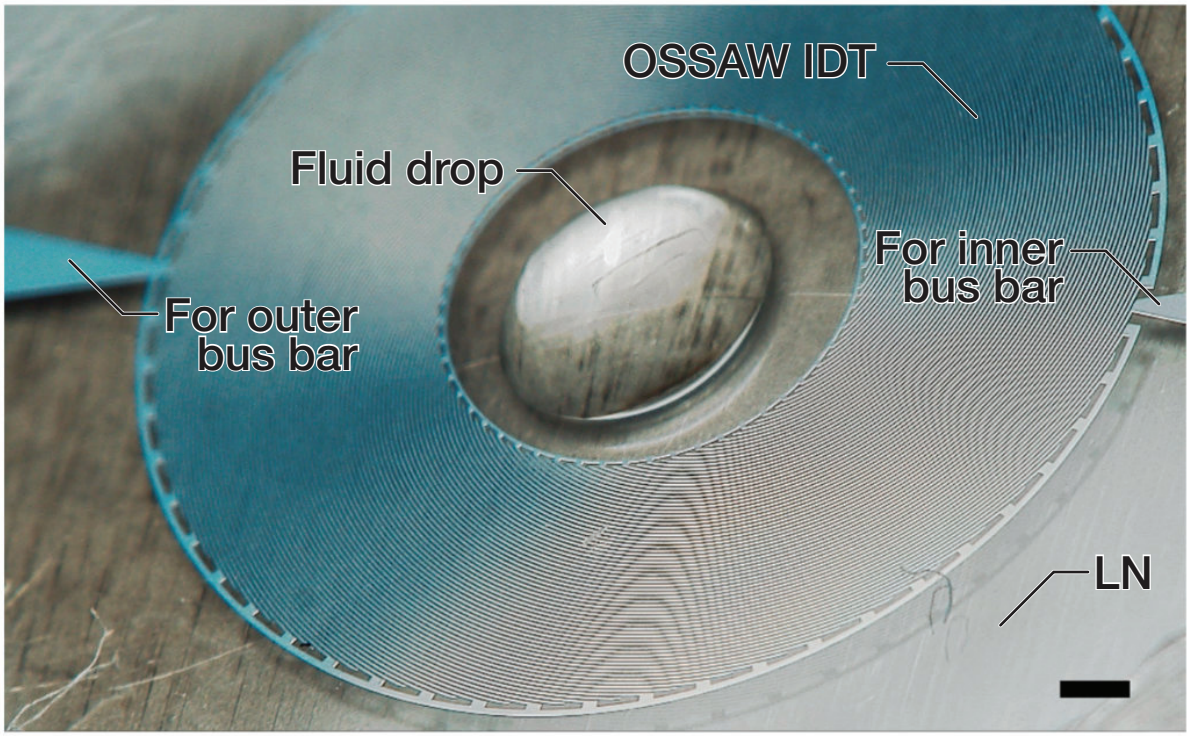

Figure 4.7: A 56.5 MHz OSSAW device with a microliter sessile drop on the inner circular region, showing the fingers and electrode connection to produce a suitable spiral SAW. The connection to the inner bus bar is via a single finger in this particular design to preserve the IDT design (at right: for inner bus bar), while the connection to the outer bus bar is at left. This device lacks the central extraction hole. (Scale bar: 0.5 mm.)

4.8.2 Extraction Platform with OSSAW

Fig. 4.7 is a photograph of a functioning OSSAW device with a deionized water droplet placed at the center, while Fig. 4.9 illustrates the basic procedure for fabricating and testing the OSSAW concentration and extraction devices.

4.8.3 Detailed Protocol for Antibody-stained Mouse Blood Cell Flow Cytometry

The separated portions of blood samples were first transferred into a 96-well, V-bottom plate (Sigma-Aldrich, St. Louis, MO, USA) with 100 $\mu\ell$ phosphate-buffered saline (PBS, 1X,

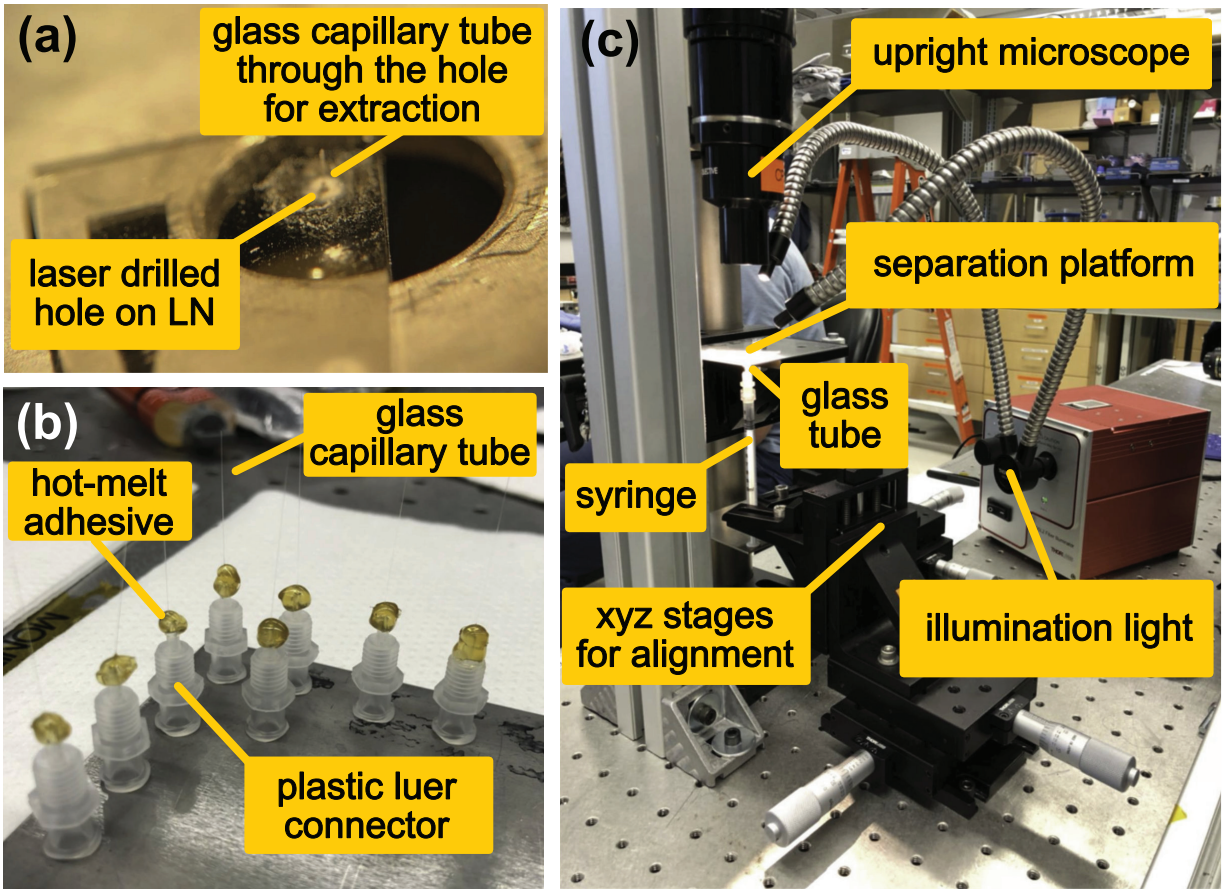

Figure 4.8: (a) An 80 μm outer diameter glass capillary tube is inserted into a 100 μm diameter hole in LN substrate for the extraction platform. (b) A luer lock connector is attached to the glass capillary tube using hot-melt adhesive to facilitate syringe attachment. (c) Image of the extraction platform, including lab-based components for system alignment.

pH 7.4, Thermo Fisher Scientific, Waltham, MA, USA) and 1.6% bovine serum albumin (BSA, Thermo Fisher Scientific, Waltham, MA, USA). Antibodies conjugated with red blood cells (RBC, FITC anti-mouse TER-119/Erythroid Cells Antibody, Biolegend, San Diego, CA, USA), white blood cells (WBC, Alexa Fluor® 594 anti-mouse CD45 Antibody, Biolegend, San Diego, CA, USA), and platelets (Alexa Fluor® 700 anti-mouse CD41 Antibody, Biolegend, San Diego, CA, USA) were added into subsequent wells, each with a volume of 0.5 $\mu\ell$, 0.1 $\mu\ell$, and 0.2 $\mu\ell$, respectively. The samples were then incubated at 4 °C for 30 min in the dark. The 96-well plate was centrifuged at 500g for 5 min. Supernatant was extracted from the centrifuged samples. Another 100 $\mu\ell$ fresh PBS with 1.6% BSA was added and resuspended in each well. The sample

was centrifuged and washed for a second time with the same procedure as described above.

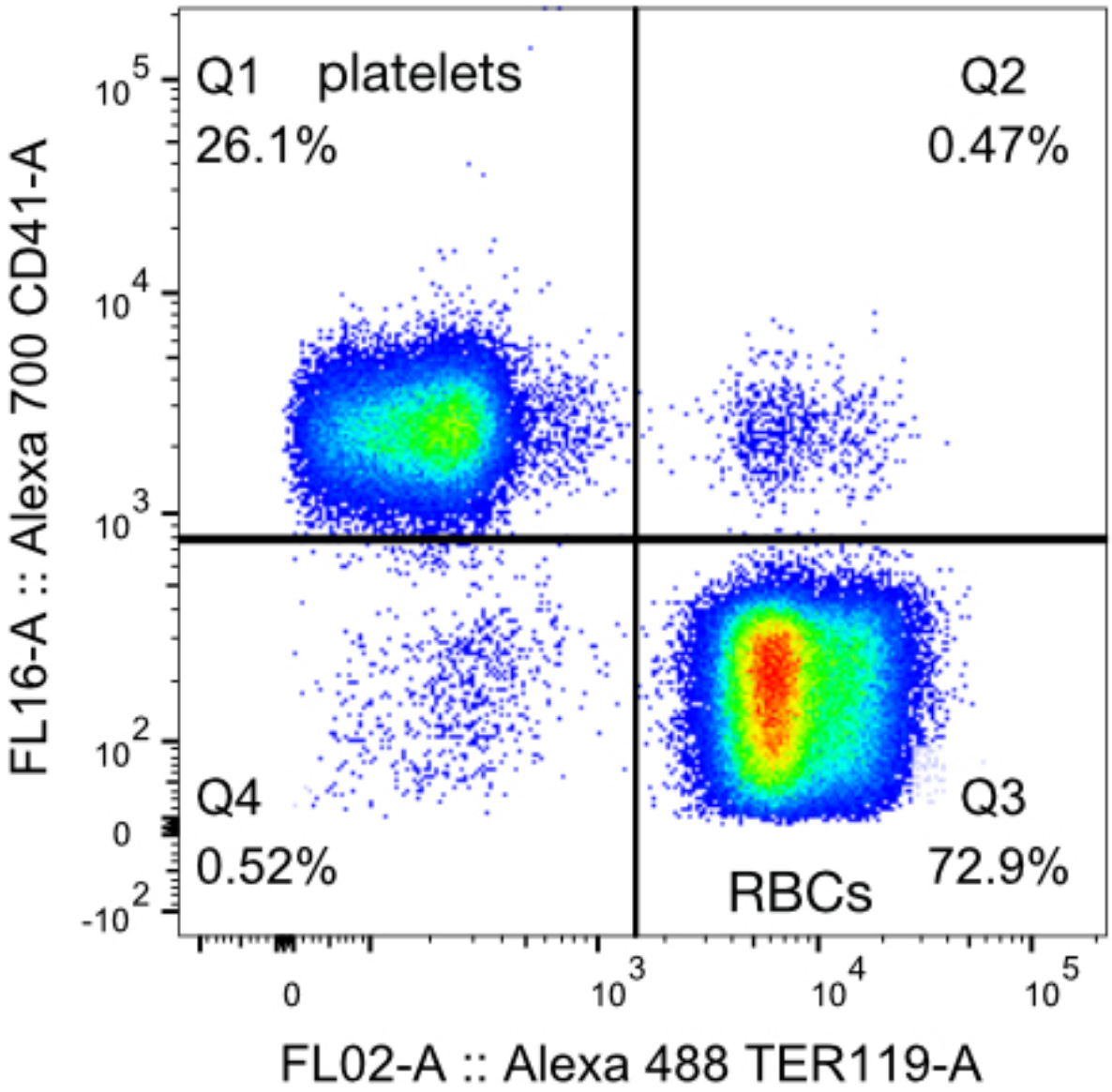

Figure 4.9: Flow cytometry on an unseparated (no OSSAW) blood sample that is otherwise identical to those used for OSSAW separation in Fig. 4.6. The composition of the sample is 72.9% RBC and 26.1% platelets. Though CD45 was used for WBC detection, the number of WBC in these 1 $\mu\ell$ blood samples was too low to justify their display here or in Fig. 4.6.

The samples were finally analyzed via flow cytometry (ZE5 Cell Analyzer, Bio-Rad, Hercules, CA, USA and Attune NxT Flow Cytometer, ThermoFisher, Waltham, MA, USA). The results of processing a blood sample without using the SAW is provided in Fig. **??** to provide a

basis for comparing the effects of OSSAW-driven cell separation. The plot omits CD45 used to stain WBC, as the number of WBCs in a 1 $\mu\ell$ sample is insufficient to produce statistically valid, quantifiable results via flow cytometry. The composition of the sample without OSSAW-driven separation is 72.9% RBC and 26.1% platelets.

4.9 Acknowledgement

We are grateful to the University of California and the NANO3 facility at UC San Diego for provision of funds and facilities in support of this work. This work was performed in part at the San Diego Nanotechnology Infrastructure (SDNI) of UCSD, a member of the National Nanotechnology Coordinated Infrastructure, which is supported by the National Science Foundation (Grant ECCS–1542148). The work presented here was generously supported by a research grant from the W.M. Keck Foundation. The authors are also grateful for the support of this work by the Office of Naval Research (via Grant 12368098), and substantial technical support by Polytec's staff in Irvine, CA and Waldbronn, Germany.

Chapter 5

MHz-order Surface Acoustic Wave Thruster for Underwater Silent Propulsion

5.1 Abstract

High frequency (MHz to GHz) surface acoustic waves (SAW) are able to generate intense fluid flow from the attenuation of acoustic radiation in viscous fluids as acoustic streaming. Though such flows are known to produce a force upon the fluid and an equivalent and opposing force upon the object producing the acoustic radiation, there is no convenient method for measuring this force. We describe a new method to accomplish this aim, noting the potential of these devices in providing essentially silent underwater propulsion by virtue of their use of the sound itself to generate fluid momentum flux. Our example employs a 40 MHz SAW device as a pendulum bob while immersed in a fluid, measuring a 1.5 mN propulsion force from an input power of 5 W power to the SAW device. Supporting details regarding the acoustic streaming profile via particle image velocimetry and an associated theoretical model are provided to aid determination of the propulsion force knowing the applied power and fluid characteristics. Finally, a simple model is provided to aid selection of the acoustic device size to maximize the propulsion

force per unit device area, a key figure of merit in underwater propulsion devices. Using this model, a maximum force of approximately 10 mN/cm^2 was obtained from 1 W input power using 40 MHz SAW in water, and producing a power efficiency of approximately 50%. Given the advantages of this technology in silent propulsion with such large efficiency and propulsion force per unit volume, it seems likely this method will be beneficial in propelling small autonomous submersibles.

5.2 Introduction

Efficient underwater propulsion has long been essential to the operation of autonomous underwater vehicles (AUV)[317]. Given the large size of most submersibles—compared to fish, bacteria, and other underwater entities—propellers are well-suited for this purpose, converting easily generated rotational motion into rectilinear underwater motion. However, the long wake propellers generate from cavitation and air entrainment, and the ample acoustic signal they radiate as a consequence are visually and acoustically detectable from long distances, to the extent that these signals can be used to identify the particular vehicle that produce them[39]. Furthermore, the associated machinery required to drive the propellers, whether from nuclear power, electrical motors, or more conventional internal combustion engines all generate detectable noise. As the size of submersibles decrease to the millimeter and smaller scales, electrical motors are all that remain to drive the propulsion mechanisms in submersibles, even though propellers are well-known to suffer from poor efficiency at such small scales, and furthermore produce torque steer that is difficult for a small craft to overcome[251]. Notwithstanding this issue,[208] recently demonstrated acoustic-induced propulsion by a lead zirconate titanate (PZT) piezoelectric element used to drive a propeller as an underwater piezoelectric thruster. But this combination combines the modest efficiency of the PZT element with the inefficient propeller to produce substantial energy loss and a low efficiency propulsion scheme. Waterjet propulsion was briefly introduced

in[39], although regardless of scale most waterjet devices still employ propellers, enclosing them within a tube instead of leaving them in the open flow with modest improvement in propulsive efficiency at small scales.

One of the key benefits of surface acoustic wave (SAW) devices is the ability to efficiently generate MHz to GHz-order acoustic waves that, because of these high frequencies, offer accelerations in excess of 10^8 m/s^2. Such large accelerations are not possible to be generated in any other known way, and are suitable for directly propelling fluids and particles in numerous micro to nano-scale fluidics applications[65,89,109]. The acoustic radiation and fluid streaming from such devices have been the subject of many publications, from fluid manipulation, particle/cell separation, colloid and nano-object patterning, to drug delivery and more[65].The attenuation of acoustic energy in viscous fluids along its propagation direction produces a momentum flux responsible for fluid motion: *acoustic streaming*. In particular, one-dimensional acoustic streaming has been investigated since at least 1948[97], and has come to be known as *Eckart streaming* from that early effort. In 1978, Lighthill described acoustic streaming from one-dimensional vibration of a point source in a viscous fluid[209].[79] further investigated SAW-induced acoustic streaming and improved Lighthill's model by considering a SAW vibration area instead of the point vibration source assumption to solve the singularity problem of Sir Lighthill's study, providing a useful tool in the analysis of microfluidics devices—but not without some work to make sense of the analysis within.

While acoustic streaming has been developed and utilized for many applications, using it as a propulsive force has only very rarely been considered in the literature, with qualitative results as more a curiosity than as a potentially beneficial mechanism. Most notably,[26] demonstrated notional movement of a toy boat on water using a small, immersed SAW device attached to the boat. But the underlying mechanism of SAW-induced propulsion was not examined in detail, and methods for measuring the force have not been provided in the literature. It is, however, possible to generate fluid propulsion directly from the attenuation of the ultrasound itself in beneficial

ways.[141] demonstrated an ultrasonic suction pump capable of delivering a maximum pressure of 20.6 kPa, remarkable as most acoustic pumping schemes are unable to produce more than a few tens of pascals of pressure and are therefore characterized as "flow generation devices" in racetrack flow schemes or the like instead[65,198].[247,463] performed fluid pumping at the nanometer scale, to produce 1 MPa pressure-driven flows, indicating a different operating mechanism that is yet to be fully explained.

Whatever the case, based on Newton's third law, the acoustic streaming-driven propulsion of a fluid from an acoustic device likewise produces an equivalent force upon that device in the opposite direction. The measurement of this force would benefit both potential applications of such devices in micro to nano-scale underwater propulsion and thruster devices, and also aid in characterization of the acoustic streaming generated by these devices, a phenomena that is today still only poorly understood. An aspect remarkably overlooked in the literature is the fact that because the attenuation of the sound is the mechanism for the generation of force in these devices, beyond about a meter from such a device there is no sound to be detected. Further, even if one were very close to such a device, the frequency of the sound would be far beyond the measurement range of standard underwater probes used today on ships. Finally, there is no electromagnetic energy radiated from such devices as the acoustic wave speed is far slower than the electromagnetic field, rendering the latter "quasistatic" and therefore unable to generate strong magnetic fields. Should such a propulsion method be feasible, it would be electromagnetically and acoustically silent.

Here we measure and model the propulsion force produced by a SAW device via acoustic wave attenuation and acoustic streaming in fluids of different viscosity. The SAW device is mounted as a simple pendulum while submerged in a fluid to quantify the propulsion force exerted upon it, using a simple force balance model that takes the orientation of the SAW device and other aspects into account. Next, a theoretical model based on acoustic radiation attenuation and force generation from the formation of an acoustic streaming jet from a finite acoustic source

is provided and used to verify the experimental results and connect the measured force to the observed acoustic streaming flow field. Finally, as an example of how the method may be used, simple straight interdigital transducer (IDT) SAW devices of different sizes are compared to determine how to identify what contributes to the important figure of merit in any proposed submersible thruster: the maximum propulsion force per unit device volume.

5.3 Fabrication Methods and Materials

We fabricated interdigital transducers (IDTs) on 500 μm thick, double-side polished 128° Y-rotated cut lithium niobate (LN, Jiaozuo Commercial FineWin Co., Ltd, Jiaozuo, Henan, China) for surface acoustic wave generation and propagation. A wavelength of $\lambda = 100$ μm was selected for an operating frequency of ~ 40 MHz (from $f = v/\lambda$) to define each IDT, comprised of twenty simple finger pairs with finger and gap widths of $\lambda/4$; frequencies less than 40 MHz for 500 μm thick LN will not produce Rayleigh SAW[65], and this is the reason for our choice of this frequency in this device. Standard UV photolithography (using AZ 1512 photoresist and AZ 300MIF developer, MicroChem, Westborough, MA, USA) was used alongside sputter deposition and lift-off processes to fabricate the 10 nm Cr / 1 μm Au IDT upon the LN substrate[65]. Dicing saw (Disco Automatic Dicing Saw 3220, Disco, Tokyo, Japan) was used to cut the entire wafer into small-size SAW device chips. A sinusoidal electric field was applied to the IDT at resonance using a signal generator (WF1967 multifunction generator, NF Corporation, Yokohama, Japan) and amplifier (ZHL–1–2W–S+, Mini-Circuits, Brooklyn, NY, USA) to generate the SAW. The actual voltage, current, and power across the device were measured using a digital storage oscilloscope (InfiniiVision 2000 X-Series, Keysight Technologies, Santa Rosa, CA).

To prepare the device for testing as a pendulum, two 50-mm segments of enameled wire (P155, 0.09-mm diameter enameled wire, Remington Industries, Johnsburg, IL, USA) were used to both deliver the electric signal and serve as pendulum strings to the device as the pendulum

bob. Insulation was removed at both ends and one end of each wire was soldered (2.2 % Flux Core Solder Wire, SMDSW.202, Chipquik, Niagara Falls, NY, USA) using appropriate flux (zinc chloride flux, Harris, Mason, Ohio, USA) to the IDT bus bar electrodes at 340°C.

5.4 Experimental Methods and Results

5.4.1 Quantifying the SAW Propulsion Force with a Simple Pendulum

In spite of ample research on SAW-induced acoustic streaming reported in the literature over the years, the ability of acoustic streaming to produce a reaction force upon the device that is the source of the acoustic streaming has not been investigated in detail. We present a simple force balance method by defining the SAW device as the bob in a pendulum while immersed in a working fluid. The angle of deflection of this pendulum can be used to quantify the force generated by acoustic streaming from the SAW device.

A SAW device was suspended from the top of a fluid tank and immersed in the fluid (*see* Figure 5.1). Acoustic streaming from the SAW produces a force that is difficult to measure. However, by Newton's third law, the reaction force upon the SAW device is equivalent to this force and may be calculated from the equilibrium angle θ of the pendulum,

$$F_p = \frac{\sin(\theta)}{\cos(\gamma+\theta)} \times (F_g - F_b), \tag{5.1}$$

where $\eta = \sin^{-1}(c/V_R) \approx 23^\circ$ is the Rayleigh angle, c is the sound velocity in the liquid, and V_R is the Rayleigh SAW velocity on the LN substrate. Further, ξ is the angle between the fluid surface and the substrate, $\gamma = 90^\circ - \eta - \xi$, F_p is the propulsion force, F_g is the SAW device weight, and F_b is the buoyancy force, respectively. A detailed derivation can be found in Appendix A.

The setup offers a simple and quick approach to quantify a traditionally difficult quantity to measure: the force generated by a SAW device via acoustic streaming. Measuring the pendulum

angle θ and the chip orientation angle ξ from the side, with knowledge of the chip weight F_g and buoyancy F_b, the propulsion force exerted on the chip can be simply obtained via eqn. (5.1).

5.4.2 Making use of the SAW Propulsion Force Pendulum Method in Modeling and Measuring Acoustic Streaming

The Basic Theory Underpinning SAW-based Acoustic Streaming Propulsion

It is now possible to construct a theoretical model of the acoustic radiation and streaming from SAW generated upon a LN device, making use of the information provided by the pendulum force balancing method. Based upon Newton's third law, the total acoustic radiation force from the device and imposed upon the fluid is the same as the propulsion force that the fluid exerts on the device. The latter is measured in our experiments, and the former can be estimated based on the fluid flow produced in acoustic streaming.

Acoustic waves propagating through a viscous medium causes acoustic streaming within it as a nonlinear phenomenon dependent upon viscous attenuation. From Lighthill's analysis of acoustic streaming in 1978[209], the net force per unit volume produced by acoustic streaming due to attenuation is $F = \beta\rho_0\bar{u^2}$. This results from the Reynolds stress component $\rho_0\bar{u^2}$ with an attenuation length β^{-1}. Another useful way of writing the net force per unit volume F, is $F = \beta c^{-1} I$, where the intensity (energy flux) I is a vector of magnitude $c\rho_0\bar{u^2}$ directed along the sound propagation direction[209], where c is the speed of sound in the fluid. This leaves the force F as a function of the acoustic intensity.

In a narrow beam, at a distance X from an acoustic source emitting power P, the intensity integrated across the area of the beam has magnitude

$$I(X) = Pe^{-\beta X}, \tag{5.2}$$

equal to the power remaining in the beam[209]. The force produced by attenuation of the acoustic

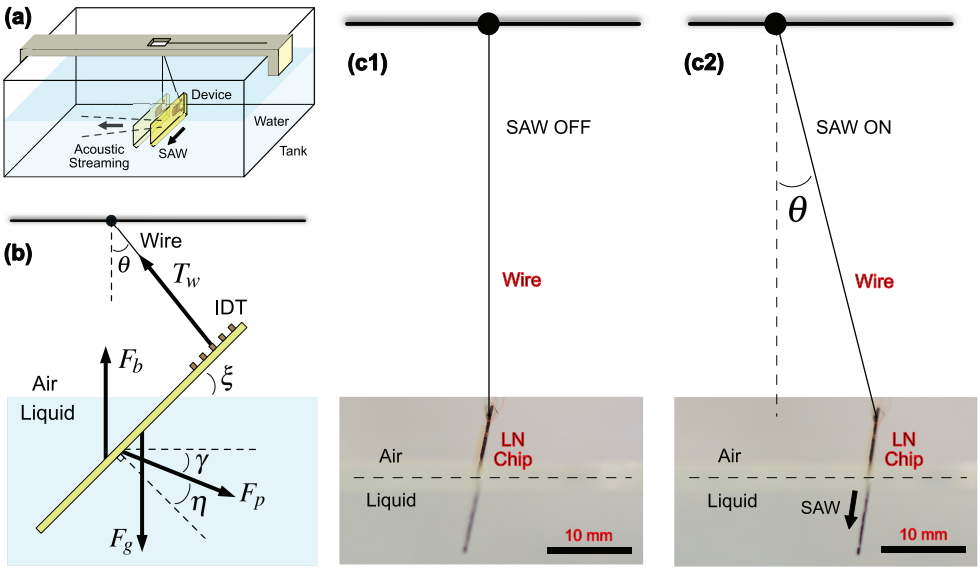

Figure 5.1: The pendulum force balancing method for measuring SAW propulsion forces via acoustic streaming, illustrated in (a) overview with a glass tank filled with the immersion fluid. A SAW device is suspended as the bob of a pendulum from a 3D-printed fixture at the top using the wires to connect the IDT of the SAW device as the pendulum arm. Taking (b) into account the tilted configuration of the SAW device, and the Rayleigh angle η of the acoustic wave propagating from it into the fluid as it swings to an angle θ, an appropriate force balance may be formed. Images taken from the side of the setup (c) of a SAW device (c1) before and (c2) after activating the SAW indicates its deflection angle θ as a pendulum. The edge of the LN chip is marked black for clarity.

wave per unit length is obtained by integrating the force per unit volume across the area of the beam,

$$F(X) = \beta c^{-1} I(X) = \beta c^{-1} P e^{-\beta X}. \tag{5.3}$$

The total force is the integration of this value along the entire length of the acoustic wave propagation into the fluid,

$$F_{tot} = \int_0^\infty F(X) dX = \int_0^\infty \beta c^{-1} P e^{-\beta X} dX = c^{-1} P, \tag{5.4}$$

representing a rate of momentum delivery equal to c^{-1} times the rate of energy delivery. Notice that changing the rate of attenuation β does not change the total force applied, although it greatly alters its distribution (5.3) along the beam.

Based on this result, the total acoustic force only depends upon the speed of sound, c, in the fluid and the input power P. Notably, the force is independent of the value of the fluid viscosity. Therefore, defining a dimensionless parameter $F_{tot}c/P$ may serve to indicate how well the device transforms input power into an output power as a propulsive force times the speed of sound.

Measurements of the SAW-driven Acoustic Streaming Propulsion Force

Propulsion forces generated by ~ 40 MHz SAW were investigated using a range of applied power and fluid viscosities. The nondimensional propulsion force $F_{tot}c/P_0$ is plotted in Fig. 5.2(a) with respect to the nondimensionalized input power P/P_0, where $P_0 = 1$ W is a nominal reference value. The speed of sound in a water and glycerol mixture may be represented by

$$c = \sqrt{\frac{\kappa}{\rho}}, \tag{5.5}$$

where κ and ρ are the bulk modulus and density of the water and glycerol mixture, respectively[49,105,340,346]. As shown in Fig. 5.2(a), the nondimensional propulsion force is linearly correlated to the nondimensional applied power. It is likewise independent of the fluid viscosity, as defined using water mixed with glycerol at the volume ratios 1:0, 0.9:0.1, 0.7:0.3, and 0.5:0.5. The quality of the linear fit shows the utility of the theory in predicting the power transmission. However, the propulsion forces were smaller than expected in a 50/50 water/glycerol mix when the input power exceeds ~ 4 W, indicating that changes in the fluid viscosity affects the propulsion force beyond its effects on the sound velocity.

As shown in eqn. (5.4), the output propulsion power generated by the SAW thruster is predicted to be $P = Fc$. The electromechanical efficiency of the SAW propulsion thruster can be defined as the ratio of output power Fc to the input power, which is plotted in Fig. 5.2(b). The efficiency ranges from 40% to 60%, independent of input power, and is only weakly dependent on the fluid viscosity. Overall, SAW thruster propulsion is rather efficient compared to typical propellors, especially at smaller scales[22].

5.4.3 Visualization of Acoustic Streaming Responsible for the SAW Propulsion Mechanism

As the force on the SAW thruster device is produced entirely by the surrounding fluid, the visualization of the SAW-induced fluid motion near the LN chip will help elucidate the SAW propulsion mechanism. Although the acoustic radiation force that produces the propulsion force can not be visualized, the acoustic streaming that causes it can be clearly seen via particle image velocimetry.

To reduce the complexity of visualizing the region of interest where fluid motion occurs, the SAW thruster device was mounted on a 3D-printed stand at a 23° incline as shown in Figure 5.3(a). The inclined plane compensates for the leaky SAW Rayleigh angle so that the acoustic wave propagating in the fluid does so horizontally. Fluorescent particles (43 μm polyethylene,

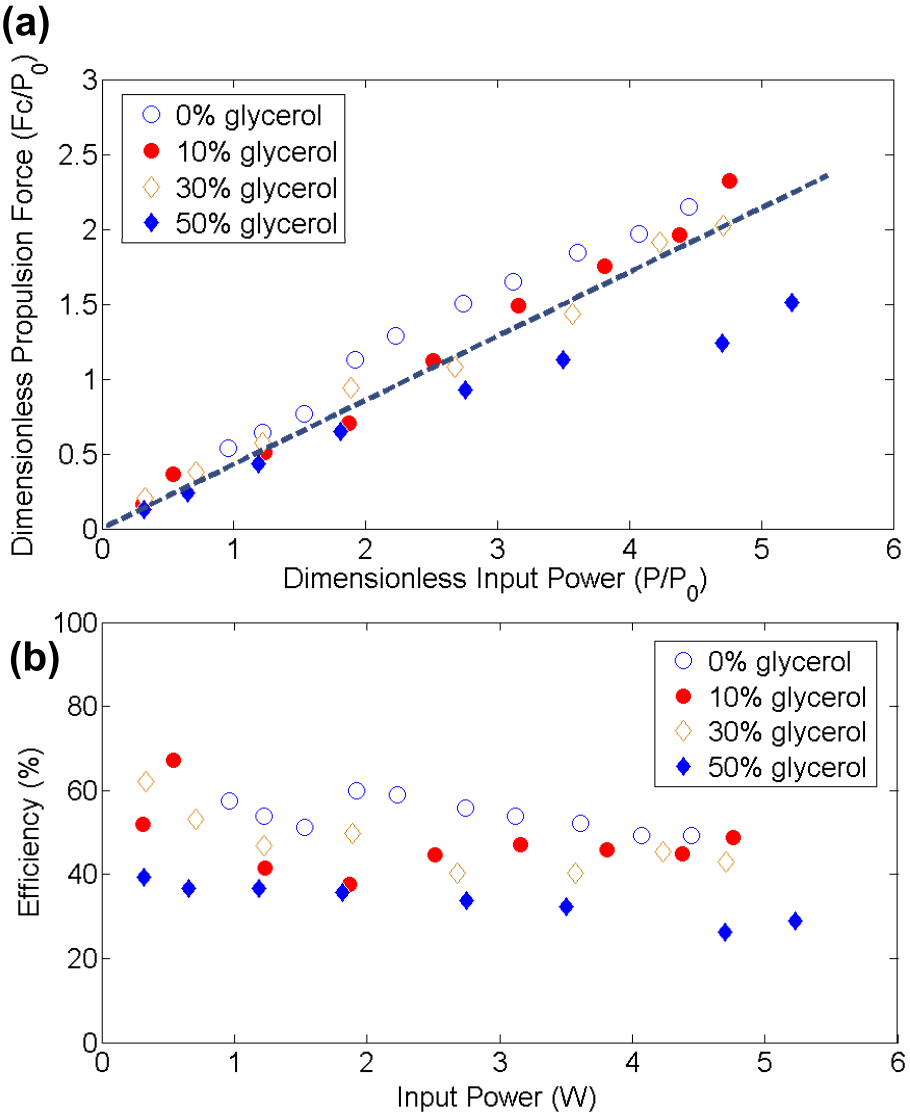

Figure 5.2: (a) Dimensionless propulsion force versus input power in water/glycerol solutions, at 0%, 10%, 30%, and 50% volume of glycerol with the remainder water volume, indicating a linear relationship between the dimensionless propulsion force and input power regardless of the fluid viscosity. (b) The electromechanical efficiency of the SAW thruster for propulsion is about 40%-60% depending upon the applied input power, with greater efficiency in lower viscosity media.

Cospheric, Santa Barbara, CA, USA) were added to the fluid to track the corresponding velocity field. The particle motion was recorded by high-speed camera (FASTCAM Mini UX100, Photron, Tokyo, Japan) and microscope (K2/CF–1, Infinity, Boulder, CO, USA) and analyzed to produce flow speed measurements (PIVlab in MATLAB, Mathworks, Natick, MA USA).]

For 90% deionized water and 10% glycerol, intensity maps of PIV analysis show the velocity field of acoustic streaming with different applied input power (see Figure 5.3b). Higher power produces faster acoustic streaming flow, while the width of the acoustic streaming-induced jet is similar to the IDT aperture. Conserving the fluid momentum, the change of fluid momentum in forming the acoustic streaming jet comes from the output power such that

$$P\eta \sim \rho h a v^2, \tag{5.6}$$

where P is the applied input power, η is the electromechanical transmission efficiency, ρ is the fluid density, a is both the IDT aperture and the effective acoustic streaming width, v is the streaming velocity, and h is the depth of acoustic streaming. The relationship $P \sim v^2$ fits well with the experimental results shown in Fig. 5.3c.

5.4.4 Using the SAW Propulsion Force Measurement Method to Improve the Propulsion Efficiency of the SAW Device

Another crucial aspect for practical underwater propulsion applications is to maximize the propulsion force for a given propulsor size. Using our simple pendulum force measurement method, the propulsion force these devices produce in water is plotted as a function of input power.

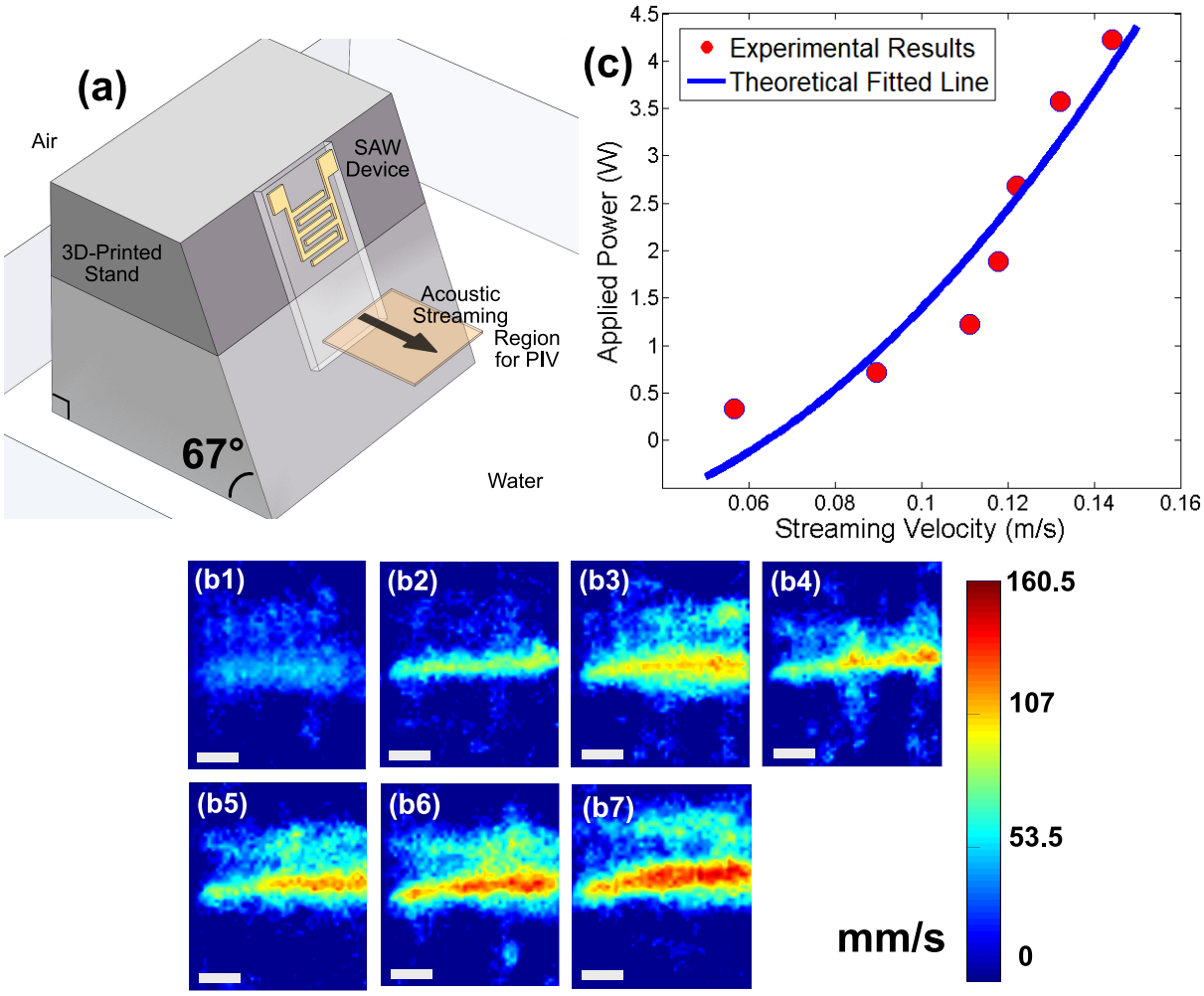

Figure 5.3: (a) Mounting the SAW device to visualize the acoustic streaming velocity field that it generates. (b) With the SAW device at left, a top view of the PIV-derived acoustic streaming flow profile in 90% water / 10% glycerol indicates acoustic streaming increases as the applied power is increased from (b1) 330 mW, (b2) 710 mW, (b3) 1.22 W, (b4) 1.89 W, (b5) 2.68 W, (b6) 3.57 W, and (b7) 4.23 W, respectively. Scale bar: 2 mm. This produces a maximum fluid flow speed in the acoustic streaming jet as (c) plotted with respect to the applied power, with a fitted line based on the theoretical model of the acoustic streaming phenomena.

Propulsion Force Measurement using Three Specific SAW Device Designs

To investigate the relationship between the size of the SAW device propulsion force and the propulsion force, we fabricated three different SAW device designs with sizes from ~ 10 mm^2 to ~ 170 mm^2, as depicted in Fig. 5.4(a), tabulating the SAW device width W, IDT aperture a, IDT length l, and SAW propagation length L in Table 5.1. Using our simple pendulum balancing method, we perform propulsion force measurements using a range different applied powers with these devices (see Fig. 5.4).

Table 5.1: Dimensions for three different SAW devices. Unit: mm.

	W	a	l	L
1	11.85	4.50	9.00	5.00
2	5.65	4.50	4.55	3.00
3	3.70	0.38	3.00	3.00

From the experimental results shown in Fig. 5.4(b), the propulsion forces are linearly dependent upon the input power across the different SAW device designs, confirming our theoretical result in eqn. (5.4). Comparing the results of designs 1 and 2, the propulsion force is of the same order of magnitude, despite significant differences in the chip width W, IDT length l, and SAW propagation length L. The two designs, however, use the same IDT aperture a. With a greater SAW propagation length L in design 1, SAW tends to transfer more energy to the fluid in this design and consequently generates a slightly larger propulsion force than design 2. The propulsion forces from designs 2 and 3 are significantly different, despite the similarity of their dimensions W, l, and L, because the IDT aperture a is quite different. In particular, design 3, with its small ~ 10 mm^2 size, suggests it is indeed possible to fabricate a SAW thruster for microscale object propulsion.

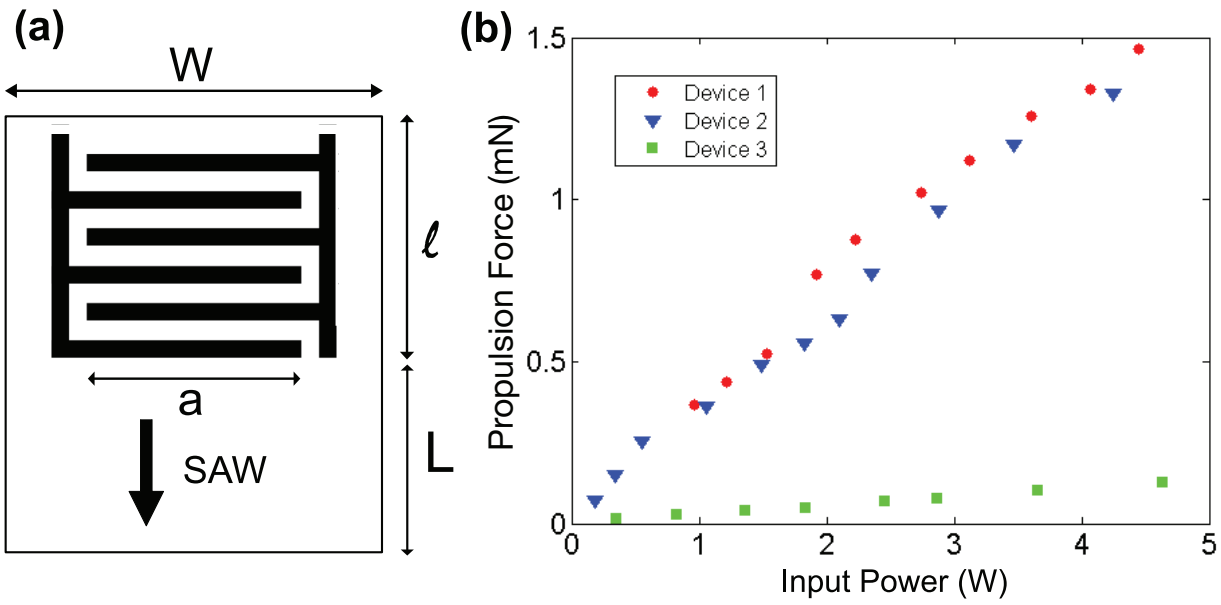

Figure 5.4: (a) The layout of the basic SAW device design in our trials using the pendulum force balance method. We denote the chip width, the IDT aperture, the IDT length, and the chip length for SAW propagation and attenuation in fluid as W, a, l, and L, respectively. We only consider SAW propagated towards the bottom of the chip, as the SAW propagating upward from the IDT is absorbed by an absorber mounted at the top edge of the chip. Three versions of this design produce (b) substantially different propulsion forces for an input power from 0 to 5 W.

Model to Maximize the Propulsion Force Density: the Propulsion Force per unit Device Volume

The experimental results from a small selection of different SAW chip sizes and designs indicate there are significant differences in the propulsion force per unit chip volume at the same applied power. We discuss and present a calculation method here to improve the SAW device configuration and maximize the propulsion force density, in other words, the propulsion force per unit device volume.

We consider a straight IDT device with dimensions as depicted in Fig. 5.4(a). The IDT aperture a directly affects the propulsion force: increasing it increases the force as shown in Fig. 5.4(b). Presuming the chip width W is chosen for a given application, the aperture should be maximized and therefore be as close as W as possible, but due consideration should be also given to the potentially adverse effects of having high capacitance in wide IDT designs[365] where a is large. Choosing to make the device smaller such that both W and a are small and the capacitance is not a problem is beneficial to increase the propulsion force per unit device volume. The IDT length l depends on the frequency and the number of finger pairs that form the IDT. With a specific SAW resonance frequency in mind, the finger width and the gap between two fingers are each defined as a quarter of wavelength in this elementary design. More sophisticated designs are possible, although the basic principle of defining the IDT geometry from the selected wavelength still applies. As for the number of finger pairs, one typically makes a balanced choice between the desired quality factor and the coupling performance of the substrate[65]. Taking the most common 128° Y-rotated cut LN as substrate for example, the ideal number of finger pairs is 21 with a bandwidth of 0.05. Thus, the IDT length l is mainly determined by the device properties and electromechanical effects. Finally, the length of the device over which the SAW is allowed to propagate, L, depends on the need to attenuate the SAW without reflection from the edge of the device. The energy absorbed in attenuation of this SAW generates sound propagating in the adjacent fluid, and that leads to acoustic streaming. Choosing the length L requires slightly more

effort than for a, W, or l.

We denote the propulsion force per aperture width as F_{tot} if the SAW radiation is entirely transferred to the fluid. Based on eqn. (5.4), the propulsion force depends only on the applied power if the sound velocity in the fluid is constant. Though we can apply a greater power to produce a larger propulsion force, we instead investigate the maximum propulsion-to-surface-area efficiency based on the SAW chip size while using the same input power. We thus assume F_{tot} to be constant as we explore the relationship between the propulsion force and the SAW propagation length L.

Due to the attenuation effect of the SAW propagation across the chip, the actual propulsion force per aperture width is

$$F_p = F_{tot}(1 - e^{-\alpha L}), \tag{5.7}$$

where $1/\alpha = [(\rho_f c)/(\rho_s v_s \lambda_{SAW})]^{-1}$ is the attenuation length for SAW on a substrate coupled with a fluid[79]. The variables ρ_f, c, ρ_s, v_s, λ_{SAW} are the fluid density, sound velocity in the fluid, substrate density, SAW velocity on substrate, and SAW wavelength respectively. Thus, the propulsion force for a SAW device per device chip area, A, can be written as

$$\frac{F_p}{A} = \frac{F_{tot}(1 - e^{-\alpha L})a}{W(l + L)} = \frac{Fa}{W} f(L), \tag{5.8}$$

which is maximized by setting the derivative $f'(L) = 0$, producing the following for the appropriate value of l:

$$e^{\alpha L} - \alpha L = \alpha l + 1. \tag{5.9}$$

The optimal choice for L has been calculated and provided in Table 5.1 for the reader's convenience. With a better understanding of the SAW-induced propulsion mechanism in hand, we now discuss the effects of the device size and IDT configuration on the propulsion force, aiming to provide a method for improving the propulsion force density of the device for acoustic-induced

thruster designs.

5.5 Discussion

The purpose of this work is to both provide a simple method for measuring the force generated by acoustic streaming and to present a possible means to silent underwater propulsion for small to microscale submersible craft. To this end, we considered the effects of viscosity on the acoustic streaming, and confirmed that indeed the force generated by the SAW device is independent of the fluid viscosity. We also considered a few simple SAW device designs to illustrate how the force balance method can help to identify what aspects of the design is most important in improving its potential use as a small thrust producing device.

The pendulum force balancing method quantifies the propulsion force exerted onto the SAW device in a simple way.[26] tested the SAW propulsion force at a lower frequency by measuring the drag force of a small toy vessel to which the device was attached. But this complicates the measurement of the force by also including the effect of hull drag from the vessel. At a higher frequency of 40 MHz, we also ensured we obtained Rayleigh SAW in a similar 0.5-mm thick LN wafer, which is not possible when using frequencies lower than this. A shorter acoustic attenuation length is an added benefit in seeking a miniaturized propulsor. Producing approximately 1.5 mN with 5 W input power in a 25 mm^3 device volume, or 60 kN/m^3 propulsion force density, the force on first glance appears small but is significant considering its volume. The magnitude of the propulsion force may furthermore be easily increased by multiplexing the devices. Altogether, compared to ultrasonic thrusters using PZT[7,382], the use of SAW via LN devices appears to provide stronger propulsion effects.

Next, a theoretical model of acoustic wave attenuation in the production of acoustic streaming and consequent fluid flow explains both the propulsion force measurement results and silent thruster performance. By offering an efficiency of 40% to 60%, the SAW thruster

device appears to possess a far higher efficiency than ultrasonic thrusters ($3.9\% \sim 33.6\%$)[7] and is comparable with propeller-driven thrusters ($\sim 50\%$)[39,96]. With a linear relationship between the propulsion force and input power, and because of the absence of hysteresis in LN, the efficiency will remain constant rather than decrease as the input power increases, as shown in Fig. 5.2(b) from 0 to 5 W, attractive especially at higher power levels where other methods tend to have reduced efficiency.

Finally, a few SAW devices of different designs and configurations were considered as a cursory application of the pendulum force balance method in discerning what is important to maximizing the output force, and the key combination of a large SAW aperture and a sufficiently long attenuation area beyond the IDT were found to be crucial in maximizing the device performance.

In future research work, different SAW frequencies and IDT designs could be considered using this approach in order to both seek improved thruster performance and to determine how these devices generate the acoustic streaming flows that are known to be so useful today.[79] discussed, in particular, the effect of frequency on acoustic streaming, showing that the choice of frequency is crucial in the design of micro/nano-scale devices employing acoustic streaming. For SAW-induced propulsion, the effects of frequency may also be a major aspect to optimize, particularly if different fluids and viscosities are anticipated. The broader exploration of viscous fluids may also provide additional information on the acoustic streaming phenomena. Finally, in the effort to devise practical and functional SAW-induced silent propulsion devices, integration of control and driver circuitry will be necessary in the device to facilitate its easy introduction, on par with the simplicity seen in propeller-based propulsion.

5.6 Appendix

5.6.1 Derivation of SAW Propulsion Force based on Pendulum Equilibrium

According to a force balance, the component of force in the horizontal and vertical directions are

$$\begin{aligned} T_w \cos(90^\circ - \gamma - \theta) + F_b \cos(90^\circ - \gamma) &= F_p + F_g \cos(90^\circ - \gamma) \\ T_w \sin(90^\circ - \gamma - \theta) + F_b \sin(90^\circ - \gamma) &= F_g \sin(90^\circ - \gamma) \end{aligned} \tag{5.10}$$

where T_w is the tension from the wire, F_b is the buoyancy force on the substrate, γ is the angle between the propulsive force and the water surface, θ is the angle of the wire relative to the vertical direction, and F_p is the propulsion force produced by the SAW device. Combining the two equations (5.10), the propulsion force is found to be

$$F = \frac{\sin\theta}{\cos(\gamma+\theta)}(mg - F_b). \tag{5.11}$$

The calculated propulsion force is plotted with different input power and fluid media in Fig. 5.5.

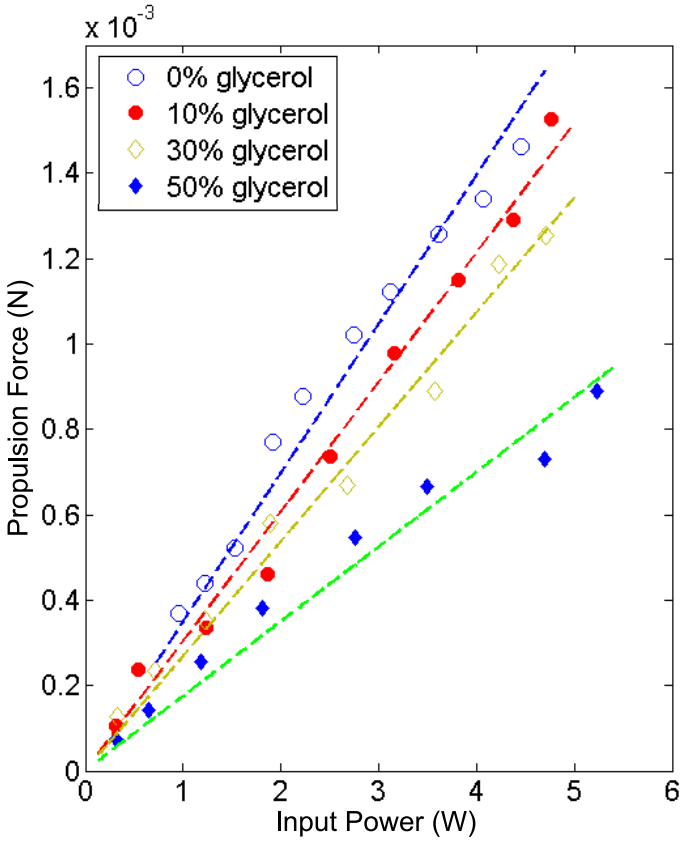

Figure 5.5: SAW propulsion force based on input power within different fluid media, indicating different propulsion force under various input power and fluid viscocity.

Chapter 6

Fabrication of Nanoheight Channels Incorporating Surface Acoustic Wave Actuation via Lithium Niobate for Acoustic Nanofluidics

6.1 Abstract

Controlled nanoscale manipulation of fluids is known to be exceptionally difficult due to the dominance of surface and viscous forces. Megahertz-order surface acoustic wave (SAW) devices generate tremendous acceleration on their surface, up to 108 m/s^2, in turn responsible for many of the observed effects that have come to define acoustofluidics: acoustic streaming and acoustic radiation forces. These effects have been used for particle, cell, and fluid manipulation at the microscale, although more recently SAW has been used to produce similar phenomena at the nanoscale through an entirely different set of mechanisms. Controllable nanoscale fluid manipulation offers a broad range of opportunities in ultrafast fluid pumping and biomacromolecule

dynamics useful for physical and biological applications. Here, we demonstrate nanoscale-height channel fabrication via room-temperature lithium niobate (LN) bonding integrated with a SAW device. We describe the entire experimental process including nano-height channel fabrication via dry etching, plasma-activated bonding on lithium niobate, the appropriate optical setup for subsequent imaging, and SAW actuation. We show representative results for fluid capillary filling and fluid draining in a nanoscale channel induced by SAW. This procedure offers a practical protocol for nanoscale channel fabrication and integration with SAW devices useful to build upon for future nanofluidics applications.

6.2 Introduction

Controllable nanoscale fluid transport in nanochannels—nanofluidics[99]—occurs on the same length scales as most biological macromolecules, and is promising for biological analysis and sensing, medical diagnosis, and material processing. Various designs and simulations have been developed in nanofluidics to manipulate fluids and particle suspensions based on temperature gradients[219], Coulomb dragging[421], surface waves[163], static electric fields[123,174,319], and thermophoresis[100] over the last fifteen years. Recently, SAW has been shown, both experimentally[247] and computationally[384], to produce nanoscale fluid pumping and draining with sufficient acoustic pressure to overcome the dominance of surface and viscous forces that otherwise prevent effective fluid transport in nanochannels. The key benefit of acoustic streaming is its ability to drive useful flow in nanostructures without concern over the details of the chemistry of the fluid or particle suspension, making devices that utilize this technique immediately useful in biological analysis, sensing, and other physicochemical applications.

Fabrication of SAW-integrated nanofluidic devices requires fabrication of the electrodes, the interdigital transducer (IDT), on a piezoelectric substrate, lithium niobate[252], to facilitate generating the SAW. Reactive ion etching (RIE) is used to form a nanoscale depression in a

separate LN piece, and LN-LN bonding of the two pieces produces a useful nanochannel. The fabrication process for SAW devices has been presented in many publications, whether using normal or lift-off ultraviolet photolithography alongside metal sputter or evaporation deposition[65]. For the LN RIE process to etch a channel in a specific shape, the effects on the etch rate and the channel's final surface roughness from choosing different LN orientations, mask materials, gas flow, and plasma power have been investigated[153,166,307,368,439]. Plasma surface activation has been used to significantly increase surface energy and hence improve the strength of bonding in oxides such as LN[45,152,297,400]. It is likewise possible to heterogeneously bond LN with other oxides, such as SiO_2 (glass) via a two-step plasma activated bonding method[450]. Room-temperature LN-LN bonding, in particular, has been investigated using different cleaning and surface activation treatments[408].

Here, we describe in detail the process to fabricate 40 MHz SAW-integrated 100-nm height nanochannels, often called nanoslit channels (Figure 1A). Effective fluid capillary filling and fluid draining by SAW actuation demonstrates the validity of both nanoslit fabrication and SAW performance in such a nanoscale channel. Our approach offers a nano-acoustofluidic system enabling investigation of a variety of physical problems and biological applications.

6.3 Protocol

6.3.1 Nano-Height Channel Mask Preparation

1.1. Photolithography: Using a LN wafer and a pattern describing the desired shape of the nanoscale depressions to be made into channels via normal photolithography and lift-off procedures. These depressions will become nanoheight channels upon wafer bonding in a later step.

NOTE: The lateral dimensions of the nanoscale depressions are microscale in this protocol. Electron beam or He/Ne ion beam lithography can be used to fabricate channels with nanoscale

lateral dimensions; Ga+-based ion beam lithography causes swelling and uneven substrate profiles. The orientation of the two LN wafers should match, otherwise, thermal stress may cause the wafers or the bond between them to fail.

1.2. Sputter deposition to protect regions from dry etching: Place wafer into the sputter deposition system. Draw down the chamber vacuum to 5×10^{-6} mTorr, allow Ar to flow at 2.5 mTorr, and sputter Cr at 200 W to produce a 400-nm thick sacrificial mask where reactive ion etching will be prevented when used in part 3 below.

1.3. Lift-off: Transfer the wafer into a beaker with sufficient acetone to completely immerse the wafer. Sonicate at medium intensity for 10 min. Rinse with DI water and dry the wafer with dry N_2 flow.

1.4. Dicing: Use a dicing saw to dice the entire wafer into individual chips with (typically) one nanoslit pattern per chip.

NOTE: The protocol can be paused here.

6.3.2 Nano-height Channel Fabrication

2.1. Reactive ion etching (RIE): Use RIE to etch nanoscale depressions into the uncovered regions of the LN substrate. Regions left covered by sacrificial Cr will be protected from etching. Set the RIE power to 200 W, heat the chamber to 50 °C, draw down the chamber vacuum to 20 mTorr, set the SF_6 flow rate to 10 sccm, and etch for 20 min to produce a 120-nm deep nanoslit in LN.

2.2. Hole drilling for channel inlets and outlets: Attach an etched LN chip to a small steel plate with double-sided tape. Use double-sided tape again to attach the plate to the bottom of a petri dish. The petri dish should be large enough to permit complete immersion of the LN chip and steel plate. Fill the petri dish with water to fully immerse the chip. Attach a 0.5-mm diameter diamond drill bit to a drill press, and drill at a high speed of at least 10,000 rpm to machine the desired inlets and outlets. Drilling through a 0.5 mm thick substrate should take about ten to

fifteen seconds (Figure 1B).

NOTE: Immersion while drilling prevents excessive local heating and particulate jamming at the drill site. Other types of drill bits are unlikely to work, and hand drilling is not possible at any speed to our knowledge. Drill bit rotation speeds of 10,000 rpm or greater are recommended to avoid shattering the LN.

2.3. Cr wet etching: Use a diamond tip engraving pen to clearly mark the flat, unetched face of the drilled LN so that you can keep track of which side the nanoheight channel is located in the remaining steps. Sonicate chips in Cr etchant.

NOTE: The protocol can be paused here. It is exceedingly difficult to determine which side of the LN chip has the etched nanoscale depression after the Cr is removed. The sonication time depends upon the etching rate and the Cr mask thickness.

6.3.3 Room-temperature Plasma Activated Bonding

3.1. Solvent cleaning LN chips: Collect chip pairs—one SAW device (fabricated by normal photolithography, sputter deposition, and lift-off procedures) and one etched nanoscale depression chip—together to prepare them for bonding. Immerse the chip pairs in a beaker of acetone placed in a sonication bath and sonicate for 2 min. Transfer the chips to methanol and sonicate for 1 min. Transfer chips to DI water.

3.2. Piranha cleaning: prepare piranha acid in a glass beaker in a well-ventilated hood, dedicated to the use of acid, by adding H_2O_2 (30% in water) to H_2SO_4 (96%) at a ratio of 1:3. Place all chips in a Teflon holder. Place the holder in the beaker and immerse all chips into the piranha solution for 10 min, then rinse the chips and holder sequentially in two separate DI water baths. Dry the chips with dry N_2 and immediately transfer them into oxygen (O_2) plasma activation equipment, keeping them covered during handling to avoid contamination.

CAUTION: Piranha solutions are highly corrosive, are strongly oxidizing, and are dangerous. Follow the specific rules handling them at your institution, but at least take extreme care and

wear the proper safety equipment. Upon completion of the work, the piranha solution must be cooled for at least one hour before pouring into a dedicated waste container.

NOTE: It is necessary to rinse the LN chips twice in two DI water baths. Rinsing them once leaves residue behind that will likely ruin the bonding. Gold electrodes are used for IDTs because of their good resistance to piranha solution.

3.3. Plasma surface activation: Activate the chip surfaces using plasma with 120 W of power while exposed to O_2 flow at 120 sccm for 150 sec. Immediately transfer the samples to a fresh DI water bath for at least 2 min.

NOTE: Plasma surface treatment quickly followed by DI water immersion will form hydroxyl groups upon the LN surface, increasing its free surface energy to later promote bonding.

3.4. Room-temperature bonding: Dry samples with dry N_2 flow and carefully lay the nanoslit chip onto the SAW device chip in the desired position. Realign to produce the desired orientation. Then use tweezers or similar to push down upon the sample from its center to initiate the bond. Gently push down in areas that failed to bond after the initial push.

NOTE: The bonding may be easily seen through the transparent LN. Bonded regions are entirely transparent. LN that is not double-side polished will be more difficult to assess.

3.5. Heating after bonding: Place bonded samples in a sprung clamp to safely exert loads on it despite thermal expansion, and place the clamped samples into an oven at room temperature (25 °C). Set the oven heating temperature to 300 °C, ramp rate to 2 °C/min maximum, dwell time to 2 hours, and then to automatically shut off to allow it and the clamped samples within to naturally cool to room temperature.

NOTE: The protocol can be paused here. The bonding between hydroxyl groups produces water at the bond, and heating removes the water to drastically increase the bond strength. Modest clamping forces are sufficient. Attempting to bond two chips of different orientations or materials may cause cracks due to mismatched thermal expansion and consequent stress.

6.3.4 Experimental Setup and Testing

4.1. Observation: Observe the nanoslit under an inverted microscope. Include and rotate a linear polarizing filter in the optical path to suitably block birefringence-based image doubling in the LN. Use ultrapure DI water via the inlet to observe fluid motion in the completed nanoslit.

NOTE: Ultrapure liquid is strongly recommended to prevent clogging, especially after evaporation.

4.2. SAW actuation: Attach absorbers at the ends of the SAW device to prevent reflected acoustic waves. Use a signal generator to apply a sinusoidal electric field to the IDT at its resonance frequency of around 40 MHz. Use an amplifier to amplify the signal. Use an oscilloscope to measure the actual voltage, current, and power applied to the device. Record the fluid motion during SAW actuation within the nanoslit using a camera attached to the microscope.

6.4 Representative Results

We perform fluid capillary filing and SAW-induced fluid draining in nano-height LN slits after successful fabrication and bonding of SAW integrated nanofluidic devices. Surface acoustic waves are generated by IDTs actuated by an amplified sinusoidal signal at the IDTs' resonance frequency of 40 MHz, and the SAW propagates into the nanoslit via a piezoelectric LN substrate. The behavior of the fluid in the nanoslit interacting with SAW may be observed using an inverted microscope.

We demonstrate fluid capillary filling in 100-nm tall channels of different widths. Figure 2 shows capillary filling of ultrapure DI water into two 100-nm tall channels, one 400 m wide and the other 40 m wide. The drop of ultrapure water is delivered into the nanoslit through the inlet. Capillary forces drive fluid filling of the entire nanoslit, and the filling occurs more quickly with the narrower channel due to its larger capillary force. Capillary force-driven fluid filling using other fluids of different viscosities and surface tensions could be used, as could nanoslits of other

heights to produce different results.

We also demonstrate SAW-induced fluid draining in a nanochannel by overcoming capillary pressure. Water in a 100-nm height slit has been drained to show a water-air interface with the maximum length at the middle (Figure 3), indicating maximum acoustic energy at middle of the SAW device. With strong acoustic pressure generated in the nanoslit, it also indicates good bonding strength using our plasma-surface-activated room-temperature LN bonding method. A threshold applied power of around 1 W is required to force the acoustic pressure to be larger than the capillary pressure and drive a visible draining phenomenon (Figure 4). The maximum length of the air cavity which represents fluid surface energy shows a linear relationship with the applied acoustic power. It offers an effective tool for fluid actuation and potentially macro-biomolecule manipulation at the nanoscale. The effect of draining various fluids using SAW with different channel heights and widths could be further investigated.

6.5 Discussion

Room-temperature bonding is key to fabricating SAW-integrated nanoslit devices. Five aspects need to be considered to ensure successful bonding and sufficient bonding strength. First: time and power for plasma surface activation. Increasing the plasma power will help increase the surface energy and accordingly increase the bonding strength. But the downside of increasing the power during plasma surface activation is the increase in surface roughness, which may adversely affect the nanoslit fabrication and fluid transport performance. It has been shown that the plasma surface activation time will not help increase the surface energy after a certain amount of time[297]. Thus, the plasma activation time and power need to be defined to maximize the surface energy but not at the expense of increased surface roughness. Second: cleaning chips before bonding. Since there is only a nanoscale height channel after bonding, any micro-size particle will be an enormous obstacle and cause bonding failure. Piranha cleaning is used to remove all organic

debris on the chip surfaces. After cleaning, it is strongly recommended to use a clean container to cover the chips and prevent contamination. Third: the orientation of the LN chip pairs prior to bonding. Due to the anisotropy of LN, bonding the upper and lower LN chip currently requires identical material orientation. Failing to do so will cause residual stress and possibly cracking during fabrication. It will also cause different SAW characteristics between the top and bottom surfaces of the nanoslit because of anisotropy. Therefore, bonding two LN chips with identical material orientation is highly recommended. Fourth: alignment of the upper and lower chips. We visually perform the manual alignment and bonding. Introducing fiduciary markers and proper microscope-aided aligned bonding would surely improve device quality and yield. Fifth: oven heating temperature after initiating room-temperature bonding. Heating at higher temperatures will help strengthen the bond. Heating to 300 °C for our LN bonding process produces at least 1 MPa bonding strength since it remains intact against comparable capillary and acoustic pressures in the nanoslit with SAW.

6.6 Acknowledgement

We are grateful to the University of California and the NANO3 facility at UC San Diego for provision of funds and facilities in support of this work. This work was performed in part at the San Diego Nanotechnology Infrastructure (SDNI) of UCSD, a member of the National Nanotechnology Coordinated Infrastructure, which is supported by the National Science Foundation (Grant ECCS–1542148). The work presented here was generously supported by a research grant from the W.M. Keck Foundation. The authors are also grateful for the support of this work by the Office of Naval Research (via Grant 12368098).

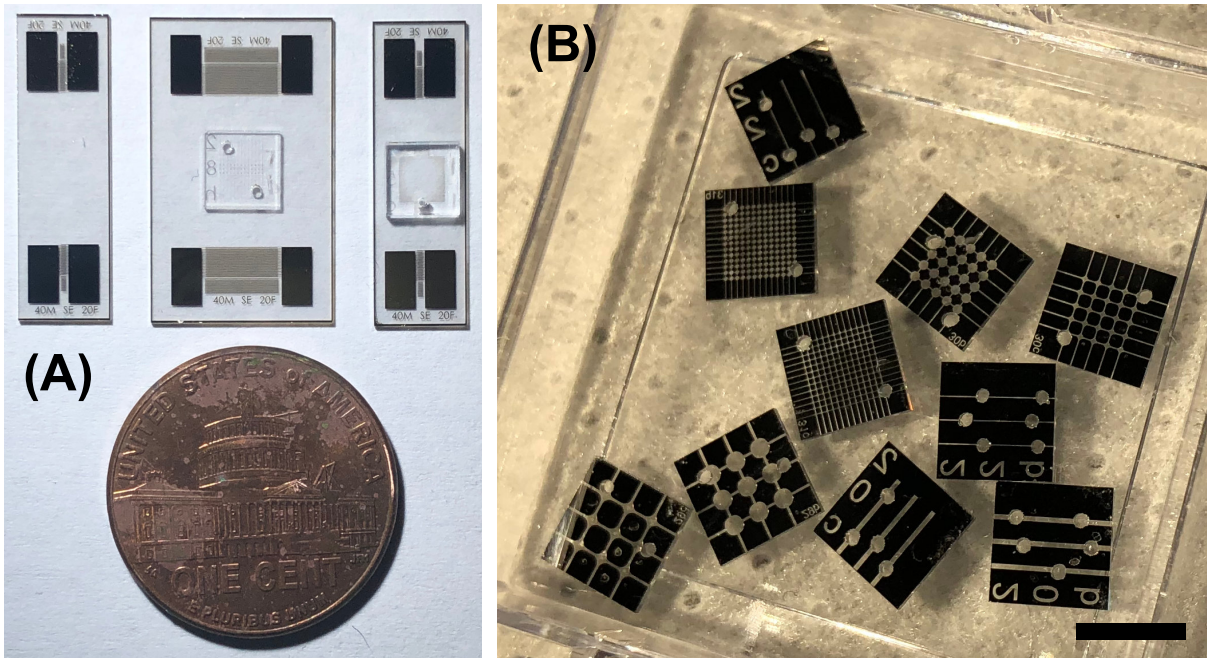

Figure 6.1: Images of fabricated devices. (A) Left: Gold electroded IDTs with a 0.7 mm aperture on LN substrate for 40 MHz SAW generation and propagation. Middle Right: Bonded LN nanoslit device integrated with SAW for fluid actuation. A one-penny coin is shown as a scale reference at bottom. (B) Various reactive-ion-etched nano-height channel LN chips are shown with chromium sacrificial mask structures and after drilling 500-m diameter holes for fluid inlets and outlets. Scale bar: 5 mm.

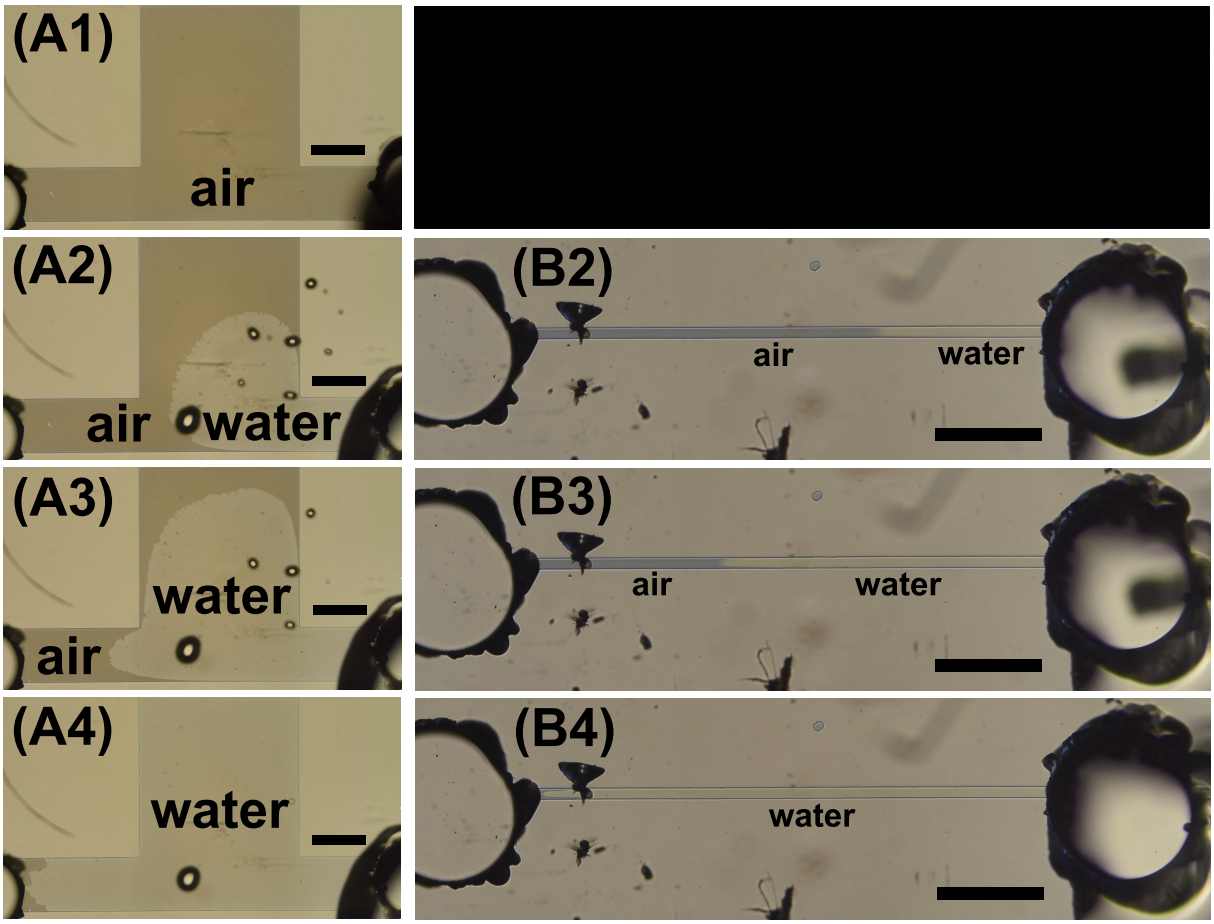

Figure 6.2: Fluid capillary filling in 100 nm-height channels. (A1-A4) Ultrapure water is drawn into a 400-m wide nanoslit via capillary force over time, shown at the start (0 sec) and 1, 2, and 4 sec later, respectively. Small water drops can be seen at the top of the superstrate. (B1-B4) Ultrapure water is drawn into a 40 μm wide nanoslit via capillary force over time, shown at the start (0 sec) and 0.1, 0.3, and 1 sec later, respectively, indicating more rapid filling due to greater capillary force on a smaller amount of fluid. The small depressions at the top of the superstrate are evidence of hitting the surface with tweezers. Scale bar: 400 μm.

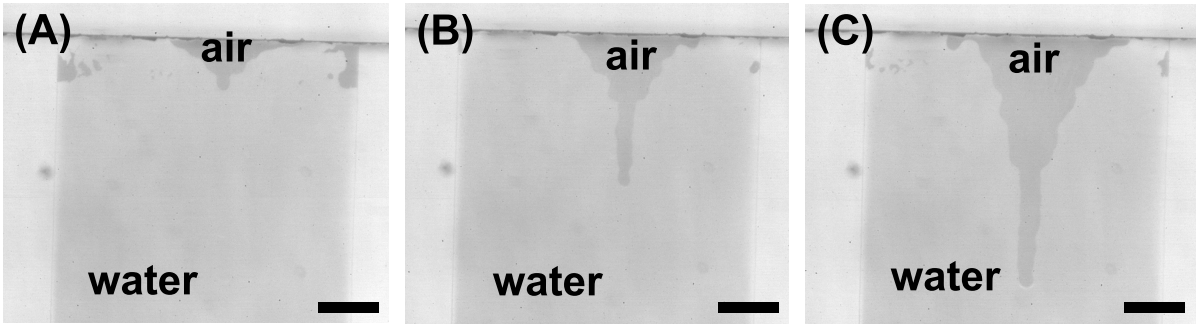

Figure 6.3: SAW-induced fluid draining in 1 mm-width 100 nm-height nanoslit. (A-C) A water-filled nanoslit is drained by 40 MHz SAW at an applied power of 1.31 W, 2.04 W, and 2.82 W, respectively. The SAW is propagating from top to bottom in the images. The interfacial line between the bonded and nanoslit regions is visible: note the color change. Scale bar: 200 μm.

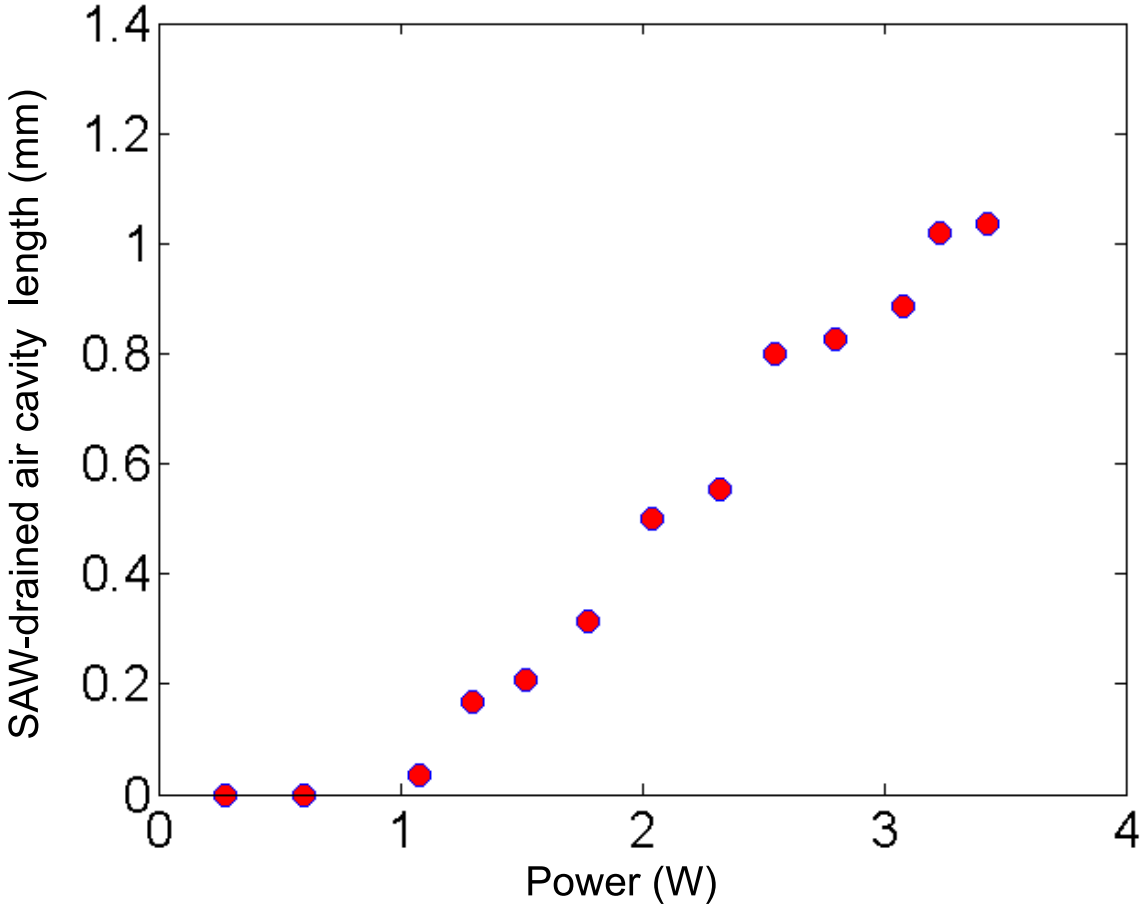

Figure 6.4: SAW-induced air cavity length with respect to SAW applied power. The dewetting cavity length is approximately linearly dependent upon the applied power. The applied power should offer an acoustic pressure greater than the capillary pressure in the nanoslit, causing fluid drainage. The threshold applied power at which drainage appears is around 1 W in this case.

Chapter 7

Powerful Acousto-Geometric Streaming from Dynamic Geometric Nonlinearity

7.1 Abstract

Past forms of acoustic streaming, named after their progenitors Eckart (1948), Schlichting (1932), and Rayleigh (1884), serve to describe fluid and particle transport phenomena from macro to micro scales. Governed by the fluid viscosity, traditional acoustic streaming arises from second-order nonlinear coupling between the fluid's density and particle velocity, with the first-order acoustic wave time-averaging to zero. We describe a form of acousto-geometric streaming that has a non-zero first-order contribution. Experimentally discovered in nanochannels of a height commensurate with the viscous penetration depth of the fluid in the channel, it arises from nonlinear interactions between the surrounding channel deformation and the leading order acoustic pressure field, generating flow pressures three orders of magnitude greater than any known acoustically-mediated mechanism. It enables the propulsion of fluids against significant Laplace pressure, sufficient to produce 6 mm/s flow in a 130–150 nm tall nanoslit. We find quantitative agreement between theory and experiment across a variety of fluids and conditions,

and identify the maximum flow rate with a channel height 1.59 times the viscous penetration depth.

7.2 Main Text

The potential of novel biological analysis and sensing, medical diagnosis, and material processing makes nanofluidics[338] an enticing research area, if not for the challenges of fluid transport at this scale. Because surface-mediated forces are overwhelmingly dominant, wetting and dewetting and the manipulation of fluid interfaces all play a key role in nanoscale fluid transport.

Acoustic waves and the acoustic streaming they generate[274] have long been proposed in various forms—including, in particular, surface acoustic waves (SAW)[65,89,109]—to produce fluid and particle transport at the milli to micro-scale. Among the many examples, Schneider *et al.* reported flow in a microfluidic racetrack structure with low resistance[337]. Both Cecchini *et al.*[44] and Girardo *et al.*[121] presented acoustic devices that used atomization to produce fluid transport in microchannels. Bauerle *et al.*, used SAW as a peristaltic pump to show that cost-efficiency of mass transport in peristalsis depends upon its phase modulation[18]. A recent paper[75] employed computation and theory to predict the motion of a fluid meniscus in a $\sim$10 μm thick channel by using a propagating wave along the channel substrate. But the underpinning assumptions limit its validity, especially in our case: the particle velocity of the excitation is assumed to be small compared to the sound's phase velocity, eliminating compressibility and acoustic effects that are important in the mechanism we observe here.

Eckart streaming,[97] driving bulk flow from viscous attenuation of acoustic waves, is responsible for many of the results described in the macro-to-micro-scale applications of the previous paragraph[65,89,109,274,337]. Other forms of acoustic streaming identified by Rayleigh[303] and Schlichting[331] prior to Eckart streaming also may be found in some of these results, and

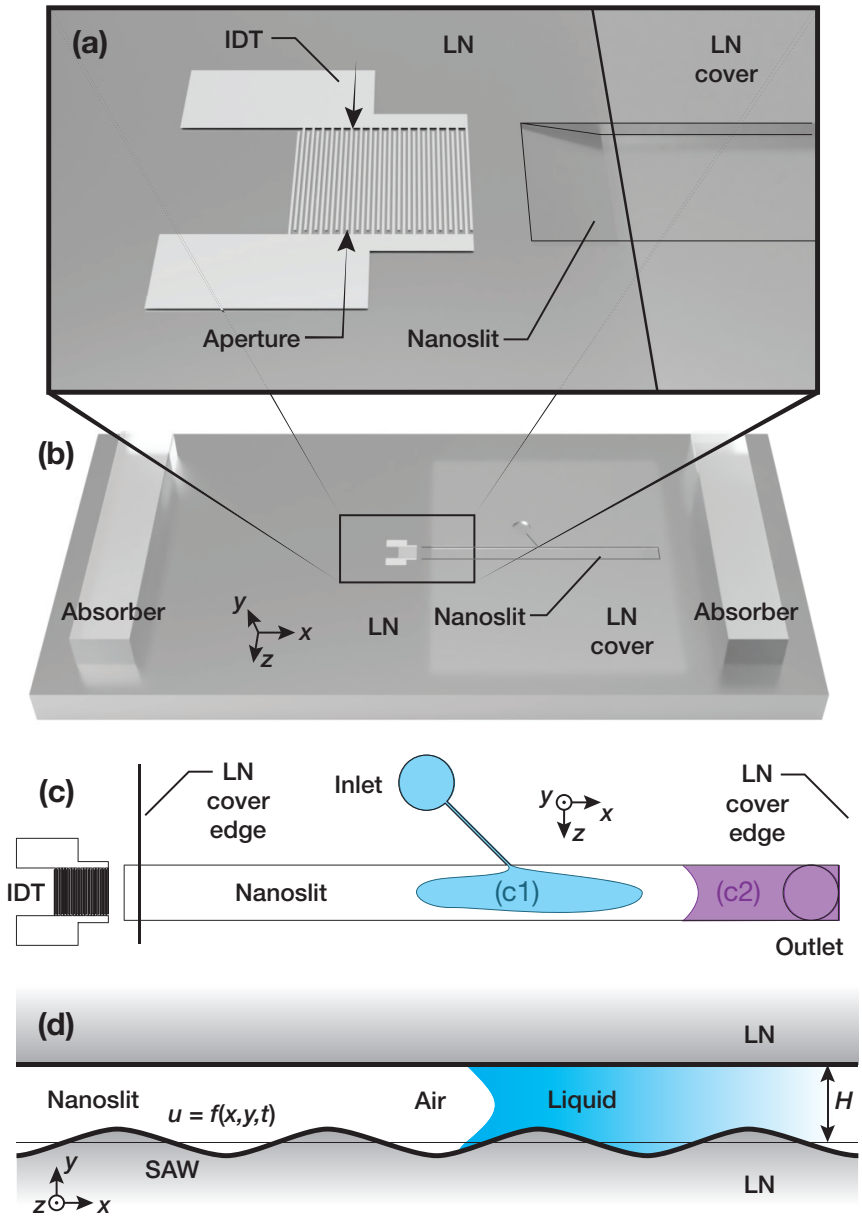

Figure 7.1: An (a) IDT with a 625 μm wide aperture produces SAW that propagates (b) underneath an aligned, 1-mm wide, 5-mm long nanoslit etched into the LN substrate with a room-temperature bonded LN cover. Absorbers eliminate reflected waves. The channel depth is *greatly* exaggerated for clarity. (c) A 20-μm wide, 500-μm long side channel, which controls the filling rate, connects the main channel at 45° to the 1-mm diameter inlet well. A 1-mm diameter (c1) outlet present at the end of the nanoslit distal from the IDT provides a means for (c2) fluid outflow.

appear, respectively, in the bulk and boundary layer of the fluid, driven by motion of the boundary. Other forms of acoustic streaming, such as microstreaming[91,217] and sharp-edge streaming[268,282]

are variations on these forms of acoustic streaming[109]. All are due to generation and convection of momentum flux, in turn dependent upon the spatiotemporal inertia from the Navier-Stokes equation and averaged over one or more time periods of the acoustic vibration[209]. The momentum flux is further associated with the spatial derivative of the time-averaged Reynolds stress in the liquid, $\langle \rho uu \rangle$, where ρ, u, and $\langle \cdot \rangle$ are the density and velocity in the liquid and a time-averaging operator, respectively[52,137]. In acoustofluidics, typically $\rho \approx 1000$ kg/m^3 and $|u| \equiv U \sim 0.01 - 1$ m/s, where U is the amplitude of particle velocity of the acoustic wave.

Consequently, the characteristic magnitude of the Reynolds stress, and therefore the pressure these three forms of acoustic streaming may bring to bear on a fluid interface, is $\rho U^2 \approx 0.1 - 1000$ Pa, sufficient to overcome Laplace pressure of the liquid meniscus and enable dynamic wetting and de-wetting of micro to macro-scale channels. However, in submicron and smaller channels, acoustically-driven wetting and dewetting is overwhelmed by the meniscus' Laplace pressure, $\Delta P \approx \gamma \cos\theta/(H/2)$, where γ, θ, and H are the fluid-air interfacial surface tension; the three-phase contact angle between the fluid, air, and the lithium niobate substrate; and the thickness of the channel; respectively. The Laplace pressure is 0.1 MPa for a 1 μm thick channel, and grows with a decrease in the channel height. Furthermore, fluid viscosity and the dynamic resistance it presents to the flow must be overcome[371]. A Laplace pressure of $\Delta P \approx 14$ MPa to 1.4 MPa in a channel of thickness $H = 10$ nm to 100 nm, respectively, is far larger than the second-order acoustic streaming-mediated pressure[92] of the order $\rho U^2 \sim 0.1$–1000 Pa, assuming in this example that $\gamma \approx 70$ mN/m for deionized water and $\theta \approx 0^\circ$ for the hydrophilic LN substrate. The acoustic *radiation* pressure[52] is *also* on the order of ρU^2, because the nanoslit channel's thickness is small compared to the wavelength of sound in the fluid, and is also insignificant.

By contrast, for the same 1 m/s particle velocity of the acoustic wave, the corresponding peak pressure is much larger. It is approximately $\rho U c_l \sim 1.5$ MPa. Here c_l is the phase velocity of sound in the liquid—water in this example. This pressure is equivalent to the Laplace pressure

Table 7.1: Physical parameters of the fluids and nanoslit channels used in our experiments.

	γ (mN/m)	μ (cP)	c_l (m/s)	ρ (kg/m^3)	δ (nm)	ω (10^8 rad/s)	H (nm)	H/δ (—)
Water	72	0.89	1482	997	86	2.42	150	1.75
IPA	22	1.96	1170	786	145	2.38	130	0.90
Methanol	22	0.543	1116	792	76	2.37	130	1.71
1-Octanol	27	7.36	1349	830	274	2.37	130	0.48

in a water-air meniscus within a 100-nm high hydrophilic channel, but it is harmonic, with a time average of zero. It is reasonable to assume that this leading order acoustic pressure is responsible for the observed transport[247] of liquid menisci in the nanochannels. However, for this to be true, there must be a rectifying mechanism that produces a net transport of the meniscus by the purely harmonic oscillation of the acoustic pressure. This mechanism was not explained in prior work[247], and is instead the focus of this paper, defined as acousto-geometric streaming from a dynamic geometric nonlinearity.

Here, rapid SAW-induced fluid interfacial transport in channels of $\sim$150 nm height (*see* Fig. 7.1) are shown to exist. Moreover, the observed flow is conclusively shown to be *not* due to known acoustic streaming—collectively Eckart[97], Rayleigh[303], and Schlichting[331] streaming—nor acoustic radiation pressure[52]. Another mechanism is at work, one associated with the leading order periodic acoustic pressure and which overcomes the Laplace pressure in the interfacial fluid menisci to produce rapid transport. This acoustic streaming mechanism is presented for the first time as both a new physical phenomena and an effective tool to transport fluids through nanochannels.

We now define an acoustic streaming mechanism that becomes significant as $H \sim \delta$, where $\delta = \sqrt{2\mu/\rho\omega}$[256] is the viscous penetration depth for acoustic energy leakage into the fluid from SAW propagating along an adjacent boundary. Here μ and ω are the liquid's viscosity and the angular frequency of the SAW, respectively. Noting Fig. 7.1, δ is the length scale where the viscosity may affect the flow at the time scale of the acoustics, $1/\omega$. In our experiments, generally $\delta \sim 100$ nm and the ratio of the channel height to the boundary layer thickness is ~ 1;

specific values are provided in Table 7.1 for the fluids in this study: water, IPA, methanol, and 1-octanol. Note the nanoslit is closer to the SAW device than the edge of the LN cover layer (*see* Fig. 7.1), leaving a gap that prevents SAW coupling into the top LN layer. This, and the fact the SAW aperture being less than the channel width leaves the SAW to propagate solely along the bottom boundary. To highlight this, we show a side view of the nanoslit in Fig. 7.1(d). This is a crucial difference from past work[247], where the SAW propagation along both the top and bottom boundaries was poorly controlled.

Neglecting the attenuation of the SAW due to acoustic energy leakage into the adjacent fluid, justified by noting the very small volume of fluid present in the nanoslit system, we assume that the deformation of the bottom channel surface by the SAW is given by

$$A = -|U/\omega| \cos(\omega[t - x/c_s]), \tag{7.1}$$

with respect to its position at rest. Referring to Fig. 7.1, we also assume the width (along z) and length of the channel (along x) are large compared to its nominal height H (along y), and that the deformation is identical across the width of the channel. The deformation A is assumed to be purely in the y direction, while the wave carrying the deformation propagates along the x axis at the SAW's phase velocity c_s, where t is the time and $|A| = U/\omega$ is the amplitude of the channel wall's normal deformation.

The corresponding leading order acoustic pressure in the thin liquid film is

$$p = \rho c_l \partial A/\partial t = \rho U c_l \sin[\omega(t - x/c_s)]. \tag{7.2}$$

We presume that x scales like the inverse of the wavelength of the SAW, $\kappa^{-1} \equiv c_s/\omega$ and that y scales like δ. The scaling for the pressure field $p \sim \rho U c_l$ is a product of eqn. (7.2). The tangent (in the x direction) and normal (in the y direction) flow velocities along the channel, u and v, respectively, satisfy to leading order a solenoidal vector field and are governed by the continuity

equation $\partial u/\partial x + \partial v/\partial y = 0$. Hence, the velocity field may be scaled according to $u \sim \kappa\delta U$ and $v \sim U$. While in practice the acoustic effect responsible for the pressure undulation in (7.2) is due to small variations in the density, these variations do not contribute at the order of magnitude of the flow field in our discussion.

The corresponding leading-order terms in the Navier-Stokes equations, assuming that $\kappa\delta \ll 1$, $U/c_l \ll 1$, and $\mu\kappa/\rho c_l \ll 1$ to match our experiments, produce

$$\rho\frac{\partial u}{\partial t} - \mu\frac{\partial^2 u}{\partial y^2} + \frac{\partial p}{\partial x} = 0; \qquad \frac{\partial p}{\partial y} = 0, \tag{7.3}$$

subject to eqn. (7.2) and a vanishing flow velocity at the channel walls. A Galilean transformation, $u = \Re\left\{-\imath f(y)e^{\imath\omega(t-x/c_s)}\right\}$ and $p = \Re\left\{-\imath\rho U c_l e^{\imath\omega(t-x/c_s)}\right\}$, simplifies the analysis, where $\Re(\cdot)$ is the real part and $\imath \equiv \sqrt{-1}$. This simplifies to the boundary value problem

$$f''(y) - \frac{\imath\rho\omega}{\mu}f(y) + \frac{\imath c_l\rho U\omega}{c_s\mu} = 0, \tag{7.4}$$

subject to $f = 0$ at $y = \{0, h\}$, where $h \equiv H - A(x,t)$ is the local spatiotemporal thickness of the excited channel and $A(x,t)$ is given in eqn. (7.1). With these boundary conditions, eqn. (7.4) is satisfied by $f(y) = C_1 e^{\left[(1+\imath)\frac{y}{\delta}\right]} + C_2 e^{\left[-(1+\imath)\frac{y}{\delta}\right]} - \imath c_l U/c_s$, where $C_1 = \imath c_l c_s U\left\{1 + e^{\left[(1+\imath)\frac{h}{\delta}\right]}\right\}^{-1}$ and $C_2 = C_1 e^{\left[(1+\imath)\frac{h}{\delta}\right]}$.

Substituting $h = H - A(x,t)$ for u in the Galilean transformation above and averaging over a long time—equivalent here to averaging over one time period of the acoustic wave—produces the leading order time-averaged volume flux per unit width of the channel, $\langle Q\rangle = \frac{1}{T}\int_0^T Q\,dt$. Expanding the solution in the small parameter $|A|/\delta \ll 1$, integrating over the local channel spatiotemporal thickness, h, and dividing the result by the channel thickness at rest, H, gives us

the average flow velocity in the channel,

$$\frac{\langle u \rangle}{U c_l/c_s} = \frac{\langle Q \rangle}{U H c_l/c_s} = \frac{|A|}{H} \frac{\sin\left(\frac{H}{\delta}\right)\sinh\left(\frac{H}{\delta}\right)}{\left(\cos\left(\frac{H}{\delta}\right)+\cosh\left(\frac{H}{\delta}\right)\right)^2}. \tag{7.5}$$

Hence, the meniscus velocity $\langle u \rangle$ is scaled by the ratio of the deformation amplitude to the thickness of the channel, $|A|/H$. The Supplemental Information includes a simplification of this equation for $H/\delta \ll 1$ at [publisher URL]. This motion is reminiscent of a peristaltic pump, with the key difference that the flow is generated here via acoustic pressure and traditional peristaltic pumps rely on hydrodynamic pressure.

As $H/\delta \to 0$, the volume flux $\langle Q \rangle \to 0$ vanishes as expected. However, as H/δ and the channel height are increased, the volume flux $\langle Q \rangle$ increases to a maximum of $\langle Q \rangle = 0.366 c_l U^2/(c_s \omega)$ at $H/\delta = 1.59$ before decreasing to zero at $H/\delta \gtrsim 3$. There is no first-order acoustically-induced flow if the channel height is even modestly large compared to the viscous penetration depth. This does not necessarily imply the absence of acoustically driven flow, however, as second and higher-order nonlinear effects—traditional forms of acoustic streaming—may cause relatively weak fluid transport.

We now turn to experimental evidence of the phenomena, employing SAW at 38.5 MHz along nanoslits fabricated to have heights on the order of the viscous penetration depth, $H \approx \delta/2 - 2\delta$. The nanoslit fabrication process is detailed in past work[247,463], but details specific to this letter are provided in the Supplemental Information at [publisher URL] as is information on the SAW generation and measurement methods. Briefly, a laser Doppler vibrometer (LDV, UHF–120, Polytec, Waldbronn, Germany) was used to measure the *y*-axis oriented, out-of-plane particle velocity of the SAW upon the LN substrate surface, making it possible to determine the acoustic power transmitted by the SAW from the IDT. Notably, the longitudinal component of the SAW along the *x* axis is not measured, but is both known to be about 0.8 of the *y*-axis oriented motion in LN and weakly coupled to a fluid if present on the surface[109].

Liquid introduced into the fluid reservoir first fills the side channel, from which the main channel slowly fills, displacing the air present in the system. Once the meniscus reached equilibrium, we activated the SAW propagating from the IDT and along the nanoslit channel, as shown in Fig. 7.1. Note that the axial filling asymmetry in these images is due to the application of SAW.

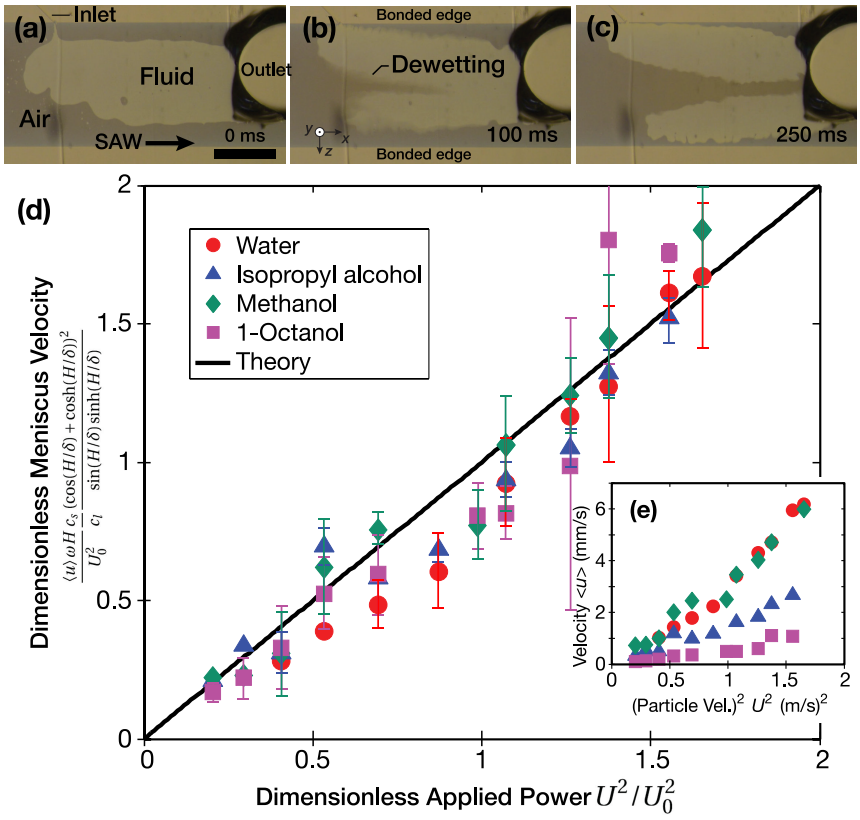

Figure 7.2: (a,b,c) Fluid transport and meniscus dewetting deionized water from within a 150 nm-thick hydrophilic nanoslit using $\sim$ 1 W, 38.5 MHz SAW, and applied from 0 ms. Scale bar: 0.5 mm. With different fluids, the meniscus velocity versus the applied power, (d) nondimensionalized using eqn. (7.6), where $U_0 = 1$ m/s is the scaled velocity, collapses the onto a line from the (e) original dimensional results. The theory is effective in representing the observed phenomena. Drainage of other fluids and videos and a version of (e) dimensional fluid velocity versus applied power with error bars are all in the Supplemental Information at [publisher URL]. Error bars indicate the max-min range of the data for each point ($N \geq 10$).

Applying SAW causes the trailing edge liquid meniscus—closer to the IDT—to be propelled away from the IDT and towards the outlet reservoir. The velocity of the meniscus,

shown in Fig. 7.2, appears proportional to the acoustic power. This was the case with water, isopropyl alcohol (IPA), methanol, and 1-octanol, fluids of significantly different properties (*see* Table 7.1). The meniscus velocities across these fluid choices and for multiple runs collapse onto a single curve in Fig. 7.2 upon application of the scaling defined in eqn. (7.6). Moreover, the experiment is in quantitative agreement with theory, notable as the latter is a consequence of the nonlinear coupling between the first-order acoustic field in the fluid and the harmonic change of the channel height with the passage of the SAW.

The time-averaged volume flux per channel width $\langle Q \rangle$ mainly depends upon the ratio of slit height to viscous boundary layer thickness H/δ when using a fixed power and frequency, as represented by $(|A|UH)/H \sim U^2/\omega$ in eqn. (7.6). This occurs because the sound velocity c_l is the same order of magnitude for most fluids, including those we considered.

Capillary forces are comparatively insignificant. The average capillary filling velocity may be derived using a straightforward rearrangement of the classic Washburn model[247,425] as shown in the Supplemental Information at [publisher URL]. We may then calculate this velocity from experimental data *without SAW* to be $\bar{v} = \gamma H \cos\theta/(3\mu) \sim 0.4$ mm/s, a time-averaged volume flux per unit width for a 150-nm high channel of 60 μm^2/s. This is one order of magnitude less than the new acoustic streaming mechanism.

We now turn to the first known observations of liquid meniscus instabilities in a nanoscale fluid channel, as illustrated in Fig. 7.3. Since the IDT responsible for generating the SAW has a finite aperture, near-field and far-field diffraction[377] generates an evolving, non-uniform amplitude distribution across the width of the propagating SAW. This produces corresponding variations in the speed at which the fluid meniscus advances within the nanochannel. Resembling viscous and granular fingering instabilities[43,50,293] and thin-film instabilities[310], the mechanism and phenomena here are unique, especially the rapid dewetting against MPa-order capillary pressures in a nanoslit.

In the near-field of the SAW (Fig. 7.3(a)) emanating from the IDT to the right [1], the water meniscus initially exhibits fingering corresponding to near-field SAW diffraction as it begins to de-wet the nanoslit in Fig. 7.3(b). In the far-field of the SAW at 394 mW, the near-Gaussian amplitude distribution drives a corresponding dewetting profile at equilibrium in Fig. 7.3(c). Increasing the input power to 830 mW causes the meniscus to be completely dewetted along a narrow region at the center of the nanoslit in Fig. 7.3(d). Beyond the fact the majority of the SAW is passing at the center of the nanoslit, as determined from the intensity of the SAW measured in the far field of the SAW at over 20λ away from the IDT and shown in Fig. 7.3(e), there is slight lateral infill of the fluid to narrow this dewetting region. The lateral distribution of the SAW intensity significantly changes from the near field to the far field, but upon reaching the far field remains relatively constant. The close correspondence between the SAW intensity in Fig. 7.3(e) at 394 mW and the meniscus displacement in Fig. 7.3(c,d) is interesting. However, the reader should remember that with greater power the meniscus can have a substantially different shape than the SAW intensity due to dewetting. The key point is that the meniscus displacement will be far lower at the edges because the SAW energy is concentrated near the center of the aperture and channel.

Because the nanoslit also has a finite width, the fluid laterally infills along the z axis to narrow the meniscus, but is prevented from completely refilling the channel due to the presence of a strong gradient in the acoustic energy, E, along the z axis from the edge of the nanoslit to the center as indicated in Fig. 7.3(d). The gradient produces an acoustic force from $F = \partial E/\partial z$ oriented towards the nanoslit sides and in opposition to the inward-facing capillary force. The net result is a slightly more narrow dewetting region than might be expected based upon the far-field SAW amplitude distribution alone.

[1] The leftward-propagating SAW from the IDT is absorbed and suppressed.

7.3 Appendix

7.3.1 Spatiotemporal Average Fluid Velocity and a Simplified Expression for it

The spatiotemporally average velocity in the channel,

$$\frac{\langle u \rangle}{U c_l/c_s} = \frac{\langle Q \rangle}{U H c_l/c_s} = \frac{|A|}{H} \frac{\sin\left(\frac{H}{\delta}\right)\sinh\left(\frac{H}{\delta}\right)}{\left(\cos\left(\frac{H}{\delta}\right)+\cosh\left(\frac{H}{\delta}\right)\right)^2}. \tag{7.6}$$

may be simplified to

$$\frac{\langle u \rangle}{U c_l/c_s} = \frac{\rho U H}{8\mu} = \frac{1}{4}\frac{|A|}{H}\left(\frac{H}{\delta}\right)^2 \tag{7.7}$$

as the channel height is decreased to $H/\delta \ll 1$. Interestingly, this result is close to eqn. (7.6) up to $H \approx \delta$, as shown in Fig. 7.4.

7.3.2 Fabrication Details

Referring to Fig. 7.5, reactive ion etching (RIE, Plasmalab 100, Oxford Instruments, Abingdon, UK) was used to create 1 mm-wide, uniform nanoscale depressions aligned along the X axis into 128° Y-rotated, X-propagating lithium niobate (LN, Precision Micro-Optics Inc., Burlington, MA, USA). These depressions are illustrated in Fig. 7.6. Chromium was used as a deposited mask to preserve the flatness of the LN during RIE[247,463], later etched away before fabrication of adjacent interdigital transducers (IDTs) to generate SAW. The IDTs were designed for 40 MHz and were deposited on the LN with an aperture of 0.625 mm. Laser-written photolithography (MLA 150, Heidelberg Instruments, Heidelberg, Germany), 5 nm chrome followed by 250 nm gold sputter deposition (Denton 18, Denton Vacuum, NJ, USA), and the lift-off technique[463] were used to fabricate the IDT. Since the 0.625-mm IDT aperture is narrower than the 1-mm width of the soon-to-be formed nanoslit, and the reservoir and SAW-nanoslit layers

do not come into physical contact over the width of the aperture, the SAW is solely confined to the SAW layer.

Inlet and outlet holes were drilled into a second (reservoir) LN layer (1-mm diameter, Dremel #4000, Mount Prospect, Illinois, USA) as liquid reservoirs. After piranha cleaning and oxygen plasma surface activation (PVA TePla PS100, Corona, CA, USA), the nanochannel and reservoir LN layers were aligned and bonded at room temperature. To improve the bond strength beyond the acoustic and capillary pressures of the fluid in the nanoslit, $\sim$1 MPa, the structure was clamped and heated to 300 °C (ramp up and down 1°C/min, HTCR 6/28, Carbolite, Hope Valley, UK).

7.3.3 SAW Signal Generation and Measurement Details

The resonance frequency of the actual IDT design was identified at 38.5 MHz. A signal generator (WF1967 multifunction generator, NF Corporation, Yokohama, Japan) and an amplifier (5U1000, Amplifier Research Corp., Souderton, PA USA) were used to provide a sinusoidal input signal at this frequency to the IDT while the instantaneous voltage and current were measured via oscilloscope (InfiniVision 2000 X-Series, Keysight Technologies, Santa Rosa, CA, USA) to compute the true input power to the device. Acoustic absorbers (Dragon Skin 10 Medium, Smooth-On, Inc., Macungie, PA USA) were attached to the periphery of the LN substrate to prevent wave reflection and interference. Fluid motion within the nanoslit was recorded with cameras (Nikon D5300, Minato, Tokyo, Japan, and FASTCAM Mini UX100, Photron, Tokyo, Japan) via inverted microscope (Amscope IN480TC-FL-MF603, Irvine, CA USA). The motion of the liquid menisci was calculated from the recordings using custom image processing code (MATLAB, Mathworks, Natick, MA USA).

7.3.4 Washburn Model for Capillary Filling of Channels

The Washburn model predicts the dynamic wetting and dewetting of a channel over time without SAW, with the position of the meniscus with respect to time $x_m(t)$ given by

$$x_m(t) = \sqrt{\frac{\gamma H \cos\theta}{3\mu}}\sqrt{t}. \tag{7.8}$$

The corresponding meniscus velocity is

$$v_m = \frac{dx_m}{dt} = \left(\frac{\gamma H \cos\theta}{6\mu}\right)\frac{1}{x_m}, \tag{7.9}$$

and consequently the time taken for the meniscus to travel a distance L in the channel is given by

$$T = \int_0^L \frac{dx_m}{v} = \frac{3\mu L^2}{\gamma H \cos\theta}. \tag{7.10}$$

Using this result, we may determine the average velocity of the meniscus in wetting a channel as $\bar{v} = L/T = \gamma H \cos\theta/(3\mu) \sim 0.4$ mm/s, a time-averaged volume flux per unit width for a 150-nm high channel of 60 μm^2/s. This is one order of magnitude less than the new acoustic streaming mechanism, as stated in the main paper.

7.3.5 Dewetting by SAW

In the main paper, the dimensional results of the fluid velocity u versus the SAW-induced particle velocity, squared, U^2, is shown as an inset to the non-dimensional results in Fig. 2. For clarity, the error bars were omitted there. Here, the dimensional results are provided with error bars in Fig. 7.8.

The device also is effective with other fluids as noted from these results, though for clarity we showed imagery solely for water. Figure 7.9 provides images of the dewetting of deionized

water, methanol, isopropyl alcohol, and 1-octanol. The dewetting appears to occur over a width equivalent to one acoustic wavelength in the fluid for each choice.

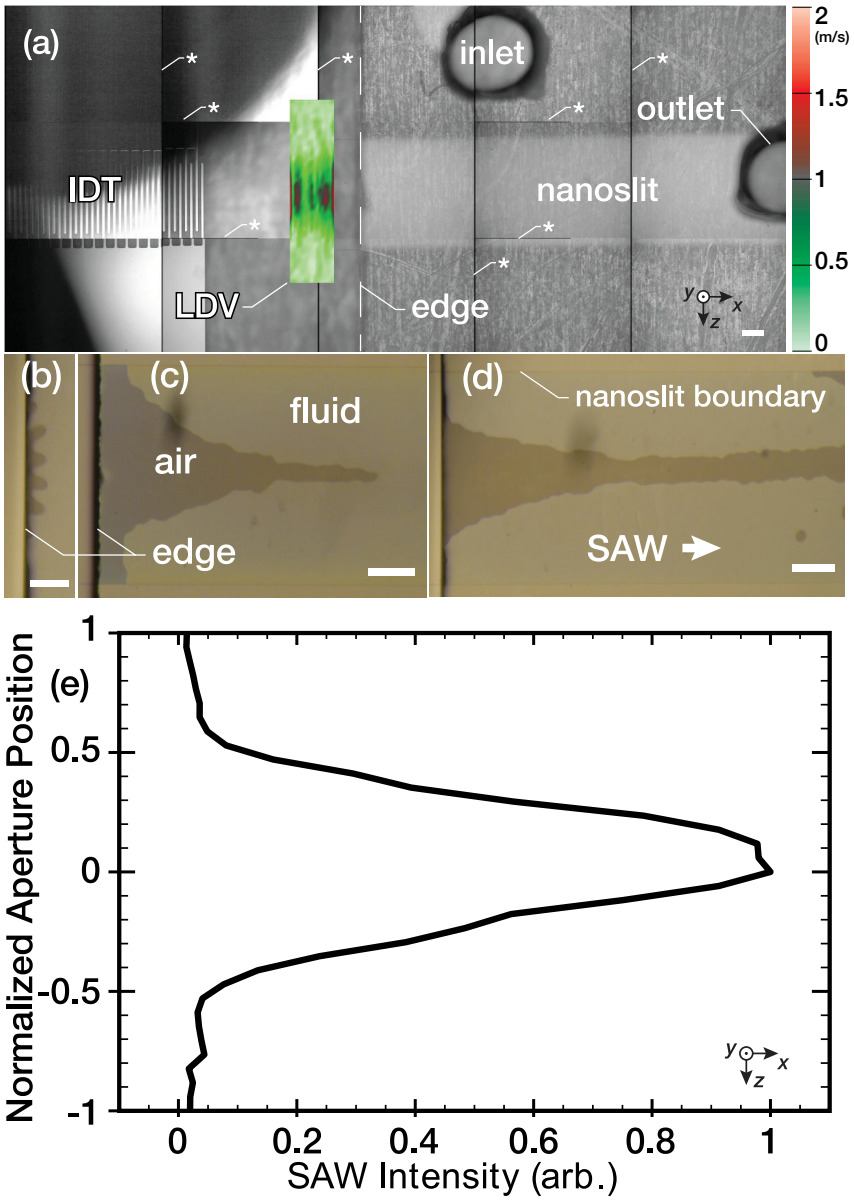

Figure 7.3: (a) The $H = 150$ nm nanoslit and IDT generating 38.5-MHz SAW from left to right with 1 W input power. An LDV-measured SAW velocity amplitude contour plot is shown before it propagates underneath the nanoslit. The color bar showing normalized SAW particle velocity amplitude from 0 to 1 is presented on the right of the image. Due to the scale, image stitching was necessary with *boundaries indicated. The initial (b) dewetting of the fluid—water in this case, *see* Table 7.1 for dimensions and details—from the edge of the nanoslit by SAW illustrates the effect of near-field Fresnel diffraction. This evolves to a (c) steady-state meniscus deformation into the nanoslit at 394 mW, the depth of which depends on the SAW amplitude. Increasing the SAW power, to 830 mW, (d) drains the water along the entire length of the nanoslit. In (e) the intensity of the SAW ($\propto U^2$) is plotted across the width of the IDT aperture, indicating why there is a (c,d) narrow channel of flow: the flow is most significant where the SAW intensity is large. Scale bar: 0.2 mm.

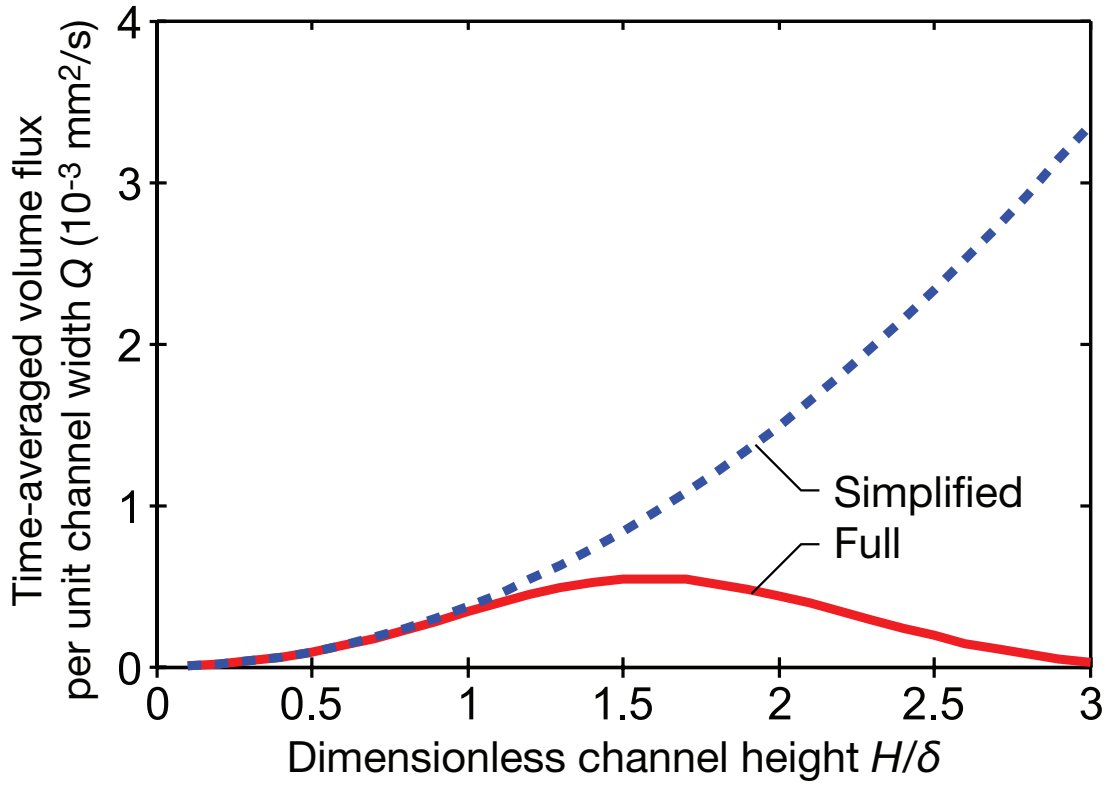

Figure 7.4: The net time-averaged volume flux per unit channel width is plotted with respect to the ratio of the channel's height, H to the viscous penetration depth, δ, using the full expression in eqn. 7.6 and the simplified expression eqn. 7.7, the latter valid only up to around $H/\delta \approx 1$. U=1 m/s, $\omega = 2\pi \times 40$ MHz, c_l = 1500 m/s, and c_s=4000 m/s are used for water as the liquid in this case.

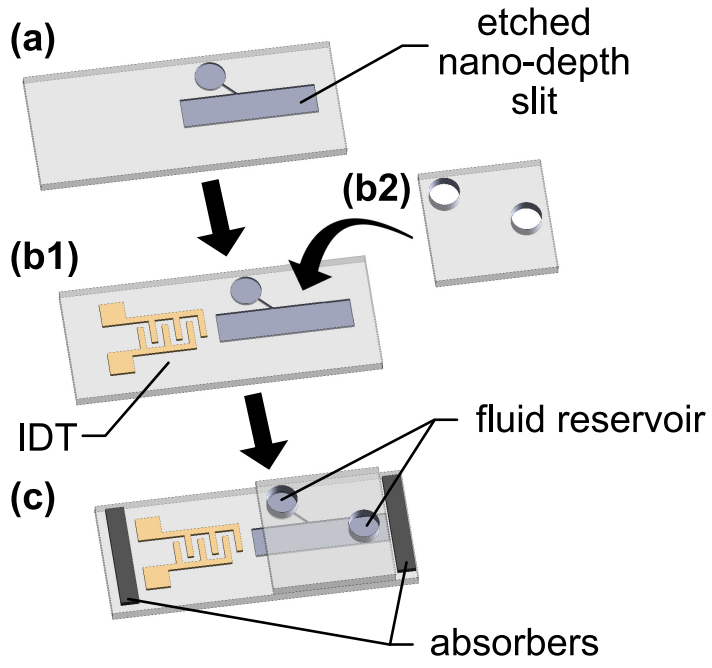

Figure 7.5: Fabricating a SAW-integrated nanoslit device via room temperature LN-LN bonding. Note: IDT, channel, and structural dimensions are not to scale and not for comparison to aid visualization. The IDT aperture (finger overlap width) is always less than the width of the nano-depth slit. (a) A nano-depth structure is etched into an LN substrate. The 5-mm long main channel is 1 mm wide, while a 20 μm wide, 500 μm long side channel connects the main channel at 45° to the inlet well, acting to control the capillary filling rate into the main nanoslit. (b1) An IDT with aperture of 0.625 mm is fabricated as aligned with the main nanoslit. (b2) Through holes of 1 mm diameter, aligned with the inlet well and the nanoslit end distal from the IDT, were machined into a second LN chip. After bonding, (c) the nanoslit device is complete, though to improve the bond the structure is clamped and heated (*see* text). Absorbers are attached at both ends of the chip to eliminate reflected waves. Note the presence of the gap between the two bonded layers that prevent SAW coupling to the (b2) reservoir LN layer over the width of the SAW generated from the aperture of the IDT. Not to scale.

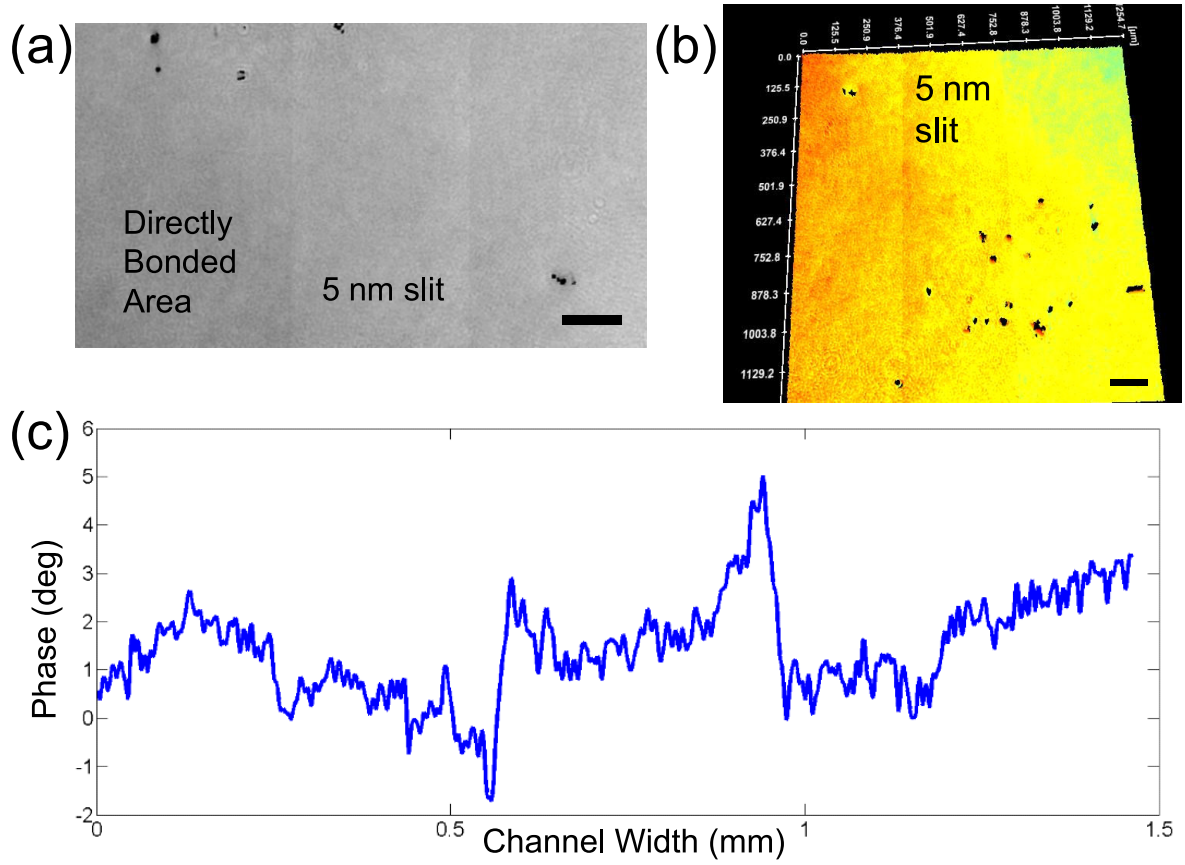

Figure 7.6: Images of an $H \sim 5$ nm deep nanoslit, captured by digital holographic microscopy (DHM, Lyncee Tec, Lausanne, Switzerland), presenting the current limit for fabrication and bonding of these devices. A (a) 2D phase image and a (b) 3D phase image showing the phase difference between LN-LN directly bonded area and the 5 nm slit area indicates the presence of the nanoslit. The DHM-measured (c) phase difference across the channel width along z (*see* Fig. 1 in main paper) indicates the presence of a channel where the phase angle increases; this phase corresponds to an optical phase shift of light propagating through the channel, corresponding to an approximately 5 nm gap. Scale bar: 333.3 μm.

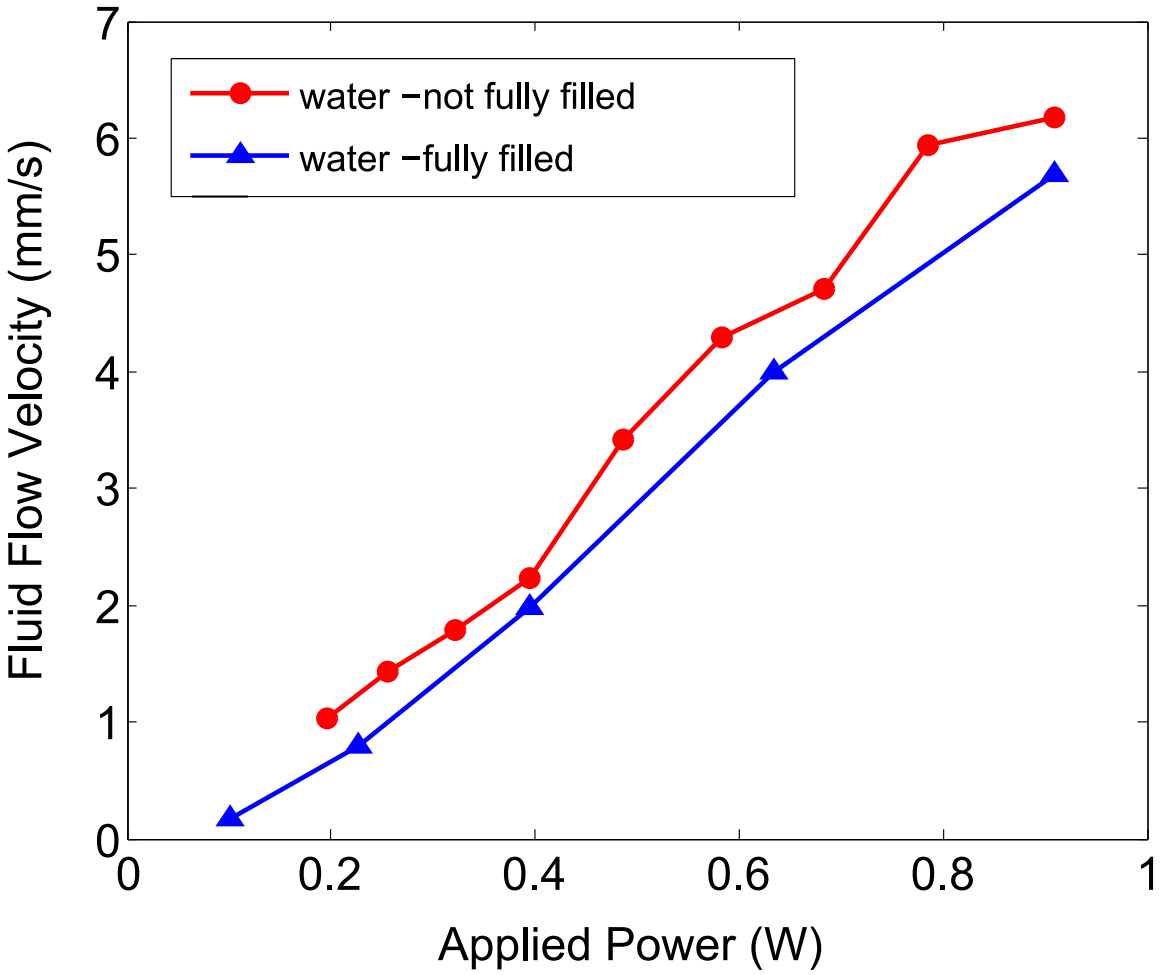

Figure 7.7: Experimental results with water not fully filled (red dots) and water fully filled (blue triangles) in the slit, showing the difference between two situations because of interfacial effect is negligible compared to the dominant first-order acoustically-driven flow regime.

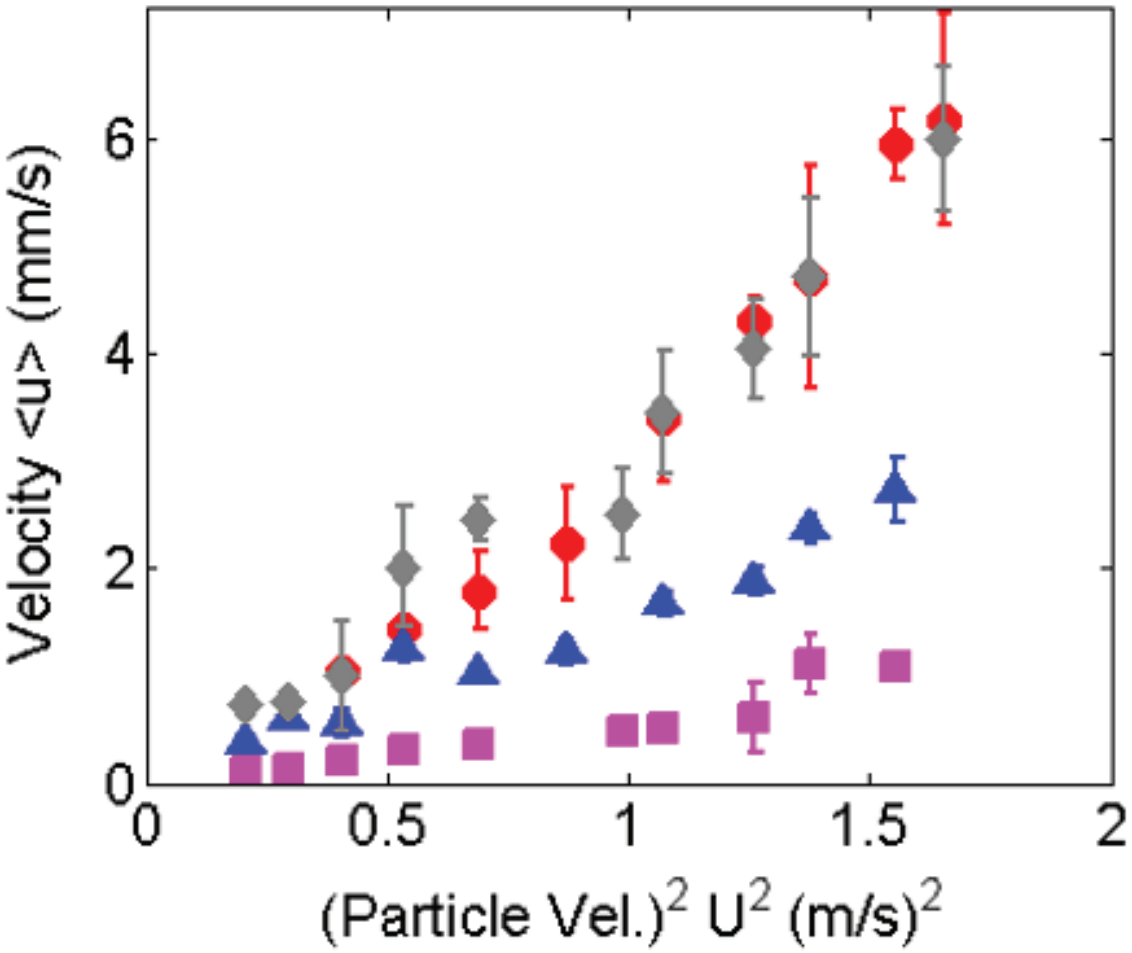

Figure 7.8: Fluid transport and meniscus dewetting deionized water from within a 150 nm-thick hydrophilic nanoslit using $\sim$ 1 W, 38.5 MHz SAW, and applied from 0 ms (*see* Fig. 2 in main paper). Scale bar: 0.5 mm. With different fluids, the meniscus velocity versus the applied power is shown. The error bars represent the range of results as low-high bars; $N \geq 10$ for each data point.

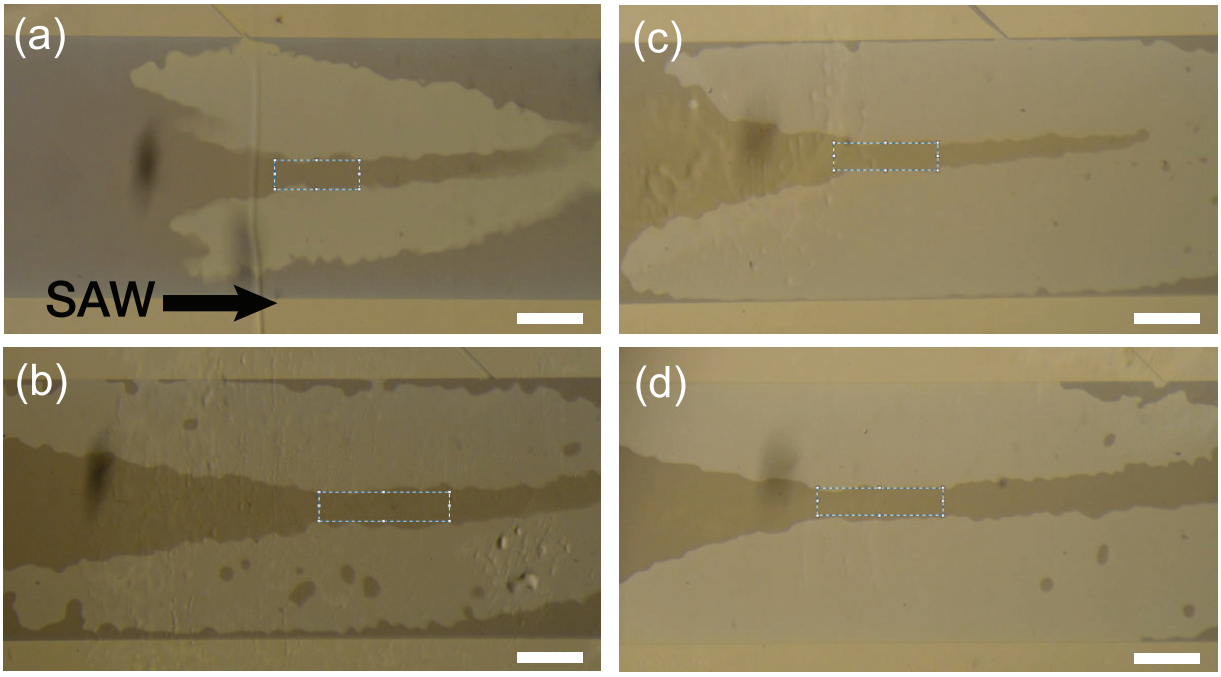

Figure 7.9: The SAW dewets the nanoslit along the central portion of the channel for (a) deionized water, (b) methanol, (c) isopropyl alcohol and (d) 1-octanol. The scale bar at bottom right for each result is 0.25 mm, and the height of each white box indicates one acoustic wavelength in the fluid, suggesting the drainage is roughly one acoustic wavelength regardless of the fluid choice.

Chapter 8

Manipulation and Mixing of 200 Femtoliter Droplets in Nanofluidic Channels using MHz-order Surface Acoustic Waves

8.1 Abstract

Controllable manipulation and effective mixing of fluids and colloids at the nanoscale is made exceptionally difficult by the dominance of surface and viscous forces. The use of MHz-order vibration has dramatically expanded in microfluidics, enabling fluid manipulation, atomization, and microscale particle and cell separation. We find even more powerful results at the nanoscale, with the key discovery of new regimes of acoustic wave interaction with 200 fL droplets of deionized water. We show that 40 MHz-order surface acoustic waves can manipulate such droplets within fully transparent, high-aspect ratio, 100 nm tall, 20–130 micron wide, 5-mm long nanoslit channels. By forming traps as locally widened regions along such a channel, individual fluid droplets may be propelled from one trap to the next, split between them, mixed, and merged. A simple theory is provided to describe the mechanisms of droplet transport and

splitting.

8.2 Introduction

Nanofluidics[99] has been proposed as a useful means to biological analysis and sensing[422], medical diagnosis[167], and material processing[117]. The analytical devices devised to work at such small scales employ nanoliter to picoliter fluid volumes, surface area-to-volume ratios of $\sim 10^7/\text{m}$ and more, and the minimum feature sizes that are possible to fabricate using massively parallelized, top-down fabrication technology[244,245,407]. A notable example is the scaling of liquid chromatography down to the nanoscale, where femtoliter (fL) to attoliter samples have been injected and successfully separated, producing vastly shorter separation times—to a few seconds, and higher separation resolution—to 7,000,000 plates/m.[164]

The idea of manipulating droplets in nanofluidics devices is enticing, as the volume of such droplets—from picoliter to attoliter[320]—approaches the size of individual large molecules and nano-objects. Consequently, it may potentially revolutionize medical diagnostics and personalized treatment[167] by increasing the sensitivity of the analytical tools underpinning these disciplines.[54,361] Manipulation of these droplets is crucial for these applications and beyond to small-volume biological integration and analysis for single molecule-in-cell applications[245,262,287].

However, manipulation of fluids and colloids at the nanoscale is made exceptionally difficult by the dominance of surface and viscous forces. Consider a typical water droplet entrapped in an air-filled, 10×10 μm square cross-section *micro*channel. the capillary (Laplace) pressure $\Delta P = \gamma(1/R_1 + 1/R_2) \approx 14.5$ kPa, where $\gamma_{\text{water}} = 72.3$ mN/m is the surface tension for water and R_1 and R_2 are the radii of curvatures. Reducing that channel to a 10×10 nm *nano*channel increases the capillary pressure to 14.5 MPa, 145 times atmospheric pressure at sea level, and very difficult to overcome by any means. Achieving this and transporting such a droplet through a nanochannel is both a significant challenge and crucial to achieving the promise

of nanofluidics.

For this purpose, a variety of pump designs that curiously employ carbon nanotubes have been proposed over the past fifteen years, using temperature gradients[218,219], Coulomb drag[421], surface waves (in theory)[163], or static electric fields[123,174,319,470]. Passive fL-scale fluid handling has also been devised using surface modification or geometric channel design[245,262]. However, despite all these attempts, due to the overwhelming dominance of surface tension, no effective active manipulation method has been experimentally demonstrated in a nanoscale enclosed fluidic channel system to date to our knowledge.

The use of MHz-order vibration has dramatically expanded in microfluidics, introducing *acoustic streaming*[253] and enabling fluid manipulation[107,233,387], atomization[112,296], and microscale to nanoscale particle/cell separation[61,129,212,284]. A novel surface acoustic wave (SAW) induced pumping method has been reported to manipulate nanoslit channel-confined fluids and suspended nanoparticles and molecules[247]. We find even more powerful results at the nanoscale, with the key discovery of a new mechanism of acoustic wave-fluid motion interaction[464]. It arises from nonlinear interactions between the surrounding channel deformation and the leading order acoustic pressure field, generating flow pressures three orders of magnitude greater than any known acoustically-mediated mechanism.

Transmitted along the length of a nanochannel, SAW was shown to be capable of delivering large pressures and rapid flows sufficient to overcome surface-mediated forces and produce fluid transport. While the production of continuous flow of fluids and colloids of particles and molecules in nanoslit channels is interesting, there may be the opportunity to exploit SAW to manipulate discrete droplets in nanoscale channels—a form of digital nanofluidics. Such confined droplets would have femtoliter to attoliter volumes, a promising result in seeking to work with extremely small quantities of analytes.

Here, we present active 200-fL fluid droplet manipulation using MHz-order SAW within high-aspect ratio, 100-nm tall, 20–130-μm wide, 5-mm long nanoslit channels, fabricated via a

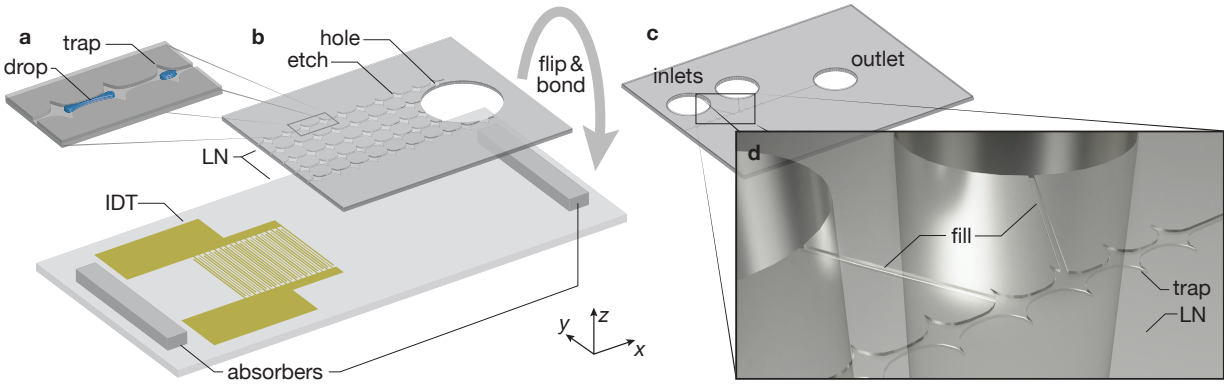

Figure 8.1: Concept and fabrication of SAW-integrated nanofluidic femtoliter droplet devices. (a) A nonuniform nanoslit channel produces fluid droplet traps. (b) By etching several of these channels into a LN layer, cutting a 1 mm hole at the end distant from the SAW interdigital transducer (IDT), and then flipping the result and bonding it with room-temperature LN-LN bonding[463], machined-side down, onto the LN substrate that has the SAW IDT, it is possible to form and transport drops in these channels with heights to less than 10 nm (figures not to scale for clarity). However, $\sim$ 100 nm height was chosen to obtain the best possible performance of the acoustic wave propagation in the nanoslit using acoustogeometric streaming[464]. Absorbers placed at the SAW LN device's ends absorbs extraneous SAW and prevents undesirable reflections. (c) Other configurations make it possible to explore drop splitting, mixing, and transport, such as this configuration with only one main channel of ten traps, two of which are connected to inlets at the side, and the x-axis-oriented main channel is open to the outside close to the IDT while it is connected to an outlet at the distant end. (d) The inlets are connected to individual, adjacent traps in this configuration by 10 μm wide channels designed to slowly carry fluid to the main channel.

direct, room-temperature bonding method[463] for lithium niobate (LN) as illustrated in Fig. 8.1. The undulating shape of wide traps connected by narrow necks was intentionally chosen to trap droplets in discrete locations and facilitate their manipulation among these traps. Contrary to the results seen in the past[247], a droplet will locate at a point where its surface energy is lower, the wider region of the trap in our system. The dimensions of the traps were chosen to entrap 200-fL droplets, which are 50 μm in diameter in a 100-nm tall channel. The radius of curvature of each of the four walls that form the trap was 60 μm, slightly larger than the trapped droplet, to ensure its central location while maintaining separation between the wall and fluid. The curvature of this shape was chosen to eliminate corners that could capture and trap droplets. These walls naturally lead to another trap via extension of one of the vertices of the trap to form a "neck" between them.

The width of the neck was chosen to be 20 μm, less than half the diameter of the 200-fL droplets but large enough to reliably fabricate in our process. Feature sizes of 2 μm may be fabricated, but the yield is better when choosing feature sizes greater than about 10 μm.

It is possible to induce $\sim$200-fL droplet splitting and transport, phenomena that are governed by the time and power of the SAW actuation for a given fluid. We provide a closed-form analytical model that accurately describes the boundaries between these handling phenomena. We also report the ability to induce merging and mixing in a $\sim$200-fL droplet, operations desirable in fluid handling whatever the scale. As an exploratory work, we set aside the issue of evaporation, actually exploiting it in forming droplets for this study. Evaporation is nonetheless an important constraint in droplet nanofluidics, more so than in droplet-based digital microfluidics, and the methods to overcome it at the microscale[46,170] may prove beneficial at the nanoscale. Altogether, our results indicate MHz-order SAW is a powerful tool for discrete fluid droplet manipulation at the nanoscale.

8.3 Results and Discussion

We designed an acoustic nanofluidic system in which the enclosed channel height was chosen to match, approximately, the viscous penetration depth of about $\sim$ 100 nm. This choice is based on some details of the acousto-geometric streaming phenomena that is unique to nanochannels when using $\sim$ 10 MHz acoustic waves. Specifically, we rely upon the physical deformation of the channel walls in direct, nonlinear coupling with the acoustic field present in the fluid to produce rapid flow against a very large pressure head[464]. This is rather different than other, traditional forms of acoustic streaming which rely on compressibility of the fluid, and which are, by comparison, exceedingly weak and would never work at the nanoscale. How this new form of acoustic streaming will act upon droplets in such a device is unclear, a key motivation for this study.

We have produced a model of the phenomena based upon an energy balance between acoustic and capillary phenomena. Details of this model along with the requisite definitions of the symbols are provided in the Methods. The model has no unknown constants and is completely independent of the experimental results.

8.3.1 Observations of Femtoliter Droplet Manipulation

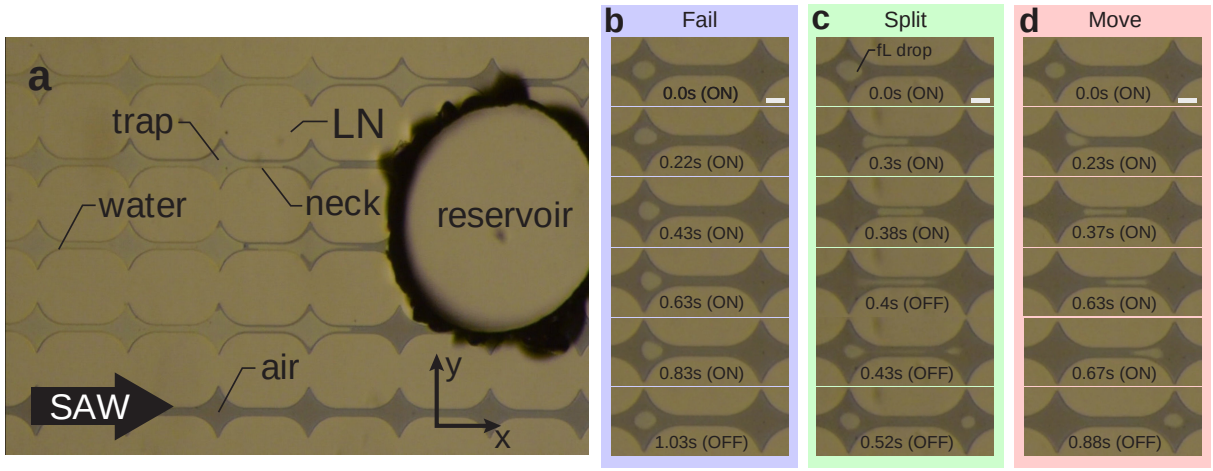

Figure 8.2: (a) The 100 nm height nanochannel matrix, with traps as shown separated by narrow regions, or *necks*. The channels are filled with DI water from the reservoir at right. SAW-driven evaporation slowly eliminates the water from the nanochannels over a period of about one minute. The experiment begins when the droplet diameter is 50 μm, corresponding to a volume of 200 fL. For scale, the narrowest width of the neck halfway between the traps is 20 μm and the trap is 130 μm at its widest in *all* figures in this study. The dark areas indicate trapped air and light areas are entrapped water. The direction of the SAW is from left to right. With judicious filling and evaporation, it is possible to form (b) a single droplet within a trap. After applying SAW, the (b-d) image sequences indicate three possible outcomes. Application of 270 mW SAW at 40 MHz for an activation time of 1.03 s (b) fails to propel a 200 fL droplet from one trap to the next. Capillary force overcomes the propulsive acoustic force. If, however, the SAW power is greater at 1.3 W for only 0.38 s, the droplet will (c) split. The droplet becomes trapped in the neck and a portion escapes to the next trap and the remainder returns to the original trap. With a longer SAW activation time of 0.67 s at the same power of 1.3 W, the SAW (d) completely moves the droplet to the next trap. Scale bars: 40 μm.

After judiciously filling the nanoslit channel structure with DI water (Fig. 8.2a), SAW-driven evaporation at an input power of 0.1 W is used to form a droplet in a single trap (e.g., the

droplet in Fig. 8.2b–d). The evaporation proceeds over $\sim$1 min to produce a droplet diameter of 50 μm, representing a 200 fL droplet in this system. Without the application of SAW, the evaporation is much slower, taking about 20 min to evaporate a 200 fL droplet of water at one of the traps. Because the manipulation of the droplets we report in this study occurs quickly, much faster than one minute, and because the anticipated applications of this technology are in devices that would need to produce results in a few minutes at most, we are able to proceed.

It becomes possible to (Fig. 8.2c–d) transport the droplet to the next trap using SAW, along the direction of the SAW's propagation. From trap to trap, the droplet must deform to pass through the neck between them, increasing its surface area and consequently its surface energy. The necks between traps, therefore, represent regions of high droplet surface energy between the lower droplet surface energy required when it is in one of the traps. With deionized (DI) water, the pressure difference from trap to neck is $\sim$ 1 kPa. While this capillary pressure is still greater than what could realistically be generated from traditional acoustic streaming, it is still three orders of magnitude less than the $\sim$ 1 MPa capillary pressure of water in filling the nanoslit channel from the outside. Lithium niobate is hydrophilic with a contact angle[151] of about 25°, so channels formed of LN tend to easily fill.

Returning now to the behavior of discrete droplets in the nanoslit channel, we find three distinct behaviors depending on the input power and duration of the activation time for the SAW. Insufficient input energy causes the failure to transport the droplet from one trap to the next, illustrated in Fig. 8.2b. A small amount of motion is observed, but the droplet remains in the same trap. With a greater amount of energy, the droplet will partially enter the neck between the two traps before splitting (*see* Fig. 8.2c). With sufficient input energy, however, the droplet may be completely moved to the next trap as in Fig. 8.2d.

An independent analytical model, detailed in the Methods, suggests (a) three regimes for droplet transport in the nanoslit device between traps in Fig. 8.3. The results from that model are plotted here using DI water with a surface tension of $\gamma = 72$ mN/m. Region 1 represents a

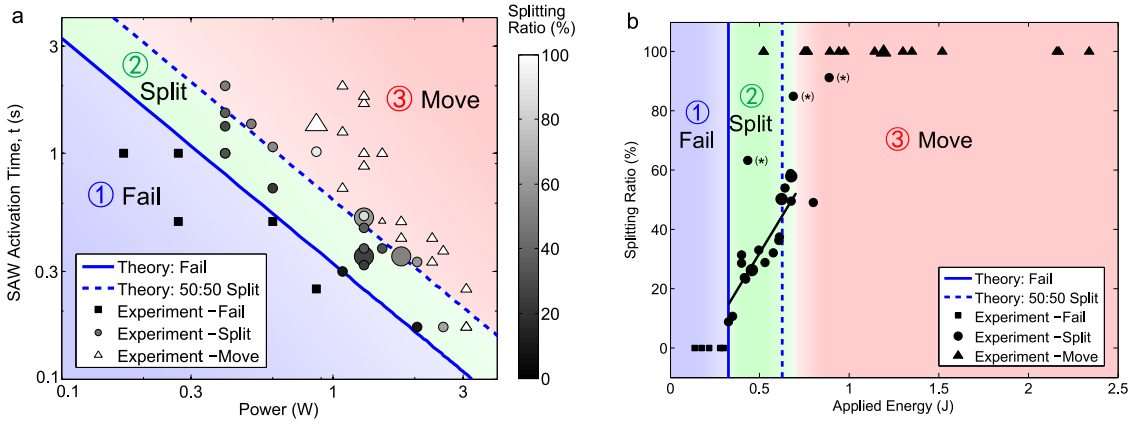

Figure 8.3: An analytical model suggests three regimes for droplet transport in the nanoslit device between traps, with comparison of experimental results using DI water with a surface tension of 72 mN/m. (a) The analytical and experimental results are log-log plotted as SAW activation time versus applied power, showing that the independent experimental results (with 43 test samples in total) are correlated with the model. The results are provided (b) again, this time in terms of the splitting ratio versus applied energy, the product of (a) SAW power and activation time. The droplet transport behavior is mainly dependent on the applied acoustic energy, with a narrow region (2) of splitting between (1) failure to transport and (3) complete movement of the droplet to the next trap. Note that successful splitting occurs in delivering 10%-60% of the parent droplet's volume to the new trap. It is generally difficult to split more than 60% of the parent droplet's volume and transport it to the new trap, with only three successful (*) examples out of 35 trials for these specific conditions. The reason this occurs is explained and discussed in the Analysis subsection of the Methods. Omitting these three points, a linear fit of the remaining splitting droplet data (with 18 test samples in total) in region 2 (black line) indicates a reasonable correlation ($R^2 = 0.779$) between the applied input energy and the volume of the split droplet present in the new trap. A linear plot of the (a) SAW activation time versus power is provided in Suppl. Fig. S1 to indicate the close correlation of the theory with experiments in DI water and isopropyl alcohol. Video footage of the droplet behaviors along with details of how the droplet volume is calculated from observations are described in the Supplementary Information. Symbol sizes here represent the droplet volume; most are a medium size for $\sim$ 200 fL, while a few are large for $\sim$ 400 fL and small for $\sim$ 100 fL. The effect of the droplet size is weak. The data was confirmed to be normally distributed via a Shapiro-Wilk test, and the text describes the outcomes from a test of monotonicity in region 2 using Spearman's rank coefficient.

failure to transport any or all of the droplet's volume from a trap. This occurs when the product of the applied SAW power and its duration, the input energy, is below a critical value, $(C_1 - C_0)h\gamma$, defined mainly by the nanoslit height, h and the surface tension of the fluid, γ. Taken from the Methods, this represents a droplet surface energy difference, from the trap to the neck, to be overcome by the input energy. The constant $(C_1 - C_0)$ represents the change in the circumference

of the droplet as it moves from the trap to the neck, with the right end of the drop at the midpoint or narrowest point of the neck. The critical energy demarcating failure (region 1) from other phenomena (regions 2 & 3) is plotted with a thick blue line in Fig. 8.3.

As the power is increased, the time required to at least obtain splitting is decreased. In our experiments, we used at least 100 mW of input power, the lower limit in our system while avoiding undue signal noise; at that power about 2 s or more would be required according to the theory. In the DI water experiments, using 200–300 mW for 1 s failed to transport the droplet. At 2 W and 0.2 s, the applied SAW split the droplet trapped in the first trap, but only delivered about 20% to the next trap. Increasing the power for this same time of application to 2.5 W delivers 50% to the next trap, and 3 W moves the entire droplet. In this system, 3 W represented the maximum power we were able to use, limited by atomization or jetting[66] and other curious effects outside the scope of this work.

There is an intermediate range of SAW energy at which it is possible to partially carry the droplet through the neck to the next trap in region 2, splitting the droplet within the neck, and causing some of the volume to return to the original trap and the remainder traveling onward to the next trap. A second, dashed line is plotted from analysis results in Fig. 8.3 to indicate equal (50:50) splitting of the droplet between the traps. The necessary deformation from a circular cylindrical droplet in the trap to a thin elliptical droplet in the neck symmetrically placed between two traps is conceptualized in Fig. 8.1a.

In the experiments, it was observed that it is possible to split between about 10% to 60% of the parent droplet's volume and transport this to the next trap. It was generally difficult to split and transport more than 60% of the parent droplet's volume, as discussed in more detail in the analysis section in the Methods. With very few exceptions (as indicated with asterisks in Fig. 8.3b), in seeking to move such a large portion of the parent droplet to the new trap, generally the entire droplet was moved instead. Omitting these three points, a linear fit of the remaining splitting droplet data in region 2 (black line, Fig. 8.3b) indicates a reasonable correlation ($R^2 = 0.779$)

between the applied input energy and the volume of the split droplet present in the new trap. This is expected as the droplet requires progressively larger amounts of energy to deform it into the neck until it reaches the 50:50 split location. It is also supported via a Spearman's rank correlation coefficient computation, producing $r = 0.901$ with a 95% confidence interval from 0.744 to 0.964, a nearly perfect increasing monotonicity of splitting ratio as a function of input energy in this regime.

Likewise, it was difficult to split less than about 10% of the droplet volume off from the parent droplet to be transported to the new trap. It is suspected that if the SAW was applied with greater precision in power and time, droplet volumes smaller than 10% could possibly be split and transported to the new trap. However, the lateral size of a droplet entrapped in the nanoslit with a volume of 20 fL, 10% of the parent 200 fL droplet, is only 8 μm, less than half of the neck width: 20 μm. Droplets smaller than 20 fL are suspected to be difficult to produce unless the neck width is also made smaller to produce greater lateral confinement and deformation of the parent drop.

If the SAW power and duration, and therefore the input energy, are even greater, the droplet will be entirely transported to the next trap as defined by region 3. The additional energy required is the kinetic energy necessary to move the majority—at least 60%—of the droplet beyond the middle of the neck. The vagueness here is due in part to the difficulty in pinching off and splitting less than 40% of the trailing portion of the droplet to return to the original trap. It is also due to the relatively slow capillary time in comparison to the time required for the droplet to traverse the neck to the next trap, detailed in the Methods.

Nonetheless, this model accurately describes the three observed droplet manipulation regions in Suppl. Fig. S1 for this and isopropyl alcohol as an example of another fluid. Video footage of the droplet behaviors is provided in the Supplementary Information for additional context.

In our device, the acoustic energy imparted into the droplet is $E_{\mathrm{ac}} = \frac{A}{w\alpha^{-1}}\eta W(1-1/\mathrm{e})t \sim$

10^{-11} J[79]. This is on the same order as the change in capillary energy required to move the droplet from a circular cylindrical shape (circumference C_0) in the trap to the narrow elliptical shape (circumference C_2) in the neck, $E_{\text{cap}} = (C_2 - C_0)h\gamma \sim 10^{-11}$ J. The fact the acoustic and surface energies are on the same order supports the notion of using SAW to transport these droplets from trap to neck—and onward to the next trap.

8.3.2 Femtoliter Droplet Merging and Mixing

Merging droplets at the nanoscale

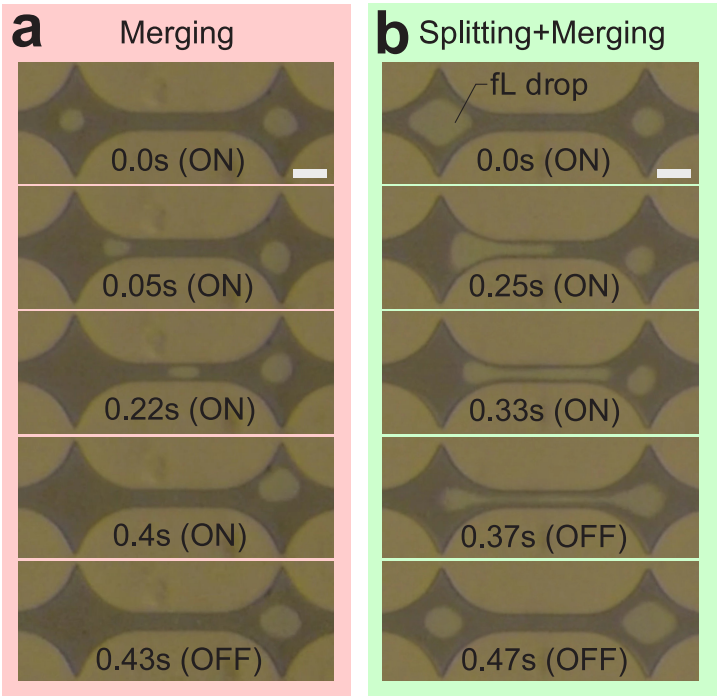

Figure 8.4: Image series showing femtoliter droplets merging via SAW actuation in a $\sim$ 100 nm-height nanochannel. The SAW propagates from left to right. (a) The droplet in the left trap is completely transported and merged with the droplet in the right trap using a SAW power of 1.78 W and activation time of 0.42 s. (b) The droplet in the left trap is split with the same SAW power of 1.78 W but a shorter activation time of 0.35 s. The split portion is merged with the droplet present in the right trap; the remainder returns to the left trap. Adjusting the SAW power and activation time controls the splitting and merging phenomenon. Scale bar: 40 μm.

After introducing SAW-induced fluid manipulation of a single droplet in a nanoscale

channel, here we present the merging of two femtoliter droplets in a nanochannel using SAW. We are able to partially (*split*) or completely (*move*) transport one femtoliter droplet to the next trap, merging it with a droplet already located there. Figure 8.4 provides two examples of the merging phenomenon while using 1.78 W SAW power. Figure 8.4a demonstrates an entire droplet transported from one trap to the next to merge it with a second droplet. Figure 8.4b shows the splitting of the parent droplet in the trap at left, followed by the merging of the portion that travels through the neck to the droplet already present there. The key difference between the two results was the use of different SAW activation time, 0.42 s for the (a) entire droplet, and 0.35 s for (b) splitting and merging, respectively.

The presence of the droplet at left in these examples acts to absorb a significant amount of SAW propagating from left to right in Fig. 8.4. The remaining SAW energy, if any, that interacts with the droplet at the right is insufficient to move or split it.

This produces another useful tool in droplet manipulation at these small scales. A careful look at Fig. 8.4 shows that the starting volume of the droplets is slightly different. This only weakly affects the splitting and moving behavior in this system.

Using the analysis from the Methods, the starting circumference of a larger droplet is itself larger. Therefore, the increment in energy required to place it into the neck might at first seem to be lower, because the starting free surface energy is larger. However, a larger droplet must also have the same semiminor axis length that matches the neck width while extending farther along the channel to produce a larger semimajor axis length. The energy required to put it in the middle of the neck for a 50:50 split, for example, is therefore also greater. These two effects are approximately the same, producing approximately the same result for different starting droplet volumes.

Whether for transport, splitting, or merging, the effect of the droplet size appears to be weak between 100 fL and 400 fL, because the basic shape undertaken by the droplet when in the trap and in the neck between the traps is similar to a 200 fL droplet. The SAW is pervasive,

present everywhere, and changing the miniscule size of these droplets has no observable effect on the SAW nor the interaction between the droplet and SAW. At less than 100 fL, the "pinching" effect of the neck is eliminated, implying droplets smaller in diameter than about 20 μm in the system will simply pass through the neck from trap to trap without any change in surface energy. Beyond 400 fL, the shape of the entrapped droplet is significantly affected by the trap shape. These effects are only due to the design, and, for example, a narrower neck combined with larger traps may improve the range of fluid volumes. However, such changes may cause other difficulties, including less ability to define the droplet size via evaporation and significantly greater time to transport, split, or merge the droplets.

There is also the matter of the product of input SAW power, W and its active duration, t producing a given input SAW acoustic energy $E_{\mathrm{ac,in}} = Wt$. In manipulating single droplets, it was apparent from Fig. 8.3 that the SAW acoustic energy alone was sufficient to describe the droplet behavior. With a pair of droplets, we have observed that the merging results—whether splitting and merging or merging alone—are generally improved for a given acoustic energy by increasing the power and decreasing the activation time.

The difference in SAW power upon the left and right droplets in their respective traps is greater as the input power increases. There is no effect of changing the time, as it is always longer than the time it takes for the SAW to propagate throughout the device. Therefore, using a greater power for a shorter time produces a greater difference in acoustic energy applied to the two droplets, and this is why the results improve.

There is an opportunity for substantial further work here, by employing different fluids, different trap-neck-trap geometries, the SAW characteristics including its frequency and modulation, programmable acoustic actuation for two-dimensional droplet manipulation, and certainly extension to practical experiments in biology and chemistry. Our main purpose was to show the existence of the basic tools to facilitate these efforts, and we now add another useful tool: mixing.

Mixing within single femtoliter droplets using SAW

Mixing has long been a desirable outcome in sample processing and chemistry whatever the scale of the sample, and is a challenge at the micro-scale and beyond to smaller dimensions. Even though the droplet is small, it is confined, and diffusion is slow. The characteristic time of diffusion is $t_{\mathrm{d}} \sim x^2/D \sim 10^2/10^1\mathrm{s} = 10\ s$ for a typical nanoparticle in water[257], though at these scales the surface chemistry of the particle can significantly affect the diffusion rate.

Nonetheless, it would still be beneficial to speed the mixing process if possible in such a droplet through convection. Here we demonstrate SAW-induced convective mixing within a single 400 fL droplet while it remains stationary in a trap, using 50 nm nanoparticles. This is accomplished by exposing it to SAW energy less than the threshold defined in Fig. 8.3 between regions 1 and 2.

To conduct this experiment, DI water mixed with 50 nm nanoparticles at a concentration of 3.64×10^{11} particles/μL were delivered into the system shown in Fig. 8.2a, filling the nanoslit channels via capillary wetting. Evaporation was allowed to proceed for about 30 s to produce the result in Fig. 8.5(a), a distinctly separated and locally concentrated suspension of nanoparticles within a fluid droplet of approximately 400 fL filling one of the traps of the device. Over time, diffusion only weakly affects the distribution of particles (Fig. 8.5a–c) without SAW. However, introducing 380 mW SAW for 0.5 s, notably in region 1 of Fig. 8.3, vortices generated by apparent acoustic streaming within the droplet cause the rapid mixing of the suspended nanoparticles to produce a relatively well-mixed result in 0.5 s (Fig. 8.5d–f).

This result may be quantified[142] by calculating the standard deviation of the pixel intensity of the captured images in Fig. 8.5a–f. If the particles remain unmixed and locally concentrated, they produce local regions of brighter fluorescence and intensity, surrounded by relatively dark regions where the particles are few in number. This produces a large range of pixel intensity, likewise producing a large standard deviation. The result for the diffusion-only nanoparticle mixing process is compared to the SAW-aided mixing in Fig. 8.5g. Notably, both begin with a

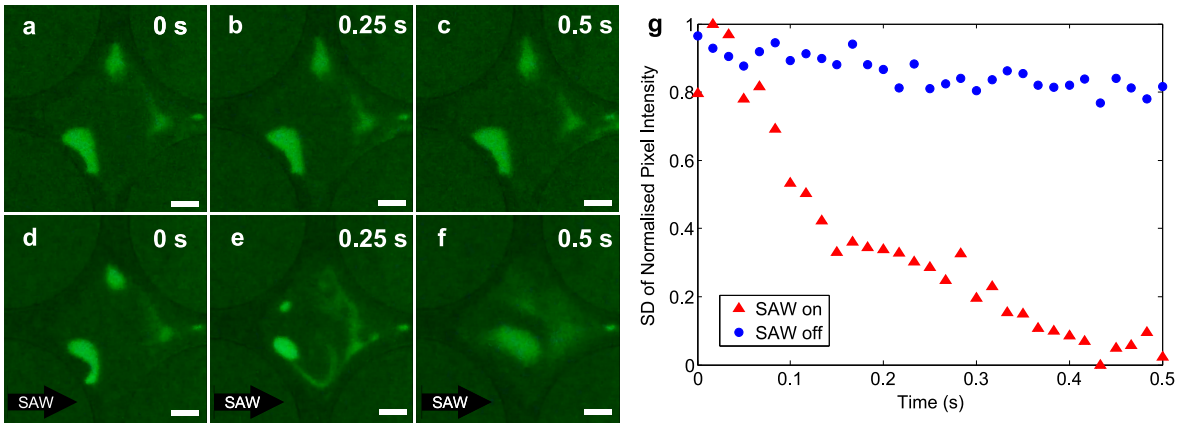

Figure 8.5: Effective SAW induced fluid mixing of 50 nm green fluorescent polystyrene particles within a 400 fL droplet in an $h = 100$ nm nanoslit trap. (a-c) Images of the trapped, nanoparticle-laden droplet in the trap without SAW at 0, 0.25, and 0.5 s, showing negligible mixing with nearly identical images. However, when using 380 mW SAW (left to right in images), (d-f) mixing occurs to produce a comparatively complete mixing result over the same time period. Scale bars: 20 μm. A plot of the (g) standard deviation (SD) of the normalised pixel intensity from these and additional images in the sequence (with 31 test samples over 0.5 s from images captured at 60 fps) with and without SAW serve to quantify the effectiveness of the mixing. With SAW, the mixing is nearly complete in 0.4 s, with SD $\rightarrow 0$ in that time. By comparison, without SAW, the SD declines from about one to 0.85 over 0.5 s. The pixel intensity data was confirmed to be normal via the Shapiro-Wilk test and the monotonic decrease for each data set was confirmed by computing Spearman's rank correlation coefficient: $r = -0.982$ while the SAW was on and $r = -0.814$ while the SAW was off.

similar standard deviation at one, reflecting the range of pixel intensities at this time from zero to one. Diffusion alone gradually reduces the standard deviation to 0.85 after 0.5 s. However, with SAW, the standard deviation goes to zero, indicating complete mixing, in just over 0.4 s. Spearman's rank correlation coefficients (r) were computed for each case to evaluate both the monotonic decrease in the standard deviation with respect to time and the effect of using SAW. The coefficient $r = -0.982$ while SAW was on with a 95% confidence interval from -0.992 to -0.962, and $r = -0.814$ while the SAW was off with a 95% confidence interval from -0.909 to -0.640. This indicates a stronger decreasing monotonic trend of the standard deviation with respect to time with SAW actuation than with thermal diffusion alone.

While most chemical processes are of course molecules, and therefore far smaller and far more rapidly diffusing than nanoparticles, the ability to mix is still believed to be beneficial in significantly speeding up the process. In Fig. 8.5g, the initial reduction in the standard deviation is very rapid, from 1 to 0.4 in 0.15 s, a consequence of most of the droplet mixing. A small region at lower left seen in Fig. 8.5d,e takes longer to mix, contributing to the slower result seen from 0.15 to 0.4 s. This is believed to be due to the fact that this portion of the droplet is not located in the main channel of the nanoslit, and the SAW is at a lower magnitude here. It may be possible to produce even more rapid mixing results if the trap is redesigned to also accommodate mixing and prevent these regions.

In this system, generally the viscous penetration depth $\delta \sim 100$ nm is nearly equal to the channel height. Thus, the mixing seen here is mixing occurring in the viscous boundary layer. The flow patterns that appear are defined by the droplet size. In other words, there are no apparent internal vortices or mixing at shorter length scales. If the droplets were larger, it may be possible that the mixing occurs on the same scale as the wavelength of the SAW, based on past observations[247,464]. However, the wavelength of the 40 MHz SAW used here is 100 μm, while the (lateral) droplet size is also about 100 μm.

8.4 Conclusions

We developed a simple technique for femtoliter droplet manipulation in a nanofluidic system using high frequency SAW. Nano-height channels were fabricated using reactive ion etching and room temperature LN-LN bonding.

We focused on water in our experiments, as most applications would employ water. We also provide results using isopropyl alcohol in the SI, showing similarly good correlation between experiment and analysis. Switching fluids at these small scales is more problematic than at the micro or larger scales. Initially, the femtoliter droplets are located in the wider region of the

nanochannels—traps—where their surface free energy is minimized. But by applying SAW, it is possible to introduce sufficient energy to permit them to be deformed and pass through the narrow necks between traps to facilitate drop splitting and transport.

A model of the phenomena was devised, and since the model has no constants to adjust, it is reasonable to conclude the simple models adequately represent the observed phenomena, based on the close correlations between the experimental results and the theoretical model. We also demonstrated the ability to merge and rapidly mix droplets in the system, additional useful tools for future digital nanofluidics.

These results suggest ideas for future changes in the channel profile to produce better droplet handling outcomes as desired when manipulating them via SAW, for example, to make it possible to manipulate a greater range of droplet sizes, to tailor the design to split extremely small portions of fluid from a parent drop, and to expand these devices to perform in a parallel fashion with many droplets at once, both laterally and axially. Furthermore, given the rapid response of SAW, it may be possible to perform more complex manipulations by modulating the SAW over time. Finally, by combining the various operations reported in this paper with novel droplet generation methods under study by other groups[144], SAW nanofluidics may become far more straightforward to use in applications, providing an extraordinary opportunity to achieve the lofty aims of "lab-on-a-chip" via useful nanofluidics.

8.5 Experimental Section

8.5.1 Device and Nanoslit Channel Fabrication

We designed an acoustic nanofluidic system in which the viscous penetration depth is approximately identical to the characteristic height of the channel (i.e., $\sim$ 100 nm). We performed fabrication of nanoheight channels incorporating surface acoustic wave actuation on 128° Y-rotated X-propagating lithium niobate (LN, Precision Micro-Optics Inc., Burlington, MA, USA)

substrate[247,463]. Reactive ion etching (Plasmalab 100, Oxford Instruments, Abingdon, UK) was first utilized to create a nanoheight depression of the undulating channels (130 μm at its widest and 20 μm at its most narrow) on an LN substrate with patterned Cr as a sacrificial mask. The Cr sacrificial mask was later removed by Cr etchant (Fig. 8.1(a1)).

A 1-mm hole was then drilled (Dremel #4000, Mount Prospect, Illinois, USA) through the chip to form an input liquid reservoir for the nanoslit system (Fig. 8.1(a2)). IDT fingers with a 25 μm width and spacing, corresponding a resonance frequency of $\sim$ 40 MHz, were fabricated on another flat LN substrate via common photolithography (MLA 150, Heidelberg Instruments, Heidelberg, Germany), 5 nm/450 nm Cr/Au sputtering deposition (Denton 18, Denton Vacuum, NJ, USA), and the lift-off process (Fig. 8.1(b1)). Room-temperature LN bonding was performed after piranha cleaning and oxygen plasma surface activation (PVA TePla PS100, Corona, CA, USA). The bonded chip was clamped and heated up to 300 °C in an oven (HTCR 6/28, Carbolite, Hope Valley, UK) to enhance the bonding strength (Fig. 8.1(c)). The bonding strength is stronger than the acoustic pressure and the capillary pressure, at least $\sim$ 1 MPa, preventing debonding when SAW is actuated into the fluid inside the nanoslit.

8.5.2 Operation of the Device

A radio frequency ($\sim$ 40 MHz) alternating current signal was generated from a signal generator (WF1967 multifunction generator, NF Corporation, Yokohama, Japan), amplified via a 5 W amplifier (5U1000, Amplifier Research Corp., Souderton, Pennsylvania, USA), and transmitted to IDT electrodes via custom connecting pogo pins. Oscilloscope (InfiniiVision 2000 X-Series, Keysight Technologies, Santa Rosa, CA, USA) was used to measure the electrical properties (e.g., voltage, current, power) applied into the SAW device. Absorbers (Dragon Skin 10 Medium, Smooth-On, Inc., Macungie, PA, USA) were attached at the edges of the LN chip to prevent reflected waves.

Ultra-pure DI water was used to avoid clogging and introduced into the reservoirs illus-

trated in Fig. 8.1b,c. Discrete droplets of the DI water appeared at the traps after evaporation; as the water evaporates, the fluid interface retracts into these trap regions to minimize surface energy. Typical droplet volumes were 200 fL, based on observations of the droplet diameter of diameter $d \sim 50$ μm and a height $h \sim 100$ nm.

The computation of the capillary pressures for a droplet from ambient to entrapped within the device at a trap and at a neck between two traps is provided in the next subsection.

Fluid motion was recorded via inverted microscope (Amscope IN480TC–FL–MF603, Irvine, CA, USA) combined with cameras (Nikon D5300, Minato, Tokyo, Japan, and FASTCAM Mini UX100, Photron, Tokyo, Japan). Fluid motion, velocity, and fluorescence intensity were analyzed via custom image processing (MATLAB, Mathworks, Natick, Massachusetts, USA) code. For experiments in mixing, fluorescent 50-nm particles (Fluorescein-5-isothiocyanate (FITC) dyed polystyrene particles, Polysciences, Inc., Warrington, PA, USA) at a rather high concentration of 3.64×10^{11} particles/μL were used to visualize the flow and ability to mix.

8.5.3 Statistical Analysis

For the results plotted in Fig. 8.3, observations were made regarding the behavior of the droplet for a combination of the SAW activation time and input power. Uncertainty in these parameters was less than one percent. Forty-three results are plotted in Fig. 8.3 without interpretation, either representing droplet splitting, movement from trap to trap, or a failure to either split or move. For the fitting of data to the expected linear relationship between the splitting ratio and applied energy in Fig. 8.3b, based on the physics, the distribution of the splitting ratio to applied energy was first confirmed to be normal via the Shapiro-Wilk test before using linear regression for the fitting line. The coefficient of determination $R^2 = 0.779$, indicating a reasonably good fit. Further, to test for the expected monotonic increase in the splitting ratio versus applied energy, Spearman's rank-order correlation coefficient was computed and found to be $r = 0.901$ with a 95% confidence interval from 0.744 to 0.964, a nearly perfect increasing monotonicity.

Regarding the droplet mixing results in Fig. 8.5, the pixel intensity data relevant to the droplet region was extracted from the images in Fig. 8.5(a–f) and an additional 56 similar images. Data associated with the walls of the trap and outside the droplet were excluded from consideration. The resulting data were found to be normally distributed over the range 0–1 (black to 100% green) via Shapiro-Wilk tests of the data per image and of all data across all images. The standard deviation (SD) of the normalised pixel intensities was then computed[142] to quantify the state of mixing. Notably, both begin with a similar standard deviation at 1, reflecting the broad range of pixel intensities at this time. Spearman's rank correlation coefficients were $r = -0.982$ while SAW was on with a 95% confidence interval from -0.992 to -0.962, and $r = -0.814$ while the SAW was off with a 95% confidence interval from -0.909 to -0.640. All statistical analysis was performed using GraphPad Prism v9 (GraphPad Software Inc., San Diego, CA, USA).

8.5.4 Analysis

The outcome of the acoustic manipulation of a droplet in the nanoslit system depends upon the acoustic energy transmitted into the droplet. This energy is a product of the input power and the duration of the SAW as plotted in Fig. 8.3, and the fraction of the actual acoustic energy taken up by the droplet from the SAW-carrying LN substrate. The behavior of the SAW-manipulated droplet was divided into three regimes, failure, splitting, and moving to the next trap.

We first calculate the surface energy of the droplet when at rest in a trap, E_0. The trapped droplet is assumed to have a circular cylindrical shape with a known radius, r_0, and height, h. Thus, the surface energy is given as $E_0 = C_0 h\gamma = 2\pi r_0 h\gamma$.

We compare this to the surface energy of the droplet when its right end just reaches the middle and narrowest region of the neck. This is the free surface energy the droplet must possess to *almost*—but not quite—pass a portion of it to the next trap, E_1, representing the boundary (*see* Fig. 8.3) between failure (1) and splitting (2).

With more input acoustic energy, the droplet should be able to travel further into the neck, deforming more and passing at least part of it into the neck widening from its midpoint. We consider the case at which the droplet is squeezed symmetrically (50:50) about the neck's midpoint. This is the definition of the boundary between regions 2 and 3, splitting and moving completely to the next trap. At this point, the droplet should have a surface energy of E_2.

Finally, we define the input acoustic energy required to completely move the droplet to the next trap. This is actually only slightly more than the energy required to place the droplet at the midpoint of the neck, due to the induction of excess kinetic energy in the droplet that propels it past the neck. This increment is small, much less than, say, $E_2 - E_1$, because the hydrodynamic time is one to two orders of magnitude greater than the time required to pass additional acoustic energy into the system to push the droplet to entirely move to the next trap (region 3). Furthermore, once the droplet passes the narrowest point of the neck, the droplet will begin to return to a circular cylindrical shape. The energy it recovers from the reduction in its free surface energy produces additional kinetic energy sufficient to carry it on to the next trap.

For this analysis, we assume that the shape of the droplet is a right circular cylinder when in the trap, a somewhat complex egg cylinder shape—a Hügelschäffer's ovoid[335]—when between the trap and neck, and an elliptical cylinder when trapped symmetrically in the neck. When symmetrically placed in the neck, one could make an improved assumption that the droplet is a Cassini (biconcave) oval cylinder, at very substantial increase in analysis complexity[115,419] as one seeks to find the circumference, without much improvement in the results.

We first consider the shape and surface energy of the droplet when it is symmetrically trapped at the neck between two traps. The surface energy of the drop is always $E_i = C_i h\gamma$, with C_i referring to the circumference of the droplet. When symmetrically trapped, this equation becomes $E_2 = C_2 h\gamma$, with C_2 as the ellipse's circumference. Unfortunately, there is no closed-form solution for the circumference of an ellipse, which is most often represented as an elliptical integral of the second kind. However, the eminent mathematician Ramanujan devised an accurate

approximations for it[300],

$$C_2 = 4a\int_0^{\pi/2}\sqrt{1-e^2\sin^2\theta}d\theta \approx \pi(a+b)\left(1+\frac{3m}{10+\sqrt{4-3m}}\right), \tag{8.1}$$

where $m=(\frac{a-b}{a+b})^2$ is defined in terms of the semimajor and semiminor axes a and b. Here we define $b=d/2$, where d is the minimum width of the neck between the two traps. The semimajor length, a, may either be measured from the images, or determined from knowledge of the droplet's original radius when a circular cylindrical shape in the trap. The droplet volume is $V=\pi abh$ in the neck, and is $V=\pi hr_0^2$ in the trap, producing $a=V/\pi bh=r_0^2/b=2r_0^2/d$.

We next consider the shape and surface energy of the droplet when its right end is located at the midpoint in the neck between the two traps. The surface energy is estimated to be determined by the equation $E_1=C_1h\gamma$, with C_1 the circumference of an asymmetric ellipse that has the same semimajor and semiminor axis lengths as the droplet, but is "egg" shaped, formally known as Hügelschäffer's ovoid. We employ the following equation for this purpose,[270,335]

$$\left(\frac{x}{a}\right)^2+\left(\frac{y}{b}e^{cx}\right)^2=1, \tag{8.2}$$

with $c=0.35$ to match the asymmetric shape of the observed droplet in this state. The circumference of this shape is given by

$$C_1=2\int_{-a}^{a}\sqrt{\left(1-\frac{x^2}{a^2}\right)^{-1}b^2e^{-2cx}\left(\frac{cx^2}{a^2}-\frac{x}{a^2}-c\right)^2+1}\,dx, \tag{8.3}$$

and there is no known approximate solution to this equation. It may, however, be solved numerically without much difficulty.

From these results, we may estimate the minimum energy required to transport the droplet to the neck but failing to transport any of the droplet to the next trap. This is E_1-E_0; the droplet will return to the original trap afterwards. Similarly, the energy required to symmetrically place

the droplet at the center of the neck in order to split it equally among the two traps is then at least $E_2 - E_0$. Before considering what is necessary to completely move the droplet to the next trap, we determine the details of the input into the device required to deliver these required changes in the surface energy.

We begin by assuming the acoustic energy is uniformly distributed across the width of the IDT's aperture, w, and that the aperture is larger than the droplet diameter, $w > 2r_0$. Along the propagation direction, we assume the SAW is weakly attenuated as defined from an attenuation length α^{-1}. Within this area, $(w)(\alpha^{-1})$, the acoustic power may be written[79] as $\eta(1-\frac{1}{e})W$, determining the width and profile of the acoustic field, where $\eta \sim 0.15$ is the electromechanical coupling coefficient of 127.86° Y-rotated, X-propagating LN[465], e is Euler's number, and W is the applied electrical power into the SAW device. Because of the assumption of a uniformly distributed acoustic power across the width of the SAW device's aperture, we may determine the acoustic energy transmitted into the droplet, E_{ac}, by considering the droplet's surface area in contact with the SAW-driven LN substrate,

$$E_{ac} = \frac{A}{w\alpha^{-1}}\eta\left(1-\frac{1}{e}\right)Wt, \tag{8.4}$$

where t is the activation time of the SAW. By setting $E_{ac} = E_i - E_0$ with $i \in \{1,2\}$ and noting every term in eqn. (8.4) is known, except for the activation time t and applied SAW power W, we may solve for the product of these two parameters, Wt, to produce

$$Wt = \frac{w\alpha^{-1}}{A\eta\left(1-\frac{1}{e}\right)}\left(C_i - C_0\right)h\gamma \tag{8.5}$$

to determine the input power and activation time required to almost transport the droplet out of the trap ($C_1 - C_0$) or split it 50:50 between the two traps ($C_2 - C_0$).

These results are used to produce the solid and dashed lines in Fig. 8.3 and are independent of the experimental results, with the exception of the droplet diameter at the start of each

experiment. They appear to be strongly correlated with the experimental observations.

Beyond the 50:50 splitting of the droplet defined by the dashed line in Fig. 8.3, there still is the possibility of splitting a droplet such that the amount traveling to the next trap is between 50–100%, leaving 0–50% to return to the original trap. We now consider how an excess in acoustic energy, $E_{\text{ac}} > E_2 - E_0$ could lead to this outcome.

Suppose we have an acoustic energy Wt_0 that precisely overcomes the surface energy of the droplet from its minimum E_0 in the trap to its maximum E_2 in the neck. In other words, set $E_{\text{ac}} = kWt_0 = E_2 - E_0$, where $k = \frac{A}{w\alpha^{-1}}\eta(1-\frac{1}{e})$, and recall the details of the acoustic energy in eqn. (8.5). The droplet would end up symmetrically trapped in the neck, eventually splitting due to the favorable decrease in surface energy as the droplet halves draw themselves away from the center of the neck.

Now we suppose the activation is longer, $t_1 > t_0$, maintaining the same applied input power, W. This increases the acoustic input energy by an amount corresponding to $kW(t_1 - t_0)$. If we assume this energy passes to the kinetic energy of the droplet, T, then

$$kW(t_1 - t_0) = T = \frac{1}{2}mv^2, \tag{8.6}$$

where m is the droplet mass and v is the droplet velocity when the SAW turns off at t_1.

As the acoustic power does not change when the SAW is on, we estimate the droplet exhibits constant acceleration so that we have

$$\frac{1}{2}v(t_1 - t_0) = l/2, \tag{8.7}$$

where l is the length of the neck from one trap to the next. Combining eqns. (8.5) and (8.7), we have

$$kW(t_1 - t_0) = \frac{1}{2}m\left(\frac{l}{t_1 - t_0}\right)^2 \tag{8.8}$$

and so

$$t_1 - t_0 = \left(\frac{ml^2 t_0}{2(C_2 - C_0)h\gamma} \right)^{\frac{1}{3}} \tag{8.9}$$

as our result. While we could seek to determine the energy produced by such an increment in time, or aim to determine the velocity the droplet would need to have at the neck to ensure its complete passage to the next trap, it is most helpful to consider the time one must leave the SAW on beyond the time to trap the droplet 50:50 in the neck, $t_1 - t_0$. By substituting values from our experiments, we have $(t_1 - t_0) \sim 10^{-3}$ s.

The time scale of the acoustic wave, 40 MHz SAW, is far less, on the order of 10^{-6} s. It is therefore possible to drive SAW for $(t_1 - t_0) \sim 10^{-3}$ s to split the droplet and put 50–100% of its volume in the next trap.

However, the hydrodynamics is much slower. The capillary time[74] is on the order of $10^{-2} \sim 10^{-1}$ s, one to two orders of magnitude larger than $t_1 - t_0$. So though it is possible to control the SAW's timing, the hydrodynamics is too slow to allow controlled splitting of a droplet such that 50–100% of its volume is in the next trap.

To pinch off a droplet of less than 50%, the speed of the droplet in its initial transport into the neck is high, with a quick response due to the presence of the SAW that is faster than the capillary time. However, the SAW stops before the droplet progresses beyond halfway through the neck, and the slow hydrodynamics associated with the capillary time takes over to define the droplet's behavior. A smaller portion of the droplet already past the midpoint of the neck may be pinched off before the entire droplet returns to the original well.

However, to pinch off a droplet of more than 50%, the SAW must be applied for a longer period of time. Once the droplet begins to move and advances more than 50% of its volume through the neck, it is impossible to arrest the hydrodynamics in time to split a small portion, say, of the droplet from the trailing edge to leave it behind. By the time that trailing edge portion would be pinched off in capillary time, the entire droplet is already in the new trap.

The implication is that while a 50:50 split is possible with the application of energy

equivalent to $E_2 - E_0$, moving the droplet completely to the next trap is simply a matter of applying slightly more energy. The dynamics takes care of the rest.

8.6 Appendix

8.6.1 Droplet Manipulation Regimes, Linearly Plotted

The behavior of a 200 fL droplet of fluid initially located in a trap in our device and exposed to SAW is provided in Suppl. Fig. 8.6(a) for DI water as a linear plot of the SAW applied power versus activation time, indicating the close correspondence of the theory and experimental results without the vagueness of a log-log plot as provided in the main text—but with less clarity as the data points are somewhat crowded here. As an example of another fluid, experimental results using isopropyl alcohol (IPA; CAS 67–63-0, SigmaAldrich, St. Louis, MO USA) with surface tension $\gamma = 22$ mN/m are plotted in Suppl. Fig. 8.6(b) against the analytical model showing a close correlation.

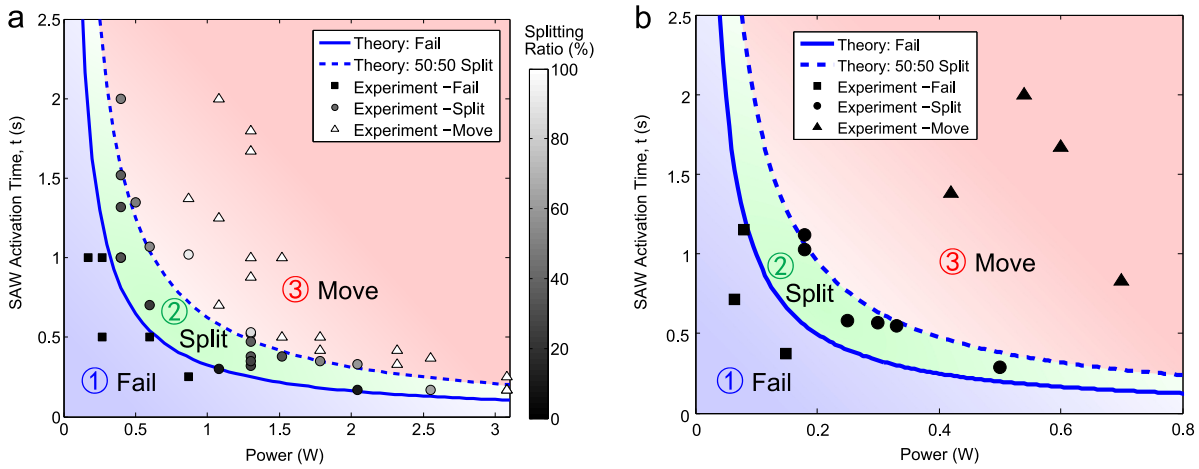

Figure 8.6: Analytical model and experimental results for droplet transport, plotted linearly as SAW activation time versus the input power. The results suggest three regimes in the nanoslit device between traps using (a) DI water and (b) IPA: failure, splitting, and complete moving of a droplet to the next well.

8.6.2 Image Processing for Droplet Splitting Ratio

The process to estimate the amount of fluid in droplets trapped in adjacent wells after splitting is illustrated in Suppl. Fig. 8.7. Thresholding here implies that the average pixel intensity was extracted from a given image, and those pixels possessing a greater value than the average were set to a value of one (white), while those less than the average were set to zero (black). Care was taken to ensure no changes to intensity occurred during the experiments, prevented by locking the camera exposure and (electronic) shutter speed, and by documenting and maintaining identical lighting and optical conditions.

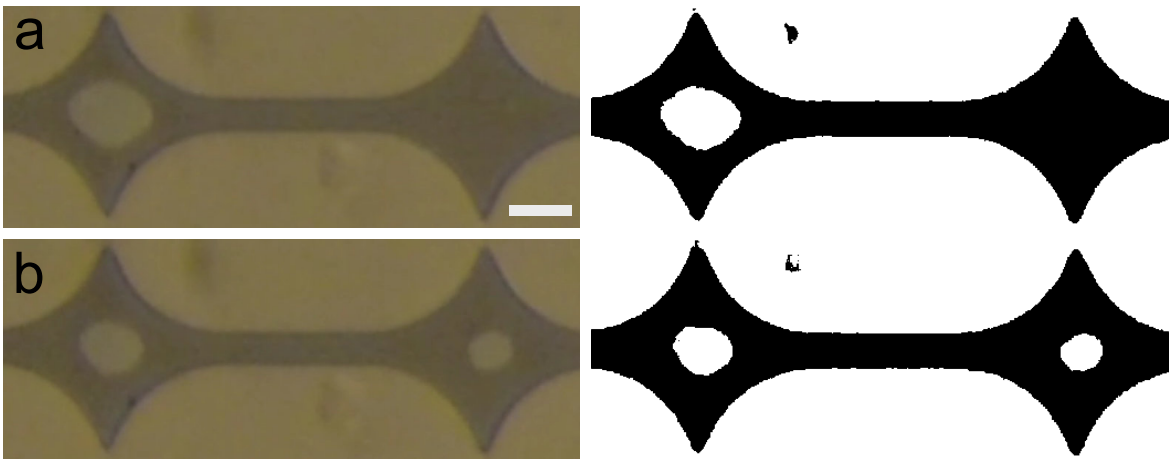

Figure 8.7: To determine the droplet splitting results, simple image processing was used. Brightfield images (left) were taken of the droplet(s) (a) before and (b) after droplet splitting. These were thresholded to produce black-and-white images (right), and the number of pixels present in the wells were counted and compared to determine the ratio of the droplet's volume in each trap. Scale bar: 40 μm.

8.6.3 Modeling the Surface Energy during Manipulation

An illustrative figure to indicate what the models produce in representing the droplet shapes is provided in Suppl. Fig. 8.8. This information was used to produce the plots in the main manuscript that denote the splitting ratio versus input energy.

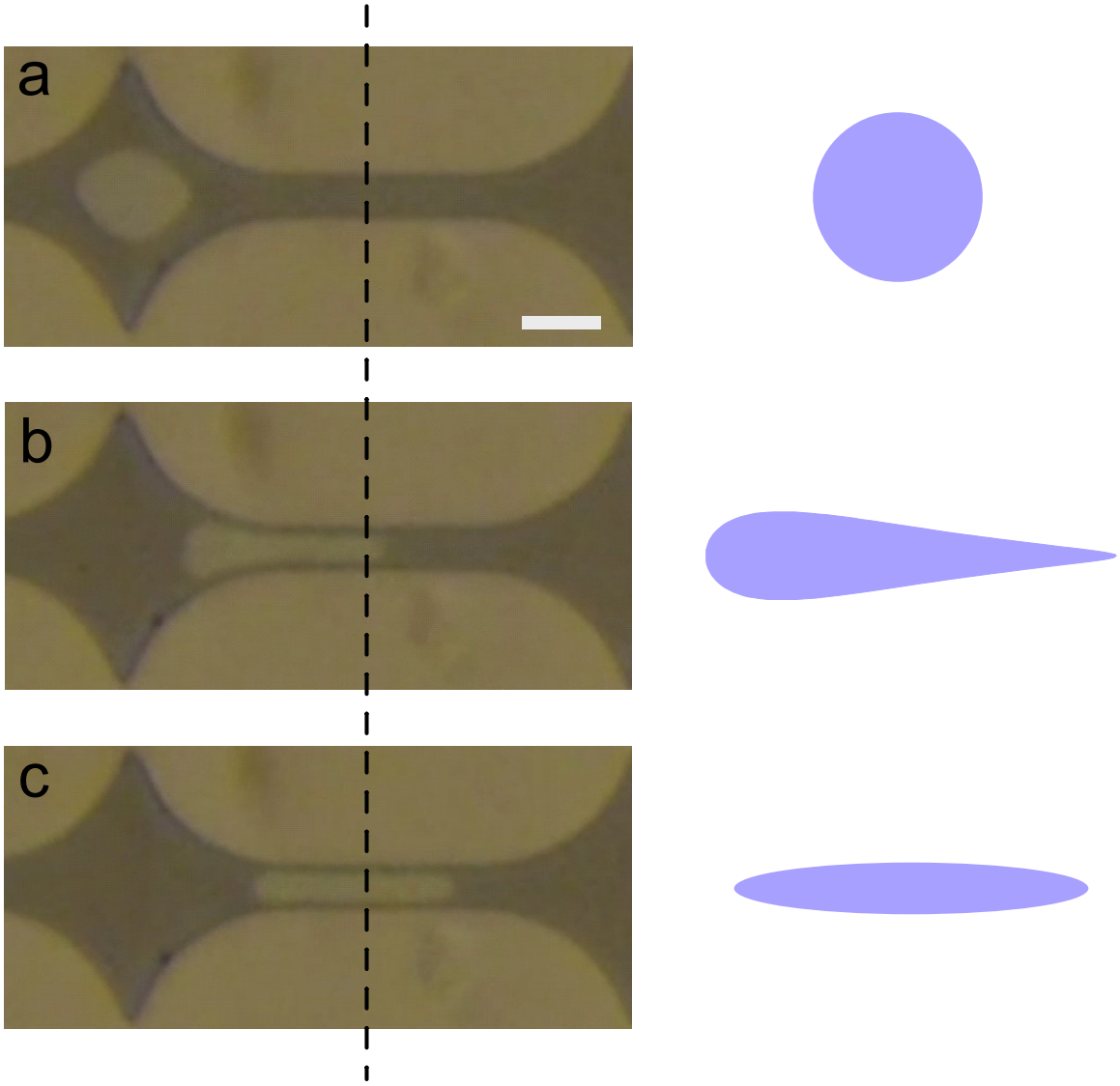

Figure 8.8: The droplet shape as it is transported from (a) its original position in the trap at left, to the (b) position corresponding with E_1 and C_1, where the droplet is at the boundary between failure (region 1 in Fig. 3) and splitting (region 2), and beyond to produce a 50:50 split between the two traps, represented by E_2 and C_2. The vertical dashed line is the midpoint of the neck between the two traps. The 50:50 split is also plotted as a dashed line in Fig. 3, main manuscript. On the left are images of the droplet for each state; on the right are corresponding plots of the droplet shape used in the analysis. Scale bar: 40 μm.

8.7 Acknowledgement

We are grateful to the University of California and the NANO3 facility at UC San Diego for provision of funds and facilities in support of this work. This work was performed

in part at the San Diego Nanotechnology Infrastructure (SDNI) of UCSD, a member of the National Nanotechnology Coordinated Infrastructure, which is supported by the National Science Foundation (Grant ECCS–1542148). The work presented here was generously supported by a research grant from the W.M. Keck Foundation. The authors are also grateful for the support of this work by the Office of Naval Research (via Grant 12368098), and substantial technical support by Polytec's staff in Irvine, CA and Waldbronn, Germany.

Bibliography

[1] 95/ec of the european parliament and of the council of 27 january 2003 on the restriction of the use of certain hazardous substances in electrical and electronic equipment. Directive, EU, 2002.

[2] E. L. Adler. Matrix methods applied to acoustic waves in multilayers. *IEEE Transactions on Ultrasonics, Ferroelectrics, and Frequency Control*, 37(6):485–490, 1990.

[3] D. Ahmed, X. Mao, B. K. Juluri, and T. J. Huang. A fast microfluidic mixer based on acoustically driven sidewall-trapped microbubbles. *Microfluidics and Nanofluidics*, 7(5): 727, 2009.

[4] D. Ahmed, X. Mao, J. Shi, B. K. Juluri, and T. J. Huang. A millisecond micromixer via single-bubble-based acoustic streaming. *Lab on a Chip*, 9(18):2738–2741, 2009.

[5] M. Alghane, B. Chen, Y. Q. Fu, Y. Li, J. Luo, and A. Walton. Experimental and numerical investigation of acoustic streaming excited by using a surface acoustic wave device on a 128° yx-linbo3 substrate. *Journal of Micromechanics and Microengineering*, 21(1): 015005, 2010.

[6] L. Alhasan, A. Qi, A. Al-Abboodi, A. Rezk, P. P. Chan, C. Iliescu, and L. Y. Yeo. Rapid enhancement of cellular spheroid assembly by acoustically driven microcentrifugation. *ACS Biomaterials Science & Engineering*, 2(6):1013–1022, 2016.

[7] E. M. Allison, G. S. Springer, and J. Van Dam. Ultrasonic propulsion. *Journal of Propulsion and Power*, 24(3):547–553, 2008.

[8] T. Anderson and T. Anderson. *Fracture Mechanics: Fundamentals and Applications, Third Edition*. Taylor & Francis, Philadelphia, PA USA, 2005. ISBN 9780849316562.

[9] M. K. Araz, C.-H. Lee, and A. Lal. Ultrasonic separation in microfluidic capillaries. In *Ultrasonics, 2003 IEEE Symposium on*, volume 2, pages 1111–1114. IEEE, 2003.

[10] R. Arzt, E. Salzmann, and K. Dransfeld. Elastic surface waves in quartz at 316 mhz. *Applied Physics Letters*, 10(5):165–167, 1967.

[11] B. Auld. *Acoustic Fields and Waves in Solids*. Number v. 1 in Acoustic Fields and Waves in Solids. R.E. Krieger, 1990.

[12] P. Bachmann. *Die analytische zahlentheorie*, volume 2. Teubner, 1894.

[13] D. Bancroft. The velocity of longitudinal waves in cylindrical bars. *Physical Review*, 59 (7):588, 1941.

[14] A. Barani, H. Paktinat, M. Janmaleki, A. Mohammadi, P. Mosaddegh, A. Fadaei-Tehrani, and A. Sanati-Nezhad. Microfluidic integrated acoustic waving for manipulation of cells and molecules. *Biosensors and Bioelectronics*, 85:714–725, 2016.

[15] A. Barker, P. Jaeger, and D. E. Oliver. Non-contacting vibration measurement: role in design and industrial applications. *Stress and Vibration: Recent Developments in Industrial Measurement and Analysis*, 1084:293–299, 1989.

[16] D. Barnett and J. Lothe. Free surface (Rayleigh) waves in anisotropic elastic half-spaces: the surface impedance method. *Proceedings of the Royal Society of London. A. Mathematical and Physical Sciences*, 402(1822):135–152, 1985.

[17] M. Baudoin and J.-L. Thomas. Acoustic tweezers for particle and fluid micromanipulation. *Annual Review of Fluid Mechanics*, 52:205–234, 2020.

[18] F. K. Bäuerle, S. Karpitschka, and K. Alim. Living system adapts harmonics of peristaltic wave for cost-efficient optimization of pumping performance. *Physical Review Letters*, 124(9):098102, 2020.

[19] H. Becker. Hype, hope and hubris: the quest for the killer application in microfluidics. *Lab on a Chip*, 9(15):2119–2122, 2009.

[20] H. Becker and C. Gärtner. Microfluidics-enabled diagnostic systems: Markets, challenges, and examples. *Microchip Diagnostics: Methods and Protocols*, pages 3–21, 2017.

[21] N. Bertin, T. A. Spelman, T. Combriat, H. Hue, O. Stéphan, E. Lauga, and P. Marmottant. Bubble-based acoustic micropropulsors: active surfaces and mixers. *Lab on a Chip*, 17(8): 1515–1528, 2017.

[22] V. Bertram. Chapter 2 - propellers. In V. Bertram, editor, *Practical Ship Hydrodynamics (Second Edition)*, pages 41 – 72. Butterworth-Heinemann, Oxford, second edition edition, 2012.

[23] H. Birol, D. Damjanovic, and N. Setter. Preparation and characterization of (k 0.5 na 0.5) nbo 3 ceramics. *Journal of the European Ceramic Society*, 26(6):861–866, 2006.

[24] J. Blamey, L. Y. Yeo, and J. R. Friend. Microscale capillary wave turbulence excited by high frequency vibration. *Langmuir*, 29(11):3835–3845, 2013.

[25] L. Bocquet and E. Charlaix. Nanofluidics, from bulk to interfaces. *Chemical Society Reviews*, 39(3):1073–1095, 2010.

[26] Y. Bourquin and J. M. Cooper. Swimming using surface acoustic waves. *PloS One*, 8(2): e42686, 2013.

[27] Y. Bourquin, J. Reboud, R. Wilson, and J. M. Cooper. Tuneable surface acoustic waves for fluid and particle manipulations on disposable chips. *Lab on a Chip*, 10(15):1898–1901, 2010.

[28] Y. Bourquin, A. Syed, J. Reboud, L. C. Ranford-Cartwright, M. P. Barrett, and J. M. Cooper. Rare-cell enrichment by a rapid, label-free, ultrasonic isopycnic technique for medical diagnostics. *Angewandte Chemie*, 126(22):5693–5696, 2014.

[29] J. C. Brenker, D. J. Collins, H. Van Phan, T. Alan, and A. Neild. On-chip droplet production regimes using surface acoustic waves. *Lab on a Chip*, 16(9):1675–1683, 2016.

[30] I. Bretos, R. Jiménez, J. Garcïa-López, L. Pardo, and M. L. Calzada. Photochemical solution deposition of lead-based ferroelectric films: Avoiding the pbo-excess addition at last. *Chemistry of Materials*, 20(18):5731–5733, 2008. doi: 10.1021/cm801269g.

[31] H. Bruus. Acoustofluidics 7: The acoustic radiation force on small particles. *Lab on a Chip*, 12(6):1014–1021, 2012.

[32] G. Bu, D. Ciplys, M. Shur, L. Schowalter, S. Schujman, and R. Gaska. Electromechanical coupling coefficient for surface acoustic waves in single-crystal bulk aluminum nitride. *Applied Physics Letters*, 84(23):4611–4613, 2004.

[33] A. Bussonnière, Y. Miron, M. Baudoin, O. B. Matar, M. Grandbois, P. Charette, and A. Renaudin. Cell detachment and label-free cell sorting using modulated surface acoustic waves (SAWs) in droplet-based microfluidics. *Lab on a Chip*, 14(18):3556–3563, 2014.

[34] T. Cacace, M. Paturzo, P. Memmolo, M. Vassalli, P. Ferraro, M. Fraldi, and G. Mensitieri. Digital holography as 3d tracking tool for assessing acoustophoretic particle manipulation. *Optics Express*, 25(15):17746–17752, 2017.

[35] C. Campbell. *Surface acoustic wave devices for mobile and wireless communications*. Academic press, 1998.

[36] C. K. Campbell. Applications of surface acoustic and shallow bulk acoustic wave devices. *Proceedings of the IEEE*, 77(10):1453–1484, 1989.

[37] C. K. Campbell. Longitudinal-mode leaky SAW resonator filters on 64/spl deg/yx lithium niobate. *IEEE Transactions on Ultrasonics, Ferroelectrics, and Frequency Control*, 42(5): 883–888, 1995.

[38] M. Carfagni, E. Lenzi, and M. Pierini. The loss factor as a measure of mechanical damping. In *SPIE proceedings series*, pages 580–584, 1998.

[39] J. Carlton. *Marine propellers and propulsion*. Butterworth-Heinemann, 2018.

[40] P. Castellini and C. Santolini. Vibration measurements on blades of naval propeller rotating in water. In *Second International Conference on Vibration Measurements by Laser Techniques: Advances and Applications*, pages 186–194. International Society for Optics and Photonics, 1996.

[41] P. Castellini, M. Martarelli, and E. Tomasini. Laser doppler vibrometry: Development of advanced solutions answering to technology's needs. *Mechanical Systems and Signal Processing*, 20(6):1265–1285, 2006.

[42] S. O. Catarino, V. C. Pinto, P. J. Sousa, R. Lima, J. M. Miranda, and G. Minas. A numerical and experimental study of acoustic micromixing in 3d microchannels for lab-on-a-chip devices. In *Engineering in Medicine and Biology Society (EMBC), 2016 IEEE 38th Annual International Conference of the*, pages 5660–5663. IEEE, 2016.

[43] A. Cazabat, F. Heslot, S. Troian, and P. Carles. Fingering instability of thin spreading films driven by temperature gradients. *Nature*, 346(6287):824–826, 1990.

[44] M. Cecchini, S. Girardo, D. Pisignano, R. Cingolani, and F. Beltram. Acoustic-counterflow microfluidics by surface acoustic waves. *Applied Physics Letters*, 92(10):104103, 2008.

[45] C.-M. Chang, C.-S. Yu, F.-C. Hsieh, C.-T. Lin, T.-T. Huang, P.-H. Lin, J.-S. Kao, C.-N. Hsiao, and M.-H. Shiao. A parametric study of icp-rie etching on a lithium niobate substrate. In *10th IEEE International Conference on Nano/Micro Engineered and Molecular Systems*, pages 485–486. IEEE, 2015.

[46] D. Chatterjee, B. Hetayothin, A. R. Wheeler, D. J. King, and R. L. Garrell. Droplet-based microfluidics with nonaqueous solvents and solutions. *Lab on a Chip*, 6(2):199–206, 2006.

[47] Y. Chen, X. Ding, S.-C. S. Lin, S. Yang, P.-H. Huang, N. Nama, Y. Zhao, A. A. Nawaz, F. Guo, W. Wang, et al. Tunable nanowire patterning using standing surface acoustic waves. *ACS Nano*, 7(4):3306, 2013.

[48] Y. Chen, S. Li, Y. Gu, P. Li, X. Ding, L. Wang, J. P. McCoy, S. J. Levine, and T. J. Huang. Continuous enrichment of low-abundance cell samples using standing surface acoustic waves (SSAW). *Lab on a Chip*, 14(5):924–930, 2014.

[49] N.-S. Cheng. Formula for the viscosity of a glycerol- water mixture. *Industrial & Engineering Chemistry Research*, 47(9):3285–3288, 2008.

[50] X. Cheng, L. Xu, A. Patterson, H. M. Jaeger, and S. R. Nagel. Towards the zero-surface-tension limit in granular fingering instability. *Nature Physics*, 4(3):234–237, 2008.

[51] E. F. F. Chladni. *Discoveries on the theory of sound*. Weidmanns, Erben und Reich, 1787.

[52] B.-T. Chu and R. E. Apfel. Acoustic radiation pressure produced by a beam of sound. *The Journal of the Acoustical Society of America*, 72(6):1673–1687, 1982.

[53] D. Ciplys and R. Rimeika. Measurements of electromechanical coupling coefficient for surface acoustic waves in proton-exchanged lithium niobate. *Ultrasound*, 33(3):14–20, 2014.

[54] L. Cohen, N. Cui, Y. Cai, P. M. Garden, X. Li, D. A. Weitz, and D. R. Walt. Single molecule protein detection with attomolar sensitivity using droplet digital enzyme-linked immunosorbent assay. *ACS Nano*, 14(8):9491–9501, 2020.

[55] M. Cohen. Optical study of ultrasonic diffraction and focusing in anisotropic media. *Journal of Applied Physics*, 38(10):3821–3828, 1967.

[56] S. Collignon, O. Manor, and J. Friend. Improving and predicting fluid atomization via hysteresis-free thickness vibration of lithium niobate. *Advanced Functional Materials*, 28 (1704359), 2018.

[57] D. J. Collins, T. Alan, K. Helmerson, and A. Neild. Surface acoustic waves for on-demand production of picoliter droplets and particle encapsulation. *Lab on a Chip*, 13(16): 3225–3231, 2013.

[58] D. J. Collins, C. Devendran, Z. Ma, J. W. Ng, A. Neild, and Y. Ai. Acoustic tweezers via sub–time-of-flight regime surface acoustic waves. *Science Advances*, 2(7):e1600089, 2016.

[59] D. J. Collins, Z. Ma, and Y. Ai. Highly localized acoustic streaming and size-selective submicrometer particle concentration using high frequency microscale focused acoustic fields. *Analytical Chemistry*, 88(10):5513–5522, 2016.

[60] D. J. Collins, A. Neild, and Y. Ai. Highly focused high-frequency travelling surface acoustic waves (SAW) for rapid single-particle sorting. *Lab on a Chip*, 16(3):471–479, 2016.

[61] D. J. Collins, B. L. Khoo, Z. Ma, A. Winkler, R. Weser, H. Schmidt, J. Han, and Y. Ai. Selective particle and cell capture in a continuous flow using micro-vortex acoustic streaming. *Lab on a Chip*, 17(10):1769–1777, 2017.

[62] D. J. Collins, Z. Ma, J. Han, and Y. Ai. Continuous micro-vortex-based nanoparticle manipulation via focused surface acoustic waves. *Lab on a Chip*, 17(1):91–103, 2017.

[63] L. Collins. Picoplatters. *IEE Review*, 50(4):44–47, 2004.

[64] T. Combriat, F. Mekki-Berrada, P. Thibault, and P. Marmottant. Trapping and exclusion zones in complex streaming patterns around a large assembly of microfluidic bubbles under ultrasound. *Physical Review Fluids*, 3(1):013602, 2018.

[65] W. Connacher, N. Zhang, A. Huang, J. Mei, S. Zhang, T. Gopesh, and J. Friend. Micro/nano acoustofluidics: materials, phenomena, design, devices, and applications. *Lab on a Chip*, 18(14):1952–1996, 2018.

[66] W. Connacher, J. Orosco, and J. Friend. Droplet ejection at controlled angles via acoustofluidic jetting. *Physical Review Letters*, 125(18):184504, 2020.

[67] E. Cosenza and G. Manfredi. Damage indices and damage measures. *Progress in Structural Engineering and Materials*, 2(1):50–59, 2000.

[68] S. H. Crandall. Relation between strain and velocity in resonant vibration. *The Journal of the Acoustical Society of America*, 34(12):1960–1961, 1962.

[69] L. A. Crum. Bjerknes forces on bubbles in a stationary sound field. *The Journal of the Acoustical Society of America*, 57(6):1363–1370, 1975.

[70] W. Cui, H. Zhang, H. Zhang, Y. Yang, M. He, H. Qu, W. Pang, D. Zhang, and X. Duan. Localized ultrahigh frequency acoustic fields induced micro-vortices for submilliseconds microfluidic mixing. *Applied Physics Letters*, 109(25):253503, 2016.

[71] J. Curie and P. Curie. Contractions and dilatations produced by electric voltages in crystals. *Compt. Makes*, 93:1137–1140, 1881.

[72] D. Curran, L. Seaman, and D. Shockey. Dynamic failure of solids. *Physics Reports*, 147 (5):253 – 388, 1987.

[73] N. Dam. Non-contact ultrasonic micromeasurement system, Mar. 9 1999. US Patent 5,880,364.

[74] P.-G. De Gennes, F. Brochard-Wyart, and D. Quéré. *Capillarity and wetting phenomena: drops, bubbles, pearls, waves*. Springer Science & Business Media, 2013.

[75] E. de Jong, J. M. J. Den Toonder, and P. R. Onck. Microfluidic slug transport on traveling-wave surface topographies by mechanowetting. *Physical Review Fluids*, 5:063604, 2020.

[76] M. de Lima Jr, R. Hey, J. Stotz, and P. Santos. Acoustic manipulation of electron–hole pairs in gaas at room temperature. *Applied Physics Letters*, 84(14):2569–2571, 2004.

[77] H. Dehghani and M. Ataee-Pour. Development of a model to predict peak particle velocity in a blasting operation. *International Journal of Rock Mechanics and Mining Sciences*, 48 (1):51–58, 2011.

[78] A. Demirbas. Fuel alternatives to gasoline. *Energy Sources, Part B: Economics, Planning, and Policy*, 2(3):311–320, 2007.

[79] M. B. Dentry, L. Y. Yeo, and J. R. Friend. Frequency effects on the scale and behavior of acoustic streaming. *Physical Review E*, 89(1):013203, 2014.

[80] G. Destgeer and H. J. Sung. Recent advances in microfluidic actuation and micro-object manipulation via surface acoustic waves. *Lab on a Chip*, 15(13):2722–2738, 2015.

[81] G. Destgeer, K. H. Lee, J. H. Jung, A. Alazzam, and H. J. Sung. Continuous separation of particles in a pdms microfluidic channel via travelling surface acoustic waves (TSAW). *Lab on a Chip*, 13(21):4210–4216, 2013.

[82] G. Destgeer, B. H. Ha, J. Park, J. H. Jung, A. Alazzam, and H. J. Sung. Microchannel anechoic corner for size-selective separation and medium exchange via traveling surface acoustic waves. *Analytical Chemistry*, 87(9):4627–4632, 2015.

[83] G. Destgeer, H. Cho, B. H. Ha, J. H. Jung, J. Park, and H. J. Sung. Acoustofluidic particle manipulation inside a sessile droplet: four distinct regimes of particle concentration. *Lab on a Chip*, 16(4):660–667, 2016.

[84] G. Destgeer, B. Ha, J. Park, and H. J. Sung. Lamb wave-based acoustic radiation force-driven particle ring formation inside a sessile droplet. *Analytical Chemistry*, 88(7):3976–3981, 2016.

[85] C. Devendran, N. R. Gunasekara, D. J. Collins, and A. Neild. Batch process particle separation using surface acoustic waves (SAW): integration of travelling and standing SAW. *RSC Advances*, 6(7):5856–5864, 2016.

[86] X. Ding, S.-C. S. Lin, B. Kiraly, H. Yue, S. Li, I.-K. Chiang, J. Shi, S. J. Benkovic, and T. J. Huang. On-chip manipulation of single microparticles, cells, and organisms using surface acoustic waves. *Proceedings of the National Academy of Sciences*, 109(28):11105–11109, 2012.

[87] X. Ding, S.-C. S. Lin, M. I. Lapsley, S. Li, X. Guo, C. Y. Chan, I.-K. Chiang, L. Wang, J. P. McCoy, and T. J. Huang. Standing surface acoustic wave (SSAW) based multichannel cell sorting. *Lab on a Chip*, 12(21):4228–4231, 2012.

[88] X. Ding, J. Shi, S.-C. S. Lin, S. Yazdi, B. Kiraly, and T. J. Huang. Tunable patterning of microparticles and cells using standing surface acoustic waves. *Lab on a chip*, 12(14): 2491–2497, 2012.

[89] X. Ding, P. Li, S.-C. S. Lin, Z. S. Stratton, N. Nama, F. Guo, D. Slotcavage, X. Mao, J. Shi, F. Costanzo, et al. Surface acoustic wave microfluidics. *Lab on a Chip*, 13(18):3626–3649, 2013.

[90] A. Doinikov. Acoustic radiation pressure on a rigid sphere in a viscous fluid. *Proceedings of the Royal Society of London. Series A: Mathematical and Physical Sciences*, 447(1931): 447–466, 1994.

[91] A. A. Doinikov and A. Bouakaz. Acoustic microstreaming around a gas bubble. *The Journal of the Acoustical Society of America*, 127(2):703–709, 2010.

[92] A. A. Doinikov, P. Thibault, and P. Marmottant. Acoustic streaming in a microfluidic channel with a reflector: Case of a standing wave generated by two counterpropagating leaky surface waves. *Physical Review E*, 96(1):013101, 2017.

[93] I. Donald. Sonar the story of an experiment. *Ultrasound in Medicine & Biology*, 1(2): 109–117, 1974.

[94] B. W. Drinkwater. Dynamic-field devices for the ultrasonic manipulation of microparticles. *Lab on a Chip*, 16(13):2360–2375, 2016.

[95] X.-h. Du, J. Zheng, U. Belegundu, and K. Uchino. Crystal orientation dependence of piezoelectric properties of lead zirconate titanate near the morphotropic phase boundary. *Applied Physics Letters*, 72(19):2421–2423, 1998.

[96] R. S. Duelley. *Autonomous underwater vehicle propulsion design*. PhD thesis, Virginia Tech, 2010.

[97] C. Eckart. Vortices and streams caused by sound waves. *Physical Review*, 73(1):68, 1948.

[98] J. Edel, A. Ivanov, and M. Kim. *Nanofluidics*, volume 41. Royal Society of Chemistry, 2016.

[99] J. C. Eijkel and A. Van Den Berg. Nanofluidics: what is it and what can we expect from it? *Microfluidics and Nanofluidics*, 1(3):249–267, 2005.

[100] M. Eslamian and M. Z. Saghir. Novel thermophoretic particle separators: numerical analysis and simulation. *Applied Thermal Engineering*, 59(1-2):527–534, 2013.

[101] S. R. Fang, S. Zhang, and Z. F. Lu. SAW focusing by circular-arc interdigital transducers on yz-linbo/sub 3. *IEEE Transactions on Ultrasonics, Ferroelectrics, and Frequency Control*, 36(2):178–184, 1989.

[102] W.-F. Fang and A. P. Lee. Lcat pump optimization for an integrated microfluidic droplet generator. *Microfluidics and Nanofluidics*, 18(5-6):1265–1275, 2015.

[103] M. Faraday. On the forms and states assumed by fluids in contact with vibrating elastic surfaces. *Philos. Trans. R. Soc. London*, 121(319):1831, 1831.

[104] W. G. Farnell. Types and properties of surface waves. In *Acoustic surface waves*, pages 13–60. Springer, 1978.

[105] F. Fergusson, E. Guptill, and A. MacDonald. Velocity of sound in glycerol. *The Journal of the Acoustical Society of America*, 26(1):67–69, 1954.

[106] M. Foquet, J. Korlach, W. Zipfel, W. W. Webb, and H. G. Craighead. Dna fragment sizing by single molecule detection in submicrometer-sized closed fluidic channels. *Analytical Chemistry*, 74(6):1415–1422, 2002.

[107] T. Franke, A. R. Abate, D. A. Weitz, and A. Wixforth. Surface acoustic wave (SAW) directed droplet flow in microfluidics for pdms devices. *Lab on a Chip*, 9(18):2625–2627, 2009.

[108] J. Friend and L. Yeo. Using laser doppler vibrometry to measure capillary surface waves on fluid-fluid interfaces. *Biomicrofluidics*, 4(2):026501, 2010.

[109] J. Friend and L. Y. Yeo. Microscale acoustofluidics: Microfluidics driven via acoustics and ultrasonics. *Reviews of Modern Physics*, 83(2):647, 2011.

[110] J. Friend, K. Nakamura, and S. Ueha. A piezoelectric micromotor using in-plane shearing of pzt elements. *IEEE/ASME Transactions on Mechatronics*, 9(3):467–473, 2004.

[111] J. R. Friend and L. Y. Yeo. Microscale acoustofluidics: Microfluidics driven via acoustics and ultrasonics. *Reviews of Modern Physics*, 83:647–704, 2011.

[112] J. R. Friend, L. Y. Yeo, D. R. Arifin, and A. Mechler. Evaporative self-assembly assisted synthesis of polymeric nanoparticles by surface acoustic wave atomization. *Nanotechnology*, 19(14):145301, 2008.

[113] Y. B. Fu and A. Mielke. A new identity for the surface–impedance matrix and its application to the determination of surface-wave speeds. *Proceedings of the Royal Society of London. Series A: Mathematical, Physical and Engineering Sciences*, 458(2026):2523–2543, 2002.

[114] Y. Q. Fu, J. Luo, N.-T. Nguyen, A. Walton, A. J. Flewitt, X.-T. Zu, Y. Li, G. McHale, A. Matthews, E. Iborra, et al. Advances in piezoelectric thin films for acoustic biosensors, acoustofluidics and lab-on-chip applications. *Progress in Materials Science*, 89:31–91, 2017.

[115] H. Funaki. Contributions on the shapes of red blood corpuscles. *The Japanese Journal of Physiology*, 5:81–92, 1955.

[116] H. Gaberson, D. Pal, and R. Chapler. Shock spectrum classification of violent environments that cause machinery failure. In *Proceedings of the 18th International Modal Analysis Conference*, pages 1126–1135, 2000.

[117] J. Gao, Y. Feng, W. Guo, and L. Jiang. Nanofluidics in two-dimensional layered materials: inspirations from nature. *Chemical Society Reviews*, 46(17):5400–5424, 2017.

[118] J. L. Garcia-Cordero and Z. H. Fan. Sessile droplets for chemical and biological assays. *Lab on a Chip*, 2017.

[119] M. Gasparetti, G. M. Revel, and E. P. Tomasini. Theoretical modeling and experimental evaluation of an in-plane laser doppler vibrometer in different working conditions. In *Third International Conference on Vibration Measurements by Laser Techniques: Advances and Applications*, pages 317–327. International Society for Optics and Photonics, 1998.

[120] M. Gedge and M. Hill. Acoustofluidics 17: Theory and applications of surface acoustic wave devices for particle manipulation. *Lab on a Chip*, 12(17):2998–3007, 2012.

[121] S. Girardo, M. Cecchini, F. Beltram, R. Cingolani, and D. Pisignano. Polydimethylsiloxane–linbo$_3$ surface acoustic wave micropump devices for fluid control into microchannels. *Lab on a Chip*, 8(9):1557–1563, 2008.

[122] J. Goldberger, R. Fan, and P. Yang. Inorganic nanotubes: a novel platform for nanofluidics. *Accounts of Chemical Research*, 39(4):239–248, 2006.

[123] X. Gong, J. Li, H. Lu, R. Wan, J. Li, J. Hu, and H. Fang. A charge-driven molecular water pump. *Nature Nanotechnology*, 2(11):709–712, 2007.

[124] I. Gralinski, T. Alan, and A. Neild. Non-contact acoustic trapping in circular cross-section glass capillaries: a numerical study. *The Journal of the Acoustical Society of America*, 132 (5):2978–2987, 2012.

[125] I. Gralinski, S. Raymond, T. Alan, and A. Neild. Continuous flow ultrasonic particle trapping in a glass capillary. *Journal of Applied Physics*, 115(5):054505, 2014.

[126] J. Green and G. Kino. SAW convolvers using focused interdigital transducers. *IEEE Transactions on Sonics Ultrasonics*, 30:43–50, 1983.

[127] J. Green, G. Kino, and B. Khuri-Yakub. Focused surface wave transducers on anisotropic substrates: a theory developed for the waveguided storage correlator. In *1980 Ultrasonics Symposium*, pages 69–73. IEEE, 1980.

[128] M. Grundy, W. Bolek, W. Coakley, and E. Benes. Rapid agglutination testing in an ultrasonic standing wave. *Journal of Immunological Methods*, 165(1):47–57, 1993.

[129] Y. Gu, C. Chen, Z. Mao, H. Bachman, R. Becker, J. Rufo, Z. Wang, P. Zhang, J. Mai, S. Yang, et al. Acoustofluidic centrifuge for nanoparticle enrichment and separation. *Science Advances*, 7(1):eabc0467, 2021.

[130] Y. V. Gulyaev. Review of shear surface acoustic waves in solids. *IEEE Transactions on Ultrasonics, Ferroelectrics, and Frequency Control*, 45(4):935–938, 1998.

[131] F. Guo, P. Li, J. B. French, Z. Mao, H. Zhao, S. Li, N. Nama, J. R. Fick, S. J. Benkovic, and T. J. Huang. Controlling cell–cell interactions using surface acoustic waves. *Proceedings of the National Academy of Sciences*, 112(1):43–48, 2015.

[132] L. J. Guo, X. Cheng, and C.-F. Chou. Fabrication of size-controllable nanofluidic channels by nanoimprinting and its application for dna stretching. *Nano Letters*, 4(1):69–73, 2004.

[133] B. H. Ha, K. S. Lee, G. Destgeer, J. Park, J. S. Choung, J. H. Jung, J. H. Shin, and H. J. Sung. Acoustothermal heating of polydimethylsiloxane microfluidic system. *Scientific Reports*, 5, 2015.

[134] S. Haeberle and R. Zengerle. Microfluidic platforms for lab-on-a-chip applications. *Lab on a Chip*, 7(9):1094–1110, 2007.

[135] A. Halfpenny. A frequency domain approach for fatigue life estimation from finite element analysis. In *Key Engineering Materials*, volume 167, pages 401–410. Trans Tech Publ, 1999.

[136] B. J. Halkon and S. Rothberg. Vibration measurements using continuous scanning laser doppler vibrometry: theoretical velocity sensitivity analysis with applications. *Measurement Science and Technology*, 14(3):382, 2003.

[137] M. F. Hamilton and D. T. Blackstock, editors. *Nonlinear Acoustics*. Acoustical Society of America, 2008.

[138] B. Hammarström, T. Laurell, and J. Nilsson. Seed particle-enabled acoustic trapping of bacteria and nanoparticles in continuous flow systems. *Lab on a Chip*, 12(21):4296–4304, 2012.

[139] J. Hancock and J. J. Bommer. A state-of-knowledge review of the influence of strong-motion duration on structural damage. *Earthquake Spectra*, 22(3):827–845, 2006.

[140] C. Hartmann. Systems impact of modern Rayleigh wave technology. In *Rayleigh-Wave Theory and Application*, pages 238–253. Springer, 1985.

[141] T. Hasegawa, J. Friend, K. Nakamura, and S. Ueha. Characteristics of ultrasonic suction pump without moving parts. *Japanese Journal of Applied Physics*, 44(6S):4658, 2005.

[142] A. Hashmi and J. Xu. On the quantification of mixing in microfluidics. *Journal of Laboratory Automation*, 19(5):488–491, 2014.

[143] M. D. Haslam and B. Raeymaekers. Aligning carbon nanotubes using bulk acoustic waves to reinforce polymer composites. *Composites Part B: Engineering*, 60:91–97, 2014.

[144] M. He, Y. Zhou, W. Cui, Y. Yang, H. Zhang, X. Chen, W. Pang, and X. Duan. An on-demand femtoliter droplet dispensing system based on a gigahertz acoustic resonator. *Lab on a Chip*, 18(17):2540–2546, 2018.

[145] J. Hechner and W. Soluch. Pseudo surface acoustic wave dual delay line on 41 yx linbo 3 for liquid sensors. *Sensors and Actuators B: Chemical*, 111:436–440, 2005.

[146] R. Herdier, D. Jenkins, E. Dogheche, D. Rèmiens, and M. Sulc. Laser doppler vibrometry for evaluating the piezoelectric coefficient d 33 on thin film. *Review of Scientific Instruments*, 77(9):093905, 2006.

[147] F. S. Hickernell. Zinc-oxide thin-film surface-wave transducers. *Proceedings of the IEEE*, 64(5):631–635, 1976.

[148] F. S. Hickernell. Surface acoustic wave technology macrosuccess through microseisms. *Physical Acoustics*, 24:135–207, 1999.

[149] C.-M. Ho. Fluidics-the link between micro and nano sciences and technologies. In *Micro Electro Mechanical Systems, 2001. MEMS 2001. The 14th IEEE International Conference on*, pages 375–384. IEEE, 2001.

[150] R. P. Hodgson, M. Tan, L. Yeo, and J. Friend. Transmitting high power RF acoustic radiation via fluid couplants into superstrates for microfluidics. *Applied Physics Letters*, 94(2):024102, 2009. doi: 10.1063/1.3049128.

[151] A. Horesh, D. Khaikin, M. Karnilaw, A. Zigelman, and O. Manor. Acoustogravitational balance in climbing films. *Physical Review Fluids*, 4(2):022001, 2019.

[152] M. Howlader, T. Suga, and M. Kim. Room temperature bonding of silicon and lithium niobate. *Applied Physics Letters*, 89(3):031914, 2006.

[153] H. Hu, R. Ricken, and W. Sohler. Etching of lithium niobate: micro-and nanometer structures for integrated optics. In *Topical Meeting" Photorefractive Materials, Effects, and Devices–Control of Light and Matter, Bad Honnef*, 2009.

[154] J. Hu and A. K. Santoso. A π-shaped ultrasonic tweezers concept for manipulation of small particles. *IEEE Transactions on Ultrasonics, Ferroelectrics, and Frequency Control*, 51(11):1499–1507, 2004.

[155] J. Hu, J. Yang, and J. Xu. Ultrasonic trapping of small particles by sharp edges vibrating in a flexural mode. *Applied Physics Letters*, 85(24):6042–6044, 2004.

[156] A. Huang, M. Miansari, and J. Friend. Driving morphological changes in magnetic nanoparticle structures through the application of acoustic waves and magnetic fields. In *APS Meeting Abstracts*, 2017.

[157] P.-H. Huang, M. Ian Lapsley, D. Ahmed, Y. Chen, L. Wang, and T. Jun Huang. A single-layer, planar, optofluidic switch powered by acoustically driven, oscillating microbubbles. *Applied Physics Letters*, 101(14):141101, 2012.

[158] P.-H. Huang, Y. Xie, D. Ahmed, J. Rufo, N. Nama, Y. Chen, C. Y. Chan, and T. J. Huang. An acoustofluidic micromixer based on oscillating sidewall sharp-edges. *Lab on a Chip*, 13(19):3847–3852, 2013.

[159] P.-H. Huang, N. Nama, Z. Mao, P. Li, J. Rufo, Y. Chen, Y. Xie, C.-H. Wei, L. Wang, and T. J. Huang. A reliable and programmable acoustofluidic pump powered by oscillating sharp-edge structures. *Lab on a Chip*, 14(22):4319–4323, 2014.

[160] S. Huang, J. Chang, L. Lu, F. Liu, Z. Ye, and X. Cheng. Preparation and polarization of 0–3 cement based piezoelectric composites. *Materials Research Bulletin*, 41(2):291–297, 2006.

[161] S.-B. Huang, M.-H. Wu, Y.-H. Lin, C.-H. Hsieh, C.-L. Yang, H.-C. Lin, C.-P. Tseng, and G.-B. Lee. High-purity and label-free isolation of circulating tumor cells (ctcs) in a microfluidic platform by using optically-induced-dielectrophoretic (odep) force. *Lab on a Chip*, 13(7):1371–1383, 2013.

[162] F. V. Hunt. Stress and strain limits on the attainable velocity in mechanical vibration. *The Journal of the Acoustical Society of America*, 32(9):1123–1128, 1960.

[163] Z. Insepov, D. Wolf, and A. Hassanein. Nanopumping using carbon nanotubes. *Nano Letters*, 6(9):1893–1895, 2006.

[164] R. Ishibashi, K. Mawatari, and T. Kitamori. Highly efficient and ultra-small volume separation by pressure-driven liquid chromatography in extended nanochannels. *Small*, 8 (8):1237–1242, 2012.

[165] S. Ito, M. Sugimoto, Y. Matsui, and J. Kondoh. Study of surface acoustic wave streaming phenomenon based on temperature measurement and observation of streaming in liquids. *Japanese Journal of Applied Physics*, 46(7S):4718, 2007.

[166] J. L. Jackel, R. E. Howard, E. L. Hu, and S. Lyman. Reactive ion etching of linbo3. *Applied Physics Letters*, 38(11):907–909, 1981.

[167] T. C. Jackson, B. O. Patani, D. E. Ekpa, et al. Nanotechnology in diagnosis: a review. *Advances in Nanoparticles*, 6(03):93, 2017.

[168] B. Jaffe. *Piezoelectric ceramics*, volume 3. Elsevier, 2012.

[169] B. Jaffe, R. Roth, and S. Marzullo. Piezoelectric properties of lead zirconate-lead titanate solid-solution ceramics. *Journal of Applied Physics*, 25(6):809–810, 1954.

[170] M. J. Jebrail, R. F. Renzi, and S. Branda. Evaporation management in digital microfluidic devices, 2016.

[171] M. C. Jo and R. Guldiken. Active density-based separation using standing surface acoustic waves. *Sensors and Actuators A: Physical*, 187:22–28, 2012.

[172] M. C. Jo and R. Guldiken. Dual surface acoustic wave-based active mixing in a microfluidic channel. *Sensors and Actuators A: Physical*, 196:1–7, 2013.

[173] M. C. Jo and R. Guldiken. Effects of polydimethylsiloxane (pdms) microchannels on surface acoustic wave-based microfluidic devices. *Microelectronic Engineering*, 113: 98–104, 2014.

[174] S. Joseph and N. Aluru. Pumping of confined water in carbon nanotubes by rotation-translation coupling. *Physical Review Letters*, 101(6):064502, 2008.

[175] J. H. Jung, G. Destgeer, B. Ha, J. Park, and H. J. Sung. On-demand droplet splitting using surface acoustic waves. *Lab on a Chip*, 16(17):3235–3243, 2016.

[176] J. H. Jung, G. Destgeer, J. Park, H. Ahmed, K. Park, and H. J. Sung. On-demand droplet capture and release using microwell-assisted surface acoustic waves. *Analytical Chemistry*, 89(4):2211–2215, 2017.

[177] S. Jyomura, K. Nagatsuma, and H. Takeuchi. SAW propagation loss mechanism in piezoelectric ceramics. *Journal of Applied Physics*, 52(7):4472–4478, 1981. doi: 10.1063/1.329374.

[178] E. B. Kalman, I. Vlassiouk, and Z. S. Siwy. Nanofluidic bipolar transistors. *Advanced Materials*, 20(2):293–297, 2008.

[179] S. Kapishnikov, V. Kantsler, and V. Steinberg. Continuous particle size separation and size sorting using ultrasound in a microchannel. *Journal of Statistical Mechanics: Theory and Experiment*, 2006(01):P01012, 2006.

[180] A. Kawamata, H. Hosaka, and T. Morita. Non-hysteresis and perfect linear piezoelectric performance of a multilayered lithium niobate actuator. *Sensors and Actuators A: Physical*, 135(2):782–786, 2007.

[181] M. S. Kharusi and G. W. Farnell. On diffraction and focusing in anisotropic crystals. *Proceedings of the IEEE*, 60(8):945–956, 1972.

[182] S. J. Kim, Y.-C. Wang, J. H. Lee, H. Jang, and J. Han. Concentration polarization and nonlinear electrokinetic flow near a nanofluidic channel. *Physical Review Letters*, 99(4): 044501, 2007.

[183] S. J. Kim, L. D. Li, and J. Han. Amplified electrokinetic response by concentration polarization near nanofluidic channel. *Langmuir*, 25(13):7759–7765, 2009.

[184] S. J. Kim, S. H. Ko, K. H. Kang, and J. Han. Direct seawater desalination by ion concentration polarization. *Nature Nanotechnology*, 5(4):297–301, 2010.

[185] J. Kimberley, R. Cooney, J. Lambros, I. Chasiotis, and N. Barker. Failure of au RF-MEMS switches subjected to dynamic loading. *Sensors and Actuators A: Physical*, 154(1):140 – 148, 2009.

[186] L. V. King. On the acoustic radiation pressure on spheres. In *Proceedings of the Royal Society of London A: Mathematical, Physical and Engineering Sciences*, volume 147, pages 212–240. The Royal Society, 1934.

[187] R. Kishor, Z. Ma, S. Sreejith, Y. P. Seah, H. Wang, Y. Ai, Z. Wang, T.-T. Lim, and Y. Zheng. Real time size-dependent particle segregation and quantitative detection in a surface acoustic wave-photoacoustic integrated microfluidic system. *Sensors and Actuators B: Chemical*, 2017.

[188] X. Kong, C. Deneke, H. Schmidt, D. Thurmer, H. Ji, M. Bauer, and O. Schmidt. Surface acoustic wave mediated dielectrophoretic alignment of rolled-up microtubes in microfluidic systems. *Applied Physics Letters*, 96(13):134105, 2010.

[189] X. Y. Kong and Z. L. Wang. Spontaneous polarization-induced nanohelixes, nanosprings, and nanorings of piezoelectric nanobelts. *Nano Letters*, 3(12):1625–1631, 2003. doi: 10.1021/nl034463p.

[190] A. Kundt. On a new kind of acoustic dust figures and on the application of the same for determining sound velocity in solid bodies and gases. *Annals of Physics*, 203(4):497–523, 1866.

[191] A. Kundt and O. Lehmann. Ueber longitudinale schwingungen und klangfiguren in cylindrischen flüssigkeitssäulen. *Annalen der Physik*, 229(9):1–12, 1874.

[192] Y. Kurashina, K. Takemura, and J. Friend. Cell agglomeration in the wells of a 24-well plate using acoustic streaming. *Lab on a Chip*, 17(5):876–886, 2017.

[193] M. Kurosawa, N. Takahashi, and T. Higuchi. An ultrasonic XY stage using 10 MHz surface acoustic waves. In *Ultrasonics Symposium, 1994. Proceedings., 1994 IEEE*, volume 1, pages 535–538. IEEE, 1994.

[194] M. Kurosawa, M. Takahashi, and T. Higuchi. Ultrasonic linear motor using surface acoustic waves. *IEEE Transactions on Ultrasonics, Ferroelectrics, and Frequency Control*, 43(5): 901–906, 1996.

[195] M. K. Kurosawa, O. Kodaira, Y. Tsuchitoi, and T. Higuchi. Transducer for high speed and large thrust ultrasonic linear motor using two sandwich-type vibrators. *IEEE Transactions on Ultrasonics, Ferroelectrics, and Frequency Control*, 45(5):1188–1195, 1998.

[196] G. Kwon, D. Panchanathan, S. R. Mahmoudi, M. A. Gondal, G. H. McKinley, and K. K. Varanasi. Visible light guided manipulation of liquid wettability on photoresponsive surfaces. *Nature Communications*, 8, 2017.

[197] J. W. Kwon, H. Yu, Q. Zou, and E. S. Kim. Directional droplet ejection by nozzleless acoustic ejectors built on ZnO and PZT. *Journal of Micromechanics and Microengineering*, 16(12):2697, 2006.

[198] S. Langelier, L. Yeo, and J. R. Friend. UV epoxy bonding for enhanced SAW transmission and microscale acoustofluidic integration. *Lab on a Chip*, 12:2970–2976, 2012.

[199] S. M. Langelier, D. S. Chang, R. I. Zeitoun, and M. A. Burns. Acoustically driven programmable liquid motion using resonance cavities. *Proceedings of the National Academy of Sciences*, 106(31):12617–12622, 2009.

[200] S. M. Langelier, L. Y. Yeo, and J. Friend. Uv epoxy bonding for enhanced SAW transmission and microscale acoustofluidic integration. *Lab on a Chip*, 12(16):2970–2976, 2012.

[201] J. P. Lata, F. Guo, J. Guo, P.-H. Huang, J. Yang, and T. J. Huang. Surface acoustic waves grant superior spatial control of cells embedded in hydrogel fibers. *Advanced Materials*, 28(39):8632–8638, 2016.

[202] V. Laude, D. Gérard, N. Khelfaoui, C. F. Jerez-Hanckes, S. Benchabane, and A. Khelif. Subwavelength focusing of surface acoustic waves generated by an annular interdigital transducer. *Applied Physics Letters*, 92(9):094104, 2008.

[203] M. Leclercq, P. Picart, G. Penelet, and V. Tournat. Investigation of 3d surface acoustic waves in granular media with 3-color digital holography. *Journal of Applied Physics*, 121 (4):045112, 2017.

[204] C.-Y. Lee, W. Pang, H. Yu, and E. S. Kim. Subpicoliter droplet generation based on a nozzle-free acoustic transducer. *Applied Physics Letters*, 93(3):034104, 2008.

[205] C.-Y. Lee, W.-T. Wang, C.-C. Liu, and L.-M. Fu. Passive mixers in microfluidic systems: A review. *Chemical Engineering Journal*, 288:146–160, 2016.

[206] A. Lenshof, M. Evander, T. Laurell, and J. Nilsson. Acoustofluidics 5: Building microfluidic acoustic resonators. *Lab on a Chip*, 12(4):684–695, 2012.

[207] H. Li, J. R. Friend, and L. Y. Yeo. Surface acoustic wave concentration of particle and bioparticle suspensions. *Biomedical Microdevices*, 9(5):647–656, 2007.

[208] X. Li, D. Chen, J. Jin, and L. Wang. A novel underwater piezoelectric thruster with one single resonance mode. *Review of Scientific Instruments*, 90(4):045007, 2019.

[209] J. Lighthill. Acoustic streaming. *Journal of Sound and Vibration*, 61(3):391–418, 1978.

[210] K.-H. Lin, C.-M. Lai, C.-C. Pan, J.-I. Chyi, J.-W. Shi, S.-Z. Sun, C.-F. Chang, and C.-K. Sun. Spatial manipulation of nanoacoustic waves with nanoscale spot sizes. *Nature Nanotechnology*, 2(11):704–708, 2007.

[211] R.-Z. Lin and H.-Y. Chang. Recent advances in three-dimensional multicellular spheroid culture for biomedical research. *Biotechnology Journal*, 3(9-10):1172–1184, 2008.

[212] S.-C. S. Lin, X. Mao, and T. J. Huang. Surface acoustic wave (SAW) acoustophoresis: now and beyond. *Lab on a Chip*, 12(16):2766–2770, 2012.

[213] Y.-H. Lin and G.-B. Lee. Optically induced flow cytometry for continuous microparticle counting and sorting. *Biosensors and Bioelectronics*, 24(4):572–578, 2008.

[214] D. K.-C. Liu, J. Friend, and L. Yeo. The axial-torsional vibration of pretwisted beams. *Journal of Sound and Vibration*, 321(1-2):115–136, 2009.

[215] R. H. Liu, J. Yang, M. Z. Pindera, M. Athavale, and P. Grodzinski. Bubble-induced acoustic micromixing. *Lab on a Chip*, 2(3):151–157, 2002.

[216] R. H. Liu, R. Lenigk, R. L. Druyor-Sanchez, J. Yang, and P. Grodzinski. Hybridization enhancement using cavitation microstreaming. *Analytical Chemistry*, 75(8):1911–1917, 2003.

[217] X. Liu and J. Wu. Acoustic microstreaming around an isolated encapsulated microbubble. *The Journal of the Acoustical Society of America*, 125(3):1319–1330, 2009.

[218] Z. Liu, Y. Wang, and R. Liu. Temperature-dependent electro-osmotic flow reversal in a nanotube with high surface charge density. *The Journal of Physical Chemistry C*, 125: 898–907, 2020.

[219] M. Longhurst and N. Quirke. Temperature-driven pumping of fluid through single-walled carbon nanotubes. *Nano Letters*, 7(11):3324–3328, 2007.

[220] A. J. Lovinger. Ferroelectric polymers. *Science*, 220(4602):1115–1121, 1983. ISSN 0036-8075. doi: 10.1126/science.220.4602.1115.

[221] C.-k. Luo, P. S. Gudem, and J. F. Buckwalter. A 0.2–3.6-ghz 10-dbm b1db 29-dbm iip3 tunable filter for transmit leakage suppression in SAW-less 3g/4g fdd receivers. *IEEE Transactions on Microwave Theory and Techniques*, 63(10):3514–3524, 2015.

[222] G. P. Luo, Cheng-kai and J. Buckwalter. A 0.4-6-ghz 17-dbm b1db 36-dbm iip3 channel-selecting low-noise amplifier for SAW-less 3g/4g fdd diversity receivers. *IEEE Transactions on Microwave Theory and Techniques*, 64(4):1110–1121, 2016.

[223] T.-D. Luong, V.-N. Phan, and N.-T. Nguyen. High-throughput micromixers based on acoustic streaming induced by surface acoustic wave. *Microfluidics and Nanofluidics*, 10 (3):619–625, 2011.

[224] B. Ma, S. Liu, Z. Gan, G. Liu, X. Cai, H. Zhang, and Z. Yang. A pzt insulin pump integrated with a silicon microneedle array for transdermal drug delivery. *Microfluidics and Nanofluidics*, 2(5):417–423, 2006.

[225] Z. Ma, J. Guo, Y. J. Liu, and Y. Ai. The patterning mechanism of carbon nanotubes using surface acoustic waves: The acoustic radiation effect or the dielectrophoretic effect. *Nanoscale*, 7(33):14047–14054, 2015.

[226] Z. Ma, D. J. Collins, and Y. Ai. Detachable acoustofluidic system for particle separation via a traveling surface acoustic wave. *Analytical Chemistry*, 88(10):5316–5323, 2016.

[227] Z. Ma, D. J. Collins, J. Guo, and Y. Ai. Mechanical properties based particle separation via traveling surface acoustic wave. *Analytical Chemistry*, 88(23):11844–11851, 2016.

[228] Z. Ma, A. J. Teo, S. H. Tan, Y. Ai, and N.-T. Nguyen. Self-aligned interdigitated transducers for acoustofluidics. *Micromachines*, 7(12):216, 2016.

[229] M. Madadi, A. C. Jones, C. H. Arns, and M. A. Knackstedt. 3d imaging and simulation of elastic properties of porous materials. *Computing in Science & Engineering*, 11(4):65, 2009.

[230] M. J. Madou. *Fundamentals of microfabrication: the science of miniaturization*. CRC press, 2002.

[231] D. Mampallil, J. Reboud, R. Wilson, D. Wylie, D. R. Klug, and J. M. Cooper. Acoustic suppression of the coffee-ring effect. *Soft Matter*, 11(36):7207–7213, 2015.

[232] A. Manbachi and R. S. Cobbold. Development and application of piezoelectric materials for ultrasound generation and detection. *Ultrasound*, 19(4):187–196, 2011.

[233] O. Manor, L. Y. Yeo, and J. R. Friend. The appearance of boundary layers and drift flows due to high-frequency surface waves. *Journal of Fluid Mechanics*, 707:482–495, 2012.

[234] Z. Mao, Y. Xie, F. Guo, L. Ren, P.-H. Huang, Y. Chen, J. Rufo, F. Costanzo, and T. J. Huang. Experimental and numerical studies on standing surface acoustic wave microfluidics. *Lab on a Chip*, 16(3):515–524, 2016.

[235] Z. Mao, P. Li, M. Wu, H. Bachman, N. Mesyngier, X. Guo, S. Liu, F. Costanzo, and T. J. Huang. Enriching nanoparticles via acoustofluidics. *ACS Nano*, 11(1):603–612, 2017.

[236] P. Marmottant and S. Hilgenfeldt. Controlled vesicle deformation and lysis by single oscillating bubbles. *Nature*, 423(6936):153–156, 2003.

[237] P. L. Marston. Phase-shift expansions for approximate radiation forces on solid spheres in inviscid-acoustic standing waves. *The Journal of the Acoustical Society of America*, 142 (6):3358–3361, 2017.

[238] F. Martin. Propagation characteristics of harmonic surface skimming bulk waves on st quartz. *Electronics Letters*, 38(16):941–942, 2002.

[239] T. Marynowski. Focusing transducer for SAW beamwidth compression on yz lithium niobate. In *1982 Ultrasonics Symposium*, pages 160–165. IEEE, 1982.

[240] L. Masini, M. Cecchini, S. Girardo, R. Cingolani, D. Pisignano, and F. Beltram. Surface-acoustic-wave counterflow micropumps for on-chip liquid motion control in two-dimensional microchannel arrays. *Lab on a Chip*, 10(15):1997–2000, 2010.

[241] I. M. Mason and E. A. Ash. Acoustic surface-wave beam diffraction on anisotropic substrates. *Journal of Applied Physics*, 42(13):5343–5351, 1971.

[242] W. P. Mason. Piezoelectricity, its history and applications. *The Journal of the Acoustical Society of America*, 70(6):1561–1566, 1981.

[243] D. Mattia and Y. Gogotsi. Static and dynamic behavior of liquids inside carbon nanotubes. *Microfluidics and Nanofluidics*, 5(3):289–305, 2008.

[244] K. Mawatari, T. Tsukahara, and T. Kitamori. Extended nanospace chemical systems on a chip for new analytical technology. *Analyst*, 136(15):3051–3059, 2011.

[245] K. Mawatari, S. Kubota, Y. Xu, C. Priest, R. Sedev, J. Ralston, and T. Kitamori. Femtoliter droplet handling in nanofluidic channels: a laplace nanovalve. *Analytical Chemistry*, 84 (24):10812–10816, 2012.

[246] J. Mei, N. Zhang, and J. Friend. Fabrication of surface acoustic wave devices on lithium niobate. *JoVE (Journal of Visualized Experiments)*, (160):e61013, 2020.

[247] M. Miansari and J. R. Friend. Acoustic nanofluidics via room-temperature lithium niobate bonding: A platform for actuation and manipulation of nanoconfined fluids and particles. *Advanced Functional Materials*, 26(43):7861–7872, 2016.

[248] M. Miansari, A. Qi, L. Y. Yeo, and J. R. Friend. Vibration-induced deagglomeration and shear-induced alignment of carbon nanotubes in air. *Advanced Functional Materials*, 25 (7):1014–1023, 2015.

[249] D. Mijatovic, J. Eijkel, and A. Van Den Berg. Technologies for nanofluidic systems: top-down vs. bottom-up; a review. *Lab on a Chip*, 5(5):492–500, 2005.

[250] M. Mikitarenko and A. Perelmuter. Safe fatigue life of steel towers under the action of wind vibrations. *Journal of Wind Engineering and Industrial Aerodynamics*, 74:1091–1100, 1998.

[251] K.-S. Min, B.-J. Chang, and H.-W. Seo. Study on the contra-rotating propeller system design and full-scale performance prediction method in rapid hull form generation. *International Journal of Naval Architecture and Ocean Engineering*, 1(1):29–38, 2009.

[252] P. Minzioni, R. Osellame, C. Sada, S. Zhao, F. Omenetto, K. B. Gylfason, T. Haraldsson, Y. Zhang, A. Ozcan, A. Wax, et al. Roadmap for optofluidics. *Journal of Optics*, 19(9): 093003, 2017.

[253] H. Mitome. The mechanism of generation of acoustic streaming. *Electronics and Communications in Japan (Part III: Fundamental Electronic Science)*, 81(10):1–8, 1998.

[254] D. Morgan. Surface acoustic wave filters. *Amsterdam: Elsevier*, 2007.

[255] D. Morgan. *Surface acoustic wave filters: With applications to electronic communications and signal processing*. Academic Press, 2010.

[256] P. M. Morse and K. U. Ingard. *Theoretical Acoustics*. Princeton University Press, 1986.

[257] E. A. Mun, C. Hannell, S. E. Rogers, P. Hole, A. C. Williams, and V. V. Khutoryanskiy. On the role of specific interactions in the diffusion of nanoparticles in aqueous polymer solutions. *Langmuir*, 30(1):308–317, 2014.

[258] M. Munasinghe and G. Farnell. Finite difference analysis of Rayleigh wave scattering at vertical discontinuities. *Journal of Geophysical Research*, 78(14):2454–2466, 1973.

[259] F. Nadal and E. Lauga. Asymmetric steady streaming as a mechanism for acoustic propulsion of rigid bodies. *Physics of Fluids*, 26(8):082001, 2014.

[260] Y. Nakagawa. A new SAW convolver using multichannel waveguide. In *Ultrasonics Symposium, 1991. Proceedings., IEEE 1991*, pages 255–258. IEEE, 1991.

[261] H. Nakahata, S. Fujii, K. Higaki, A. Hachigo, H. Kitabayashi, S. Shikata, and N. Fujimori. Diamond-based surface acoustic wave devices. *Semiconductor Science and Technology*, 18(3):S96, 2003.

[262] T. Nakao, Y. Kazoe, K. Morikawa, L. Lin, K. Mawatari, and T. Kitamori. Femtoliter volumetric pipette and flask utilizing nanofluidics. *Analyst*, 145(7):2669–2675, 2020.

[263] S. M. Nakhmanson, M. B. Nardelli, and J. Bernholc. Collective polarization effects in β-polyvinylidene fluoride and its copolymers with tri- and tetrafluoroethylene. *Phys. Rev. B*, 72:115210, Sep 2005. doi: 10.1103/PhysRevB.72.115210.

[264] J. Nam and C. S. Lim. A conductive liquid-based surface acoustic wave device. *Lab on a Chip*, 16(19):3750–3755, 2016.

[265] J. Nam, Y. Lee, and S. Shin. Size-dependent microparticles separation through standing surface acoustic waves. *Microfluidics and Nanofluidics*, 11(3):317–326, 2011.

[266] J. Nam, H. Lim, D. Kim, and S. Shin. Separation of platelets from whole blood using standing surface acoustic waves in a microchannel. *Lab on a Chip*, 11(19):3361–3364, 2011.

[267] J. Nam, H. Lim, C. Kim, J. Yoon Kang, and S. Shin. Density-dependent separation of encapsulated cells in a microfluidic channel by using a standing surface acoustic wave. *Biomicrofluidics*, 6(2):024120, 2012.

[268] N. Nama, P.-H. Huang, T. J. Huang, and F. Costanzo. Investigation of acoustic streaming patterns around oscillating sharp edges. *Lab on a Chip*, 14(15):2824–2836, 2014.

[269] N. Nama, P.-H. Huang, T. J. Huang, and F. Costanzo. Investigation of micromixing by acoustically oscillated sharp-edges. *Biomicrofluidics*, 10(2):024124, 2016.

[270] V. G. Narushin, M. N. Romanov, and D. K. Griffin. A universal formula for avian egg shape. *BioRxiv*, 2020. doi: 10.1101/2020.08.15.252148.

[271] T. Nishihara, T. Yokoyama, T. Miyashita, and Y. Satoh. High performance and miniature thin film bulk acoustic wave filters for 5 ghz. In *Ultrasonics Symposium, Proceedings*, volume 1, pages 969–972. IEEE, 2002.

[272] A. Noy, H. G. Park, F. Fornasiero, J. K. Holt, C. P. Grigoropoulos, and O. Bakajin. Nanofluidics in carbon nanotubes. *Nano Today*, 2(6):22–29, 2007.

[273] H. Nwosu, C. Obieke, and A. Ameh. Failure analysis and shock protection of external hard disk drive. *Nigerian Journal of Technology*, 35(4):855–865, 2016.

[274] W. L. Nyborg. Acoustic streaming due to attenuated plane waves. *The Journal of the Acoustical Society of America*, 25(1):68–75, 1953.

[275] W. L. M. Nyborg. *Physical Acoustics*, volume 2, chapter Acoustic Streaming, pages 265–331. Academic Press, 1965.

[276] S. Oberti, A. Neild, and T. W. Ng. Microfluidic mixing under low frequency vibration. *Lab on a Chip*, 9(10):1435–1438, 2009.

[277] K. E. O'Connell, A. M. Mikkola, A. M. Stepanek, A. Vernet, C. D. Hall, C. C. Sun, E. Yildirim, J. F. Staropoli, J. T. Lee, and D. E. Brown. Practical murine hematopathology: a comparative review and implications for research. *Comparative Medicine*, 65(2):96–113, 04 2015.

[278] S.-W. Ohl and C.-D. Ohl. Acoustic cavitation in a microchannel. *Handbook of Ultrasonics and Sonochemistry*, pages 99–135, 2016.

[279] S. Orbay, A. Ozcelik, J. Lata, M. Kaynak, M. Wu, and T. J. Huang. Mixing high-viscosity fluids via acoustically driven bubbles. *Journal of Micromechanics and Microengineering*, 27(1):015008, 2016.

[280] N. D. Orloff, J. R. Dennis, M. Cecchini, E. Schonbrun, E. Rocas, Y. Wang, D. Novotny, R. W. Simmonds, J. Moreland, I. Takeuchi, et al. Manipulating particle trajectories with phase-control in surface acoustic wave microfluidics. *Biomicrofluidics*, 5(4):044107, 2011.

[281] R. O'Rorke, C. Wood, C. Wälti, S. Evans, A. Davies, and J. Cunningham. Acousto-microfluidics: transporting microbubble and microparticle arrays in acoustic traps using surface acoustic waves. *Journal of Applied Physics*, 111(9):094911, 2012.

[282] M. Ovchinnikov, J. Zhou, and S. Yalamanchili. Acoustic streaming of a sharp edge. *The Journal of the Acoustical Society of America*, 136(1):22–29, 2014.

[283] A. Ozcelik, D. Ahmed, Y. Xie, N. Nama, Z. Qu, A. A. Nawaz, and T. J. Huang. An acoustofluidic micromixer via bubble inception and cavitation from microchannel sidewalls. *Analytical Chemistry*, 86(10):5083, 2014.

[284] A. Ozcelik, J. Rufo, F. Guo, Y. Gu, P. Li, J. Lata, and T. J. Huang. Acoustic tweezers for the life sciences. *Nature Methods*, 15(12):1021–1028, 2018.

[285] M. Ozgul, K. Takemura, S. Trolier-McKinstry, and C. A. Randall. Polarization fatigue in pb (zn 1/3 nb 2/3) o 3–pbtio 3 ferroelectric single crystals. *Journal of Applied Physics*, 89 (9):5100–5106, 2001.

[286] J. Park, J. H. Jung, G. Destgeer, H. Ahmed, K. Park, and H. J. Sung. Acoustothermal tweezer for droplet sorting in a disposable microfluidic chip. *Lab on a Chip*, 17(6): 1031–1040, 2017.

[287] S.-Y. Park and P.-Y. Chiou. Light-driven droplet manipulation technologies for lab-on-a-chip applications. *Advances in OptoElectronics*, 2011:909174, 2011.

[288] M. V. Patel, I. A. Nanayakkara, M. G. Simon, and A. P. Lee. Cavity-induced microstreaming for simultaneous on-chip pumping and size-based separation of cells and particles. *Lab on a Chip*, 14(19):3860–3872, 2014.

[289] M. Pekarcikova, M. Hofmann, S. Menzel, H. Schrnidt, T. Gemming, and K. Wetzig. Investigation of high power effects on Ti/Al and Ta-Si-N/Cu/Ta-Si-N electrodes for SAW devices. *IEEE Transactions on Ultrasonics, Ferroelectrics, and Frequency Control*, 52(5): 911–917, May 2005. ISSN 0885-3010. doi: 10.1109/TUFFC.2005.1503977.

[290] T. Pezeril, C. Klieber, S. Andrieu, and K. Nelson. Optical generation of gigahertz-frequency shear acoustic waves in liquid glycerol. *Physical Review Letters*, 102(10):107402, 2009.

[291] A. Piruska, M. Gong, J. V. Sweedler, and P. W. Bohn. Nanofluidics in chemical analysis. *Chemical Society Reviews*, 39(3):1060–1072, 2010.

[292] J. Poittevin, F. Gautier, C. Pézerat, and P. Picart. High-speed holographic metrology: principle, limitations, and application to vibroacoustics of structures. *Optical Engineering*, 55(12):121717–121717, 2016.

[293] O. Pouliquen, J. Delour, and S. B. Savage. Fingering in granular flows. *Nature*, 386(6627): 816–817, 1997.

[294] T. Pritz. Frequency dependences of complex moduli and complex poisson's ratio of real solid materials. *Journal of Sound and Vibration*, 214(1):83–104, 1998.

[295] Q. Pu, J. Yun, H. Temkin, and S. Liu. Ion-enrichment and ion-depletion effect of nanochannel structures. *Nano Letters*, 4(6):1099–1103, 2004.

[296] A. Qi, J. R. Friend, L. Y. Yeo, D. A. Morton, M. P. McIntosh, and L. Spiccia. Miniature inhalation therapy platform using surface acoustic wave microfluidic atomization. *Lab on a Chip*, 9(15):2184–2193, 2009.

[297] S. Queste, E. Courjon, G. Ulliac, R. Salut, V. Petrini, J. Rauch, and F. Besançon Cedex. Deep reactive ion etching of quartz, lithium niobate and lead titanate. *JNTE Proceedings*, 2008.

[298] R. Raghavan, J. R. Friend, and L. Y. Yeo. Particle concentration via acoustically driven microcentrifugation: microPIV flow visualization and numerical modelling studies. *Microfluidics and Nanofluidics*, 8:73–84, 2010.

[299] B. Rallabandi, C. Wang, and S. Hilgenfeldt. Two-dimensional streaming flows driven by sessile semicylindrical microbubbles. *Journal of Fluid Mechanics*, 739:57–71, 2014.

[300] S. Ramanujan. Modular equations and approximations to π. *Quarterly Journal of Mathematics*, 45:350–372, 1914.

[301] R. Rambach, J. Taiber, C. Scheck, C. Meyer, J. Reboud, J. Cooper, and T. Franke. Visualization of surface acoustic waves in thin liquid films. *Scientific Reports*, 6, 2016.

[302] K. Ramesh, J. D. Hogan, J. Kimberley, and A. Stickle. A review of mechanisms and models for dynamic failure, strength, and fragmentation. *Planetary and Space Science*, 107:10 – 23, 2015.

[303] L. Rayleigh. On the circulation of air observed in kundt's tubes, and on some allied acoustical problems. *Philosophical Transactions of the Royal Society of London*, 175:1–21, 1884.

[304] L. Rayleigh. On waves propagated along the plane surface of an elastic solid. *Proceedings of the London Mathematical Society*, 1(1):4–11, 1885.

[305] W. Reisner, K. J. Morton, R. Riehn, Y. M. Wang, Z. Yu, M. Rosen, J. C. Sturm, S. Y. Chou, E. Frey, and R. H. Austin. Statics and dynamics of single dna molecules confined in nanochannels. *Physical Review Letters*, 94(19):196101, 2005.

[306] L. Ren, Y. Chen, P. Li, Z. Mao, P.-H. Huang, J. Rufo, F. Guo, L. Wang, J. P. McCoy, S. J. Levine, et al. A high-throughput acoustic cell sorter. *Lab on a Chip*, 15(19):3870–3879, 2015.

[307] Z. Ren, P. Heard, J. M. Marshall, P. A. Thomas, and S. Yu. Etching characteristics of linbo 3 in reactive ion etching and inductively coupled plasma. *Journal of Applied Physics*, 103 (3):034109, 2008.

[308] A. R. Rezk, A. Qi, J. R. Friend, W. H. Li, and L. Y. Yeo. Uniform mixing in paper-based microfluidic systems using surface acoustic waves. *Lab on a Chip*, 12(4):773–779, 2012.

[309] A. R. Rezk, J. R. Friend, and L. Y. Yeo. Simple, low cost MHz-order acoustomicrofluidics using aluminium foil electrodes. *Lab on a Chip*, 14(11):1802–5, 2014.

[310] A. R. Rezk, O. Manor, L. Y. Yeo, and J. R. Friend. Double flow reversal in thin liquid films driven by megahertz-order surface vibration. In *Proc. R. Soc. A*, volume 470, page 20130765. The Royal Society, 2014.

[311] A. R. Rezk, L. Y. Yeo, and J. R. Friend. Poloidal flow and toroidal particle ring formation in a sessile drop driven by megahertz order vibration. *Langmuir*, 30(37):11243–11247, 2014.

[312] A. Riaud, M. Baudoin, J.-L. Thomas, and O. Bou Matar. Cyclones and attractive streaming generated by acoustical vortices. *Physical Review*, 90(013008):8, 2014. doi: 10.1103/PhysRevE.90.013008.

[313] A. Riaud, J.-L. Thomas, E. Charron, A. Bussonnière, O. B. Matar, and M. Baudoin. Anisotropic swirling surface acoustic waves from inverse filtering for on-chip generation of acoustic vortices. *Physical Review Applied*, 4(3):034004, 2015.

[314] A. Riaud, M. Baudoin, J.-L. Thomas, and O. Bou Matar. SAW synthesis with idts array and the inverse filter: toward a versatile SAW toolbox for microfluidics and biological applications. *Physics of Fluid Dynamics*, 2016.

[315] A. Riaud, M. Baudoin, O. Bou Matar, J.-L. Thomas, and P. Brunet. On the influence of viscosity and caustics on acoustic streaming in sessile droplets: an experimental and a numerical study with a cost-effective method. *Journal of Fluid Mechanics*, Not yet pu, 2017.

[316] A. Riaud, M. Baudoin, O. B. Matar, L. Becerra, and J.-L. Thomas. Selective manipulation of microscopic particles with precursor swirling Rayleigh waves. *Physical Review Applied*, 7(2):024007, 2017.

[317] P. Ridao, M. Carreras, D. Ribas, P. J. Sanz, and G. Oliver. Intervention AUVs: the next challenge. *Annual Reviews in Control*, 40:227–241, 2015.

[318] J. Rife, M. Bell, J. Horwitz, M. Kabler, R. Auyeung, and W. Kim. Miniature valveless ultrasonic pumps and mixers. *Sensors and Actuators A: Physical*, 86(1):135–140, 2000.

[319] K. F. Rinne, S. Gekle, D. J. Bonthuis, and R. R. Netz. Nanoscale pumping of water by ac electric fields. *Nano Letters*, 12(4):1780–1783, 2012.

[320] Á. Ríos, M. Zougagh, and M. Avila. Miniaturization through lab-on-a-chip: Utopia or reality for routine laboratories? a review. *Analytica Chimica Acta*, 740:1–11, 2012.

[321] W. B. Robertson. The ultrasonic cleaner in the laboratory. *J. Chem. Educ*, 44(8):460, 1967.

[322] P. Rogers and A. Neild. Selective particle trapping using an oscillating microbubble. *Lab on a Chip*, 11(21):3710–3715, 2011.

[323] P. R. Rogers, J. R. Friend, and L. Y. Yeo. Exploitation of surface acoustic waves to drive size-dependent microparticle concentration within a droplet. *Lab on a Chip*, 10(21): 2979–2985, 2010.

[324] S. Rothberg, M. Allen, P. Castellini, D. Di Maio, J. Dirckx, D. Ewins, B. J. Halkon, P. Muyshondt, N. Paone, T. Ryan, et al. An international review of laser doppler vibrometry: Making light work of vibration measurement. *Optics and Lasers in Engineering*, 2016.

[325] L. Rozenberg. Efficiency of ultrasonic cleaning. In *Physical Principles of Ultrasonic Technology*, pages 270–318. Springer, 1973.

[326] S. Saadon and O. Sidek. A review of vibration based mems piezoelectric energy harvesters. *Energy Conversion and Management*, 52(1):500–504, 2011.

[327] J. M. Sabatier and N. Xiang. Laser-doppler-based acoustic-to-seismic detection of buried mines. In *AeroSense'99*, pages 215–222. International Society for Optics and Photonics, 1999.

[328] E. K. Sackmann, A. L. Fulton, and D. J. Beebe. The present and future role of microfluidics in biomedical research. *Nature*, 507(7491):181, 2014.

[329] J. E. Sader and J. R. Friend. Note: Calibration of atomic force microscope cantilevers using only their resonant frequency and quality factor. *Review of Scientific Instruments*, 85 (11):116101, 2014.

[330] Y. Saito, H. Takao, T. Tani, T. Nonoyama, K. Takatori, T. Homma, T. Nagaya, and M. Nakamura. Lead-free piezoceramics. *Nature*, 432(7013):84–87, 11 2004.

[331] H. Schlichting. Berechnung ebener periodischer grenzschichtströmungen. *Phys. Z*, 33 (1932):327–335, 1932.

[332] L. Schmid and T. Franke. SAW-controlled drop size for flow focusing. *Lab on a Chip*, 13 (9):1691–1694, 2013.

[333] L. Schmid, A. Wixforth, D. A. Weitz, and T. Franke. Novel surface acoustic wave (SAW)-driven closed pdms flow chamber. *Microfluidics and Nanofluidics*, 12(1-4):229–235, 2012.

[334] L. Schmid, D. A. Weitz, and T. Franke. Sorting drops and cells with acoustics: acoustic microfluidic fluorescence-activated cell sorter. *Lab on a Chip*, 14(19):3710–3718, 2014.

[335] H. Schmidbauer. Eine exakte eierkurvenkonstruktion mit technischen anwendungen (an exact egg curve construction with technical applications). *Elemente der Mathematik eine Zeitschrift der Schweizerischen Mathematischen (Elements of Mathematics — a Journal of the Swiss Mathematical Society)*, 3:68–71, 1948.

[336] A. Schmitt, J. Guichard, J. M. Massé, N. Debili, and E. M. Cramer. Of mice and men: comparison of the ultrastructure of megakaryocytes and platelets. *Exp Hematol*, 29(11): 1295–1302, Nov 2001.

[337] S. Schneider, S. Nuschele, A. Wixforth, C. Gorzelanny, A. Alexander-Katz, R. Netz, and M. F. Schneider. Shear-induced unfolding triggers adhesion of von willebrand factor fibers. *Proceedings of the National Academy of Sciences*, 104(19):7899–7903, 2007.

[338] R. B. Schoch, J. Han, and P. Renaud. Transport phenomena in nanofluidics. *Reviews of Modern Physics*, 80(3):839, 2008.

[339] K. M. Seemann, J. Ebbecke, and A. Wixforth. Alignment of carbon nanotubes on pre-structured silicon by surface acoustic waves. *Nanotechnology*, 17(17):4529, 2006.

[340] J. B. Segur and H. E. Oberstar. Viscosity of glycerol and its aqueous solutions. *Industrial & Engineering Chemistry*, 43(9):2117–2120, 1951.

[341] M. Sesen, T. Alan, and A. Neild. Microfluidic on-demand droplet merging using surface acoustic waves. *Lab on a Chip*, 14(17):3325–3333, 2014.

[342] M. Sesen, T. Alan, and A. Neild. Microfluidic plug steering using surface acoustic waves. *Lab on a Chip*, 15(14):3030–3038, 2015.

[343] M. Sesen, C. Devendran, S. Malikides, T. Alan, and A. Neild. Surface acoustic wave enabled pipette on a chip. *Lab on a Chip*, 17(3):438–447, 2017.

[344] N. Setter, D. Damjanovic, L. Eng, G. Fox, S. Gevorgian, S. Hong, A. Kingon, H. Kohlstedt, N. Park, G. Stephenson, et al. Ferroelectric thin films: Review of materials, properties, and applications. *Journal of Applied Physics*, 100(5):051606, 2006.

[345] I. Sevostianov and M. Kachanov. On approximate symmetries of the elastic properties and elliptic orthotropy. *International Journal of Engineering Science*, 46(3):211–223, 2008.

[346] P. Shankar and M. Kumar. Experimental determination of the kinematic viscosity of glycerol-water mixtures. *Proceedings of the Royal Society of London. Series A: Mathematical and Physical Sciences*, 444(1922):573–581, 1994.

[347] J. Shi, X. Mao, D. Ahmed, A. Colletti, and T. J. Huang. Focusing microparticles in a microfluidic channel with standing surface acoustic waves (SSAW). *Lab on a Chip*, 8(2): 221–223, 2008.

[348] J. Shi, D. Ahmed, X. Mao, S.-C. S. Lin, A. Lawit, and T. J. Huang. Acoustic tweezers: patterning cells and microparticles using standing surface acoustic waves (SSAW). *Lab on a Chip*, 9(20):2890–2895, 2009.

[349] J. Shi, H. Huang, Z. Stratton, Y. Huang, and T. J. Huang. Continuous particle separation in a microfluidic channel via standing surface acoustic waves (SSAW). *Lab on a Chip*, 9(23): 317–326, 2011.

[350] J. Shi, S. Yazdi, S.-C. S. Lin, X. Ding, I.-K. Chiang, K. Sharp, and T. J. Huang. Three-dimensional continuous particle focusing in a microfluidic channel via standing surface acoustic waves (SSAW). *Lab on a Chip*, 11(14):2319–2324, 2011.

[351] K. Shibayama, K. Yamanouchi, H. Sato, and T. Meguro. Optimum cut for rotated Y-cut $LiNbO_3$ crystal used as the substrate of acoustic-surface-wave filters. *Proceedings of the IEEE*, 64(5):595–597, 1976.

[352] C. W. Shields IV, C. D. Reyes, and G. P. López. Microfluidic cell sorting: A review of the advances in the separation of cells from debulking to rare cell isolation. *Lab on a Chip*, 15 (5):1230–1249, 2015.

[353] R. Shilton, M. Tan, L. Yeo, and J. Friend. Concentration and mixing of particles in microdrops driven by focused surface acoustic waves. *Proceedings - IEEE Ultrasonics Symposium*, pages 930–933, 2008. ISSN 10510117. doi: 10.1109/ULTSYM.2008.0224.

[354] R. Shilton, M. K. Tan, L. Y. Yeo, and J. R. Friend. Particle concentration and mixing in microdrops driven by focused surface acoustic waves. *Journal of Applied Physics*, 104(1): 014910, 2008.

[355] R. J. Shilton, L. Y. Yeo, and J. R. Friend. Quantification of surface acoustic wave induced chaotic mixing-flows in microfluidic wells. *Sensors and Actuators B: Chemical*, 160(1): 1565–1572, 2011.

[356] R. J. Shilton, M. Travagliati, F. Beltram, and M. Cecchini. Microfluidic pumping through miniaturized channels driven by ultra-high frequency surface acoustic waves. *Applied Physics Letters*, 105(7):074106, 2014.

[357] R. J. Shilton, M. Travagliati, F. Beltram, and M. Cecchini. Nanoliter-droplet acoustic streaming via ultra high frequency surface acoustic waves. *Advanced Materials*, 26(29): 4941–4946, 2014.

[358] R. J. Shilton, V. Mattoli, M. Travagliati, M. Agostini, A. Desii, F. Beltram, and M. Cecchini. Rapid and controllable digital microfluidic heating by surface acoustic waves. *Advanced Functional Materials*, 25(37):5895–5901, 2015.

[359] S. Shiokawa, Y. Matsui, and T. Moriizumi. Experimental study on liquid streaming by SAW. *Japanese Journal of Applied Physics*, 28(S1):126, 1989.

[360] S. Shiokawa, Y. Matsui, and T. Ueda. Study on SAW streaming and its application to fluid devices. *Japanese Journal of Applied Physics*, 29(S1):137, 1990.

[361] K. Shirai, K. Mawatari, R. Ohta, H. Shimizu, and T. Kitamori. A single-molecule elisa device utilizing nanofluidics. *Analyst*, 143(4):943–948, 2018.

[362] G. Siegmund. Sources of measurement error in laser doppler vibrometers and proposal for unified specifications. In *Proc. SPIE*, volume 7098, pages 70980Y–1, 2008.

[363] N. Sivanantha, C. Ma, D. J. Collins, M. Sesen, J. Brenker, R. L. Coppel, A. Neild, and T. Alan. Characterization of adhesive properties of red blood cells using surface acoustic wave induced flows for rapid diagnostics. *Applied Physics Letters*, 105(10):103704, 2014.

[364] A. Slobodnik and E. Conway. New high-frequency high-coupling low-beam-steering cut for acoustic surface waves on linbo3. *Electronics Letters*, 6(6):171–173, 1970.

[365] A. J. Slobodnik. Surface acoustic waves and SAW materials. *Proceedings of the IEEE*, 64 (5):581–595, 1976.

[366] A. Slobodnik Jr and E. Conway. Microwave acoustics handbook. volume 1. surface wave velocities. Technical report, Air Force Cambridge Research Labs, Hanscom, Afb, Ma, 1970.

[367] R. E. Smalley, M. S. Dresselhaus, G. Dresselhaus, and P. Avouris. *Carbon nanotubes: synthesis, structure, properties, and applications*, volume 80. Springer Science & Business Media, 2003.

[368] S. E. Smith et al. *Investigation of nanoscale etching and poling of lithium niobate*. PhD thesis, Montana State University-Bozeman, College of Engineering, 2014.

[369] V. Soluch and M. Lysakowska. Surface acoustic waves on x-cut linbo/sub 3. *IEEE Transactions on Ultrasonics, Ferroelectrics, and Frequency Control*, 52(1):145–147, 2005.

[370] W. v. Sparreboom, A. Van Den Berg, and J. Eijkel. Principles and applications of nanofluidic transport. *Nature Nanotechnology*, 4(11):713–720, 2009.

[371] T. M. Squires and S. R. Quake. Microfluidics: Fluid physics at the nanoliter scale. *Reviews of Modern Physics*, 77(3):977, 2005.

[372] K. Sritharan, C. Strobl, M. Schneider, A. Wixforth, and Z. v. Guttenberg. Acoustic mixing at low reynolds numbers. *Applied Physics Letters*, 88(5):054102, 2006.

[373] M. Standard. Environmental test methods and engineering guidelines. *MILSTD-810E, AMSC F*, 4766, 1989.

[374] V. L. Strashilov and V. M. Yantchev. Surface transverse waves: properties, devices, and analysis. *IEEE Transactions on Ultrasonics, Ferroelectrics, and Frequency Control*, 52(5): 812–821, 2005.

[375] C. Strobl, C. Schäflein, U. Beierlein, J. Ebbecke, and A. Wixforth. Carbon nanotube alignment by surface acoustic waves. *Applied physics Letters*, 85(8):1427–1429, 2004.

[376] F. G. Strobl, D. Breyer, P. Link, A. A. Torrano, C. Bräuchle, M. F. Schneider, and A. Wixforth. A surface acoustic wave-driven micropump for particle uptake investigation under physiological flow conditions in very small volumes. *Beilstein Journal of Nanotechnology*, 6(1):414–419, 2015.

[377] T. L. Szabo and A. Slobodnik. The effect of diffraction on the design of acoustic surface wave devices. *IEEE transactions on Sonics and Ultrasonics*, 20(3):240–251, 1973.

[378] T. Tachizaki, T. Muroya, O. Matsuda, Y. Sugawara, D. H. Hurley, and O. B. Wright. Scanning ultrafast sagnac interferometry for imaging two-dimensional surface wave propagation. *Review of Scientific Instruments*, 77(4):043713, 2006.

[379] H. Takagi, R. Maeda, N. Hosoda, and T. Suga. Room-temperature bonding of lithium niobate and silicon wafers by argon-beam surface activation. *Applied Physics Letters*, 74 (16):2387–2389, 1999.

[380] A. Takayanagi, K. Yamanouchi, and K. Shibayama. Piezoelectric leaky surface wave in linbo3. *Applied Physics Letters*, 17(5):225–227, 1970.

[381] D. Taller, K. Richards, Z. Slouka, S. Senapati, R. Hill, D. B. Go, and H.-C. Chang. On-chip surface acoustic wave lysis and ion-exchange nanomembrane detection of exosomal rna for pancreatic cancer study and diagnosis. *Lab on a Chip*, 15(7):1656–1666, 2015.

[382] A. Tan and F. Hover. Thrust and wake characterization in small, robust ultrasonic thrusters. In *Oceans 2010 MTS/IEEE Seattle*, pages 1–9. IEEE, 2010.

[383] M. Tan, L. Yeo, and J. Friend. Rapid fluid flow and mixing induced in microchannels using surface acoustic waves. *EPL (Europhysics Letters)*, 87(4):47003, 2009.

[384] M. K. Tan and L. Y. Yeo. Hybrid finite-difference/lattice boltzmann simulations of microchannel and nanochannel acoustic streaming driven by surface acoustic waves. *Physical Review Fluids*, 3(4):044202, 2018.

[385] M. K. Tan, J. R. Friend, and L. Y. Yeo. Microparticle collection and concentration via a miniature surface acoustic wave device. *Lab on a Chip*, 7(5):618, 2007. ISSN 1473-0197. doi: 10.1039/b618044b.

[386] M. K. Tan, J. R. Friend, and L. Y. Yeo. Direct visualization of surface acoustic waves along substrates using smoke particles. *Applied Physics Letters*, 91(22):224101, 2007.

[387] M. K. Tan, J. R. Friend, and L. Y. Yeo. Interfacial jetting phenomena induced by focused surface vibrations. *Physical Review Letters*, 103(2):024501, 2009.

[388] M. K. Tan, R. Tjeung, H. Ervin, L. Y. Yeo, and J. Friend. Double aperture focusing transducer for controlling microparticle motions in trapezoidal microchannels with surface acoustic waves. *Applied Physics Letters*, 95(13):134101, 2009.

[389] M. K. Tan, L. Y. Yeo, and J. R. Friend. Unique flow transitions and particle collection switching phenomena in a microchannel induced by surface acoustic waves. *Applied Physics Letters*, 97(23):234106, 2010.

[390] M. Tanter, J.-L. Thomas, and M. Fink. Time reversal and the inverse filter. *The Journal of the Acoustical Society of America*, 108(1):223–234, 2000.

[391] L. Taupin, A. Lhémery, and G. Inquiété. A detailed study of guided wave propagation in a viscoelastic multilayered anisotropic plate. In *Journal of Physics: Conference Series*, volume 269, page 012002. IOP Publishing, 2011.

[392] J. O. Tegenfeldt, C. Prinz, H. Cao, S. Chou, W. W. Reisner, R. Riehn, Y. M. Wang, E. C. Cox, J. C. Sturm, P. Silberzan, et al. The dynamics of genomic-length dna molecules in 100-nm channels. *Proceedings of the National Academy of Sciences of the United States of America*, 101(30):10979–10983, 2004.

[393] L. H. Thamdrup, A. Klukowska, and A. Kristensen. Stretching dna in polymer nanochannels fabricated by thermal imprint in pmma. *Nanotechnology*, 19(12):125301, 2008.

[394] W. Thielicke and E. Stamhuis. Pivlab–towards user-friendly, affordable and accurate digital particle image velocimetry in matlab. *Journal of Open Research Software*, 2(1), 2014.

[395] E. T. Thostenson, Z. Ren, and T.-W. Chou. Advances in the science and technology of carbon nanotubes and their composites: a review. *Composites Science and Technology*, 61 (13):1899–1912, 2001.

[396] R. N. Thurston, A. D. Pierce, and E. P. Papadakis. *Reference for Modern Instrumentation, Techniques, and Technology: Ultrasonic Instruments and Devices I: Ultrasonic Instruments and Devices I*, volume 23. Academic Press, 1998.

[397] L. Tian, N. Martin, P. G. Bassindale, A. J. Patil, M. Li, A. Barnes, B. W. Drinkwater, and S. Mann. Spontaneous assembly of chemically encoded two-dimensional coacervate droplet arrays by acoustic wave patterning. *Nature Communications*, 7, 2016.

[398] Z. Tian, S. Yang, P.-H. Huang, Z. Wang, P. Zhang, Y. Gu, H. Bachman, C. Chen, M. Wu, Y. Xie, et al. Wave number–spiral acoustic tweezers for dynamic and reconfigurable manipulation of particles and cells. *Science Advances*, 5(5):eaau6062, 2019.

[399] H. F. Tiersten. Wave propagation in an infinite piezoelectric plate. *The Journal of the Acoustical Society of America*, 35(2):234–239, 1963.

[400] Y. Tomita, M. Sugimoto, and K. Eda. Direct bonding of linbo3 single crystals for optical waveguides. *Applied Physics Letters*, 66(12):1484–1485, 1995.

[401] S. Tonami, A. Nishikata, and Y. Shimizu. Characteristics of leaky surface acoustic waves propagating on linbo 3 and litao 3 substrates. *Japanese Journal of Applied Physics*, 34 (5S):2664, 1995.

[402] A. Tovar, M. Patel, and A. P. Lee. Acoustic cavity transducers for the manipulation of cells and biomolecules. In *BiOS*, pages 757402–757402. International Society for Optics and Photonics, 2010.

[403] A. R. Tovar and A. P. Lee. Lateral cavity acoustic transducer. *Lab on a Chip*, 9(1):41–43, 2009.

[404] A. R. Tovar, M. V. Patel, and A. P. Lee. Lateral air cavities for microfluidic pumping with the use of acoustic energy. *Microfluidics and Nanofluidics*, 10(6):1269–1278, 2011.

[405] S. Tran, P. Marmottant, and P. Thibault. Fast acoustic tweezers for the two-dimensional manipulation of individual particles in microfluidic channels. *Applied Physics Letters*, 101 (11):114103, 2012.

[406] W.-K. Tseng, J.-L. Lin, W.-C. Sung, S.-H. Chen, and G.-B. Lee. Active micro-mixers using surface acoustic waves on y-cut 128 linbo3. *Journal of Micromechanics and Microengineering*, 16(3):539, 2006.

[407] T. Tsukahara, K. Mawatari, and T. Kitamori. Integrated extended-nano chemical systems on a chip. *Chemical Society Reviews*, 39(3):1000–1013, 2010.

[408] D. Tulli, D. Janner, and V. Pruneri. Room temperature direct bonding of linbo3 crystal layers and its application to high-voltage optical sensing. *Journal of Micromechanics and Microengineering*, 21(8):085025, 2011.

[409] F. I. Uba, B. Hu, K. Weerakoon-Ratnayake, N. Oliver-Calixte, and S. A. Soper. High process yield rates of thermoplastic nanofluidic devices using a hybrid thermal assembly technique. *Lab on a Chip*, 15(4):1038–1049, 2015.

[410] T. Uchida, T. Suzuki, and S. Shiokawa. Investigation of acoustic streaming excited by surface acoustic waves. In *Ultrasonics Symposium, 1995. Proceedings., 1995 IEEE*, volume 2, pages 1081–1084. IEEE, 1995.

[411] K. Uchino and S. Hirose. Loss mechanisms in piezoelectrics: how to measure different losses separately. *IEEE Transactions on Ultrasonics, Ferroelectrics, and Frequency Control*, 48(1):307–321, 2001.

[412] P. Utko, F. Persson, A. Kristensen, and N. B. Larsen. Injection molded nanofluidic chips: fabrication method and functional tests using single-molecule dna experiments. *Lab on a Chip*, 11(2):303–308, 2011.

[413] P. van Capel, E. Péronne, and J. Dijkhuis. Nonlinear ultrafast acoustics at the nano scale. *Ultrasonics*, 56:36–51, 2015.

[414] J. W. van Honschoten, N. Brunets, and N. R. Tas. Capillarity at the nanoscale. *Chemical Society Reviews*, 39(3):1096–1114, 2010.

[415] H. Van Phan, M. B. Coşkun, M. Şeşen, G. Pandraud, A. Neild, and T. Alan. Vibrating membrane with discontinuities for rapid and efficient microfluidic mixing. *Lab on a Chip*, 15(21):4206–4216, 2015.

[416] L. Van Valen. A new evolutionary law. *Evol Theory*, 1:1–30, 1973.

[417] J. Vanherzeele, M. Brouns, P. Castellini, P. Guillaume, M. Martarelli, D. Ragni, E. P. Tomasini, and S. Vanlanduit. Flow characterization using a laser doppler vibrometer. *Optics and Lasers in Engineering*, 45(1):19–26, 2007.

[418] J. Vanneste and O. Bühler. Streaming by leaky surface acoustic waves. In *Proceedings of the Royal Society of London A: Mathematical, Physical and Engineering Sciences*, page rspa20100457. The Royal Society, 2010.

[419] H. W. Vayo. Some red blood cell geometry. *Can J Physiol Pharmacol*, 61(6):646–649, Jun 1983.

[420] D. J. Walther, J.-U. Peter, S. Winter, M. Höltje, N. Paulmann, M. Grohmann, J. Vowinckel, V. Alamo-Bethencourt, C. S. Wilhelm, G. Ahnert-Hilger, and M. Bader. Serotonylation of small gtpases is a signal transduction pathway that triggers platelet alpha-granule release. *Cell*, 115(7):851–862, Dec 2003.

[421] B. Wang and P. Král. Coulombic dragging of molecules on surfaces induced by separately flowing liquids. *Journal of the American Chemical Society*, 128(50):15984–15985, 2006.

[422] C. Wang, Y. Wang, Y. Zhou, Z.-Q. Wu, and X.-H. Xia. High-performance bioanalysis based on ion concentration polarization of micro-/nanofluidic devices. *Analytical and Bioanalytical Chemistry*, pages 1–10, 2019.

[423] S. Wang, Z. Jiao, X. Huang, C. Yang, and N.-T. Nguyen. Acoustically induced bubbles in a microfluidic channel for mixing enhancement. *Microfluidics and Nanofluidics*, 6(6): 847–852, 2009.

[424] Z. Wang and J. Zhe. Recent advances in particle and droplet manipulation for lab-on-a-chip devices based on surface acoustic waves. *Lab on a Chip*, 11(7):1280–1285, 2011.

[425] E. W. Washburn. The dynamics of capillary flow. *Physical Review*, 17(3):273, 1921.

[426] B. Watson, J. Friend, and L. Yeo. Piezoelectric ultrasonic micro/milli-scale actuators. *Sensors and Actuators A: Physical*, 152(2):219–233, 2009.

[427] K. M. Weerakoon-Ratnayake, C. E. O'Neil, F. I. Uba, and S. A. Soper. Thermoplastic nanofluidic devices for biomedical applications. *Lab on a Chip*, 17(3):362–381, 2017.

[428] R. Weis and T. Gaylord. Lithium niobate: summary of physical properties and crystal structure. *Applied Physics A*, 37(4):191–203, 1985.

[429] M. Weiser, R. Apfel, and E. Neppiras. Interparticle forces on red cells in a standing wave field. *Acta Acustica united with Acustica*, 56(2):114–119, 1984.

[430] M. Whitby and N. Quirke. Fluid flow in carbon nanotubes and nanopipes. *Nature Nanotechnology*, 2(2):87–94, 2007.

[431] R. White. Acoustic and vibration transducers and measurement techniques. *Journal of Physics E: Scientific Instruments*, 18(9):790, 1985.

[432] R. M. White and F. W. Voltmer. Direct piezoelectric coupling to surface elastic waves. *Applied Physics Letters*, 7(12):314–316, 1965.

[433] G. M. Whitesides. The origins and the future of microfluidics. *Nature*, 442(7101):368, 2006.

[434] J. Z. Wilcox and R. E. Brooks. Time-fourier transform by a focusing array of phased surface acoustic wave transducers. *Journal of Applied Physics*, 58(3):1148–1159, 1985.

[435] R. Williamson. Case studies of successful surface-acoustic-wave devices. In *Ultrasonics Symposium, 1977*, pages 460–468. IEEE, 1977.

[436] R. Wilson, J. Reboud, Y. Bourquin, S. L. Neale, Y. Zhang, and J. M. Cooper. Phononic crystal structures for acoustically driven microfluidic manipulations. *Lab on a Chip*, 11(2): 323–328, 2011.

[437] A. Winkler, P. Bergelt, L. Hillemann, and S. Menzel. Influence of Viscosity in Fluid Atomization with Surface Acoustic Waves. *Open Journal of Acoustics*, 6:23–33, 2016. ISSN 2162-5786. doi: 10.4236/oja.2016.63003.

[438] A. Winkler, S. Harazim, D. Collins, R. Brünig, H. Schmidt, and S. Menzel. Compact SAW aerosol generator. *Biomedical Microdevices*, 19(1):9, 2017.

[439] S. Winnall and S. Winderbaum. Lithium niobate reactive ion etching. Technical report, DEFENCE SCIENCE AND TECHNOLOGY ORGANIZATION SALISBURY (AUSTRALIA), 2000.

[440] C. Witte, J. Reboud, R. Wilson, J. Cooper, and S. Neale. Microfluidic resonant cavities enable acoustophoresis on a disposable superstrate. *Lab on a Chip*, 14(21):4277–4283, 2014.

[441] A. Wixforth, C. Strobl, C. Gauer, A. Toegl, J. Scriba, and Z. v. Guttenberg. Acoustic manipulation of small droplets. *Analytical and Bioanalytical Chemistry*, 379(7-8):982–991, 2004.

[442] H. Wohltjen. Mechanism of operation and design considerations for surface acoustic wave device vapour sensors. *Sensors and Actuators*, 5(4):307–325, 1984.

[443] C. Wood, S. Evans, J. Cunningham, R. O'Rorke, C. Wälti, and A. Davies. Alignment of particles in microfluidic systems using standing surface acoustic waves. *Applied Physics Letters*, 92(4):044104, 2008.

[444] C. Wood, J. Cunningham, R. O'Rorke, C. Wälti, E. Linfield, A. Davies, and S. Evans. Formation and manipulation of two-dimensional arrays of micron-scale particles in microfluidic systems by surface acoustic waves. *Applied Physics Letters*, 94(5):054101, 2009.

[445] J. Wu, R. Chantiwas, A. Amirsadeghi, S. A. Soper, and S. Park. Complete plastic nanofluidic devices for dna analysis via direct imprinting with polymer stamps. *Lab on a Chip*, 11 (17):2984–2989, 2011.

[446] M. Wu, Z. Mao, K. Chen, H. Bachman, Y. Chen, J. Rufo, L. Ren, P. Li, L. Wang, and T. J. Huang. Acoustic separation of nanoparticles in continuous flow. *Advanced Functional Materials*, 27(14), 2017.

[447] M. Wu, Y. Ouyang, Z. Wang, R. Zhang, P.-H. Huang, C. Chen, H. Li, P. Li, D. Quinn, M. Dao, et al. Isolation of exosomes from whole blood by integrating acoustics and microfluidics. *Proceedings of the National Academy of Sciences*, page 201709210, 2017.

[448] T.-T. Wu, H.-T. Tang, and Y.-Y. Chen. Frequency response of a focused SAW device based on concentric wave surfaces: simulation and experiment. *Journal of Physics D: Applied Physics*, 38(16):2986, 2005.

[449] T.-T. Wu, H.-T. Tang, Y.-Y. Chen, and P.-L. Liu. Analysis and design of focused interdigital transducers. *IEEE Transactions on Ultrasonics, Ferroelectrics, and Frequency Control*, 52 (8):1384–1392, 2005.

[450] J. Xu, C. Wang, Y. Tian, B. Wu, S. Wang, and H. Zhang. Glass-on-linbo3 heterostructure formed via a two-step plasma activated low-temperature direct bonding method. *Applied Surface Science*, 459:621–629, 2018.

[451] S. Xu and Z. L. Wang. One-dimensional ZnO nanostructures: solution growth and functional properties. *Nano Research*, 4(11):1013–1098, 2011.

[452] K. Yamanouchi and K. Shibayama. Propagation and amplification of Rayleigh waves and piezoelectric leaky surface waves in $LiNbO_3$. *Journal of Applied Physics*, 43(3):856–862, 1972.

[453] D. Yang. Ultrasonic range finder, Feb. 12 2008. US Patent 7,330,398.

[454] Z. Yang, S. Matsumoto, H. Goto, M. Matsumoto, and R. Maeda. Ultrasonic micromixer for microfluidic systems. *Sensors and Actuators A: Physical*, 93(3):266–272, 2001.

[455] G. G. Yaralioglu, I. O. Wygant, T. C. Marentis, and B. T. Khuri-Yakub. Ultrasonic mixing in microfluidic channels using integrated transducers. *Analytical Chemistry*, 76 (13):3694–3698, 2004.

[456] L. Yarovoi and G. Siegmund. The effect of three-wave interference in laser doppler vibrometry. *Measurement Science and Technology*, 15(10):2150, 2004.

[457] L. Y. Yeo and J. R. Friend. Surface acoustic wave microfluidics. *Annual Review of Fluid Mechanics*, 46:379–406, 2014.

[458] K. Yosioka and Y. Kawasima. Acoustic radiation pressure on a compressible sphere. *Acta Acustica united with Acustica*, 5(3):167–173, 1955.

[459] H. Yu, Q. Zou, J. W. Kwon, D. Huang, and E. S. Kim. Liquid needle. *Journal of Microelectromechanical Systems*, 16(2):445–453, 2007.

[460] T. A. Zangle, A. Mani, and J. G. Santiago. Theory and experiments of concentration polarization and ion focusing at microchannel and nanochannel interfaces. *Chemical Society Reviews*, 39(3):1014–1035, 2010.

[461] Q. Zeng, H. Chan, X. Zhao, and Y. Chen. Enhanced particle focusing in microfluidic channels with standing surface acoustic waves. *Microelectronic Engineering*, 87(5):1204–1206, 2010.

[462] G.-Q. Zhang, K.-y. Hashimoto, and M. Yamaguchi. Liquid streaming by high-frequency ultrasonic waves. *Japanese Journal of Applied Physics*, 35(5S):3248, 1996.

[463] N. Zhang and J. Friend. Fabrication of nanoheight channels incorporating surface acoustic wave actuation via lithium niobate for acoustic nanofluidics. *JoVE (Journal of Visualized Experiments)*, (156):e60648, 2020.

[464] N. Zhang, A. Horesh, O. Manor, and J. Friend. Powerful acoustic streaming from dynamic geometric nonlinearity. *Physical Review Letters*, page (in revision).

[465] N. Zhang, J. Mei, T. Gopesh, and J. Friend. Optimized, omnidirectional surface acoustic wave source: 152 degree Y-rotated cut of lithium niobate for acoustofluidics. *IEEE Transactions on Ultrasonics, Ferroelectrics, and Frequency Control*, 67(10):2176–2186, 2020. doi: 10.1109/TUFFC.2020.2993766.

[466] N. Zhang, A. Horesh, and J. Friend. Manipulation and mixing of 200 femtoliter droplets in nanofluidic channels using mhz-order surface acoustic waves. *Advanced Science*, (Accepted 12 March 2021), 2021.

[467] N. Zhang, A. Horesh, O. Manor, and J. Friend. Powerful acoustogeometric streaming from dynamic geometric nonlinearity. *Physical Review Letters*, (Accepted 19 March 2021), 2021.

[468] P. Zhang, H. Bachman, A. Ozcelik, and T. J. Huang. Acoustic microfluidics. *Annual Review of Analytical Chemistry*, 13:17–43, 2020.

[469] Q. B. Zhang and J. Zhao. A review of dynamic experimental techniques and mechanical behaviour of rock materials. *Rock Mechanics and Rock Engineering*, 47(4):1411–1478, 2014.

[470] Y. Zhang, B. Zhu, Y. Liu, and G. Wittstock. Hydrodynamic dispensing and electrical manipulation of attolitre droplets. *Nature Communications*, 7(1):1–7, 2016.

[471] L. Zhu, K. Hallamasek, and D. Bogy. Measurement of head/disk spacing with a laser interferometer. *IEEE Transactions on Magnetics*, 24(6):2739–2741, 1988.